Fluid and MHD Instabilities: Non-Trivial and Time-Dependent Basic States

Patrick Martin Lewis

Submitted in accordance with the requirements for the degree of

Doctor of Philosophy

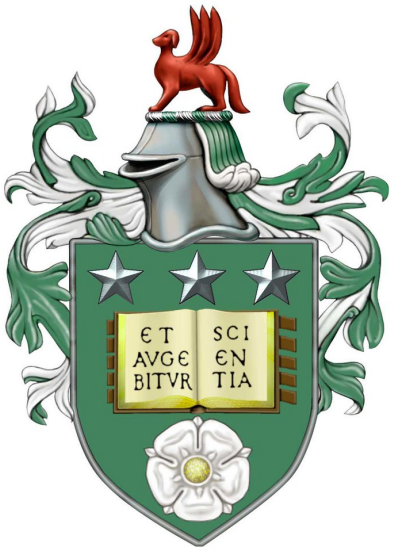

University of Leeds

Science and Technology Facilities Council

August 2022

To my Mum and late Dad.

"One must imagine Sisyphus happy."

— Albert Camus

Intellectual Property Statement

The candidate confirms that the work submitted is his own and that appropriate credit has been given where reference has been made to the work of others.

This copy has been supplied on the understanding that it is copyright material and that no quotation from the thesis may be published without proper acknowledgement.

Acknowledgements

I would like to extend my gratitude to all of those who helped me complete this work, both academically and personally.

First, I would like to thank my supervisors, Prof. David W. Hughes and Dr. Evy Kersalé, for their wisdom and guidance throughout the duration of my PhD study — words cannot express my gratitude for their patience and feedback, especially during the uncertainty and lifestyle changes associated with SARS-CoV-2. Without their consistent support and advice this work would not have been possible. I will be forever grateful for the chance to have worked with them. I would like to thank my examiners Prof. Rainer Hollerbach and Prof. Alan Hood for their constructive feedback. Further recognition must be given to current and former members of the Astrophysical and Geophysical Fluid Dynamics Research group in Leeds, specifically Christina, Daniela, and Joseph for supporting me and sharing in the day-to-day experience of completing my PhD and being good friends outside University.

On a personal note I would like to thank my Mother and Step-Father; Patsy and James. Both of you have listened when times were tough and gave me the strength to carry on while being there throughout the good, but more importantly the bad. My sisters; April and Kitty, for encouraging me throughout many years of education despite not really understanding what I was doing. Finally, thank you to Lottie: you believed in me when I did not, and put up with me unwaveringly through the toils of research. Your love, friendship, and support has helped me more than you know.

This research has been funded by a grant (2106273) from the Science and Technology Facilities Council, to whom I would like to also extend my thanks.

Abstract

It is widely accepted that the coherent structures that we observe on the solar surface are the result of magnetic field interactions across a wide range of scales. The leading suggestion is that flux tubes rise throughout the convection zone via a mechanism called magnetic buoyancy. The mechanism by which large scale, toroidal magnetic fields are generated is understood through dynamo theory, and most dynamo models agree that poloidal magnetic fields are wound up in a location of strong velocity shear called the Solar Tachocline. The solar dynamo, and therefore modelling the Sun is made difficult by the fact that the magnetic field reacts back in the flow through the Lorentz force. In addition to this, the Solar Tachocline lives at the base of the convection zone, and therefore an understanding of solar convection is significantly important. All of this considered, modelling the Sun, and hence magnetic buoyancy can be a complex nonlinear problem. While there have been nonlinear studies into the relationship between shear, convection, and magnetic buoyancy, nonlinear numerical experiments are hard to conduct and the results can be hard to interpret. In addition to this, the interactions between shear flow and magnetic field within the Tachocline are ultimately a time-dependent process, and so linear studies where the basic state is steady are limited in their scope.

With this motivation, we consider a set of linear stability problems where the basic state is either non-trivial or time-dependent, with the ultimate aim to study magnetic buoyancy instabilities of a time-evolving magnetic field generated by the transverse shearing of a perpendicular uniform magnetic field. We consider the joint linear stability of a steady parallel shear flow and magnetic field, which are linked self-consistently. We find that on one end of parameter space, the resultant instabilities are hydrodynamic and can be described through the Orr-Sommerfeld equation. On the opposite end of the parameter space, we find that the dominant instability is a tearing mode, which can be understood through an equation analogous to the Orr-Sommerfeld equation, in which we consider a parallel resistive magnetic field. In the middle of this parameter space, we find that instabilities are possible where both field and flow are important. We find that a hydrodynamically stable flow can enhance the instability of an unstable basic magnetic field. Taking another step towards the main enterprise, we then consider the same process of generating the field and flow, however the shearing takes place in the presence of a stably-stratified and compressible atmosphere. We find that a multitude of instabilities, i.e.

undular and interchange modes are possible. In addition to this, we derive a stability criterion for magnetic buoyancy in terms of the imposed shear flow. We find that this instability criterion is reasonable at predicting the onset of interchange and undular mode instabilities. Furthermore, we find that 2D undular modes are possible in such a system. This is surprising, as in the absence of a velocity shear, 2D undular modes are understood to be hard to destabilise. In addition to this, viscosity is thought to have a stabilising effect, however we find that increasing the viscosity can lead to destabilisation of the basic state. The role of viscosity is shown through the basic state analysis which shows that the amplitude of the basic state horizontal magnetic field is linearly proportional to viscosity.

We then wish to incorporate time-dependence into the analysis. Performing a time-dependent linear stability analysis is difficult as one cannot perform a typical modal analysis, in which solutions are separated into exponentially decaying/growing waves. The main hurdle is therefore defining a suitable measure of instability. We study the time-dependent linear stability analysis of a classical problem — Rayleigh Bénard convection. We consider two types of time-dependent basic temperature fields which are considered within the literature: i) linear cooling at the top boundary, and ii) period modulation of the temperature at the top and bottom boundary. We reproduce the results within the literature and extend the investigation to unstudied asymptotic regimes. We find that when the amplitude of the periodic modulation at the boundaries is increasingly large, then the system becomes asymptotically unstable, i.e. $Ra_c \to 0$. In this chapter the main aim is to illustrate the difficulties associated with performing a time-dependent linear stability analysis. We show that the definition of a stability boundary is often problem specific, and either involves characteristics of the problem, or defining a global measure.

With this in mind, we investigate magnetic buoyancy instabilities of a time-varying magnetic field. First, we find that the transient evolution of the basic state configuration depends heavily on the initial conditions. Then, through a frozen-in-time analysis, we find a multitude of instabilities are present throughout the evolution of the basic state. Finally, we define a global measure of kinetic and magnetic energy to characterise the onset of instability. We consider two sets of initial conditions for the perturbed quantities, and show that there is an initial condition which results in optimal growth of the disturbed quantities. We then justify the choice of parameters and discuss extensions to the problem considered.

Contents

List of Figures

List of Tables

Chapter 1

Introduction

1.1 The History of the Sun

There are more than 200 billion trillion stars within the observable Universe. Within the Milky Way — which is a galaxy comparatively small to the observable Universe — there is still a vast number of stars — approximately 100 thousand million. On an even smaller scale is our solar system, home to planet Earth. For perspective, our Solar system is approximately 160 million times smaller than the extent of the Milky Way, but stretches the distance of roughly 36 billion Earths back-to-back. Despite the large extent of the solar system, it is home to just one star — the Sun.

The earliest observations of the Sun date back to the times of ancient astronomers, who observed the position of the Sun. This is not surprising as the Sun is a necessary life force for life on Earth, as it provides energy, light, and heat through radiation. Following the advent of the scientific method, formal observations of the Sun were made, for example the Babylonians and Greeks were known to record incidences of solar eclipses, which were taken to be astrological omens of great significance. Concurrently, ancient Chinese astronomers had recorded a more ephemeral phenomenon with the naked eye — dark blemishes that would later be found to move along the solar surface, which were coined sunspots. The records of the ancient Chinese astronomers can be dated back to as early as 800BC; much later, in 1128, is the earliest surviving drawing of a sunspot, drawn by a monk named John of Worcester.

Despite the long history of sunspots prior to the 17th Century, it was not until after the invention of the telescope that observations of sunspots were fully formalised. Around 1610, independent astronomers, namely Johann Goldsmid (1587-1616, a.k.a. Fabricius) in Holland, Thomas Harriot (1560-1621) in England, Galileo Galilei (1564-1642) in Italy, and the Jesuit Christoph Scheiner (1575-1650) in Germany, pointed their telescopes towards the Sun, and subsequently published documents on sunspots. Fabricius was first to publish his results: he documented the motion of sunspots to be caused by the axial rotation of the Sun. Galileo and Scheiner were interested in using sunspots to infer physical properties of the Sun: Scheiner suggested these dark blemishes were actually small mercurial-like

planets closely orbiting the Sun. Galileo refuted this and was credited with presenting a convincing case that sunspots are a feature of the solar surface. Interestingly, priority over sunspot discovery was a catalyst in the worsening of the relationship between the pair. Scheiner presented his work under the pseudonym Appelles to avoid embarrassment of the Religious Order of the Catholic Church in case his findings were spurious. He subsequently pursued the observation of sunspots for another 15 years.

Humankind observed sunspots more, and it became apparent that sunspot formation occurred on a cycle with a period of approximately 11 years. Incidences of sunspots were found to reach a maximum, before falling off before the end of the 11-year cycle. It was observed that sunspots generally started at higher latitudes on the solar surface, with the pattern moving towards the solar equator as the solar cycle reaches its maximum incidence of sunspots. Generally, it was observed that sunspots occurred in pairs, or other complex groupings, and these observations were key to our further understanding of the solar interior. Due to technology limitations and a lack of theory at the time, the interior of the Sun along with its associated magnetic field was poorly understood. Hale (1908) suggested that sunspots were intimately linked to the interior of the Sun, as they were inherently associated with the solar magnetic field, and were indicators of the evolution of the large-scale field over the whole solar cycle. It is understood that sunspots appear dark, as strong magnetic flux pierces the solar surface, inhibiting convection in a localised area. Due to this, hot material cannot rise as efficiently from the interior of the Sun, and thus less emission is produced within these regions. The explanation by Hale (1908) accounts for the fact that sunspots appear in pairs or other complex groupings, as magnetic fields must be divergence free ($\nabla \cdot \boldsymbol{B} = 0$), and so the magnetic field lines cannot end — that is, magnetic flux that pierces the solar atmosphere must re-pierce at a different location. It was therefore thought that sunspots are 'footprints' of the solar magnetic field, which is interesting since, despite the complex nature of the solar magnetic field, we generally observe that sunspots are organised in both occurrence and position.

Sunspots can lead to energetic explosions at the solar surface known as Coronal Mass Ejections (CMEs) and solar flares. Generally, CMEs occur when highly twisted magnetic fields contained within the Sun become too stressed, and undergo a process, understood as magnetic reconnection, in which they rejoin and align in a less tense configuration. This reconnection event can expel billions of tonnes of coronal material that is embedded with a magnetic field that is stronger than the background solar wind interplanetary magnetic field. While the majority of these events have no impact on Earth, they can have negative impacts, with one of the only positive results being the Aurora Polaris. Earth's magnetic field protects us from the resultant influx of radiation, but is occasionally overcome, resulting in geomagnetic storms. This can lead to disruptions in satellite communications, high altitude navigation systems, and the electric grid.

1.2 Solar Structure & Observations

In this section, we first give a brief overview of the gross properties of the Sun. We will then look in more detail at the internal solar structure, discussing the individual layers — in particular, the convection zone, the tachocline, and the radiative zone. We will discuss theoretical results and observations within the literature, providing a brief discussion of the relevant physical mechanisms and their importance for solar modelling.

The Sun has a mass of around $M_\odot = 2 \times 10^{30}$kg, with a surface temperature of $5,778$K. Stars are classified generally by their surface temperature, with the Sun being a G-type main-sequence star: the majority of energy in G-type stars is produced inside the core through nuclear fusion reactions, in which hydrogen is converted into helium. The solar radius is given by $R_\odot \approx 7 \times 10^8$m.

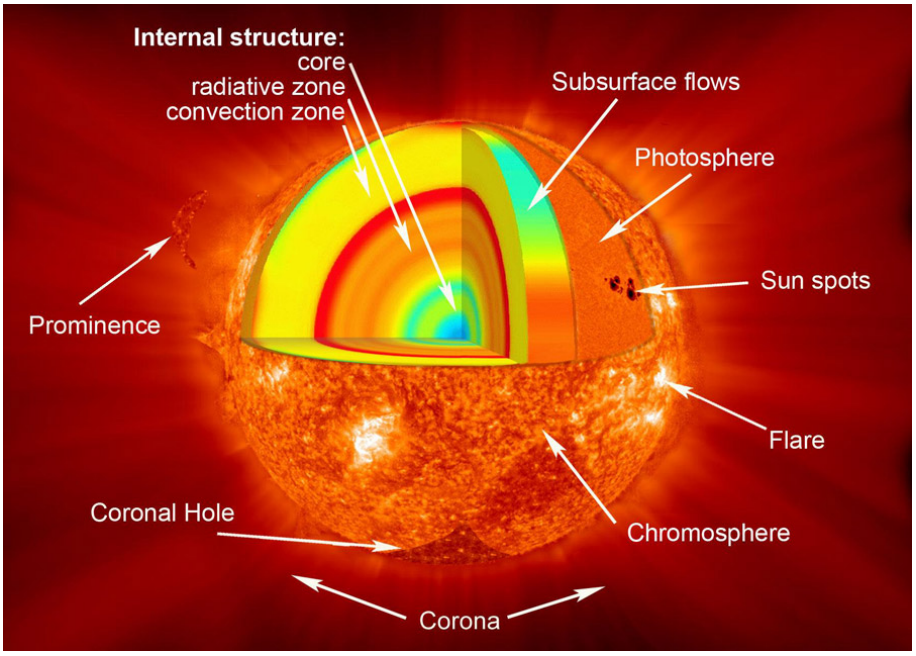

Figure 1.1: The structure of the Sun, image courtesy of UCAR — Center of Science Education.

Figure 1.1 qualitatively describes the solar structure. The Sun is generally split into three main regions: the interior, the solar atmosphere, and the visible 'surface' of the Sun which is labelled the photosphere. The interior is itself split into three regions: the core, the radiative zone, and the convective zone. The core is the hottest region of the Sun and accounts for approximately 34% of the Sun's mass, but only 0.8% of the solar volume. The temperature and pressure are significant enough for hydrogen nuclei to overcome the Coulomb repulsion, binding into larger elements such as Helium. The nuclear fusion reaction responsible for generating all of the energy of the Sun is the proton-proton chain reaction. Assuming a uniform temperature, we can simply calculate the power generation of the core through the Stefan-Boltzmann law — this result is in excess of observations, but this discrepancy is accounted for by the variation in temperature which varies radially outwards from the core. It is this difference in radiation powers that mainly determines

the net power generation and heat transfer from the solar core.

Characterised by its low temperature, the next layer outwards is called the radiation zone which is defined by the region $0.2R_\odot - 0.7R_\odot$. The radiative zone is dense in material and so photons travel only a short distance before they are scattered or absorbed, and therefore the time-scale for gamma rays to escape is significantly large. This region is strongly stratified and therefore stable against convection, inhibiting the formation of convection cells.

The outermost region of the interior of the Sun is called the convection (or convective) zone. Unsurprisingly, the dominant mode of energy transfer in this layer is convection; heat moves upwards via rolling convection, similar to bubbles in a boiling kettle. This is roughly understood through considering a fluid parcel moving upwards within the convection zone. Under adiabatic expansion, the fluid parcel's density will become less than that of its surroundings and will experience a net upwards force. The criteria for rise is given by

$$\frac{\mathrm{d}\log\rho}{\mathrm{d}\log P} > \frac{1}{\gamma}, \tag{1.1}$$

where P is the pressure, ρ is the density, and γ is the heat capacity ratio. The convective zone is well mixed, and the surface of the convection zone is the origin of most of the photons that escape from the Sun (the Photosphere). We can only directly observe the outer region of the convection zone, and telescopic images (with an appropriate filter) show the surface of the Sun as white with sunspots. We can however probe the lower regions of the convection zone using helioseismology; a technique which measures oscillations of the Sun caused primarily by sound waves.

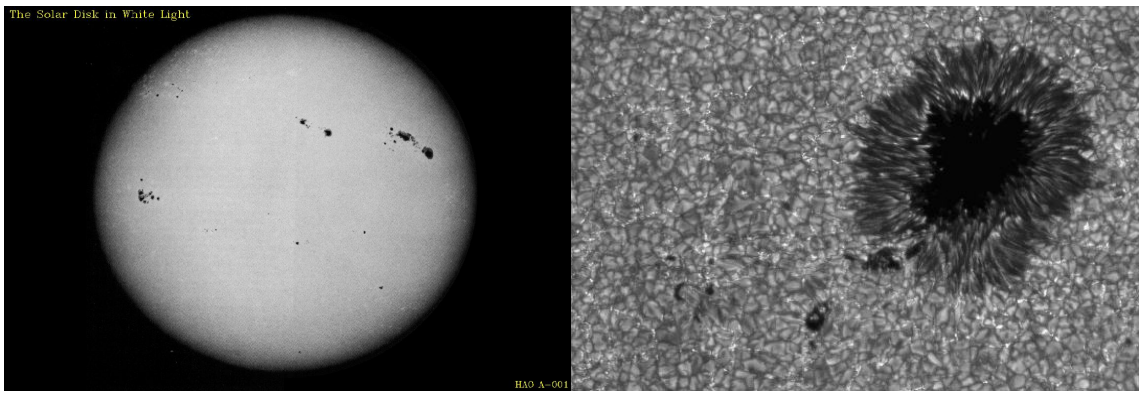

(a) Image courtesy of High Altitude Observatory

(b) Image taken by T. Berger at La Palma using Swedish Solar Telescope

Figure 1.2: X-Ray images of the solar surface at different levels of magnification.

In Figs 1.2, white zones are hot and darker regions are cold. Figure 1.2a shows the outermost region of the convection zone — sunspots are clearly seen on the surface, appearing in complex configurations and generally grouped around the solar equator as previously described. Figure 1.2b shows a more detailed picture of a sunspot. As well as the dark

sunspot, we can see the convection cells — which give the solar surface a granular appearance and are characteristic of thermal convection. As we will discuss later, simulating the convection zone is a challenge; for one, the plasma is not very viscous and so motions are complicated and therefore turbulence ensues. Another key feature of the convection zone is that it is rotating. This results in the Coriolis force, which causes a swirling motion as fluid rises or falls.

1.2.1 The Solar Cycle

It is important to clarify that the solar cycle is not the same as the sunspot cycle. It so happens that the solar magnetic field reverses polarity every 11 years, and hence a full solar cycle occurs with a 22-year cycle. This is an important distinction, as it leads to the sunspot cycle being characterised only by the incidence of said structures.

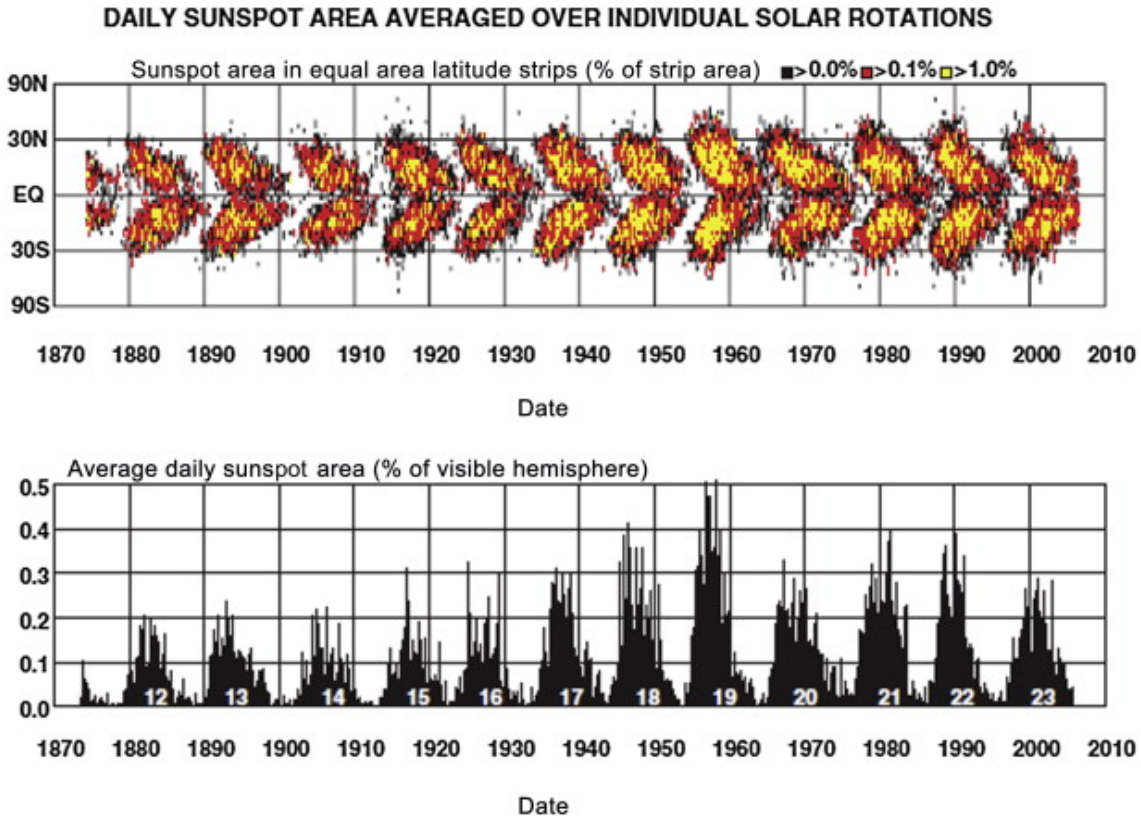

Figure 1.3: Butterfly diagram showing temporal evolution of sunspot position (top) and the average sunspot coverage vs. time, which is a similar measure of the solar cycle activity as the sunspot number (bottom). Image courtesy of nasa.gov.

The most active phase of the solar cycle is characterised by a maximum in sunspot incidence. Figure 1.3 demonstrates that, over the solar cycle, collections of sunspots move from higher latitudes towards the equator — this figure is known as a butterfly diagram. We can see that sunspot number is at its maximum in the middle of a sunspot cycle, and since sunspots are inherently linked to the internal magnetic field, it is understood that this corresponds to a maximum in magnetic activity. It is at this solar maximum when solar flares and CMEs are most frequent. Groupings of sunspots appear at around 30° to

45° above and below the equator and Fig 1.3 illustrates that more sunspots appear near the equator as the cycle continues — this variation was first observed in 1961 by Richard Christopher Carrington and later became known as Spörer's Law.

Despite the regular variation of sunspots observed on the solar surface, there have been periods in which sunspots were not observed. For approximately 70 years from A.D. 1645 to 1715 there was no documentation of sunspots — this period of disruption to the cycle is known as the *Maunder Minimum*. The Maunder Minimum is indicated in Fig 1.4.

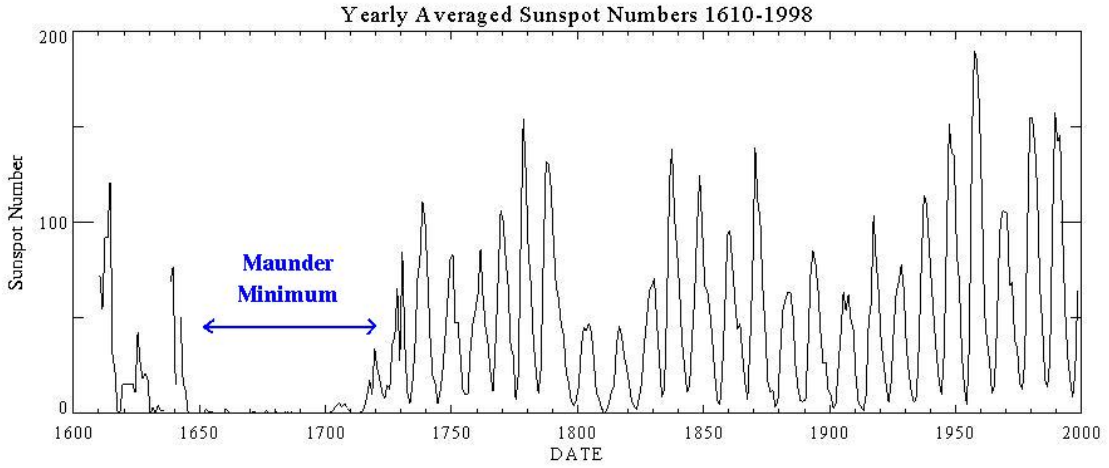

Figure 1.4: Evolution of sunspot count from ∼1600 to 2000. The Maunder Minimum is labelled, where very few sunspots were observed Image credit: nwra.com.

Initially, one would assume that the drop in sunspot incidence was a consequence of a lack of solar observation, or at least a drop in systematic observations. However, there had been several influential astronomers observing the Sun at this time; one in particular, Jean Picard, a French astronomer who was credited with accurately measuring the size of Earth. During the Maunder Minimum, the average temperature on Earth was colder than usual, and there was a subsequent period of colder weather in Western Europe. This period is known as the Little Ice Age, but colder temperatures had set in much earlier than the Maunder Minimum. Scientists speculated that there was a connection between sunspot incidence (and hence solar magnetic activity) and climate — whether this is true remains unclear and is under further research. Interestingly, scientists have identified other periods of low solar magnetic activity, which are concurrent with colder temperatures on Earth.

1.2.2 Solar Rotation and the Solar Tachocline

All celestial bodies are formed from condensed clouds. A situation in which these bodies lack any angular momentum would be a true anomaly and has not been observed. Even if the cloud is slowly rotating, when it collapses into a more dense object such as a planet, star, or cluster of stars, conservation of angular momentum dictates that the rotation speed will increase. In conclusion, it is highly likely that all celestial bodies rotate, e.g., the

Sun. There are typically two types of rotation in mechanics — solid body and differential rotation. If we consider a solid sphere, then each point at a given radius will rotate at the same speed — this is typically what we think of in terms of rotation, for example a football. Differential rotation is when different points of a rotating object move with different rotational velocities at different latitudes and/or depths. Galileo is credited with observing the rotational velocity of the Sun, and Christoph Scheiner later reported that the Sun's rotational velocity varied latitudinally from the equator to the poles, therefore suggesting the Sun is differentially rotating. In particular, the rotational period at the equator is 25 days, whereas it is 34 days at the poles — this can be seen in Fig 1.5.

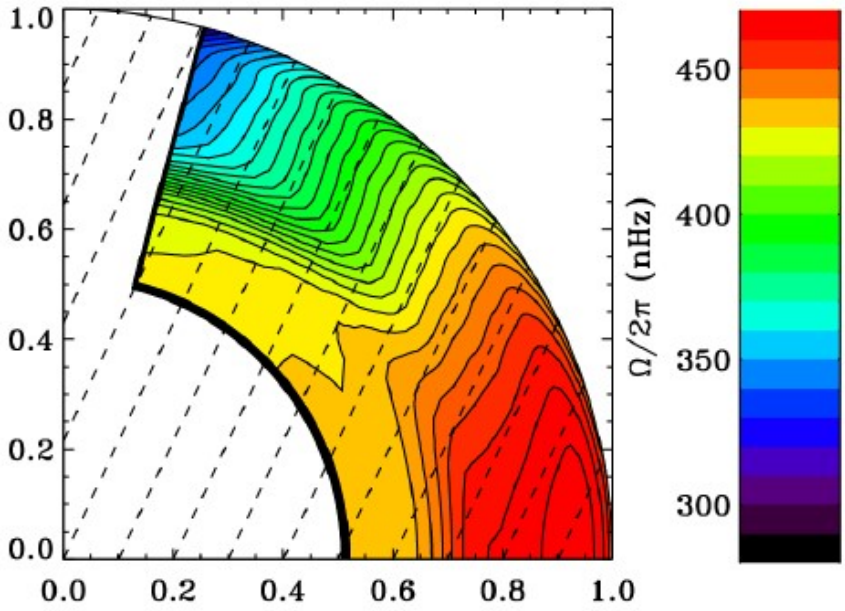

Figure 1.5: Observation of differential rotation profile for the outer convection zone from helioseismological measurements over 1995-2009. Image credit: NSO/GONG, 2009.

As previously stated, the use of helioseismology has allowed us to gain insight into the interior of the Sun. Figure 1.5 shows that, within the convective zone, the angular velocity at a given latitude remains roughly constant with depth, with red corresponding to higher rotational speeds and blue to slower. Throughout the convection zone, the rotational speed at a fixed radius may be approximated by

$$\Omega(\theta) = \Omega_{eq}(1 - a\cos^2\theta - b\cos^4\theta), \tag{1.2}$$

where Ω_{eq} is the rotation rate at the equator, θ the colatitude, and a, b are determined by observations. Helioseismology measurements have shown that this rotation profile does not persist through to the radiation zone and beyond. Figure 1.6 illustrates the rotational profile as a function of relative radius for the Sun. This observational data indicates that while the convection zone is generally differentially rotating, the radiation zone rotates like a solid body. This abrupt change in rotation at the base of the convection zone gives rise to a thin $(0.02 - 0.05R_\odot)$ interface layer which is home to a strong velocity shear — this special region is called the solar tachocline. The function and maintenance of the solar

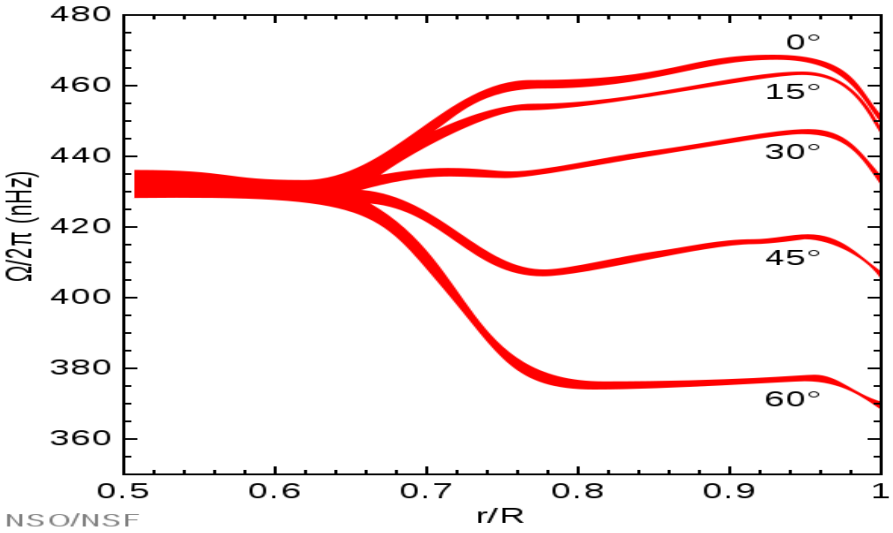

Figure 1.6: Internal rotational speeds for the Sun as a function of relative radius. Image credit: NSO/GONG.

tachocline is a complex process, involving considerations of angular momentum and the transition between the super-adiabatic convection zone and the sub-adiabatic radiation zone. Precisely how the tachocline exists is a topic of considerable research interest (see, for example, Hughes et al. (2007)).

The solar tachocline plays a crucial role in the transport of energy, mass, and magnetic field throughout the Sun — for more detail, one should consult Hughes et al. (2007). The naming of the solar tachocline was first coined by Spiegel and Zahn (1992), and there have been observational studies before and after this which characterised properties of the solar tachocline such as position and rotation (Basu et al., 1994; Brown, 1985; Duvall et al., 1984).

The strong velocity shear due to the solar tachocline is a necessary component of a process within the Sun called the solar dynamo. This mechanism is crucial for the self-sustaining generation of the solar magnetic field. We will discuss this process along with associated dynamo theory, in the next section.

1.3 Progress Towards Modelling The Sun

Conducting high fidelity numerical simulations of the Sun is a complicated process and a global enterprise. The solar structure is rich in complexity, and involves many aspects of computational mathematics and multiple facets of physics: electromagnetism, fluid dynamics, and thermodynamics. Not only are there multiple complex processes taking part in the Sun, we are faced with unique challenges associated with time and spatial scales. Solar processes act across a wide range of scales — we observe both large and small scale magnetic structures, we observe a multitude of convective cell sizes, and the convective region is highly turbulent: this in itself is an unsolved problem within fluid mechanics.

Improving existing numerical methods is an active area of research; see, for example, Tang et al. (2022), Degond and Deluzet (2017), Jardin (2012) who investigate implicit methods for magnetically confined plasma across multiple scales. Another hurdle to overcome is due to the shear number of dimensional numbers. Incorporating too many variations at once can obscure the important or dominant physical processes and so it is useful to consider a couple of physical mechanisms relative to one another. The typical modelling philosophy incorporates non-dimensional parameters. However doing so comes with some caveats. For example, the Reynolds number, Re — which is a measure of inertial forces to viscous forces — is $\mathcal{O}(10^9)$ in the solar interior, and therefore simulations require an increasingly small resolution to accurately determine the evolution. Estimates for the dimensional values at the base of the convection zone are given in Table 1.1.

Definition	Symbol	Value
Density	ρ	$0.21\mathrm{g\,cm^{-3}}$
Pressure	P	$6.7 \times 10^{13}\mathrm{g\,cm^{-2}\,s^{-2}}$
Temperature	T	$2.3 \times 10^{6}\mathrm{K}$
Sound speed	c_s	$2.3 \times 10^{7}\mathrm{cm\,s^{-1}}$
Gravitational Acceleration	g	$5.4 \times 10^{4}\mathrm{cm\,s^{-2}}$
Buoyancy Freq.	N	$8 \times 10^{-4}\mathrm{s^{-1}}$
Adiabatic Exponent	γ	1.556
Density Scale Height	H_ρ	$0.12R_\odot$
Pressure Scale Height	H_P	$0.08R_\odot$
Kinematic Diffusivity	ν	$2.7 \times 10^{1}\mathrm{cm^2\,s^{-1}}$
Thermal Diffusivity	κ	$1.4 \times 10^{7}\mathrm{cm^2\,s^{-1}}$
Magnetic Diffusivity	η	$4.1 \times 10^{2}\mathrm{cm^2\,s^{-1}}$

Table 1.1: Estimates of parameter values within the tachocline, i.e. at $R = 0.7R_\odot$ (Gough, 2007).

There is also emerging research utilising modern developments in Machine Learning and computational science; extensive reviews on this subject are given by Zawawi et al. (2018) and Brunton et al. (2020). A complete solar model must predict all the aforementioned observations, however a full global model is unachievable and hence we need to concentrate on specific aspects of the problem: there has therefore been a continuous effort to study the multiple layers of the Sun individually. Not all research has been focused on high level nonlinear global simulations: there has been extensive work on topics such as convection and magnetic buoyancy within the linear regime, although these processes are highly nonlinear inside the Sun. We will give an overview of the literature and advancements in the areas of most interest for modelling of the Sun's interior — that is, the solar dynamo, convection, and subsequently, magnetic buoyancy.

1.3.1 The Solar Dynamo, Magnetism, and Velocity Shear

The solar dynamo is an important physical process that generates the solar magnetic field and, consequently, is partly responsible for driving the features we observe at the solar surface. Moving charges within the solar interior generate electric currents and a magnetic field — this process is explained through the laws of magnetohydrodynamics, Ampère, Faraday, and Ohm.

Generally, the solar dynamo is a complicated process. The crucial point is the role of inductive processes, i.e. field line stretching and folding overcome dissipative processes. The problem is made particularly difficult by the fact that the magnetic field reacts back on the flow through the Lorentz force. Thus it is a complex nonlinear problem in which flow and field must exist in such a way as to maintain the magnetic field.

By estimating the time-scales of rising flux tubes within the convection zone, Parker (1975) argued that the solar dynamo is located at the lowest part of the convection zone. This led to an interface, which Parker (1993) proposed as the deep seated dynamo. It was suggested that both the radial and latitudinal shear within the tachocline are responsible for producing strong toroidal magnetic fields from the Sun's much weaker poloidal field. It was then thought that this strong toroidal field can become unstable, resulting in features observed at the solar surface — sunspots, active regions, and solar flares. While this model lacks any other complicated processes such as convection or any descriptive turbulence, it is a good first start. In fact, it is still widely debated how the solar dynamo operates and it is generally still poorly understood (Tobias, 2002): for example, cooler stars have been observed to sustain strong solar-strength magnetic fields despite having no radiation zone, and therefore no tachocline — this could suggest the convection zone alone may be sufficient for sustaining dynamo action (Route, 2016). Despite this debate, it is generally agreed that any solar dynamo winds up large-scale poloidal magnetic fields to generate toroidal magnetic fields, which later rise through the convection zone before converting back into poloidal field to restart the process.

Under the right conditions, a solar dynamo could consistently generate the solar magnetic field. However, the diffusive time-scale, namely the Ohmic time-scale of the Sun is approximately $\mathcal{O}(10^{10})$ years, which is of the same order of magnitude as the age of the Sun. It is therefore possible that the solar magnetic field could be slowly decaying away, and any magnetic field we do observe on the solar surface is 'fossilised' within the Sun. However, as previously discussed, the Sun exhibits a solar cycle with a period of only a few years. It is therefore reasonable to assume that the reversal process within the Sun is indicative of a solar dynamo, and therefore of a self-generating magnetic field.

Derived from Maxwell's equations in the MHD approximation and Ohm's Law, the induc-

tion equation is given by

$$\frac{\partial \boldsymbol{B}}{\partial t} = \nabla \times (\boldsymbol{u} \times \boldsymbol{B}) - \nabla \times (\eta \nabla \times \boldsymbol{B}), \tag{1.3}$$

where $\boldsymbol{B}$ is the magnetic field, $\boldsymbol{u}$ is the velocity, and η is the magnetic diffusivity. In Eq 1.3, η can be spatially dependent, however, in this thesis we shall take η to be constant. Under this assumption, and using $\nabla \cdot \boldsymbol{B} = 0$, the induction equation is therefore given by

$$\frac{\partial \boldsymbol{B}}{\partial t} = \nabla \times (\boldsymbol{u} \times \boldsymbol{B}) + \eta \nabla^2 \boldsymbol{B}. \tag{1.4}$$

It is important to understand that, in general, $\boldsymbol{u}$ and $\boldsymbol{B}$ are solutions to the Navier-Stokes and induction equation respectively. Alternatively, one can think of the induction equation as describing how $\boldsymbol{B}$ evolves under a flow $\boldsymbol{u}$. Then one can think of the Navier-Stokes equation as how the field reacts back on the flow. In a 'dynamic' dynamo, the flow $\boldsymbol{u}$ follows self-consistently and is derived as a solution from the magnetic field. This problem is difficult to investigate both computationally and analytically, and therefore there is a simpler approach — the 'kinematic' dynamo. The kinematic dynamo assumes that the flow $\boldsymbol{u}$ is prescribed: this is motivated from the fact that the evolution of the magnetic field depends on the advection with flow as well as diffusion. From that, one seeks to find a fixed flow, $\boldsymbol{u}$ which does not result in the decay of $\boldsymbol{B}$ in the long term. The kinematic dynamo has been found to be useful from an astrophysical perspective, for example, Choudhuri et al. (1995); Dikpati and Charbonneau (1999); Guerrero and Muñoz (2004) investigated a kinematic dynamo with meridional circulation and was able to observe butterfly patterns similar to that seen in the solar cycle.

We will not discuss the mathematical details of the solar dynamo in depth, however since the magnetic field is divergence free in nature, one can express an axisymmetric field as the sum of a poloidal and toroidal component. One can then obtain an expression for the evolution of the toroidal component, which shows the toroidal field is generated from a poloidal field by differential rotation (the $\omega-$effect), and is advected by a meridional flow. Furthermore, one can write an expression for the evolution of the poloidal component of the magnetic field. This expression shows that there is no source term to generate the poloidal field, and hence the poloidal component will just decay. From this, Cowling (1933) states that an axisymmetric field can not be maintained by dynamo action. This hurdle is overcome through mean-field electrodynamics, in which small-scale turbulent motion generates large-scale poloidal magnetic fields. This effect is known as the α-effect. We will not discuss mean-field dynamo theory, but, for an extensive review of the theory and literature, one should consult Hughes (2018).

Due to the strong velocity gradient within the solar tachocline, it is a suitable candidate for generating strong toroidal magnetic fields. However, the dynamo mechanism over the full dynamo cycle is widely debated. It is at least clear that most models agree that large-scale weak poloidal magnetic fields are wound up into strong toroidal magnetic fields

through the abrupt velocity shear within the solar tachocline. The toroidal magnetic field then rises through the convection zone, resulting in the ephemeral phenomenon observed at the solar surface. That is to say, it is generally accepted that the ω-effect is the result of differential rotation, whereas the α-effect is invoked in multiple different ways across various dynamo models. Figure 1.7 is a schematic diagram which illustrates the ω-effect and α-effect: this illustration is known as the dynamo 'loop'.

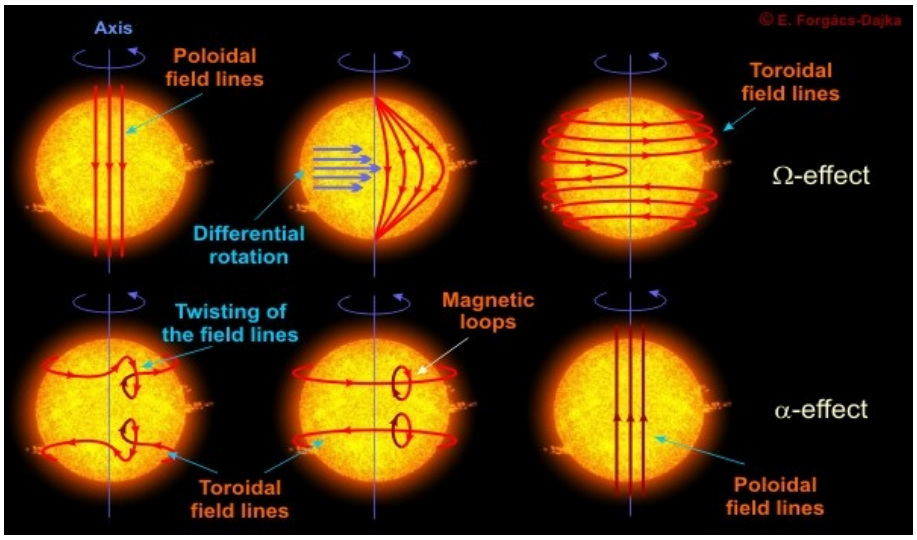

Figure 1.7: A schematic diagram illustrating the ω- and α-dynamo mechanisms.

It is clear that in the $\alpha\omega-$dynamo scenario, the interaction between velocity shear and magnetic field is necessary. While the jury is still out on the exact location of the solar dynamo, there is some agreement on the role of the solar tachocline, in particular, its role in generating large velocity shear and storing the magnetic field. Furthermore, convection plays a fundamental role in the transport of energy and magnetic field throughout the Sun. The remaining piece to the puzzle, and hence this thesis, is magnetic buoyancy — the means by which the magnetic field rises through the solar interior. We discuss magnetic buoyancy next, but in general, it is understood to be an instability mechanism, but is also responsible for the rise of flux tubes. We are interested in the former, discussed in the next section and Chapter 3. A more in depth discussion of magnetic buoyancy can be found in Hughes et al. (2007).

1.3.2 Magnetic Buoyancy

In this section, we will give a brief literary overview of the magnetic buoyancy instability along with advancements in research: a detailed mathematical description will be given later in §3.3. The general idea of magnetic buoyancy was first introduced by Newcomb (1961), and for the rise of flux tubes by Parker (1955). In this paper, Parker describes a magnetic flux tube in pressure equilibrium with a non-magnetic environment. Without the magnetic field within the flux tube, pressure balance would be achieved by the external and internal gas pressures balancing one another, i.e. $p_{ext} = p_{int}$. The presence of the magnetic field adds an internal magnetic pressure, and therefore the equilibrium balance

is given by

$$p_{int} + \frac{B^2}{2\mu_0} = p_{ext}. \tag{1.5}$$

When the flux tube is at pressure equilibrium with its surroundings, then Eq (1.5) is satisfied. It is then the case that the thermal pressure inside the tube is less than that of its surroundings, and therefore $\rho_{int} < \rho_{ext}$. The tube which is now less dense than its surroundings will become buoyant and will rise under the influence of gravity. It is generally understood that this mechanism is typically thought of as a lack of equilibrium (see Hughes et al. (2007)), and it is important to understand that magnetic flux tubes are not found in isolation in the solar interior — magnetic buoyancy instabilities occur in regions of stratified magnetic fields.

The magnetic buoyancy instability mechanism as it is understood today has been extensively researched within the linear and nonlinear regimes, and a detailed review is given in Hughes et al. (2007). It was shown by Newcomb (1961) that in the absence of diffusion and rotation, the preferred mode of instability are 3D, and that 2D interchange modes are more robust to instability. Hughes (1985a) investigated the linear stability of the magneto-Boussinesq system, in which he derived an instability criteria describing instability of modes once thought to be stable (in a regime with B/ρ increasing with height) — this mechanism is known as overstability. Hughes and Cattaneo (1987) extensively researched the difference between interchange and undular modes, showing that interchange modes can be more stable than undular modes, despite the fact that 3D modes require work against magnetic tension. Hughes (1985b) was able to show that rotation caused viscosity to have a destabilising effect under certain circumstances — this result is surprising, as viscosity plays a purely stabilising role in the absence of rotation. Parker (1993) proposed the deep seated dynamo — suggesting that magnetic buoyancy is the mechanism responsible for magnetic fields rising from the solar interior. Subsequently, papers emerged in which magnetic buoyancy was studied with the incorporation of additional effects. Hughes and Tobias (2001) showed that a magnetic field can stabilise a hydrodynamically-unstable shear flow. However, through a combination of numerical and analytic methods, Tobias and Hughes (2004) later went on to show that a magnetic field susceptible to magnetic buoyancy instabilities can also be stabilised in the presence of an imposed shear flow. Tobias and Hughes (2004) showed that the stabilising effect does not depend on the shear profile, provided that the velocity shear is sufficiently strong. It is generally the case that velocity shear has a stabilising effect on magnetic buoyancy instability.

As well as the previously mentioned studies within the linear regime, progress was made towards studying the nonlinear evolution of magnetic buoyancy instabilities. Cattaneo and Hughes (1988) investigated the nonlinear evolution of interchange modes of a magnetic layer embedded in a convectively stable atmosphere. The conclusion is that after the initial release of gravitational potential energy, the dominant driving mechanism of the instability is that of neighboring vortices located at the interface between magnetic material and gas. It was suggested that any strong toroidal magnetic field below a non-magnetised

layer will be broken up by magnetic Rayleigh-Taylor instabilities, and interactions between neighboring vortices can have a net downward motion on the fluid, despite the presence of buoyancy. Matthews et al. (1995) and Wissink et al. (2000) subsequently studied the instability mechanism and nonlinear evolution of the same basic state but in 3D. Matthews et al. (1995) observe the formation of markedly arched flux tubes due to nonlinear interactions between flux tubes of opposite polarity. Wissink et al. (2000) did not observe arched structures, but showed that instability is suppressed by rotation, inhibiting the subsequent formation of interlocking flux tubes. Kersalé et al. (2007) investigated the 3D evolution of magnetic buoyancy instabilities resultant from a smoothly varying magnetic field. Here, the authors were able to show that coherent magnetic structures can be formed owing to an underlying nonlinear process, where the instability is maintained through the boundary conditions. Interestingly, the majority of numerical experiments prior to the work of Kersalé et al. (2007) were run-down calculations. It was pointed out by the authors that while the time-scale of magnetic buoyancy instabilities are relatively short compared to the resistive time-scale — and therefore mostly likely captured by run-down calculations — the maintenance of the toroidal magnetic field by the dynamo depends on a continuous source of instability.

Three papers which are of special interest for this thesis are Vasil and Brummell (2008, 2009), Silvers et al. (2009). Motivated by the solar tachocline, the authors study the nonlinear evolution of magnetic buoyancy instabilities in the presence of a forced shear flow. In particular, the authors investigate the generation of strong toroidal magnetic fields, by shearing a weak poloidal magnetic field. To simulate this process, the authors consider a uniform vertical magnetic field, sheared by a transverse, z-dependent, forcing which is conceptualized as a locally applied stress in the form of the second derivative of a target velocity. Vasil and Brummell (2008) showed that, in their setup, the conditions on the target velocity are incredibly stringent for magnetic buoyancy to ensue — the authors observed that, to achieve magnetic buoyancy, the system must be forced with a highly supersonic target velocity (15 Ma). Vasil and Brummell (2008) concluded that the flux transport by magnetic buoyancy in this instance is markedly inefficient, as the unstable flow is susceptible to turbulence and Kelvin-Helmholtz instabilities. Silvers et al. (2009) studied an ostensibly similar problem, and showed that magnetic buoyancy instability is possible with a much smaller target velocity amplitude (0.05 Ma), claiming that double-diffusive effects are the main driving mechanism. Silvers et al. (2009) stated that the main reason Vasil and Brummell (2008) required such a large target velocity amplitude was their parameters. We will show in Chapter 5 that this is not the case — the main difference between Silvers et al. (2009); Vasil and Brummell (2008) can be understood through an analysis of their respective basic states.

1.4 Thesis Outline

As all the previous literature has shown, the relationship between shear, convection, and magnetic buoyancy is complicated. All three processes are intimately linked and have been

studied both independently and together. While there is steady progress within the nonlinear regime, nonlinear numerical experiments are hard to implement and interpret. The ultimate aim of this thesis is to study the magnetic buoyancy instability within the linear regime of the model investigated by Vasil and Brummell (2008, 2009), with the added complication of time-dependent basic states; this is not a straight-forward endeavour. When one performs a linear stability analysis, the first step is to consider small perturbations around a basic state. After that, the governing equations are linearised, such that any terms which are not linear in the perturbed quantities are discarded. Now, suppose the basic state is steady and depends only on z in Cartesian geometry: the typical approach is to perform a normal-mode analysis, and seek solutions of the form

$$f(\boldsymbol{x};t) = \hat{f}(z)e^{ikx+ily+st} + \text{c.c.} \tag{1.6}$$

where c.c. is the complex conjugate, s is the complex growth rate, and k and l are wavenumbers. The real component of s is the growth rate and it is understood that when $R(s) > 0$ then the perturbations will grow exponentially, whereas when $R(s) < 0$ the perturbations will decay exponentially. There are many important reasons for performing a linear stability analysis, but a key point is that it is an instructive first step, as there is a natural stability boundary, i.e., $R(s)$ which separates growing/decaying solutions. Performing a steady linear stability analysis often revolves around solving an eigenvalue problem for s, as will be shown in Chapters 2 and 3. However, the inclusion of time-dependence in the basic state leads to source-terms in the full system of linear equations, and therefore the functional form of the time-dependence of the perturbations is unknown a priori. That is to say, one cannot perform a normal mode analysis and look for perturbations of the form given by Eq (1.6). This means that there is no natural stability boundary, and so, before we can perform any useful calculations, one must motivate a physically meaningful definition of the stability boundary that allows the separation of growing and decaying solutions. This is an interesting conceptual question, which is often problem-specific. One must ask: what would we consider stability to be in such a problem? After we have defined a stability boundary, one can then performs a non-modal analysis and looks for solutions of the form

$$f(\boldsymbol{x};t) = \hat{f}(z;t)e^{ikx+ily} + \text{c.c.} \tag{1.7}$$

The idea of performing a stability analysis without eigenvalues is not new, for example Schmid (2007) gives an extensive review of the prominent literature. Performing a non-modal stability analysis for the case of magnetic buoyancy is of great research interest, as the main mechanism responsible for magnetic buoyancy instabilities in the Sun is inherently a time-dependent process and, hence, a steady linear stability analysis may not be sufficient. Therefore, the main enterprise of this thesis is to work towards a time-dependent linear stability analysis of a compressible Magnetohydrodynamic (MHD) system. To work towards this goal, we solve a range of linear stability problems involving shear, magnetism, and convection, all with non-trivial or non-steady background states.

First in Chapter 2, we will start with the joint instability of a magnetised layer of fluid in the presence of a shear flow, but in the absence of gravity. As discussed earlier, magnetic fields and shear flows are ubiquitous in many astrophysical contexts and so this problem is of great research interest and is an instructive first step into understanding interactions between magnetic fields and flows. In this problem, the basic state is the solution of a set of self-consistent linear Ordinary Differential Equations (ODEs) and, while it is steady, it is nevertheless non-trivial. We will also use this chapter to familiarise the reader with our typical framework for linear stability analysis and with the numerical and analytic techniques developed throughout the thesis. We will then move onto the first instance of magnetic buoyancy instabilities in Chapter 3. Here, the model which generates the field and flow remains the same as in Chapter 2. However, to study magnetic buoyancy, the shearing will take place in the presence of a stably-stratified and compressible atmosphere. Again, the basic state is steady and is governed by a set of linear ODEs, and subsequent instabilities will be explained through the criteria first proposed by Newcomb (1961).

After studying the linear stability of two steady, non-trivial basic state configurations, we would like to move on to developing the techniques for performing a time-dependent linear stability analysis in Chapter 4. Due to the complexities of magnetic buoyancy instabilities, it is necessary to return to a classical problem which has been studied extensively: Rayleigh Bénard Convection (RBC). While performing the time-dependent linear stability analysis of any problem is not trivial by any means, studying a system such as RBC has less variables, i.e. no magnetic field, and is an instructive step before studying the full time-dependent magnetic buoyancy instability problem. We consider two time-dependent forms of source of heating for the basic state. We show that the definition of a suitable stability boundary is problem specific, and that the inclusion of time-dependence can lead to complexities. Equipped with the necessary numerical methods and understanding of performing both normal and non-normal modal linear stability analyses for both non-steady and non-trivial linear stability analysis, we move onto the full magnetic buoyancy problem in Chapter 5. Here, we consider multiple initial conditions in both the basic state and in the perturbations. We first show how changing the initial condition in the basic state horizontal flow affects the subsequent magnetic field generation. By starting with an initially established target flow, the magnetic field generation is shown to be four orders of magnitude larger. We then perform a frozen-in-time (quasi-static) linear stability analysis, which involves taking the time-dependent basic state at a fixed time and performing a modal analysis. We show that throughout various stages of evolution of the basic state, multiple instabilities, e.g., undular and interchange modes are possible, with the dominant mode changing with time. Finally, we show that the evolution of the perturbed quantities depends heavily on the initial condition. We consider a set of initial conditions, in either the perturbed velocity or magnetic field components, which can be grouped: the set of individual Fourier modes characterised by n, and a set of centrally peaked functions characterised by a width $1/\beta$. Using this set of initial conditions, we show that, by initially

perturbing the initial flow or magnetic field only, the perturbations which grow the fastest in time prefer varying structure and more/less localisation in the initial condition.

Chapter 2

The Joint Instability of a Flow-Forced Magnetic Field

2.1 Introduction

The interaction between shear flows and magnetic fields is a problem of considerable interest, particularly in an astrophysical context. Previous studies have shown that magnetic fields can inhibit hydrodynamic shear instabilities, e.g. Chandrasekhar (1952), Michael (1953), Stuart (1954). In addition to this, Stern (1963) concluded that magnetic fields can have the opposite effect; demonstrating that parallel magnetic fields can destabilise hydromagnetic field configurations that are separately stable to both magnetic and hydrodynamic instabilities.

Since the work by, for example, Michael (1953) and Stuart (1954), there has been a continued effort to understand the linear and nonlinear evolution of systems in which magnetic fields and flows are present – for example Dahlburg et al. (1998). Such background state configurations serve as models in many physical systems including the magnetotail (Sato and Walker, 1982), solar surges (Carbone et al., 1987; Dahlburg and Karpen, 1994), and the heliospheric current sheet (Wang et al., 1988).

Despite the wide range of applicability of the above references, they all share a common approach: that is to prescribe background state flow and field in an arbitrary, but physically motivated fashion. For example, one line of enquiry has been to assume a fixed magnetic field, and then to study how characteristics of the flow affect its stability. The model in this chapter goes a step further and investigates the Magnetohydrodynamic (MHD) instability of a hydromagnetic configuration in which field and flow are linked *self-consistently* through a set of governing Ordinary Differential Equations (ODEs).

In §2.2, we introduce the model and illustrate the governing equations with the associated non-dimensional parameters. We motivate our choice of forcing, which will be applied through a shear flow. For each shear flow, we study the basic state solutions within specific parameter regimes through numerical and analytic techniques. We subsequently perform

a linear stability analysis of the basic state by solving the resultant eigenvalue problem. Even though in our model, the basic state is the result of an interaction between the flow and magnetic field, we will show that classical problems such as the Orr-Sommerfeld and the current sheet problem studied by Dahlburg et al. (1983) are useful tools. In §2.4 we then study the Orr-Sommerfeld equation. Here, we use asymptotic methods to find a neutral stability curve in the limit where $k \to 0$. §2.5 illustrates results for the current sheet problem. Here, we show the existence of oscillatory instabilities which were not noted in Dahlburg et al. (1983). In §2.7-§2.8 we then perform a parameter survey for the full linear system of equations and demonstrate through numerical results that a magnetic field can either be stabilising or destabilising to a hydrodynamically unstable or stable flow respectively. We are able to describe the instability mechanisms in specific parameter regimes, by introducing a set of simple sub-problems and showing that there is good quantitative agreement between the full and reduced systems. In particular, we are able to identify the hydrodynamic and magnetic limits in parameter space of the full system and also identify a region of joint instability where both field and flow are important players. We show the existence of travelling and stationary instabilities and find the eigenfunctions for the optimal mode of growth. We then finish by showing the role of total magnetic flux in the instability problem, by considering a set of different basic state magnetic fields with non-zero flux.

2.2 Mathematical Formulation

2.2.1 Governing Equations

We focus on a plane-parallel approximation within Cartesian geometry (x, y, z). The domain is unbounded in the (x, y) plane and has an extent $2d$ in the z-direction where $-d \leq z \leq d$ — we will refer to this as vertical. The box is filled with an incompressible, electrically conducting fluid in the absence of gravity, subject to some transverse body forcing which will vary vertically. The forcing is modelled by the second derivative of a chosen target flow with typical scale $\mathcal{U}_0$. The domain is threaded with a vertical uniform magnetic field with strength $\mathcal{B}_0$ and has a constant resistivity, η, and kinematic viscosity, ν. Using d as the length scale, with $\mathcal{U}_0$ and $\mathcal{B}_0$ as the typical velocity and magnetic field scales, the governing equations of the incompressible fluid are given as

$$\frac{\partial \mathbf{U}}{\partial t} + (\mathbf{U}\cdot\nabla)\mathbf{U} = -\nabla P + \frac{Q}{R_m Re}(\mathbf{B}\cdot\nabla)\mathbf{B} + Re^{-1}\left(\nabla^2\mathbf{U} + \frac{\mathrm{d}^2 U_0}{\mathrm{d}z^2}\hat{\mathbf{x}}\right), \tag{2.1}$$

$$\frac{\partial \mathbf{B}}{\partial t} = \nabla\times(\mathbf{U}\times\mathbf{B}) + R_m^{-1}\nabla^2\mathbf{B}, \tag{2.2}$$

$$\nabla\cdot\mathbf{U} = 0, \tag{2.3}$$

$$\nabla\cdot\mathbf{B} = 0, \tag{2.4}$$

where $Q = \mathcal{B}_0^2 d^2/\mu_0\rho_0\nu\eta$ is the Chandrasekhar number, $R_m = \mathcal{U}_0 d/\eta$ is the magnetic Reynolds number, and $Re = U_0 d/\nu$ is the Reynolds number. It was shown by Drazin

(1961) that, at least within the long wavelength limit, shear flows fall into two classes: tangential shear flows and jets. Therefore, we consider the two *target profiles* for $U_0(z)$:

$$U_0(z) = \tanh \lambda z, \tag{2.5}$$

$$U_0(z) = \operatorname{sech}^2 \lambda z, \tag{2.6}$$

which represent a typical tangential shear layer and jet respectively and λ is an inverse measure of the width of the shear region. It is understood that when $\lambda \gg 1$ then for each flow there will be an abrupt change in U_0 at $z = 0$. In the absence of a magnetic field, the resultant flow will be given by the target flow, and hence will contain a boundary layer of width $\sim 1/\lambda$.

2.2.2 The Equilibrium State

We consider a non-trivial steady equilibrium state where the transverse body-forcing (Eqs (2.5)-(2.6)) is applied to a uniform field in the z-direction. This equilibrium state given by $\boldsymbol{U}_0 = (U(z), 0, 0), \boldsymbol{B}_0 = (B(z), 0, 1)$, is the solution to

$$\frac{Q}{R_m Re}\frac{\mathrm{d}B}{\mathrm{d}z} + \frac{1}{Re}\left(\frac{\mathrm{d}^2 U}{\mathrm{d}z^2} - \frac{\mathrm{d}^2 U_0}{\mathrm{d}z^2}\right) = 0, \tag{2.7}$$

$$\frac{\mathrm{d}U}{\mathrm{d}z} + \frac{1}{R_m}\frac{\mathrm{d}^2 B}{\mathrm{d}z^2} = 0. \tag{2.8}$$

Because of the symmetries associated with Eqs (2.7)-(2.8) we can only consider certain boundary conditions for the equations in this form. To show this, we integrate Eq (2.7) to show that there exists a consistency condition such that

$$\frac{Q}{R_m} B + \frac{\mathrm{d}U}{\mathrm{d}z} - \frac{\mathrm{d}U_0}{\mathrm{d}z} = c, \tag{2.9}$$

where c is an integration constant. Equation (2.9) must be satisfied for either target profile and set of boundary conditions we consider, and so the choice of boundary conditions on U and B must be consistent with the symmetry of U_0'. It is helpful to make use of the stream- and flux-functions

$$\psi(z) = \int_{-1}^{z} U(s)\mathrm{d}s, \tag{2.10}$$

$$\phi(z) = \int_{-1}^{z} B(s)\mathrm{d}s. \tag{2.11}$$

The flow, $U(z)$, and field, $B(z)$, are then the solution to the system

$$R_m \frac{\mathrm{d}^3 \psi}{\mathrm{d}z^3} + Q\frac{\mathrm{d}^2 \phi}{\mathrm{d}z^2} = R_m \frac{\mathrm{d}^2 U_0}{\mathrm{d}z^2}, \tag{2.12}$$

$$R_m \frac{\mathrm{d}^2 \psi}{\mathrm{d}z^2} + \frac{\mathrm{d}^3 \phi}{\mathrm{d}z^3} = 0. \tag{2.13}$$

Equations (2.12)-(2.13) form a set of coupled third order ODEs. We therefore need a total of six boundary conditions on ϕ and ψ. By construction, $\psi(-1) = \phi(-1) = 0$. We then consider stress-free boundary conditions, and therefore are left with a choice for the remaining two. A natural choice is to fix the mean flow and mean field, which is denoted by angle brackets, $< \cdots >$. The boundary conditions are given by

$$\psi(-1) = \phi(-1) = 0, \qquad \text{(by construction)} \tag{2.14}$$

$$\psi''(\pm 1) = 0, \qquad \text{(stress-free)} \tag{2.15}$$

$$\psi(1) = 2\langle U_0 \rangle, \qquad \text{(mean flow)} \tag{2.16}$$

$$\phi(1) = H, \qquad \text{(total magnetic flux)} \tag{2.17}$$

where H is a constant. Since we have motivated the basic state as the result of a self-consistent interaction between field and flow, it is essential to illustrate its dynamics within particular parameter regimes. In the following subsections we employ boundary layer techniques and order of magnitude estimations to map out the basic state in parameter space. In particular, we are going to consider two regimes: $Q \ll \lambda^2$ and $Q \gg \lambda^2$. This is motivated by considering Eq (2.7). We can see that, for either Eqs (2.5)-(2.6), then U_0'' introduces a factor of λ^2, which will compete with the Lorentz force, with a pre-factor $Q/R_m Re$.

Case $Q \ll \lambda^2$

When the forcing term in Eq (2.7) is dominant compared to the Lorentz force, we expect the resultant basic flow to be given by the target flow. We can approximate this solution using a boundary layer analysis in the case where $Q \ll \lambda^2$. We will refer to the shearing region of width $\Delta z \sim 1/\lambda$, as the inside region of the solution, and therefore $|z| > 1/\lambda$ in the outer region. Integrating Eq (2.8) and combining it with Eq (2.7) yields

$$\frac{\mathrm{d}^2 U}{\mathrm{d}z^2} - QU = \frac{\mathrm{d}^2 U_0}{\mathrm{d}z^2} + c, \tag{2.18}$$

where c is an integration constant. Within the outer region, both Eqs (2.5)-(2.6) result in $|U_0''| \ll 1$. Therefore Eq (2.18) becomes

$$\frac{\mathrm{d}^2 U_{(o)}}{\mathrm{d}z^2} - QU_{(o)} = c, \tag{2.19}$$

whose solution for $z \in [0, 1]$,

$$U_{(o)} = \alpha \cosh\Big(\sqrt{Q}(1 - z)\Big) + \beta, \tag{2.20}$$

satisfies the boundary condition $U'_{(o)}(1) = 0$, with particular integral $\beta = -c/Q$ (we can determine the solution on $z \in [-1, 0]$ by symmetry). The inner solution when $c, Q \ll \lambda^2$ satisfies the equation

$$\frac{\mathrm{d}^2 U_{(i)}}{\mathrm{d}z^2} = \frac{\mathrm{d}^2 U_0}{\mathrm{d}z^2}, \tag{2.21}$$

where z has been scaled. The inner solution is given by

$$U_{(i)}(z) = U_0(z) + \gamma, \tag{2.22}$$

where terms linear in z have been removed to ensure the solution remains bounded as $z \to \infty$. We perform a uniform matching of the inner and outer solution which gives

$$\lim_{z\to\infty} U_{(i)} = U_\infty = \lim_{z\to 0} U(o) = \alpha \cos\Big(\sqrt{Q}\Big) + \beta, \tag{2.23}$$

where $U_\infty = \gamma + \lim_{z\to\infty} U_0$. The approximate solution is therefore

$$U(z) \approx \alpha \cos\Big(\sqrt{Q}(1-z)\Big) + \beta + U_0(z) + \gamma - U_\infty. \tag{2.24}$$

The magnetic field can be approximated using Eq (2.8)

$$\begin{aligned} B(z) &= -R_m \int U(z)\mathrm{d}z + A_1 z + A_2, \\ &= \frac{\alpha R_m}{\sqrt{Q}} \sinh\Big(\sqrt{Q}(1-z)\Big) - R_m \int U_0(z)\mathrm{d}z + A_1 z + A_2. \end{aligned} \tag{2.25}$$

Shear Flow: For $U_0(z) = \tanh \lambda z$, the solution $U(z)$ must be odd and therefore $\gamma \equiv 0$ and $\lim U_{0,z\to 1} = 1$. Similarly for reasons of symmetry, the outer solution near $z = \pm 1$ we obtain $c = 0$ and hence $\beta = 0$. Equation (2.23) gives $\alpha = 1/\cosh\big(\sqrt{Q}\big)$ and the approximate solution is given by

$$U(z) \approx \frac{\cosh\big(\sqrt{Q}(1-z)\big)}{\cosh\big(\sqrt{Q}\big)} + \tanh \lambda z - 1. \tag{2.26}$$

From Eq (2.26) we see that $U \to U_0$ when $Q \to 0$. The magnetic field is then given by Eq (2.25),

$$B(z) \approx R_m(A_1 z + A_2) + \frac{R_m}{\sqrt{Q}} \frac{\sinh\left(\sqrt{Q}(1-z)\right)}{\cosh\sqrt{Q}} - \frac{R_m}{\lambda} \ln\left(\cosh(\lambda z)\right). \tag{2.27}$$

Then the condition that $B'(0) = 0$ implies that $A_1 = 1$ and the constant A_2 is obtained from $\phi(1) = H = 0$, in terms of the dilogarithm function Li_2 (see Zagier, 1989):

$$\begin{aligned} \frac{H}{2} = \int_0^1 B(z)\mathrm{d}z = R_m \left[\frac{z^2}{2} + A_2 z\right]_0^1 - \frac{R_m}{Q}\left[\frac{\cosh\left(\sqrt{Q}(1-z)\right)}{\cosh\sqrt{Q}}\right]_0^1 \\ - \frac{R_m}{\lambda^2}\left[\frac{1}{2}\mathrm{Li}_2(-e^{-2\lambda z}) - \lambda z \ln\Big(e^{-2\lambda z}+1\Big) + \lambda z \ln\cosh(\lambda z) - \frac{1}{2}\lambda^2 z^2\right]_0^1. \end{aligned} \tag{2.28}$$

Thus

$$A_2 = \frac{1-\cosh\sqrt{Q}}{Q\cosh\sqrt{Q}} + \frac{1}{2\lambda^2}\left(\mathrm{Li}_2(-e^{-2\lambda}) + \frac{\pi^2}{12}\right) + \frac{1}{\lambda}\Big(\ln\cosh\lambda - \ln\left(e^{-2\lambda}+1\right)\Big) - 1, \tag{2.29}$$

since $\mathrm{Li}_2(-1) = -\pi^2/12$. Notice that for $\lambda = 10$, $A_2 \approx (1 - \cosh\sqrt{Q})/(Q\cosh\sqrt{Q}) + (\ln\cosh\lambda)/\lambda - 1$, since $e^{-2\lambda} \approx 10^{-9}$ and we know that $\mathrm{Li}_2(0) = 0$. Furthermore, the term $\pi^2/2400$ is a small, but noticeable correction. Note, we have written the flow and field in one half of the layer, i.e. $z \in [0, 1]$; the full solution can be inferred from symmetry arguments.

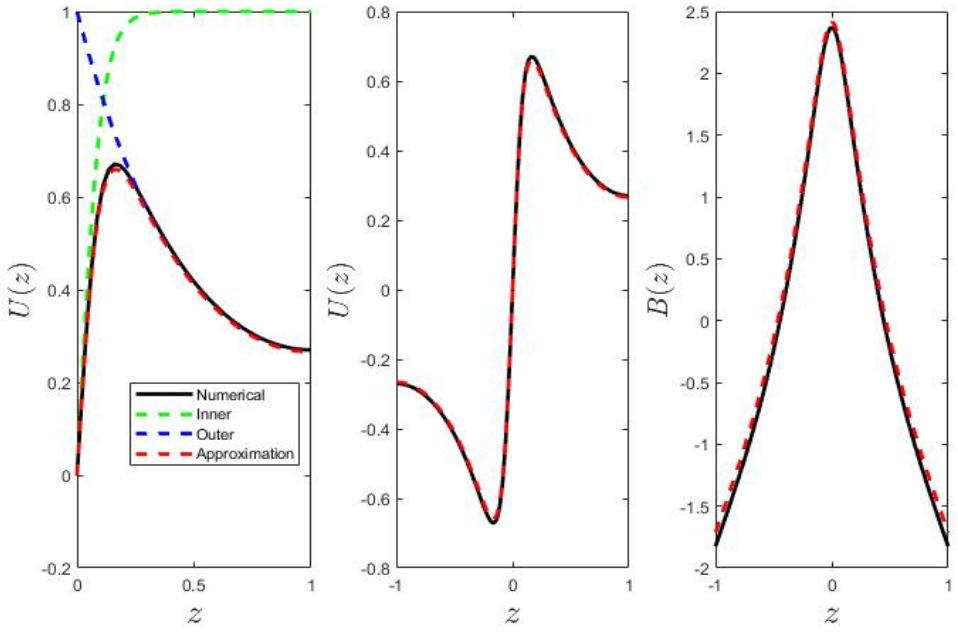

Figure 2.1: Comparison of the numerical solution with the outer, inner, and composite asymptotic solutions. Here, $Q = 4$, $\lambda = 10$, $R_m = 10$, $H = 0$, and $U_0(z) = \tanh(10\lambda)$.

Figure 2.1 shows that there is good agreement between the approximate solution obtained from the boundary analysis and the numerical solution to Eqs (2.12)-(2.17). Likewise, there is good agreement between the numerical solution and the outer and inner solutions, where the boundary layer is characterised by $1/\lambda$. It is important to note that in Fig 2.1, Q is not necessarily much less than λ^2, and the asymptotic solutions are still reasonable approximations to the numerical solution.

Jet: For the jet, given by $U_0 = \mathrm{sech}^2(\lambda z)$, then we know U is an even function, and that $U_\infty = \gamma + \lim_{z\to\infty} U_0 = \gamma$. Equation (2.23) gives $\gamma = \alpha\cosh\left(\sqrt{Q}\right) + \beta$, and therefore the approximate solution is given by

$$U(z) \approx \alpha\cosh\left(\sqrt{Q}(1-z)\right) + \beta + \mathrm{sech}^2(\lambda z). \tag{2.30}$$

Since the flow must be even, then we expect that $U'(0) = 0$. However, this cannot be achieved by the approximate solution as $U'(0) = 0 \to \alpha\sinh\sqrt{Q} = 0$. This implies that $\alpha = 0$, and therefore the approximation would result in the target flow. The constant β,

however, can be eliminated using the condition on the mean flow, $\langle U \rangle$,

$$\begin{aligned} \langle U \rangle &= 2\int_0^1 U \mathrm{d}z = 2\int_0^1 \left(\alpha \cosh\left(\sqrt{Q}(1-z)\right) + \beta + \operatorname{sech}^2(\lambda z)\right) \mathrm{d}z, \\ &= 2\left(\alpha \frac{\sinh\left(\sqrt{Q}\right)}{\sqrt{Q}} + \beta + \frac{\tanh\lambda}{\lambda}\right). \end{aligned} \tag{2.31}$$

Therefore, we can write β as,

$$\beta = -\alpha \frac{\sinh\left(\sqrt{Q}\right)}{\sqrt{Q}}, \tag{2.32}$$

for $\langle U \rangle = \langle U_0 \rangle = 2\tanh\lambda/\lambda$. The approximate solution therefore becomes

$$U(z) = \alpha\left(\cosh\left(\sqrt{Q}(1-z)\right) - \frac{\sinh\sqrt{Q}}{\sqrt{Q}}\right) + \operatorname{sech}^2(\lambda z). \tag{2.33}$$

The coefficient α is evaluated using the inner and outer solutions for the horizontal magnetic field, B. Equation (2.25) with $U(z) = U_{(o)} = \alpha\cosh\left(\sqrt{Q}(1-z)\right)$ yields the outer magnetic field solution as

$$B_{(o)}(z) = \frac{\alpha R_m}{\sqrt{Q}} \sinh\left(\sqrt{Q}(1-z)\right) + c_1 z + c_2, \tag{2.34}$$

where c_1 and c_2 are general constants. The inner magnetic field solution is given by Eq (2.25) with $U_{(i)} = \operatorname{sech}^2(\lambda z) + \gamma$ as,

$$B_{(i)}(z) = -\frac{R_m}{\lambda}\tanh(\lambda z) + d_1 z + d_2, \tag{2.35}$$

where d_1 and d_2 are integration constants. Using the condition that $\phi(1) = H = 0$, then we can obtain $c_2 = 0$. Integration of Eq (2.7) over the layer, i.e., $z \in [-1, 1]$ yields

$$R_m(U'(1) - U'(-1)) + Q(B(1) - B(-1)) = R_m(U_0'(1) - U_0'(-1)), \tag{2.36}$$

and since $U'(\pm 1) = 0$, then

$$Q(B(1) - B(-1)) = R_m(U_0'(1) - U_0'(-1)) = 4R_m\lambda\tanh\lambda\operatorname{sech}^2(\lambda z). \tag{2.37}$$

Thus, $B_{(o)}(-1) = B_{(o)}(1) = 0$, since B is odd, and hence $c_1 = 0$. Furthermore, since the inner solution must remain bounded as $z \to \infty$, then $d_1 = d_2 = 0$. Matching the inner and outer solution gives

$$-\frac{R_m}{\lambda} = \frac{\alpha R_m}{\sqrt{Q}}\sinh\sqrt{Q} \to \alpha = -\frac{\sqrt{Q}}{\lambda\sinh\sqrt{Q}}. \tag{2.38}$$

Therefore, the approximate basic state flow and horizontal magnetic field are given by

$$U(z) \approx -\frac{\sqrt{Q}}{\lambda \sinh \sqrt{Q}} \cosh\left(\sqrt{Q}(1-z)\right) + \frac{1}{\lambda} + \operatorname{sech}^2(\lambda z), \tag{2.39}$$

$$B(z) \approx -\frac{R_m}{\lambda}\left(\frac{\sinh\left(\sqrt{Q}(1-z)\right)}{\sinh\sqrt{Q}} + \tanh\lambda z - 1\right). \tag{2.40}$$

When $H \neq 0$, B is raised by $H/2$ throughout. We have written the flow and field in one half of the layer, i.e. $z \in [0,1]$; the full solution can be inferred from symmetry arguments. Figure 2.2 shows that there is good agreement between the approximate solution obtained

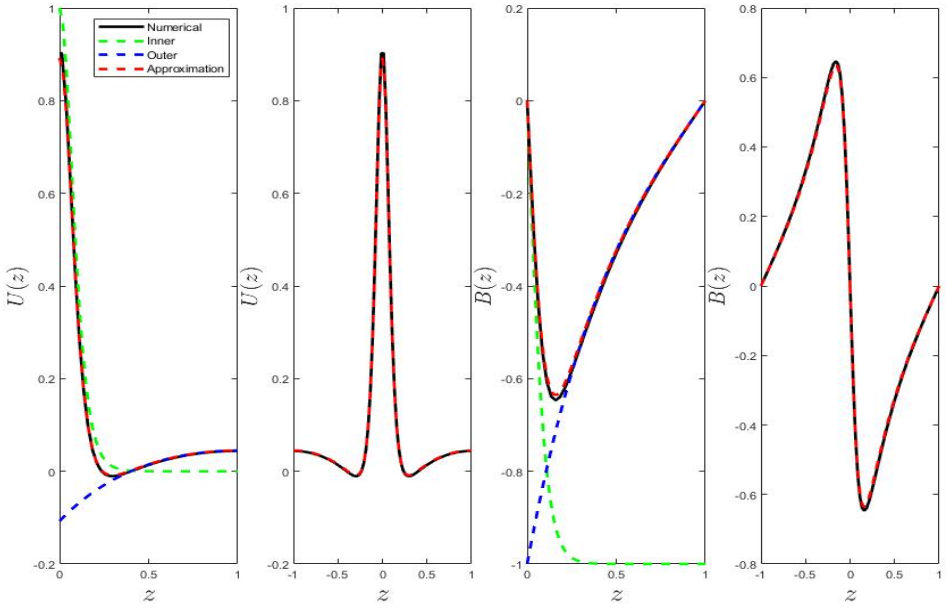

Figure 2.2: Comparison of the numerical solution with the outer, inner, and composite asymptotic solutions. Here, $Q = 4$, $\lambda = 10$, $R_m = 10$, and $U_0(z) = \operatorname{sech}^2(\lambda z)$.

from the boundary analysis and the numerical solution to Eqs (2.12)-(2.17). Again, there is good agreement between the numerical solution and the outer and inner solutions, where the boundary layer is characterised by $1/\lambda$. It is important to note that in Fig 2.2, Q is not necessarily much less than λ^2, and the asymptotic solutions are still reasonable approximations to the numerical solution.

Case $Q \gg \lambda^2$

In the limit $Q \gg \lambda^2, c$ the dominant balance in Eq (2.18) is not obvious. We attempt a leading balance between QU and the forcing term which yields

$$U(z) \sim \frac{1}{Q}\frac{\mathrm{d}^2 U_0}{\mathrm{d}z^2} \sim \frac{\lambda^2}{Q}. \tag{2.41}$$

This leading order balance does not lead to a contradiction, since the balance of terms gives

$$\frac{\mathrm{d}^2U}{\mathrm{d}z^2}\Big/QU \sim \frac{\lambda^2}{Q} \ll 1. \tag{2.42}$$

and we have assumed $Q \gg \lambda^2$. We determine B from Eq (2.8) and it then follows that

$$U(z) \approx -(1/Q)U_0'', \tag{2.43}$$

$$B(z) \approx (R_m/Q)U_0'. \tag{2.44}$$

Equations (2.43)-(2.44) demonstrate the dependence of Q and the role of R_m on the equilibrium state when $Q \gg \lambda^2$ — we can see that the basic state magnetic field depends linearly on R_m. We compare the approximations given above to the numerical solution with stress-free boundary conditions, along with $\psi(1) = 2\langle U_0\rangle$, and $B(1) = 0$. Figure

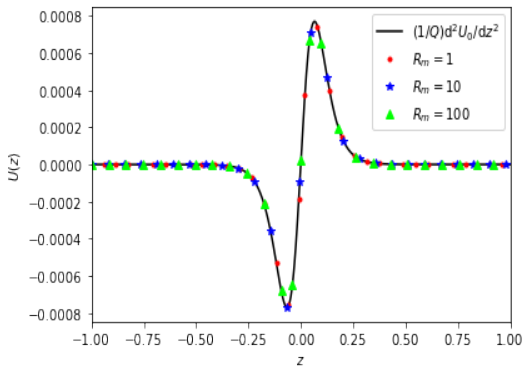

(a) $U_0 = \tanh \lambda z$

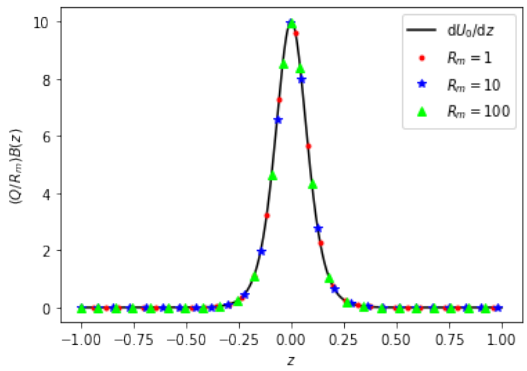

(b) $U_0 = \tanh \lambda z$

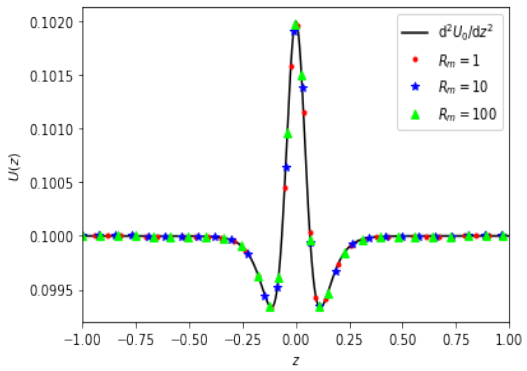

(c) $U_0 = \mathrm{sech}^2 \lambda z$

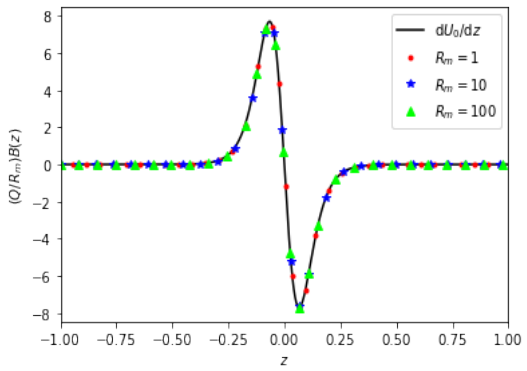

(d) $U_0 = \mathrm{sech}^2 \lambda z$

Figure 2.3: The velocity (left panels) and the magnetic field (right panels) for the two different target profiles. We compare the numerical solution for a series of R_m against the asymptotic approximations. Here $Q = 10^5$ and $\lambda = 10$.

2.3 demonstrates that the approximation given by Eq (2.43)-(2.44) is accurate for both target profiles, $U_0(z)$. We have also illustrated the linear dependence of the equilibrium magnetic field on R_m and furthermore shown that the velocity does not depend on R_m when $Q \gg \lambda^2$.

2.3 Linear Stability Analysis

2.3.1 Eigenvalue Problem

We now consider small perturbations to the basic state, expressing the magnetic field, velocity, and pressure as

$$\mathbf{B} = \mathbf{B}_0 + \mathbf{b}, \tag{2.45}$$
$$\mathbf{U} = \mathbf{U}_0 + \mathbf{u}, \tag{2.46}$$
$$P = p, \tag{2.47}$$

where the perturbations are given by the lower case quantities such that $\boldsymbol{u} = (u, v, w), \boldsymbol{b} = (b_x, b_y, b_z)$, and it is understood that $\boldsymbol{U}_0, \boldsymbol{B}_0$ are the basic state quantities. On substituting these expressions into Eq (2.1)-(2.4) and retaining only the lowest order terms in the perturbations, the linearised form of the MHD system becomes

$$\frac{\partial \boldsymbol{u}}{\partial t} + (\boldsymbol{u}\cdot\nabla)\boldsymbol{U}_0 + (\boldsymbol{U}_0\cdot\nabla)\boldsymbol{u} = -\nabla P + \frac{Q}{R_m Re}\left((\boldsymbol{b}\cdot\nabla)\boldsymbol{B}_0 + (\boldsymbol{B}_0\cdot\nabla)\boldsymbol{b}\right) + Re^{-1}\nabla^2\boldsymbol{u}, \tag{2.48}$$

$$\frac{\partial \boldsymbol{b}}{\partial t} = \nabla\times(\boldsymbol{u}\times\boldsymbol{B}_0 + \boldsymbol{b}\times\boldsymbol{U}_0) + R_m^{-1}\nabla^2\boldsymbol{b}, \tag{2.49}$$

$$\nabla\cdot\boldsymbol{u} = 0, \tag{2.50}$$

$$\nabla\cdot\boldsymbol{b} = 0. \tag{2.51}$$

We postulate normal mode solutions to Eq (2.48)-(2.51) of the form

$$\{u, v, w\} = \{\hat{u}, \hat{v}, \hat{w}\}(z)\exp\{ikx + ily + st\} + \text{c.c.} \tag{2.52}$$
$$\{b_x, b_y, b_z\} = \{\hat{b}_x, \hat{b}_y, \hat{b}_z\}(z)\exp\{ikx + ily + st\} + \text{c.c.} \tag{2.53}$$
$$p = \hat{p}(z)\exp\{ikx + ily + st\} + \text{c.c.} \tag{2.54}$$

where quantities with a hat denote complex eigenfunctions; k and l are the horizontal wavenumbers of a particular mode; and s is the complex eigenvalue, which determines the stability of the system. Furthermore, to ensure that the perturbed magnetic field remains divergence free, we perform a poloidal-toroidal decomposition such that

$$\mathbf{b} = \nabla\times\nabla\times h(x, y, z; t)\hat{\mathbf{z}} + \nabla\times g(x, y, z; t)\hat{\mathbf{z}}, \tag{2.55}$$

where h, g are scalar functions. Substituting Eqs (2.52)-(2.54) into Eqs (2.48)-(2.51) results in the linear eigenvalue problem:

$$s\hat{u} = -ikU_0\hat{u} - U_0'\hat{w} - ik\hat{p} + \Gamma\alpha^2 B'\hat{h} - i\delta\Gamma k\alpha^2\hat{h} + i\delta\Gamma k\hat{h}'' + i\delta\Gamma l\hat{g}' - Re^{-1}(\alpha^2 u - \hat{u}''), \tag{2.56}$$

$$s\hat{v} = -ikU_0\hat{v} - il\hat{p} + \Gamma\alpha^2 B\hat{g} - i\delta\Gamma l\alpha^2\hat{h} + i\delta\Gamma l\hat{h}'' - i\delta\Gamma k\hat{g}' - Re^{-1}(\alpha^2\hat{v} - \hat{v}''), \quad (2.57)$$

$$s\hat{w} = -ikU_0\hat{w} - \hat{p}' + i\Gamma k\alpha^2 B\hat{h} - i\Gamma k(B\hat{h}')' + i\Gamma l(B\hat{g})' - Re^{-1}(\alpha^2\hat{w} - \hat{w}''), \quad (2.58)$$

$$\alpha^2\hat{h} = -ik\alpha^2 U_0\hat{h} + ikB\hat{w} + \delta\hat{w}' - R_m^{-1}\alpha^2(\alpha^2\hat{h} - \hat{h}''), \quad (2.59)$$

$$\begin{aligned}\alpha^2 s\hat{g} = &-il\delta\hat{u}' + ik\delta\hat{v}' - B\hat{v} + ilB'\hat{w} + ilB\hat{w}' + (il^3U_0 + ik^2lU_0 - il\alpha^2)\hat{h}' \\ &- \alpha^2 ilU_0'\hat{h} + \left(-kl^2U_0 - ik^3U_0 - R_m^{-1}\alpha^2\left(\alpha^2\hat{g} - \hat{g}''\right)\right),\end{aligned} \quad (2.60)$$

$$0 = ik\hat{u} + il\hat{v} + \hat{w}', \quad (2.61)$$

where $\Gamma = Q/(R_m Re)$, $\alpha^2 = k^2 + l^2$, primes denote derivatives with respect to z, and δ is a switch for the uniform vertical magnetic field, $\mathcal{B}_0$ — it takes the value 0 or 1 and will be useful later. Eqs (2.56)-(2.61) may be cast in the form

$$\mathcal{L}_1\mathbf{G} = s\mathcal{L}_2\mathbf{G}, \quad (2.62)$$

for the solution vector $\mathbf{G} = (\hat{u}, \hat{v}, \hat{w}, \hat{h}, \hat{g}, \hat{p})^T$, where $\mathcal{L}_1, \mathcal{L}_2$ denote linear differential operators. The boundary conditions are given by

$$\hat{u}' = \hat{v}' = \hat{w} = \hat{h}' = \hat{g} = 0 \quad \text{at } z = \pm 1, \quad (2.63)$$

where the velocity boundary conditions come from stress-free considerations, and the magnetic field boundary conditions are derived from considering zero magnetic current across the boundaries. To solve Eq (2.62) numerically, we make use of both uniform and spectral finite difference spatial discretisation schemes. To efficiently solve the eigenvalue problem in (k, l) space, we make use of the uniform finite difference methods as the differentiation matrices are sparse, and to further enhance computation time, we employ inverse iteration, which is well suited to matrices with a banded structure. The finite difference stencils are second or fourth order and are checked against a spectral solver which has superior exponential convergence.

For optimisation problems, we employ the Nelder-Mead simplex algorithm and the method of steepest descent in MATLAB and Python. We generally use unconstrained optimisation, however, in the case that this method does not converge to the global minimum, we make use of a bounded solver, in which we specify an interval over which to optimise the function. This will ensure convergence, however some knowledge of where the minimum is located is necessary.

2.3.2 2D vs. 3D Modes

To make progress with Eqs (2.56)-(2.61) we consider the possibility of reducing the amount of parameters in an appropriate way. Typically, one might perform a suitable Squire's transformation and limit the investigation to 2D disturbances only. Now, if it is the case that we have either a parallel flow *or* parallel magnetic field then we may invoke Squire's theorem — Squire's theorem states that the disturbances which grow the fastest are those with wavenumbers parallel to the basic state. In the presence of both parallel field *and* flow, there have been previous investigations that have restricted attention to

2D disturbances (Dahlburg et al., 1998, 1983). However, Hunt (1966) proves that Squire's theorem is not necessarily true. It is therefore essential to consider 3D modes and hence we must consider both k and l.

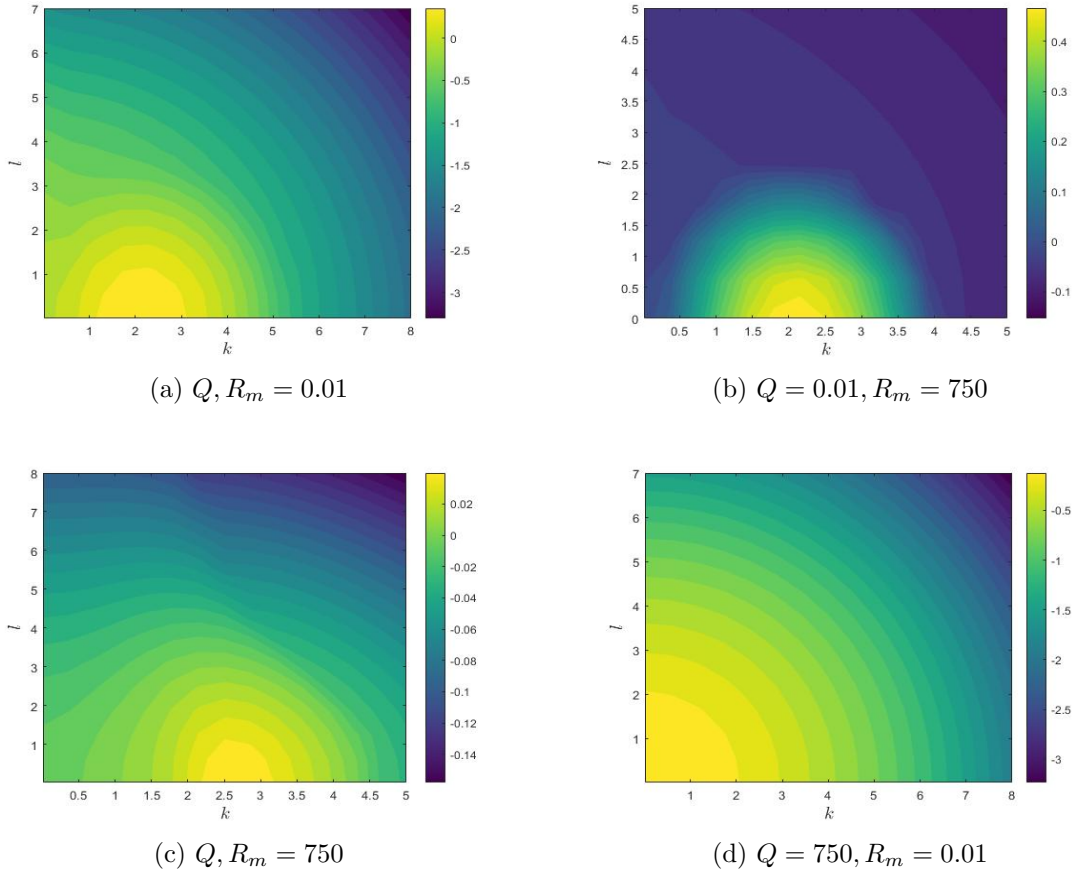

(a) $Q, R_m = 0.01$

(b) $Q = 0.01, R_m = 750$

(c) $Q, R_m = 750$

(d) $Q = 750, R_m = 0.01$

Figure 2.4: Contour plots for $Re(s)$ in $k - l$ space for a range of values of Q and R_m. In all these plots $Re = 35$ and $\lambda = 10$. Here $\delta = 1$.

Figures 2.4 shows the maximum growth rate in (k, l) space for various values of Q and R_m with $\lambda = 10$ and $Re = 35$. It can be seen that for a range of parameters, the dominant mode of instability is 2D. This will be useful in subsequent optimisations, since we can consider a coarse grid in l when performing calculations in (k, l) space. It is worth noting, however, that this is not in contradiction with Hunt (1966). Furthermore, it is not an exhaustive proof that dominant 3D instabilities are impossible in this system.

2.4 Relation to the Orr-Sommerfeld Equation

Here, we take a step back and consider the hydrodynamic instability of the target profiles, i.e., the linear stability of a flow in the absence of magnetic effects. Studying the linear stability of the target flow is of particular interest to this work. The instability in the purely hydrodynamic problem is governed by one non-dimensional parameter, the Reynolds number, Re. It is therefore necessary to calculate the neutral stability curve for each target profile in (k, Re) space: this will allow us to chose Re in the full problem, such that we are forcing a hydrodynamically unstable target flow. The linear stability of

a purely hydrodynamic flow is governed by the classic Orr-Sommerfeld equation, which is obtained by performing a Squire transformation (see Squire, 1933) on Eqs (2.56)-(2.58). After performing some manipulations and introducing the stream-function, ψ, we obtain

$$\frac{1}{i\alpha Re}\left(\frac{\mathrm{d}^2}{\mathrm{d}z^2}-\alpha^2\right)^2\psi=(U_0-s)\left(\frac{\mathrm{d}^2}{\mathrm{d}z^2}-\alpha^2\right)\psi-U_0''\psi, \tag{2.64}$$

where the stream-function has a wave-like form $\psi \propto \exp(i\alpha(\tilde{x}-st))$, with $\tilde{x}$ and α related to (x,y) and (k,l) through the suitable Squire transform (Squire, 1933). We do not directly solve Eq (2.64) but the equivalent equations given by Eqs (2.56)-(2.58) as an eigenvalue problem for s and look for the roots in (k, Re) space. For both target profiles given by Eqs (2.5)-(2.6), we calculate the neutral stability curve numerically, and in the case of the tangent shear layer, we perform an asymptotic analysis using the approach of Drazin (1961).

2.4.1 Shear Layer

We calculate the neutral stability curve $R(s) = 0$, and the global minimum, which we define by (k_c, Re_c). The marginal stability curve for the shear layer with $\lambda = 10$ is shown

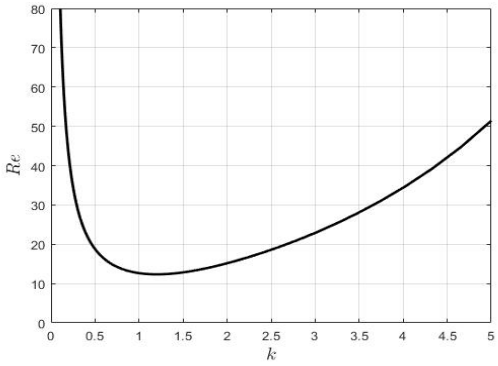

(a) Marginal stability curve with local minimum $(k_c, Re_c) \approx (1.2013, 12.3360)$

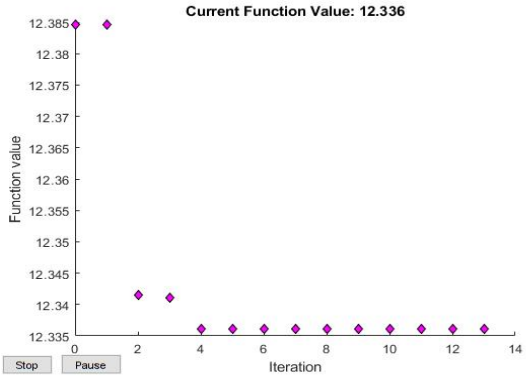

(b) Minimisation Routine — function value against iteration for the Nelder-Mead Simplex.

Figure 2.5: Marginal stability curve along with the minimisation routine for $U_0 = \tanh 10z$.

in Fig 2.5a. As Re is increased, we cross this marginal stability curve, and $R(s)$ changes sign and the system becomes unstable. We employ a minimisation routine to calculate the critical wavenumber and Reynolds number, given by $(1.2013, 12.3360)$ respectively. Figure 2.5b shows that the iterative minima algorithm converges quickly to the minimum, i.e., within ~ 10 iterations. We plot the eigenmodes in (x, z) space, for a whole period, in Figs 2.6. Panel (b) shows localisation at $z = 0$, with a central peak that changes sign as x increases. Panel (a) illustrates that the x-component of the velocity fills the whole domain — there is some structure in the centre but for $|x| \geq 0$ there are rolls that have opposite sign and are centered. Furthermore, since $\phi \sim w$, panel (b) shows streamlines. When we non-dimensionalised our governing equations to obtain Eqs (2.56)-(2.58) we

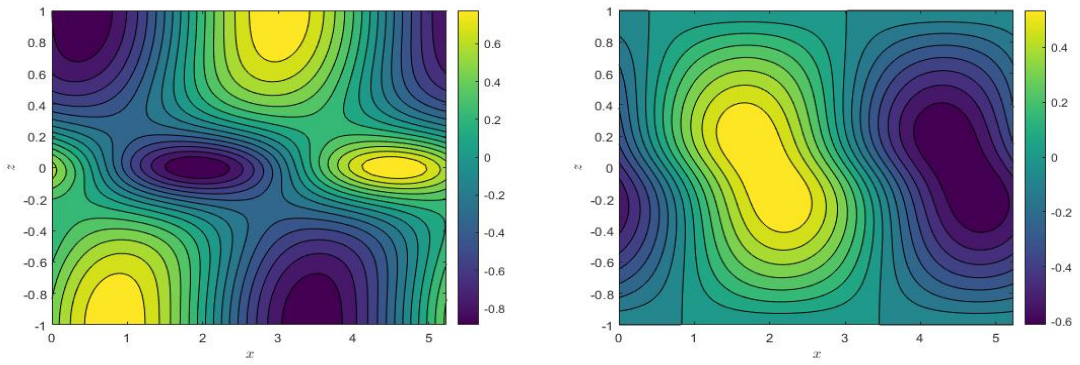

(a) $Re\{u(z)e^{ikx}\}$ (b) $Re\{w(z)e^{ikx}\}$

Figure 2.6: The horizontal and vertical velocity eigenmodes at critical onset for the shear layer. The eigenmodes are plotted in $x - z$ space where $x \in [0, k]$.

based our length scale d on the vertical extent of the layer, i.e $Re = \rho_0 \mathcal{U}_0 d/\mu$. Now suppose we consider an alternative length scale based on the shear width $\tilde{d} = 1/\lambda$. This leads to the Reynolds number $\tilde{Re} = \rho_0 \mathcal{U}_0/\lambda\mu$, noting that the wavenumbers will also be scaled, and in the new scaling, the shear flow becomes

$$\tilde{U}_0 = \tanh z, \tag{2.65}$$

where $z \in [-\lambda, \lambda]$. In the original scaling, when λ is large, the flow is essentially uniform on either side of the shearing region with a sharp jump at $z = 0$. The stability of the flow is independent of the scaling, and therefore we would expect the neutral stability curves to agree under the suitable transformation. We compare neutral stability curves obtained using the two sacalings, for two values of λ.

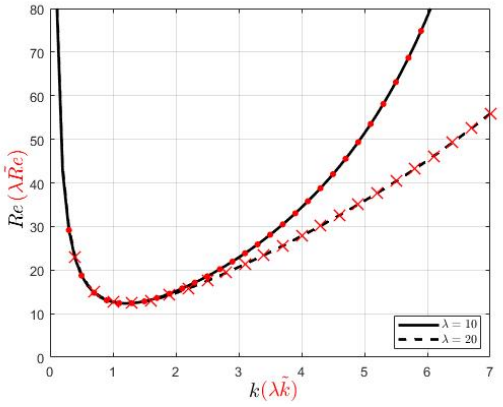

Figure 2.7: Neutral stability curve for two values of λ for both scaling. Dots correspond to $\lambda = 10$ and crosses correspond to $\lambda = 20$. Notice the re-scaling in red on both axis for the extended domain problem, $z \in [-\lambda, \lambda]$.

Figure 2.7 demonstrates that the two scales are consistent with one another under the correct transformation; $Re = \lambda\tilde{Re}$ and $k = \lambda\tilde{k}$. Interestingly, Fig 2.7 suggests that, for both $\lambda = 10$ and 20, the neutral stability curves tend to a limit when $k \ll 1$ as the curves

overlap. For $\lambda = 20$ we see that the instability region becomes wider and therefore shorter wavelength instabilities are possible at lower values of Re than for $\lambda = 10$. This result, as is to be expected, illustrates that shear layers with sharper gradients are more unstable.

When $\lambda \to \infty$ then this problem can be thought of as the instability of a piece-wise linear flow that is discontinuous at $z = 0$. A similar problem was actually studied by Drazin (1961) where it was found that, when $k \ll 1$ the marginal Reynolds number is linear in k: however, Drazin considers an infinite domain and therefore assumes the solution is exponentially decaying waves. From there, Drazin performs a standard matching procedure, writing down the system as a determinant to be solved for Re and k. However, we have shown that in the finite-domain problem that this is not the case. If we consider an exponentially decaying solution, $\psi \propto e^{-kz}$, then for $k \ll 1$ the domain must be infinite in extent to accommodate the Dirichlet boundary conditions — in other words, the solution does not decay sufficiently fast over a finite domain as $k \to 0$.

Using Drazin's formulation, we make analytic progress towards finding an asymptotic expression for our finite domain problem when $k \ll 1$. If we consider $\lambda \to \infty$ then we write down the solution to Eq (2.64) in either half of the domain as

$$\psi(z) = \begin{cases} A \sinh k(z-1) + B \sinh \beta_1 (z-1), & (z > 0) \\ D \sinh k(z+1) + E \sinh \beta_2 (z+1), & (z < 0) \end{cases} \tag{2.66}$$

where

$$\beta_1 = +[k^2 - ikRe(s-1)]^{1/2}, \quad \beta_2 = +[k^2 - ikRe(s+1)]^{1/2}. \tag{2.67}$$

To be consistent with Drazin, we use no-slip boundary conditions. The solution must then be continuous at the interface where $z = 0$, and hence the matching conditions are given by

$$[\psi] = 0, \tag{2.68}$$

$$[\mathcal{D}\psi] = 0, \tag{2.69}$$

$$[(\mathcal{D}^2 - \beta^2)\psi] = 0, \tag{2.70}$$

$$[(\mathcal{D}^2 - \beta^2)\mathcal{D}\psi] = 0, \tag{2.71}$$

where $\mathcal{D} \equiv \partial/\partial z$ and β refers to Eq (2.67). Then, using the approach of Drazin, a non-trivial solution exists if and only if Eqs (2.68)-(2.71) result in zero discriminant, i.e.,

$$\begin{vmatrix} -\sinh k & -\sinh \beta_1 & \sinh k & \sinh \beta_2 \\ k \cosh k & \beta_1 \cosh \beta_1 & k \cosh k & \beta_2 \cosh \beta_2 \\ -(\beta_1^2 + k^2) \sinh k & -2\beta_1^2 \sinh \beta_1 & (\beta_2^2 + k^2) \sinh k & 2\beta_2^2 \sinh \beta_2 \\ k(k^2 - \beta_1^2) \cosh k & 0 & k(k^2 - \beta_2^2) \cosh k & 0 \end{vmatrix} = 0. \tag{2.72}$$

When $k \ll 1$ we assume $Re \sim 1/k^n$ for some value of n. Therefore we neglect all powers of k and keep any terms of order unity in the leading order balance, i.e., kRe, and $\beta_{1,2} \approx$

$[-ikRe(s \pm 1)]^{1/2}$. To leading order, $\sinh k \approx k$ and $\cosh k \approx 1$ when $k \to 0$. We can therefore simplify the determinant given in Eq (2.72), leading to the polynomial

$$-2k^2(\beta_1^4\beta_2 \cosh\beta_2 \sinh\beta_1 + \beta_2^4\beta_1 \cosh\beta_1 \sinh\beta_2 - (\beta_1^2 - \beta_2^2)^2 \sinh\beta_1 \sinh\beta_2) = 0. \quad (2.73)$$

where β_1, β_2 are given by

$$\beta_1 \approx +[-ikRe(s-1)]^{1/2}, \quad \beta_2 \approx +[-ikRe(s+1)]^{1/2}. \quad (2.74)$$

Since we are not interested in the solution $k = 0$, we consider the solution given by the term inside the parenthesis in Eq (2.73). We take this expression and divide through by $\sinh\beta_1 \sinh\beta_2$ which gives

$$\beta_1^4\beta_2 \coth\beta_2 + \beta_2^4\beta_1 \coth\beta_1 = (\beta_1^2 - \beta_2^2)^2. \quad (2.75)$$

Then we substitute in for $\beta_{1,2}$ with $s = 0$ and ignore terms of the order k^2 which gives

$$(1-i)y \coth(1-i)y + (1+i)y \coth(1+i)y = 4, \quad (2.76)$$

where $y = \sqrt{kRe/2}$. We then use the identity

$$\coth(a+b) = \frac{\coth a \coth b + 1}{\coth a + \coth b}, \quad (2.77)$$

which gives

$$(1-i)y\frac{\coth y \coth -iy + 1}{\coth y + \coth -iy} + (1+i)y\frac{\coth y \coth iy + 1}{\coth y + \coth iy} = 4. \quad (2.78)$$

where $\coth(-y) = -\coth y$ and $\coth iy = -i\cot y$. Expanding Eq (2.78) leads to the imaginary parts cancelling. The real part of Eq (2.78) equates to

$$y\frac{\cot y \operatorname{cosech}^2 y + \coth y \csc^2 y}{\coth^2 y + \cot^2 y} = 2. \quad (2.79)$$

The roots of Eq (2.79) give the correct scaling for the relationship between k and Re. Equation (2.79) has the root $y^* \approx 2.0178$, which gives the relationship between k and Re,

$$Re = 8.1435/k. \quad (2.80)$$

We compare the neutral stability curve obtained through numerical methods with the asymptotic solution given by Eq (2.80). Figure 2.8 illustrates that there is excellent agreement when $k \ll 1$ and even when k is small but not asymptotically small.

2.4.2 The Jet

We can perform a similar numerical analysis for the jet profile, $U_0 = \operatorname{sech} 10z$, and solve the hydrodynamic linear system numerically for (k, Re) at the onset of instability, i.e

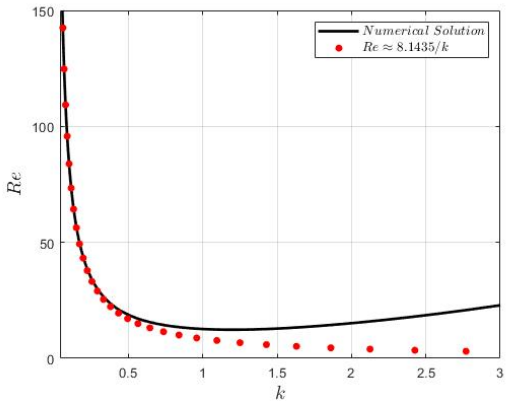

Figure 2.8: Comparison of the neutral stability curve from numerical results with the asymptotic solution for $k \ll 1$ for $U_0 = \tanh 10z$.

$R(s) = 0$.

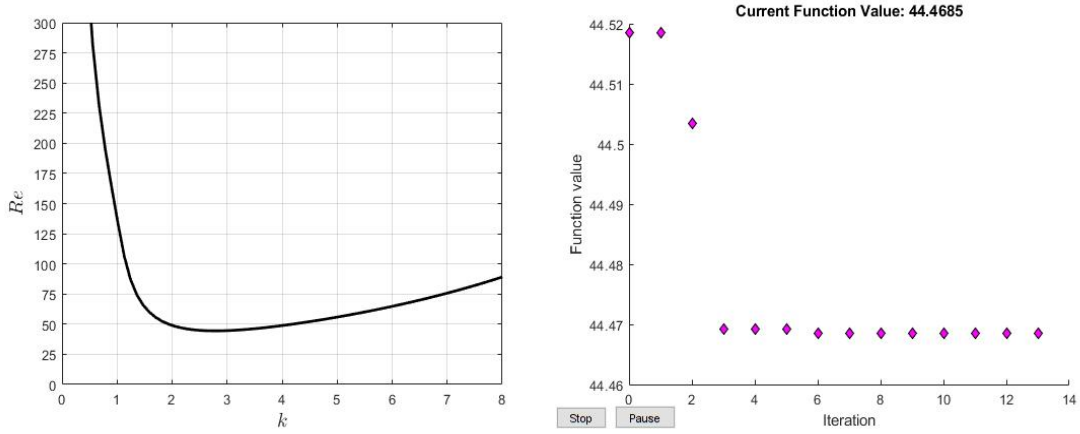

(a) $(k_c, Re_c) = (2.7836, 44.4685)$ (b) Minimisation Routine

Figure 2.9: Marginal stability curve along with the minimisation routine for $U_0 = \text{sech}^2 10z$.

Figures 2.9a-2.9b are analogous to Figs 2.5a-2.5b. It can be seen by comparison of Figs 2.5a and 2.9a that the jet is more stable than the shear layer and must be forced with a larger Reynolds number to achieve instability, as $\min(Re(k))$ is less for the shear layer.

Figure 2.10 shows that the structure of the preferred eigenmodes at critical onset is localized predominately at $z = 0$. Again, the vertical velocity is symmetric in z and is zero at the boundaries. The horizontal velocity shows some structure near the boundaries, but the bulk of the structure is localized at $z = 0$. Figure 2.10b shows streamlines.

We now have a comprehensive understanding of the hydrodynamic instability of both target profiles. This has been achieved by producing marginal stability curves and performing an optimisation to find the critical parameter values. We have further shown a brief example of the structure of the eigenmodes at the critical onset of instability for both choices of target flow. In addition to this, we have utilised the previous literature on the

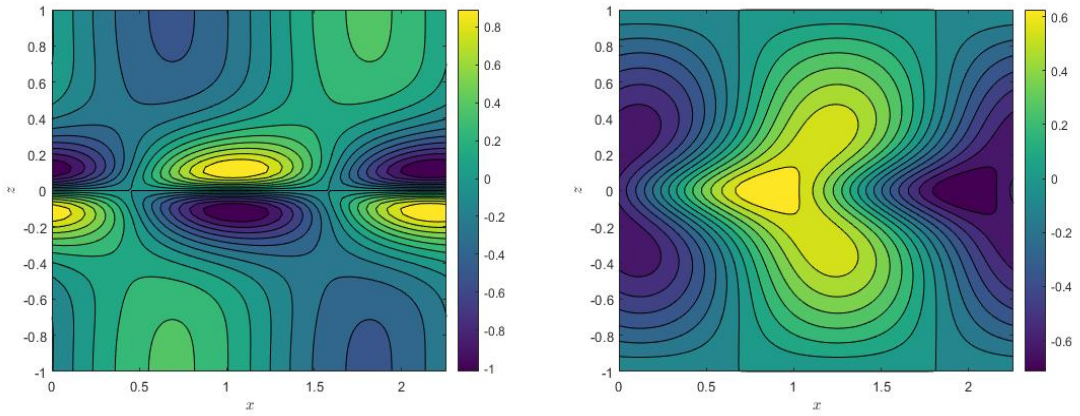

(a) $Re\{u(z)e^{ikx}\}$ (b) $Re\{w(z)e^{ikx}\}$

Figure 2.10: The horizontal and vertical velocity eigenmodes at critical onset for the jet. The eigenmodes are plotted in (x, z) space where $x \in [0, 2\pi/k]$.

Orr-Sommerfeld equation to make analytic progress for the shear layer in the limit of large wavenumber.

The following work will be useful in subsequent sections as we will show that, in certain parameter regimes, the dominant instabilities are in fact the hydrodynamic instabilities of the target flow. We will use this information to inform our choice of Re when exploring the 3D parameter space, (Q, R_m, Re).

2.5 Instability of a Current Sheet

We now briefly turn our attention to the other limiting case — the linear stability of a resistive current sheet, described by Eqs (2.56)-(2.61) with $U_0 = 0$. As mentioned, this problem has been studied in the literature, and the associated instability is often referred to as the tearing instability. In particular, we look at the work of Dahlburg et al. (1983), in which the authors investigate a range of magnetic fields, paying particular attention to the following form

$$B_0(z) = \tan^{-1}\gamma z - \gamma z(\gamma^2 + 1)^{-1}, \tag{2.81}$$

which is shown in Fig 2.11. In this problem, there is no background velocity, so we base the typical velocity scale on the Alfv́en speed. To be consistent with Dahlburg et al. (1983), the viscous and magnetic Reynolds numbers now become M and S, which are defined by

$$M = c_\alpha d/\nu, \qquad S = c_\alpha d/\eta, \tag{2.82}$$

where c_α is the mean Alfvén speed, given by $c_\alpha = \bar{B}(4\pi\rho)^{-1/2}$. From their numerical studies, Dahlburg et al. (1983) observed that, as M or S is raised, a first unstable eigenvalue always appears with $R(s) > 0$ and $I(s) = 0$ — that is, the resultant instabilities are stationary.

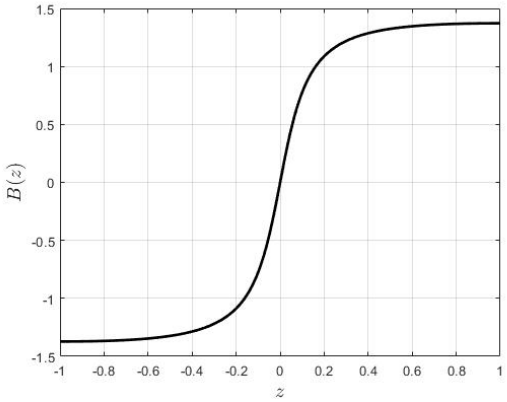

Figure 2.11: The basic state magnetic field considered by Dahlburg et al. (1983) with $\gamma = 10$.

Dahlburg et al. (1983) restrict their investigation to that of 2D instabilities. Using Eqs (2.56)-(2.61) we are able to reproduce the results of Dahlburg et al. (1983) and furthermore demonstrate that no information is lost in their investigation as all optimal instabilities are 2D. Motivated by the basic state analysis performed in §2.2.2, we consider an alternative magnetic field. In particular, we restrict our attention to a magnetic field given by the solution to Eqs (2.7)-(2.8) for the shear layer, in the regime where $Q \gg \lambda^2$, i.e.,

$$B(z) = \operatorname{sech}^2 10z. \tag{2.83}$$

We look for instabilities in 3D and numerically solve the subsequent eigenvalue problem. We perform a parameter survey in (M, S) space. It is shown in Fig 2.12 that 3D instabil-

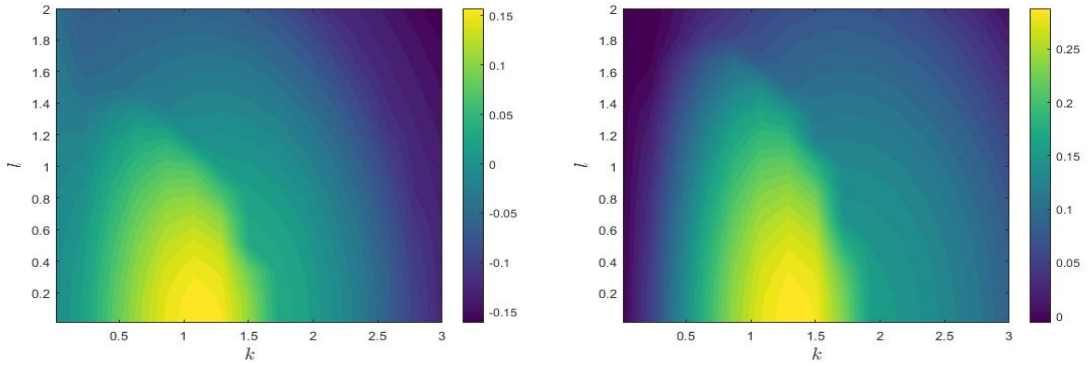

(a) $S = 100, M = 100$ (b) $S = 100, M = 1000$

Figure 2.12: $R(s)$ in $k - l$ space for the basic state magnetic field given by Eq (2.83).

ities are possible, however, the optimal instabilities are in fact 2D. To compute marginal stability curves in an efficient manner, we restrict our attention now to 2D modes and set $l = 0$. This system depends on both the magnetic and viscous Reynolds numbers, but we fix M, and look for solutions to $R(s(S, k)) = 0$ and hence locate the neutral stability curve.

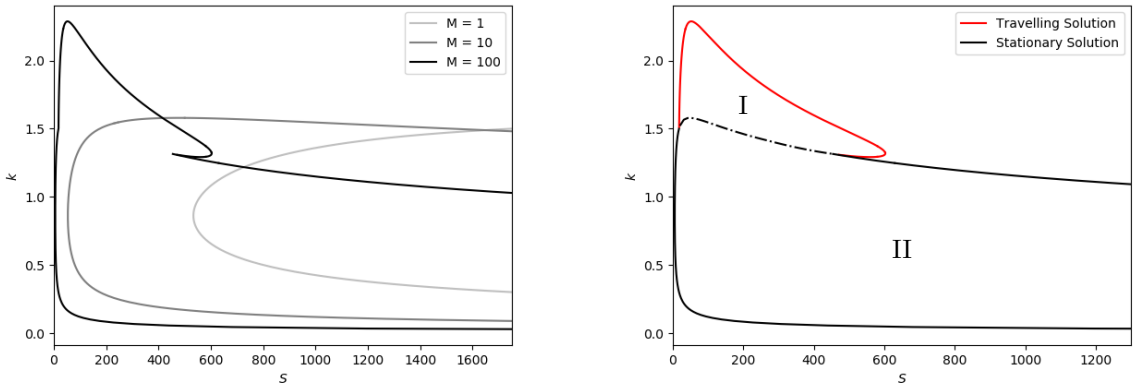

(a) (b)

Figure 2.13: Neutral stability curves for the magnetic jet in (S, k) space. (a) shows the marginal curves for three values of M; (b) shows the marginal stability curve for $M = 100$, highlighting the two branches of instability: stationary and travelling.

Figure 2.13a illustrates that for larger values of M, instability occurs at much lower values of S and the range of unstable wavenumbers is increased. Dahlburg et al. (1983) state that the stability threshold is given by a hyperbola in (M, S) space. We see this result in Fig 2.13a as the global minimum in (S, k) decreases at the rate at which M increases. Interestingly, we observe a new phenomenon not seen in Dahlburg et al. (1983) which we illustrate more clearly in Fig 2.13b. For $M = 100$ the neutral stability curve is split into two regions; labelled I and II. In region II there is only one unstable mode for a given set of parameters and the instability is stationary, i.e $I(s) = 0$. We also have region I, which is shown by the upper lobe enclosed within the red curve and black dashed line. Within region II, there is two unstable modes which are travelling waves ($I(s) \neq 0$) which propagate in opposite directions with equal frequency (a complex pair). We could not find oscillatory instabilities for the magnetic field given by Eq (2.81), and so travelling solutions were not reported by Dahlburg et al. (1983). To further understand the instability mechanisms in the two branches we take a look at the dispersion curves for the growth rate and frequency by taking vertical cross sections of Fig 2.13b.

To illustrate the stationary and travelling modes, we fix $M = 100$, take three values of $S = 200$, 590, and 1000, and solve Eqs (2.56)-(2.61) with $U = U_0 = 0$ for varying k. We chose these particular values of S, as they coincide to three regions of interest in Fig 2.13b: $S = 200$ corresponds to a region in which travelling modes are unstable; $S = 590$ corresponds to the tip of the red curve in Fig 2.13b, here travelling modes are marginally stable; $S = 1000$ corresponds to a region in which travelling modes are stable. Figures 2.14 show the growth rate against k (left) and the frequency against k (right). We can see a pair of travelling solutions is present for large k, but they are not necessarily unstable. We conclude from Figs 2.14 that the mode of maximum growth rate is a stationary solution, and, at larger values of k, the two stationary solutions with $R(s) > 0$ combine to form a complex pair of travelling waves which can be unstable for the region under the red curve

defined by II shown in Fig 2.13b.

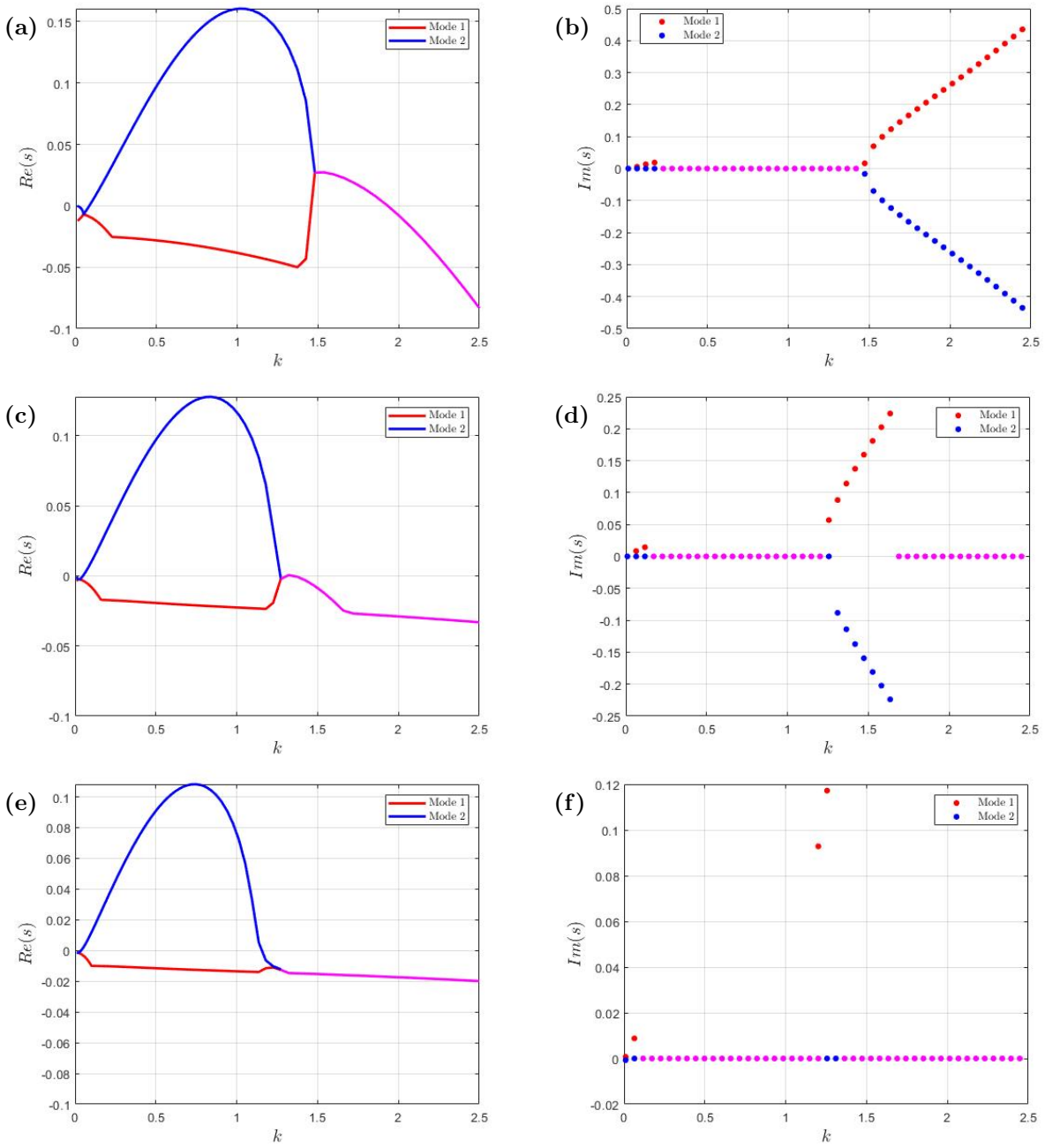

Figure 2.14: Growth rate (left) and frequency (right) of the eigenmode with the largest growth rate, i.e. $R(s) > 0$. $M = 100$ throughout with; in (a,b) $S = 200$; in (c,d) $S = 590$; in (e,f) $S = 1000$. The purple line represents the overlapping of red and blue data.

2.6 Reduced Cases of the Linear System

In this short section we introduce a set of sub-problems which will be crucial to understanding the instability mechanisms present within the full linear system. In each of these reduced cases, it is important to note that we consider the modified flow and field, which result from Eqs (2.12)-(2.13). We consider the following set of sub-problems to Eqs (2.56)-(2.61):

- **Sub-Problem I:** The purely hydrodynamic instability of the magnetic field modified viscous flow — in this case, $B = \delta = h = g = 0$ and the basic state in the linear problem is given by $(U(z), 0, 0), \boldsymbol{B} = 0$. This is analogous to the Orr-Sommerfeld problem studied in §2.4 but with $U(z)$ instead of $U_0(z)$.

- **Sub-Problem II:** The resistive instability of a current sheet with the flow modified magnetic field with no uniform vertical field. Here, $\delta = 0$, and the basic state in the linear problem is given by $\boldsymbol{U} = 0, \boldsymbol{B} = (B(z), 0, 0)$. This is analogous to the Dahlburg et al. (1983) problem studied in §2.5.

- **Sub-Problem III:** The linear stability of a current sheet in the presence of a vertical uniform magnetic field. This is a slight modification to Sub-Problem II with the basic state in the linear problem being given by $\boldsymbol{U} = 0$ and $\boldsymbol{B} = (B(z), 0, 1)$, and $\delta = 1$ in Eqs (2.56)-(2.61).

- **Sub-Problem IV:** Here we consider the joint instability of the basic state magnetic field field and flow with no vertical uniform magnetic field — here $\delta = 0$, and the basic state is given by $\boldsymbol{U} = (U(z), 0, 0)$ and $\boldsymbol{B} = (B(z), 0, 0)$.

We will see in subsequent sections that these reduced cases play a fundamental role in illustrating the dominant instability dynamics in the full system. We will show that, in certain parameter regimes, the full system correlates well with the range of sub-problems and that, in other regimes, the instability cannot be accurately explained by the sub-problems above.

2.7 Instability of a Shear Layer Target Flow

Throughout the rest of this chapter, we will set $\lambda = 10$, and in the next two sections, $H = 0$. First, we will solve the full system of linear equations given by Eqs (2.56)-(2.61), and then solve the sub-problems referred to in §2.6.

2.7.1 Surveying $Q - R_m$ Space

We begin the parameter survey by looking at the mode of maximum growth rate, and its associated frequency and wavenumber for a fixed Re. The choice of Re is informed through our previous study on the Orr-Sommerfeld equation for the target profile. In the following subsections, Re_c will refer to the critical Reynolds number from the Orr-Sommerfeld problem of the target profile. For the shear layer given by Eq (2.5), $Re_c \approx 12$. We investigate three times above, and a half below this critical value, i.e. $3Re_c$ and $\frac{1}{2}Re_c$. We restrict our attention to Q, R_m in the range $10^{-2} - 10^3$. Considering a larger range would result in coefficients $\mathcal{O}(10^{\pm 6})$ in Eqs (2.56)-(2.61) due to the factor of Γ — this would require a smaller resolution to ensure convergence. At each point in (Q, R_m) space, we maximise the growth rate over (k, l); it turns out that all the preferred modes are in fact 2D, with $l = 0$. This process is generally computationally expensive, and so the plots in Figs 2.15 are generated from a grid of 150×150 data points. Figure 2.15(a) shows that, above the stability boundary there are three local maxima, with the most unstable parameter regime being $Q, R_m \ll 1$ (the lower left quadrant). Figure 2.15(b) illustrates that for $Re < Re_c$, there are two local maxima. Comparison of Figs 2.15(a,b) demonstrates that the instabilities where $R_m, Q \gg 1$ do not depend heavily on Re. The dominant instability in Fig 2.15(a) has become stable when the target flow is stable. Therefore, we expect that this instability is governed mostly by hydrodynamic effects. Figures 2.15(c,d) demonstrate that these local maxima occur at different wavenumbers. Furthermore, these instabilities are due to different modes — this can be seen by the steep (almost discontinuous) contours shown in Figs 2.15(c,d). Figures 2.15(e,f) demonstrates that only one of the modes of instability is oscillatory. Comparison of Figs 2.15(e,f) shows that the frequency of the 'middle' local maximum depends on the Reynolds number, as the contours of frequencies in (Q, R_m) space changes between $3Re_c$ and $\frac{1}{2}Re_c$. Therefore, we might expect this to depend on both field and flow. We might also expect that the top-right instability is dominated by magnetic effects as it is independent of the Reynolds number.

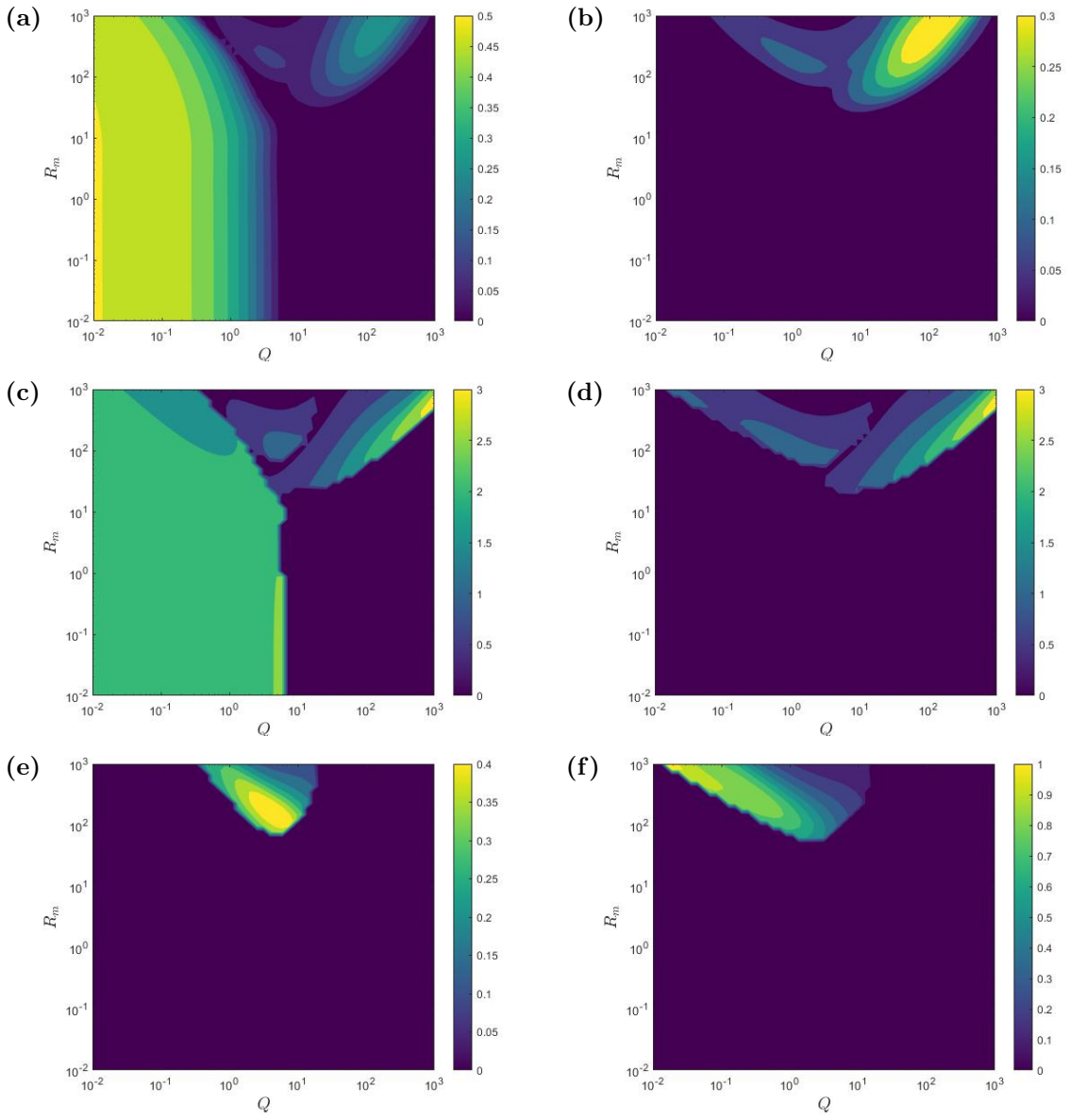

Figure 2.15: In the left column, $Re = 3Re_c$ and the right column is $\frac{1}{2}Re_c$ where $Re_c = 12.2$. The optimal growth rate (a,b); optimal horizontal wavenumber, k, (c,d); the frequency (e,f).

2.7.2 Understanding The Instabilities

To understand the instabilities in Figs 2.15 we utilise the sub-problems discussed in §2.6. Since there is a total of five problems, we do not perform a parameter survey in (Q, R_m) but instead take horizontal cross-sections through Figs 2.15, which is equivalent to fixing R_m, Re and varying Q. Since we know that the mode of maximum growth is 2D from previous investigations, we restrict our attention mostly to the case when $l = 0$ — this results in a decrease in computational time. However, it is important to note that we do sample k-space with a coarse grid to confirm that the mode of maximum growth is in fact 2D.

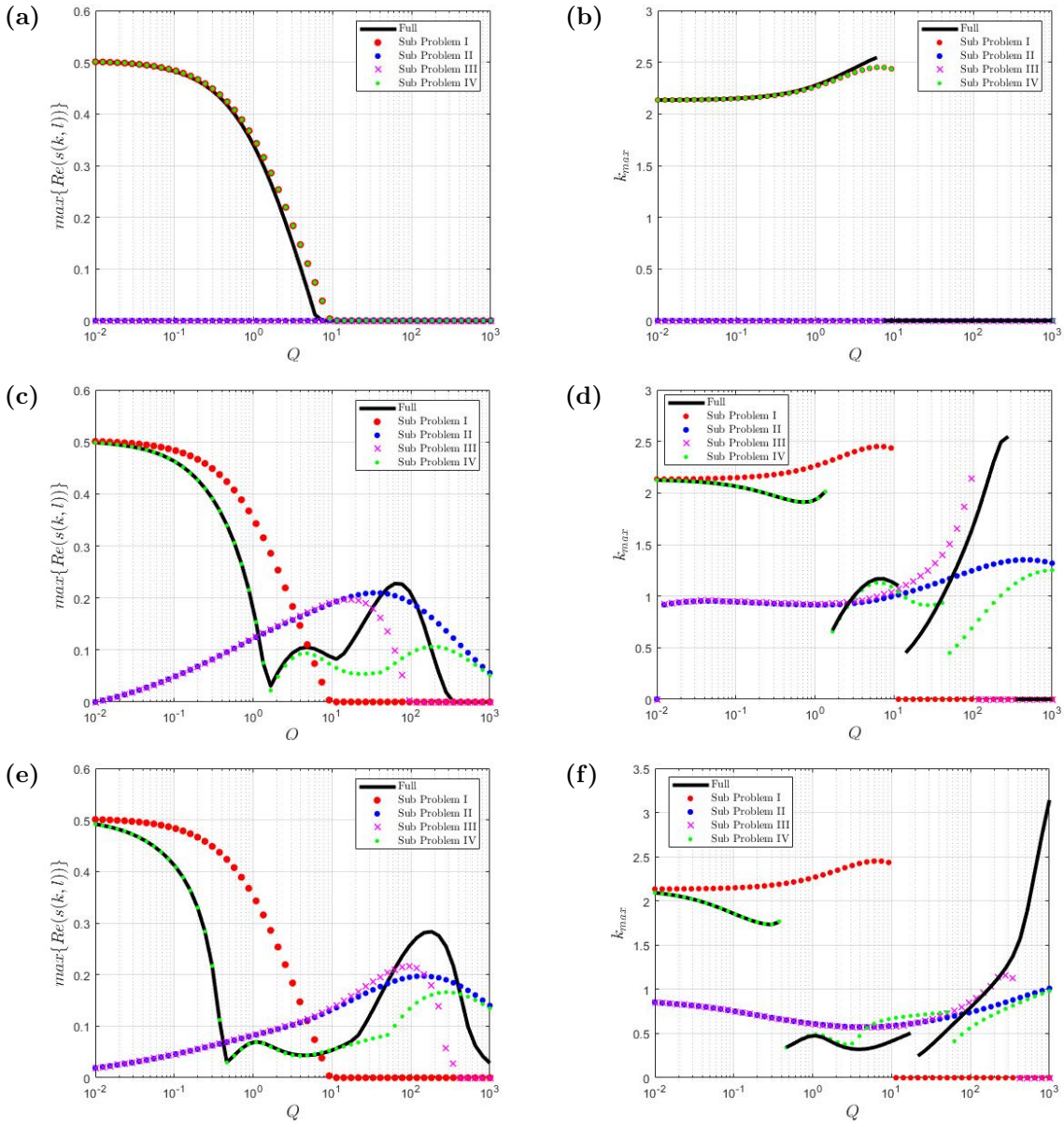

Figure 2.16: The left and right columns show the maximum growth rate and associated wavenumber, respectively. Here $Re = 3Re_c$, and $R_m = 0.01$ (a,b); $R_m = 150$ (c,d); $R_m = 750$ (e,f).

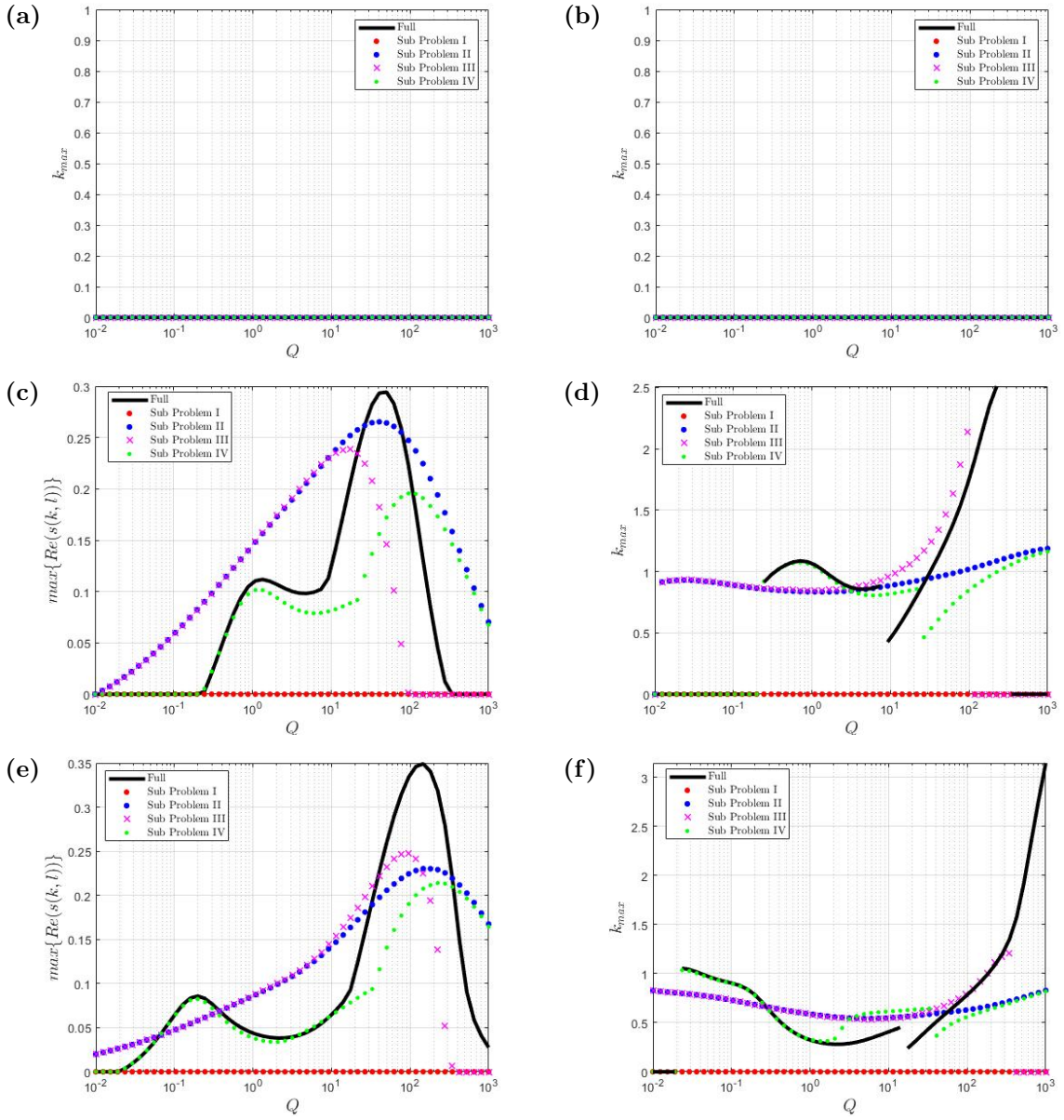

Figure 2.17: The left and right columns show the maximum growth rate and associated wavenumber, respectively. Here $Re = \frac{1}{2}Re_c$, and $R_m = 0.01$ (a,b); $R_m = 150$ (c,d); $R_m = 750$ (e,f).

We perform this procedure for both values of Re in Fig 2.15, and for three values of R_m, 0.01, 150, and 750. Figure 2.16(a) demonstrates that when $Q, R_m \ll 1$, the magnetic effects are negligible — this is shown first by the correlation between the full problem and sub-problem I. Furthermore, we can see explicitly that the effect of $B(z)$ is small as there is no difference between sub-problem I and IV. Figure 2.16(a) demonstrates that there is good agreement with the Orr-Sommerfeld problem, and hence the instability is mainly dominated by hydrodynamic effects, for all values of Q, when $R_m \ll 1$. However, we note slight stabilisation due to the vertical magnetic field in the full problem. Equation (2.44) states that as we increase R_m the amplitude of the magnetic field becomes larger. We can see in Figs 2.16(c)-(d) that, as R_m is increased, this magnetic field configuration becomes

unstable (shown by sub-problem II). As Q increases, the uniform vertical magnetic field has a stabilising effect on this magnetic instability and the system is stable for $Q \gg 1$. We can see across Figs 2.16(e,f)-2.17(e,f) that when $Q, R_m \gg 1$ then the influence of the flow is negligible — this is shown by the correlation between sub-problems II and IV in this particular regime. This is expected, as Eq (2.43) states that when $Q, R_m \gg \lambda^2$, $|U| \sim 1/Q$ and so the flow is weak. The stabilising effect of the uniform vertical magnetic field is due to the fact that $|B| \sim R_m/Q$ and so when $Q \sim R_m \gg 1$, the horizontal magnetic field is comparable to the uniform magnetic field.

Figures 2.17 illustrates the magnetic instability on a more clear scale, as the target flow is hydrodynamically stable. Figures 2.17(c-f) demonstrates that the full problem correlates with sub-problem IV until $Q \approx 1$. Figure 2.17(e) shows that adding a flow to sub-problem III can enhance the current sheet instability; or adding a uniform magnetic field to sub-problem IV can enhance the joint instability of parallel flow and field. In the regime with $R_m \gg 1$ we see that the full problem is the most unstable out of them all, for a range of values of Q. In addition to this, Figs 2.16 illustrates that the uniform vertical magnetic field can enhance instability. Furthermore, a 'hydrodynamically-stable' flow has a destabilising effect, although it does not seem to play a role in sub-problem IV. This suggests that $\mathcal{B}_0$ and U are both important.

2.7.3 The Eigenfunctions

We have shown that a range of instabilities are possible due to either flow, field, or both, and we have also shown that the instabilities present can be travelling or stationary solutions. To examine the instabilities further, we look at how the largest growth rate and corresponding frequency varies with k for each (Q, R_m, Re) and examine the eigenfunctions for the optimal wavenumber. To examine the eigenfunctions, the subsequent figures will show the basic state (a)-(b); the growth rate and frequency against k (c); and the stream and flux-eigenfunctions (d) for the optimal value of k in (c).

First we set $Q = R_m = 0.01$ — here, magnetic effects are weak and therefore this regime is mostly hydrodynamic. We can see in Figs 2.18(a)-(b) that the amplitude of the magnetic field is small, and the velocity profile is approximately equal to the target profile. Figure 2.18(c) demonstrates that the mode with the second largest growth rate (s_2) is a stable travelling solution which eventually becomes part of a complex conjugate pair at approximately $k = 5.3$. The largest mode (s_1) is unstable, which is to be expected, and agrees with the results from the Orr-Sommerfeld equation — this unstable mode is stationary, before becoming a travelling mode. Figures 2.18(d)-(e) shows the stream- and flux-functions respectively for optimal k in 2.18(c) over two periods in x. The amplitude of the flux-function is small compared to that of the stream-function. We further observe that the stream-function is localised in z.

In the Figs 2.19, $Q = 1.125$ and $R_m = 750$ — sub-problems have shown that both magnetic and hydrodynamic effects are important. Figures 2.19(a)-(b) shows that the flow is not too different to the target, and the Orr-Sommerfeld problem has shown that this is flow is unstable to purely hydrodynamic instabilities. The basic state magnetic field has a much larger amplitude compared with $R_m = 0.01$. The two most dominant modes are a complex conjugate pair of travelling solutions, and we can see in Figs 2.19 that the stream-function is localized in the lower half of the domain whereas the flux-function is localized near $z = 0$.

In Figs 2.20 we are in the 'magnetic' regime, in which magnetic affects dominate, with $Q = 750$ and $R_m = 1000$. In this regime, we know the configuration of the basic state is given by Eq (2.43)-(2.44). Figure 2.20(c) shows that the most dominant mode is generally an unstable stationary solution which becomes a decaying travelling wave for increasing k. Figure 2.20 illustrates that the flux-function is larger in amplitude than the stream-function and it is generally localized at $z = 0$.

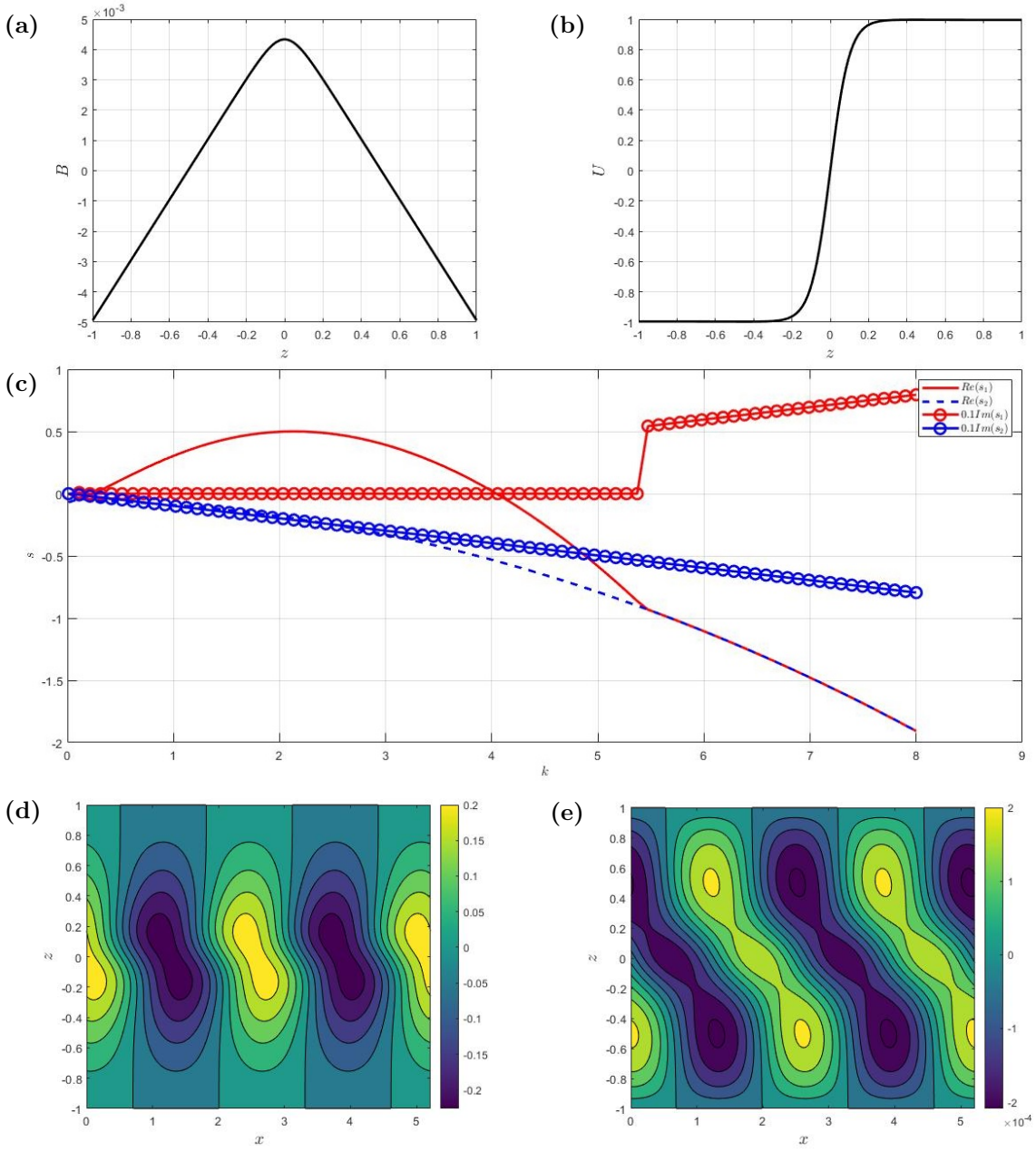

Figure 2.18: $Q = R_m = 0.01$, and $Re = 3Re_c$. The basic state (a,b) with associated growth and frequency (c). The stream- and flux-functions for the optimal wavenumber, $k_{max} \approx 2.22$ (d,e).

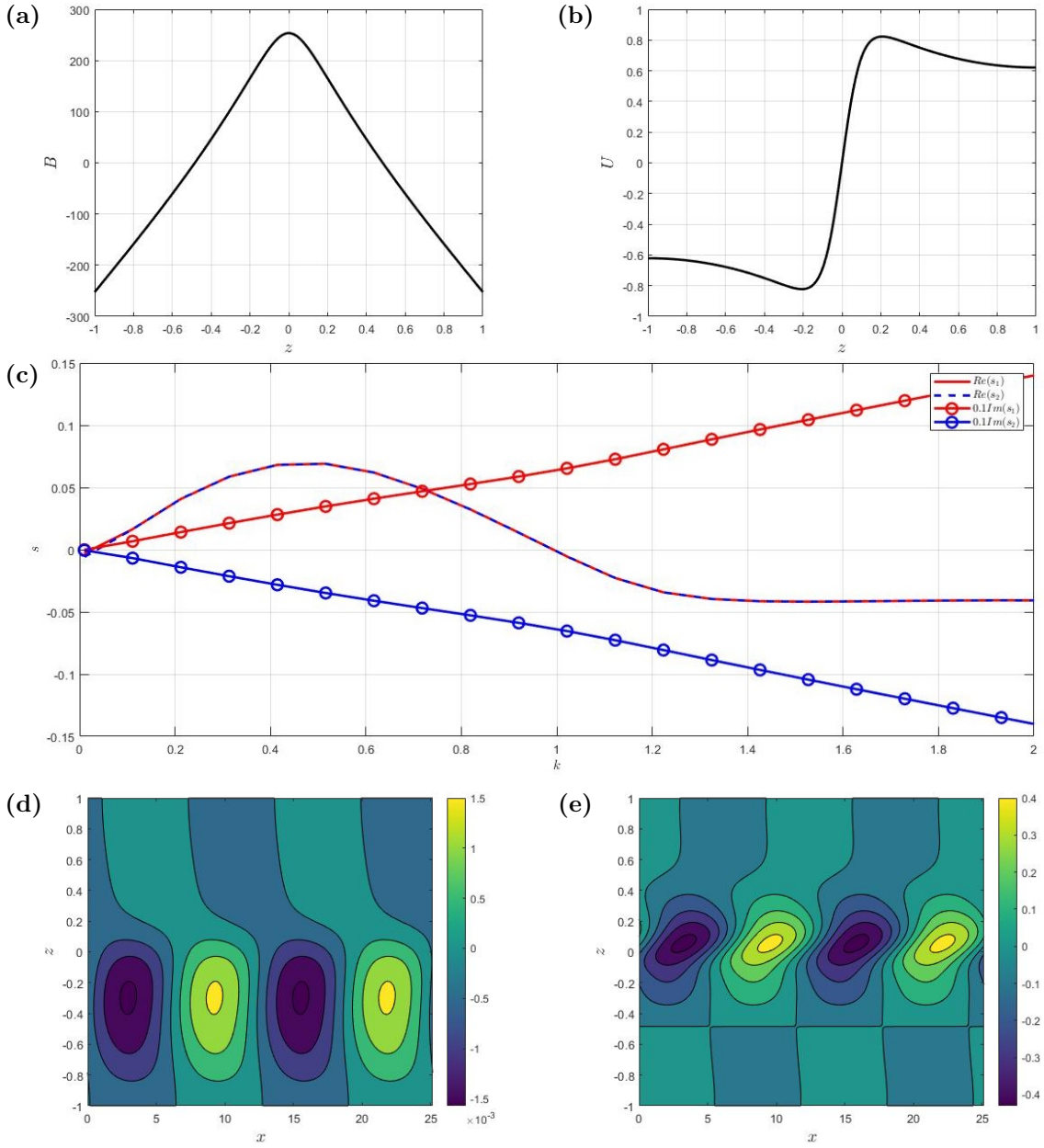

Figure 2.19: $Q = 1.125, R_m = 750$, and $Re = 3Re_c$. The basic state (a,b) with associated growth and frequency (c). The stream- and flux-functions for the optimal wavenumber, $k_{max} \approx 0.51$ (d,e).

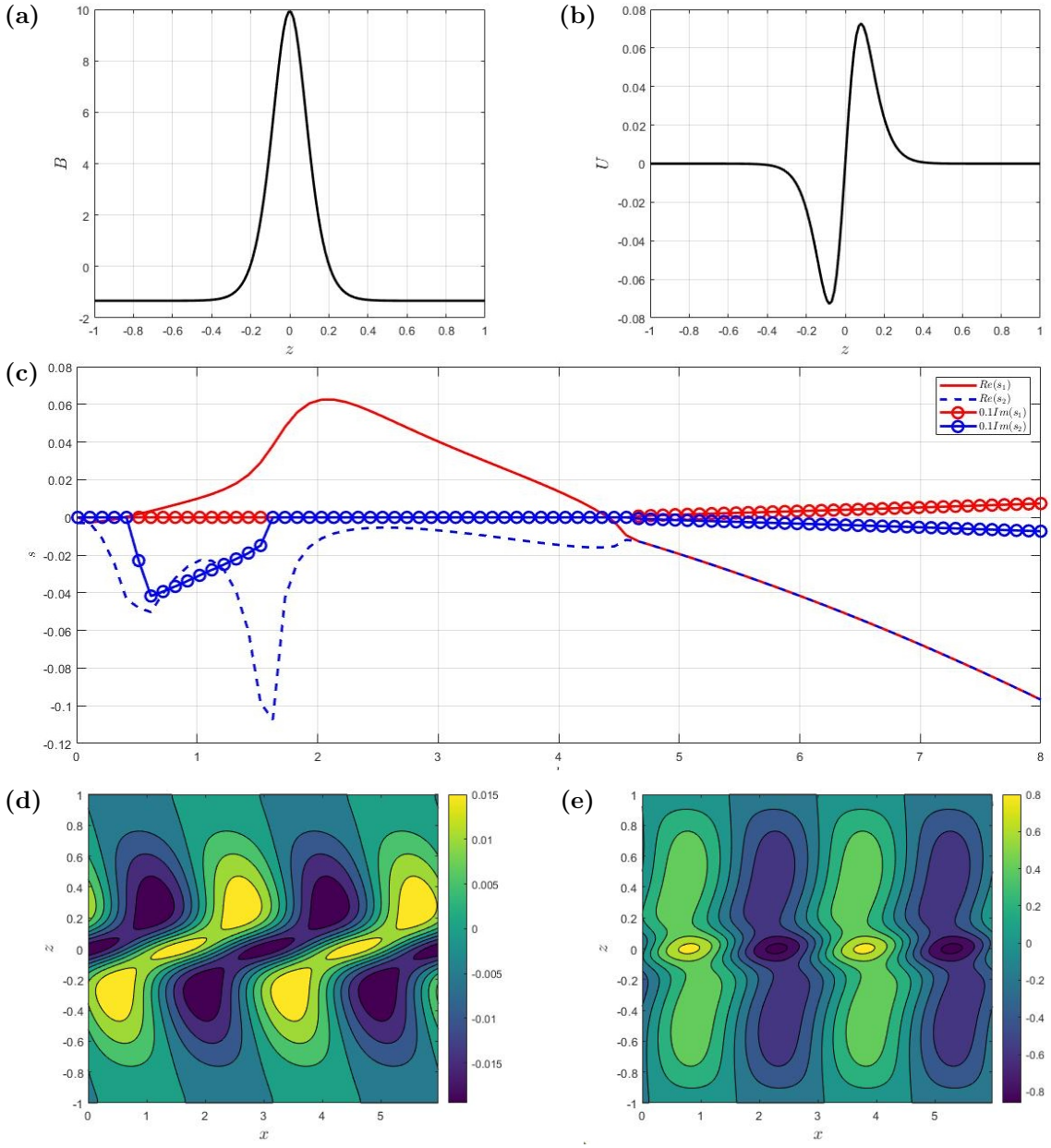

Figure 2.20: $Q = 750, R_m = 1000$, and $Re = 3Re_c$. The basic state (a,b) with associated growth and frequency (c). The stream- and flux-functions for the optimal wavenumber, $k_{max} \approx 2.16$ (d,e).

2.7.4 The Role of Magnetic Flux

Recall that in §2.2.2, the magnetic flux in the magnetic field, $\langle B \rangle = H$, is at our disposal. In this section, we perform an investigation into the role magnetic flux plays in the full linear problem. We follow a similar line of enquiry to that in §2.7.1 for a range of fluxes, where $Re = 3Re_c$.

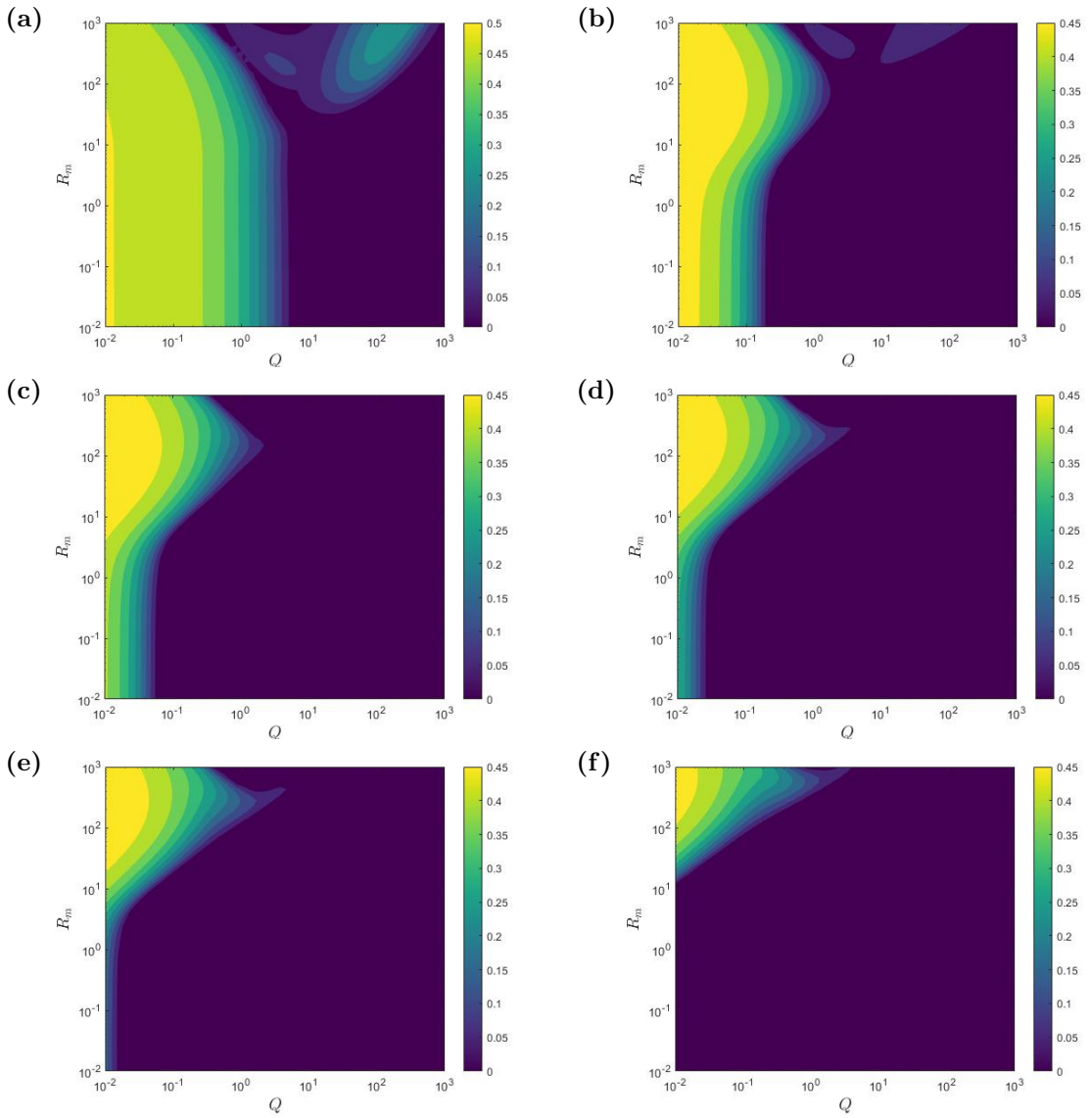

Figure 2.21: Growth rate for $Re = 3Re_c$ for a series of fluxes, (a) $H = 0$, (b) $H = 25$, (c) $H = 50$, (d) $H = 75$, (e) $H = 100$, (f) $H = 250$.

Figures 2.21 show the optimal growth rate in (Q, R_m) space for a series of different fluxes, obtained through optimising over (k, l) space for a series of (Q, R_m, Re) — again, the dominant mode of instability was 2D, and hence $l = 0$. Figures 2.21 show that increasing the flux in general inhibits the purely hydrodynamic instability in the regime when $Q, R_m \ll 1$ — when $H = 250$ this regime is totally stable. We can see from Fig 2.21(c) that the instability in the regime where $Q, R_m \gg 1$ has fully stabilised. The key feature of Figs 2.21 is that, as the flux is increased, we observe a narrowing of possible instability in

(Q, R_m) space were $Q \ll 1$ and $R_m \gg 1$. We can see that increasing the flux generally inhibits instability everywhere across (Q, R_m) space and appears to saturate at $R(s) \approx 0.45$, shifting to larger values of R_m and is optimal for $Q \to 0$.

Having a non-zero magnetic flux shifts the basic magnetic field by a value of $H/2$. When $Q, R_m \ll 1$, this means that the basic horizontal magnetic field is essentially a uniform horizontal field where $B \approx H/2$. Since $|B|$ is no longer small, this parameter regime is no longer purely hydrodynamic, therefore the influence of the magnetic field is significant, and further inhibits the destabilising effect due to the flow. As R_m is increased, we are now in a parameter regime where $B \approx R_m$, and therefore, the instability is governed by sub-problem IV. This can be shown by Fig 2.21(f) — when $R_m \gg 1, Q \ll 1$ the instability is still strong and is governed by mostly hydrodynamic effects, while for $R_m \ll 1, Q \ll 1$, the instability has been inhibited due to the large uniform horizontal magnetic field.

2.8 Instability of a Jet Target Flow

2.8.1 Surveying $Q - R_m$ Space

We perform a similar analysis for the target profile given by Eq (2.6) which corresponds to a jet, i.e., we perform an exhaustive survey of the mode of maximum growth rate in (Q, R_m) space for two values of the Reynolds number. Again, three times above, and half below the critical value, $Re_c \approx 44$, which was determined by the purely hydrodynamic investigation in §2.4.

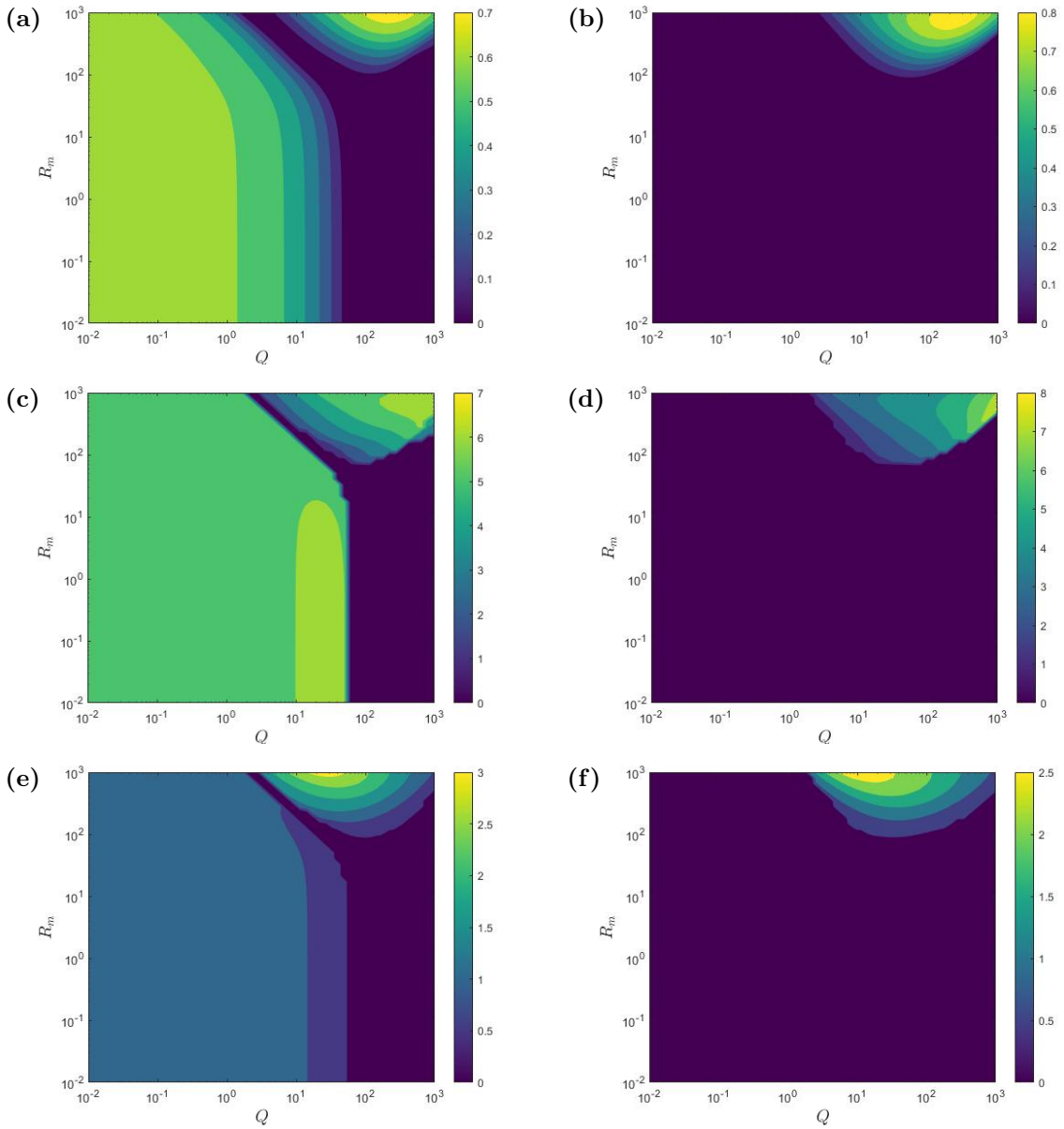

Figure 2.22: In the left column, $Re = 3Re_c$, in the right column $Re = \frac{1}{2}Re_c$, where $Re_c = 44$. The optimal growth rate (a,b); optimal horizontal wavenumber, k, (c,d); the frequency (e,f).

Figures 2.22 shows the growth rate (top), the optimal wavenumber (middle), and the frequency (bottom) for $Re = 3Re_c$ (left) and $Re = \frac{1}{2}Re_c$ (right). Figure 2.22(a) shows

that there are now only two local maxima. We note the absence of the central instability observed in the case of a tangent shear layer (see Fig 2.15). We observe a similar behaviour in that, in the regime where $Q, R_m \ll 1$, there is an instability which we will later show is predominantly due to hydrodynamic effects. A key feature of 2.22(a) is that the instability in the regime where $Q, R_m \gg 1$ is dominant over the hydrodynamic instability. This is not surprising as the basic magnetic field in this case is completely different. Figures 2.22 show that, in the hydrodynamic regime — which has been shown to be when $Q, R_m \ll 1$ — the preferred wavenumber does not significantly vary, until at $Q \approx 10$ at which, the critical wavenumber increases before rapidly falling off. At $Q \approx 10$, this particular mode becomes stable owing to a hydrodynamically stable basic flow. Another key feature of Figs 2.22 is that the dominant instabilities are travelling wave solutions. In the region where $Q, R_m \ll 1$, it is consistent with what we calculate in the Orr-Sommerfeld case, but interestingly, the dominant instability when $Q, R_m \gg 1$ is also travelling, which was not the case for the shear layer forcing — this can be seen by comparison of Figs 2.15(e) and 2.22(e) .

2.8.2 Understanding The Instabilities

Similarly to the tangent shear flow case, we utilise the sub-problems discussed in §2.6 to understand the resultant instabilities in Figs 2.22. Since there is a total of five problems, we do not perform a parameter survey in (Q, R_m) but instead take horizontal cross-sections through Figs 2.22, which is equivalent to fixing R_m, Re and varying Q — this is shown below in Figs 2.23-2.24. Since we know that the mode of maximum growth is 2D from previous investigations, we restrict our attention to the case when $l = 0$. Again, we perform calculation across a coarse grid in $k-$space to ensure no 3D instabilities are missed.

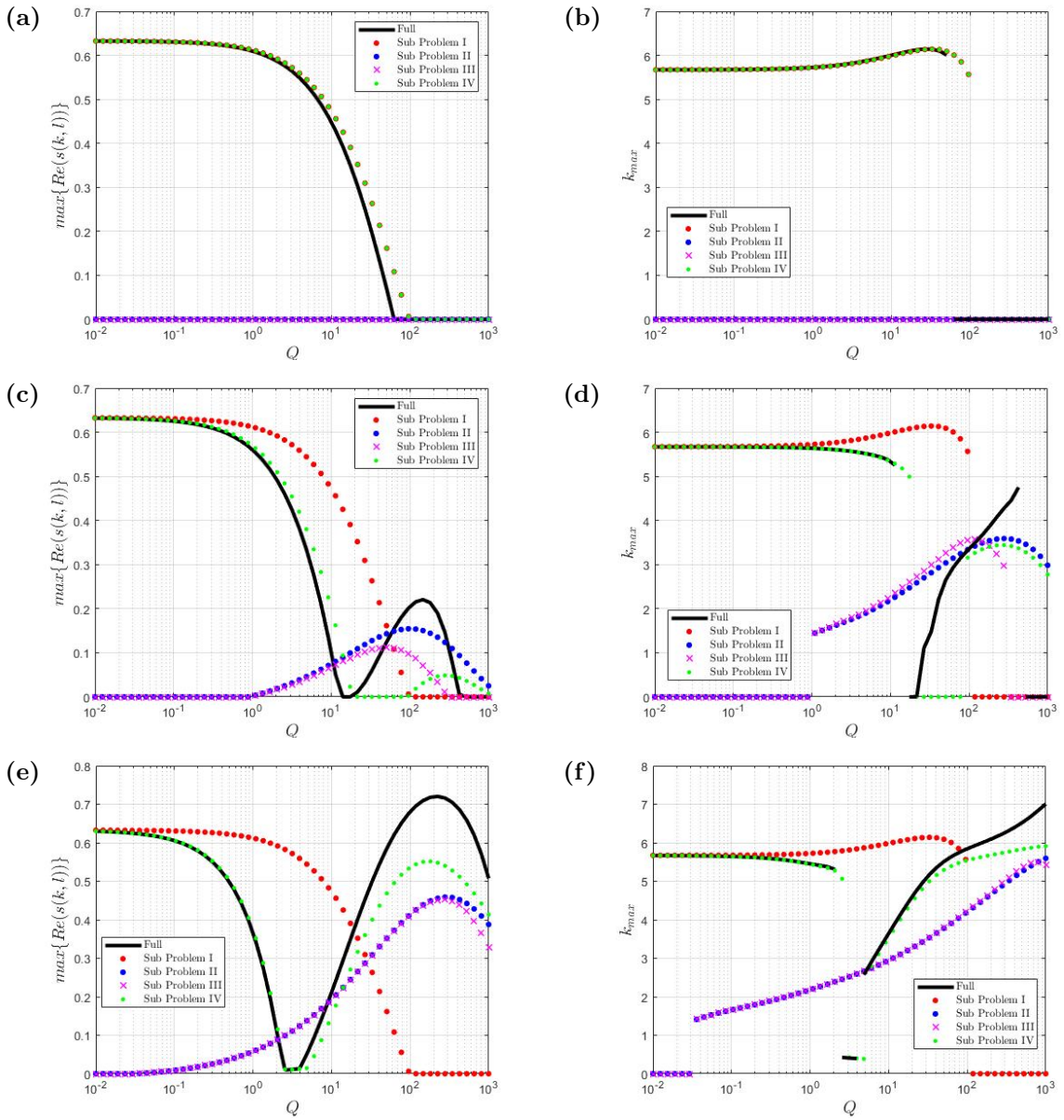

Figure 2.23: The left and right columns show the maximum growth rate and the associated wavenumber, respectively. Here $Re = 3Re_c$, and $R_m = 0.01$ (a,b); $R_m = 150$ (c,d); $R_m = 750$ (e,f).

Figures 2.23(a)-(b) show that when $Q, R_m \ll 1$, the influence of the horizontal magnetic

field is negligible, as we observe the green dots correlate well with the Orr-Sommerfeld system (red dots). Figures 2.23(a)-(b) show that within the hydrodynamic regime, there is a slight stabilising effect due to the vertical magnetic field, as the full problem is slightly less unstable than the Orr-Sommerfeld problem.

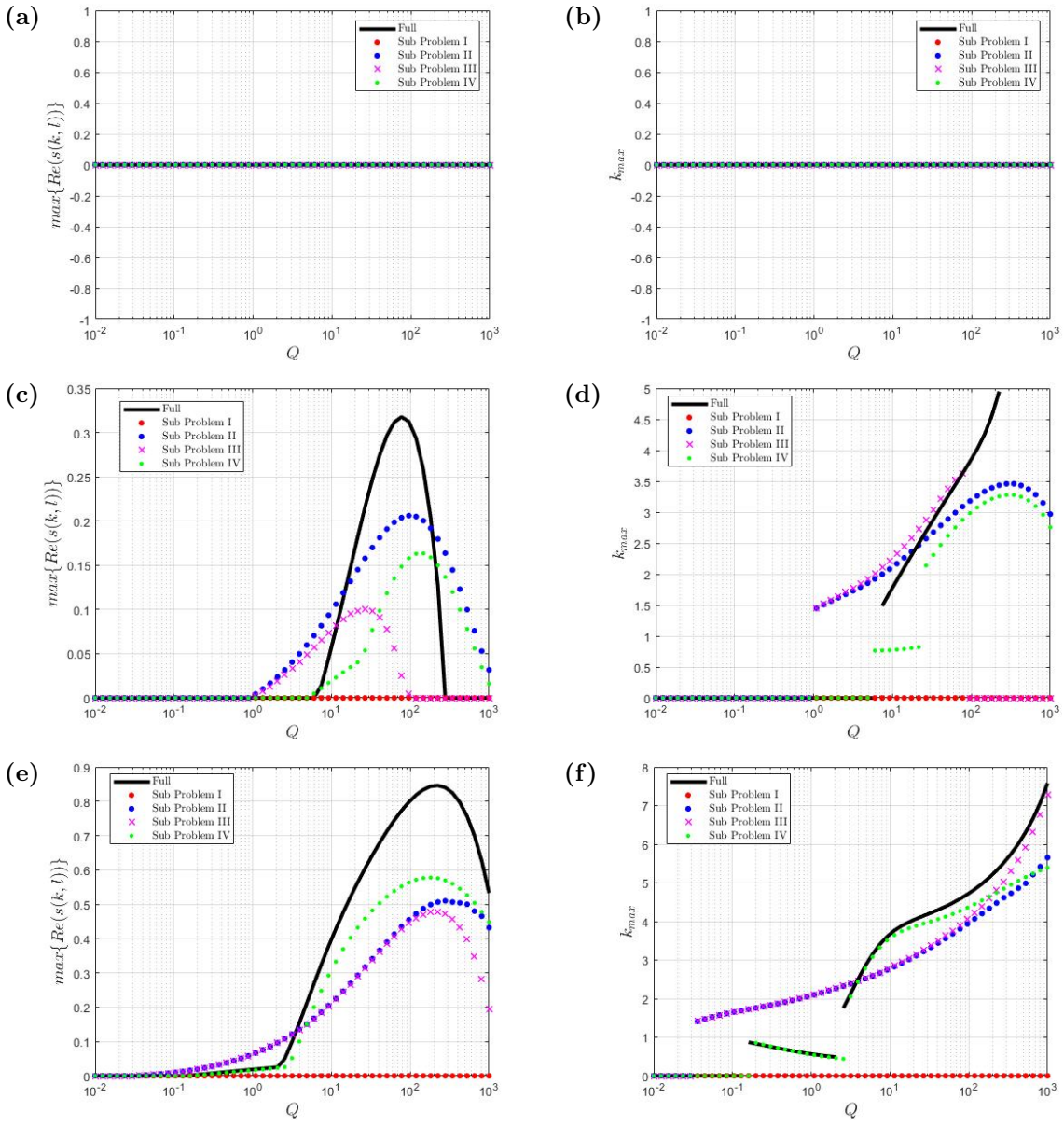

Figure 2.24: The left and right columns show the maximum growth rate and the associated wavenumber, respectively. Here $Re = Re_c/2$, and $R_m = 0.01$ (a,b); $R_m = 150$ (c,d); $R_m = 750$ (e,f).

As R_m is increased, Figs 2.23(c)-(d) show a thin region of stability. The discontinuity in k_{max} shown in Fig 2.23(d) demonstrates that this second instability is a separate mode. It is shown in Figs 2.23(c)-(d) that, as R_m is increased, the stabilising effect due to the horizontal magnetic field becomes stronger: the green dots diverge from the Orr-Sommerfeld problem (red dots) and the hydrodynamic mode becomes stable at smaller value of Q

compared with that in Figs 2.23(a)-(b). Moreover, Figs 2.23(c)-(f) illustrate that there is good agreement between sub-problems II and III until Q becomes sufficiently large, such the horizontal magnetic field is of order unity (see §2.2.2). This effect appears clearly in Fig 2.23(e) where the sub-problems diverges at a larger Q, since $R_m = 750$ here. In the case of a jet shear flow, there is no notable instability for $Q \sim 1$, however, Figs 2.23(e)-(f) show a weak instability where both field and flow are present — this instability is an entirely independent mode which is shown in Fig 2.23(f). Comparison of Figs 2.16 and 2.23 shows that, the jet forcing results in a tearing mode instability that is more unstable than the hydrodynamic instability shown when $Q, R_m \ll 1$ — this is an interesting point, as it demonstrates that the magnetic field that results from a jet is more optimal for instability than that generated from a tangent shear layer.

Figures 2.24 illustrate how the sub-problems correlate with the full problem for a stable target flow. As expected, when the target flow is stable, none of the problems exhibit instabilities for $Q \ll 1$ across the range of R_m shown. As we increase R_m we see an instability sets in at $Q, R_m \gg 1$, with a growth rate that generally increases with R_m. Figures 2.24(c)-(e) again show good correlation between both magnetic sub-problems until $Q \approx R_m$ and then we see a stabilising effect due to the uniform vertical magnetic field.

Interestingly, Figs 2.24(c)-(f) show that, depending on R_m, a hydrodynamically stable flow can either enhance or inhibit instability due to a horizontal magnetic field; this is illustrated by sub-problem IV. In 2.24(c)-(d), where $R_m = 150$, we see the flow has a stabilising effect since the green dots lie below the purely magnetic problem II (blue dots), and in Figs 2.24(e)-(f), where $R_m = 750$, the basic flow enhances the tearing mode. Comparison of Figures 2.23(e)-(f) and Figs 2.24(e)-(f) show that the growth rate in the regime where $Q, R_m \gg 1$ does not vary significantly with Re, however the optimal wavenumber is pushed to larger values of k. In fact, comparison of Figs 2.23(f) and 2.24(f) shows that the optimal wavenumber, k_{max}, varies significantly across all sub-problems as Re is decreased. For example, k_{max} begins to decrease for $Q \approx 10^3$ in sub-problem III (purple crosses) for $Re = 3Re_c$, whereas k_{max} continues to increase with Q for $Re = Re_c/2$.

2.8.3 The Eigenfunctions

Again, all previous investigations in this section have looked at the optimal wavenumber and its associated growth rate and frequency. To examine the instabilities further, we look at how the growth rate and frequency varies with k for each (Q, R_m, Re) and examine the eigenfunctions for the optimal wavenumber. To examine the eigenfunctions, the subsequent figures will show the basic state (a)-(b); the growth rate and frequency against k (c); and the stream and flux-eigenfunctions (d) for the optimal value of k in (c).

Figures 2.25(a)-(b) show the basic state configuration in the hydrodynamic regime, where $Q = R_m = 0.01$. Figures 2.25(c) show that the two most dominant modes are an unstable travelling solution and a stationary stable solution: this is shown by the red and blue curves respectively. The optimal wavenumber in Fig 2.25(c) is given by $k \approx 5.8$ and is consistent with that obtained from the Orr-Sommerfeld equation: this is further evidence that, in the regime where $Q, R_m \ll 1$, the instabilities are dominated by hydrodynamic effects.

We plot the stream- and flux-functions in Fig 2.25(d)-(e) — we can see that the stream-function is consistent with the Orr-Sommerfeld equation shown in Fig 2.10, and the flux-function is small in comparison to the stream-function. Both eigenfunctions are localized around the center of the domain, with the stream-function being peaked $z = 0$, whereas the flux-function undergoes a sign change across $z = 0$.

Figures 2.26 is analogous to Figs 2.25, for $Q = 750$ and $R_m = 1000$. It is shown in Fig 2.26(c) that the most unstable mode is a travelling mode solution, with an optimal wavenumber $k \approx 7.1$. In this parameter regime, the mode with the second largest growth rate is also unstable with a non-zero frequency for $k < 3$. It eventually becomes stable at larger wavenumbers. Figures 2.26(d)-(e) show that while the flux-function is larger in amplitude, the relative difference between flux- and stream-functions is not as large as that shown in 2.25(d)-(e). Both eigenfunctions in Figs 2.26(d)-(e) show localisation about $z = 0$.

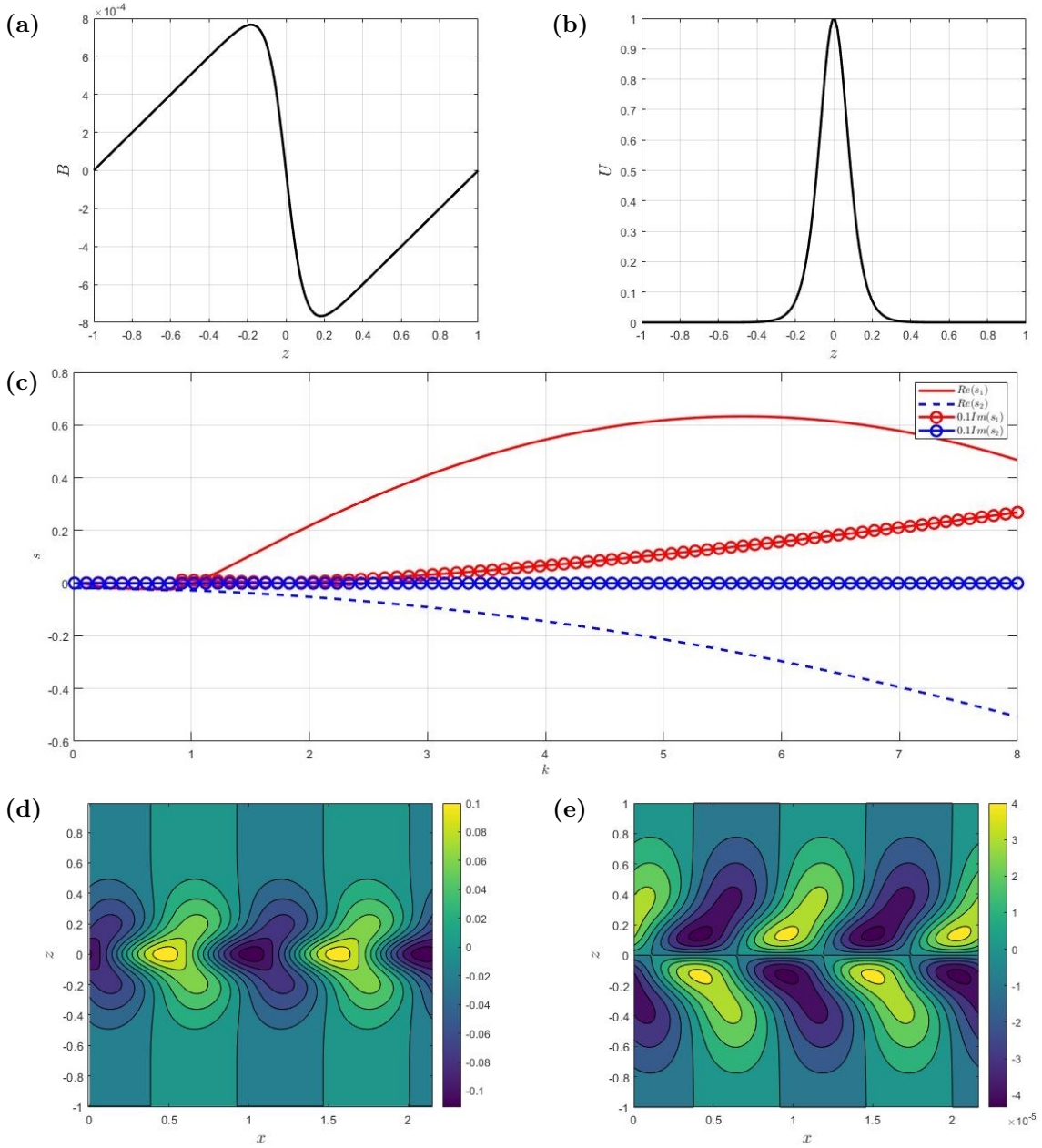

Figure 2.25: $Q = 0.01, R_m = 0.01$, and $Re = 3Re_c$. The basic state (a,b) with associated growth and frequency (c). The stream- and flux-functions for the optimal wavenumber, $k_{max} \approx 5.96$ (d,e).

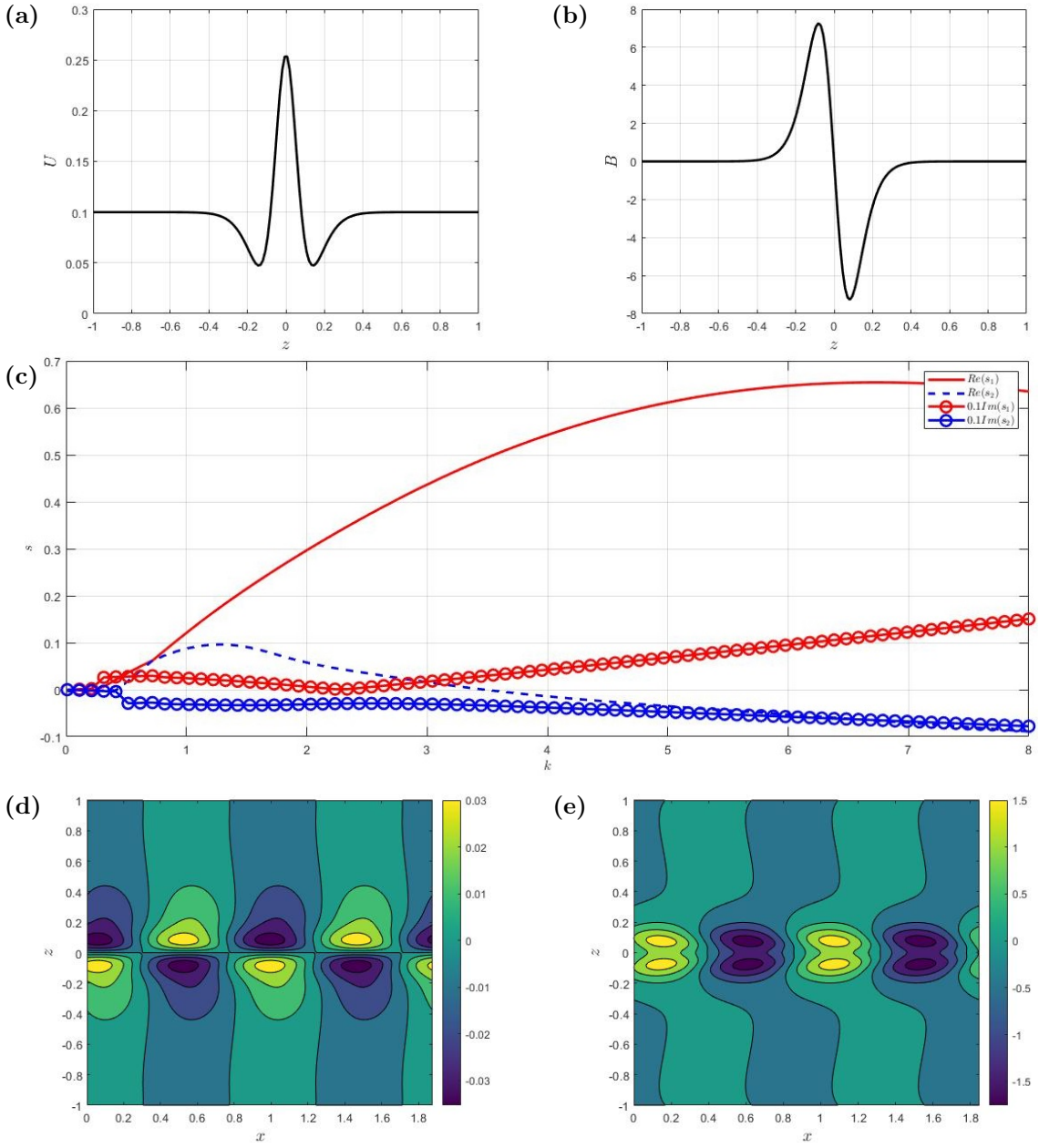

Figure 2.26: $Q = 750, R_m = 1000$, and $Re = 3Re_c$. The basic state (a,b) with associated growth and frequency (c). The stream- and flux-functions for the optimal wavenumber, $k_{max} \approx 6.78$ (d,e).

2.8.4 The Role of Magnetic Flux

We investigate the role of total magnetic flux in the case of an unstable jet target flow. Similarly to the tangent shear forcing case, Figs 2.27 shows the optimal growth rate in (Q, R_m)-space for a series of different fluxes, H.

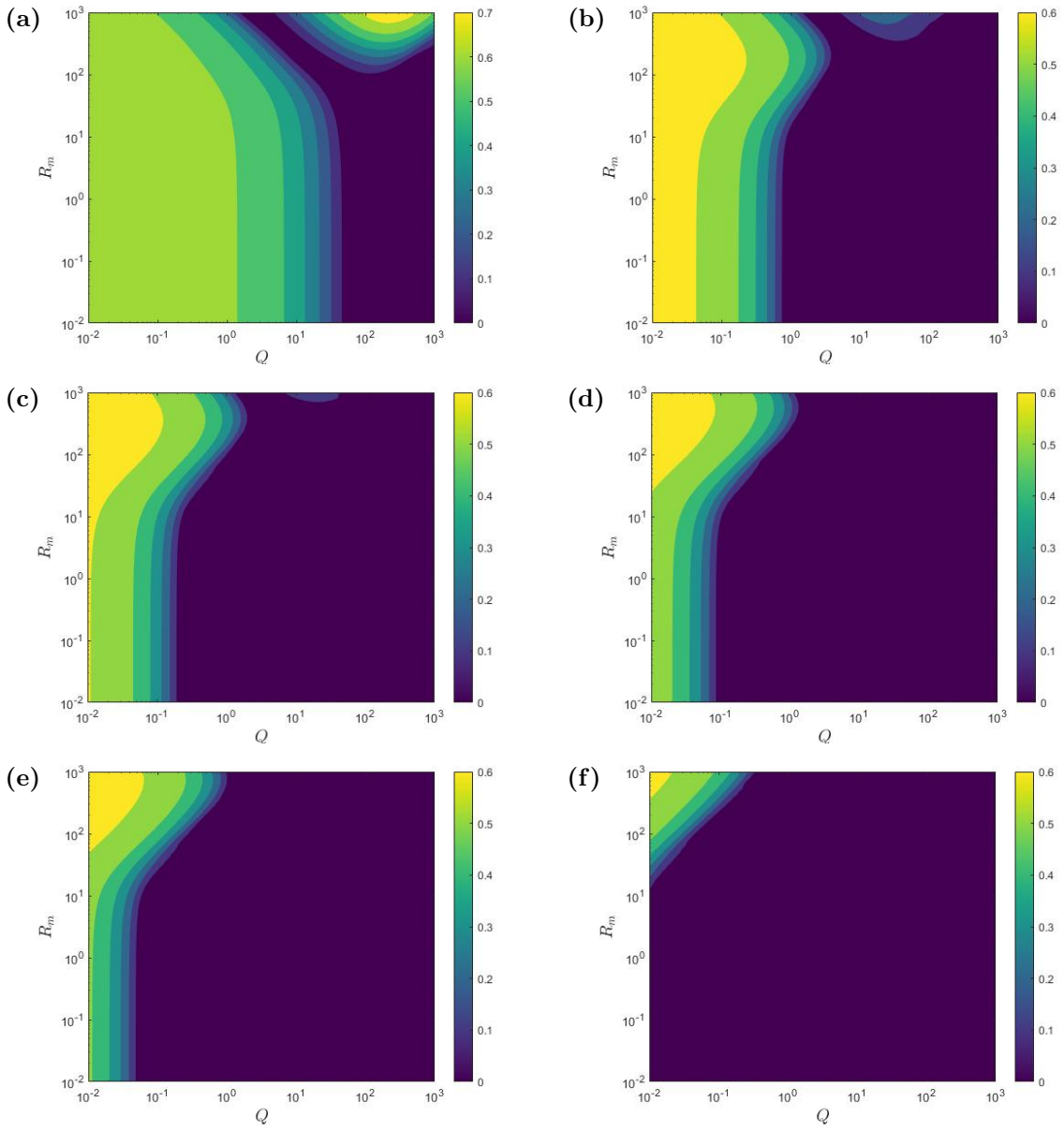

Figure 2.27: Growth rate for $Re = 3Re_c$ for a series of fluxes, (a) $H = 0$, (b) $H = 25$, (c) $H = 50$, (d) $H = 75$, (e) $H = 100$, (f) $H = 250$.

Figure 2.27 shows that increasing the flux suppresses the hydrodynamic instability in the regime where $Q, R_m \ll 1$, until the flux becomes large enough to completely stabilise this mode. It can be seen in Figs 2.27(a)-(c) that as the flux is increased, the growth rate in the regime where $Q, R_m \gg 1$ is reduced.

Similarly in Figs 2.21, Figs 2.27 shows a narrowing of the region of instability, as the

hydrodynamic instability saturates to $\max(R(s)) \approx 0.6$, with the optimal R_m increasing with H, in the limit where $Q \to 0$. It is important to reiterate that, for $R_m \ll 1$, the horizontal magnetic field is essentially uniform, such that $B \approx H/2$. This large uniform magnetic field stabilises the flow. As R_m is further increased, $B \approx R_m$, and the magnetic field has a significant gradient; so, in the regime $R_m \gg 1$, the magnetic field is stabilising, but does not completely inhibit the hydrodynamic instability.

2.9 Conclusions and Future Considerations

In this chapter, we have proposed a novel mathematical model which incorporates both field and flow in a self-consistent manner, through a viscous forcing provided by a target velocity. In general, shear velocities boil down to either jets or tangential shears and, in these cases, we have made analytic and numerical progress on classical problems, such as the linear stability of parallel viscous shear flows. We have reproduced numerical results within the literature and gained important insights into less-studied problems such as the linear stability of a resistive magnetic field. We are able to show this complicated system reduces to well-studied problems and can partially be understood through studying a set of reduced problems.

The Orr-Sommerfeld equation has proven invaluable, as we utilised the purely hydrodynamic case to reduce our 5D parameter space to a 4D parameter space through informing the choice of Reynolds number. The linear stability analysis has elucidated the role of both viscous and magnetic Reynolds numbers, as well as the Chandrasekhar number in the joint linear stability of both field and flow. We have demonstrated that a fully hydrodynamically stable flow can either enhance or inhibit the resistive instability of a horizontal magnetic field. In addition to this, the vertical uniform magnetic field which generates the horizontal magnetic field through a tangential stretching plays an important role in the stabilisation of the resistive current sheet instability in certain parameter regimes. Depending on where we are in parameter space, we have shown that both unstable travelling and unstable stationary solutions are possible.

Finally, we have shown the role of a non-zero total magnetic flux in the basic state for both a jet and tangent layer target profile. The investigation has demonstrated how varying the flux plays a role in the stabilisation of hydrodynamic instabilities, even in regimes which would otherwise be governed purely by hydrodynamic effects. Moreover, we have shown that while increasing the flux is enough to stabilise flows in the hydrodynamic regime where $Q, R_m \ll 1$, increasing the flux leads to the dominant instability existing at larger values of R_m while $Q \to 0$.

The shearing of a magnetic field is found in nature, inherently in evolving systems. A suitable next step for this problem would be to perform a linear stability analysis of the

time evolving basic state $U(z,t)$, $B(z,t)$, given by

$$\frac{\partial U}{\partial t} = \frac{Q}{R_m Re}\frac{\partial B}{\partial z} + \frac{1}{Re}\left(\frac{\partial^2 U}{\partial z^2} - \frac{\mathrm{d}^2 U_0}{\mathrm{d}z^2}\right), \tag{2.84}$$

$$\frac{\partial B}{\partial t} = \frac{\partial U}{\partial z} + \frac{1}{R_m}\frac{\partial^2 B}{\partial z^2}. \tag{2.85}$$

An analysis of Eq (2.84)-(2.85) has shown that, for a set of parameter values (Q, R_m, Re), we can obtain solutions at a fixed time t^* which are approximately equal to solutions from the steady problem for a different set of parameters (Q^*, R_m^*, Re^*). An important question arises: Would instability ensue before an equilibrium state is reached through diffusive processes? The linear stability analysis has given us insight into the linear stability properties of the final state to Eqs (2.84)-(2.85) but, for certain parameter values, instabilities and therefore nonlinearity may be at play before such a state is reached. Therefore, a quasi-static or full-time dependent linear stability analysis, and subsequently a nonlinear stability analysis is essential. In the next chapters, and therefore by the end of the thesis, we will illustrate the importance of time-dependent basic states, and show that, in some cases, the linear stability theory of the final state is not necessarily sufficient.

Chapter 3

The Magnetic Buoyancy Instability of a Shear-Generated Equilibrium

3.1 Introduction

In this chapter we will study magnetic buoyancy instabilities of a time-independent, non-trivial background state. The process which generates the field and flow is the same as in Chapter 2, namely through a forced target flow. However, to study magnetic buoyancy instabilities, this shearing takes place in the presence of a stably-stratified and compressible atmosphere. The general idea is to emulate an equatorial section within the solar tachocline, by considering a box in Cartesian geometry. The uniform vertical field, $\mathcal{B}_0\hat{\boldsymbol{z}}$, can be seen as the weak poloidal field, and the resulting flow, U, simulates the strong velocity shear within the tachocline. First, we remind the reader of the basic state model, along with the dimensional compressible Magnetohydrodynamics (MHD) equations, which are then non-dimensionalised through the choice of suitable length and time scales. We will formulate the basic state equations and discuss key features, utilising the asymptotic analysis in §2.2 — it turns out that the basic state field and flow completely decouple from the temperature and density and so the analysis in §2.2.2 is still useful. The problem will then be linearised and, after introducing the linear system of equations, we will provide a thorough discussion of the numerical methods that are useful in this chapter.

Before we discuss any numerical results, we outline the local parcel arguments mentioned in Chapter 1, and give a detailed overview of the literature surrounding the development of the understanding of the magnetic buoyancy instability. After a detailed discussion of the magnetic buoyancy instability mechanism, we take a necessary detour to benchmark our numerical solver against known results through studying magnetic buoyancy instabilities in a simpler setting — the linear stability of a static magnetic field varying linearly with depth, in a stably-stratified atmosphere (see Kersalé et al., 2007).

We then return to discussion of the full problem, incorporating velocity shear and a self-consistently generated magnetic field. Using the basic state analysis derived in §2.2.2, we derive an alternative stability criteria for magnetic buoyancy in the presence of a shear flow. We show that, while these criteria are local in nature, they are still useful in determining instability boundaries, even when basic state variations are not necessarily small. We then perform numerical calculations of the full problem and discuss a wide range of instabilities — we will observe the simultaneous existence of 2D and 3D undular modes as well as interchange instabilities. Here, we will show the eigenfunctions associated with the wavenumbers that are optimal for exponential growth.

3.2 The Model and Governing Equations

First, we introduce the governing equations of compressible MHD. We then non-dimensionalise the governing equations in terms of the sound speed, and write down the corresponding non-dimensional parameters. We then recall the motivation underlying the target flow, illustrating the model with a diagram. We will then write down the basic state equations, discuss the boundary conditions, and will refer to the basic state analysis in §2.2.2 in terms of our new non-dimensional parameters.

3.2.1 The Governing Equations

The governing equations of compressible MHD in Cartesian coordinates are given by

$$\frac{\partial \rho}{\partial t} + \nabla \cdot (\rho \boldsymbol{u}) = 0, \tag{3.1}$$

$$\frac{\partial (\rho \boldsymbol{u})}{\partial t} + \nabla \cdot \left(\rho \boldsymbol{u}\boldsymbol{u} - \frac{\boldsymbol{B}\boldsymbol{B}}{\mu_0} \right) = -\nabla \left(P + \frac{B^2}{2\mu_0} \right) + \rho \boldsymbol{g} + \mu \left(\nabla^2 \boldsymbol{u} + \frac{1}{3} \nabla (\nabla \cdot \boldsymbol{u}) \right) + \boldsymbol{F}, \tag{3.2}$$

$$c_v \left(\frac{\partial (\rho \Theta)}{\partial t} + \nabla \cdot (\rho \Theta \boldsymbol{u}) \right) = -P \nabla \cdot \boldsymbol{u} + \kappa \nabla^2 \Theta + \mu \Phi + \frac{\eta}{\mu_0} (\nabla \times \boldsymbol{B})^2, \tag{3.3}$$

$$\frac{\partial \boldsymbol{B}}{\partial t} = \nabla \times (\boldsymbol{u} \times \boldsymbol{B}) + \eta \nabla^2 \boldsymbol{B}, \tag{3.4}$$

$$\nabla \cdot \boldsymbol{B} = 0, \tag{3.5}$$

where

$$\Phi = \frac{\partial u_i}{\partial x_j} \left(\frac{\partial u_i}{\partial x_j} + \frac{\partial u_j}{\partial x_i} - \frac{2}{3} \frac{\partial u_k}{\partial x_k} \delta_{ij} \right), \tag{3.6}$$

$$P = (c_p - c_v) \rho \Theta, \tag{3.7}$$

and $\boldsymbol{F}$ is a general forcing term. We scale magnetic field, pressure, density, and temperature with the scales $\mathcal{B}_0$, P_0, ρ_0 and Θ_0, where Θ_0 is the temperature at the top boundary, and ρ_0 is proportional to the total mass within the domain. We scale lengths with layer depth d, and times with the sound crossing time, $t_0 = d/\sqrt{P_0/\rho_0}$. Non-dimensionalising

Eqs (3.1)-(3.7) then yields

$$\frac{\partial \rho}{\partial t} + \nabla \cdot (\rho \boldsymbol{u}) = 0, \tag{3.8}$$

$$\frac{\partial (\rho \boldsymbol{u})}{\partial t} + \nabla \cdot (\boldsymbol{u}\boldsymbol{u} - \alpha \boldsymbol{B}\boldsymbol{B}) = -\nabla \left(\rho T + \alpha \frac{B^2}{2} \right) + \theta(m+1)\rho \hat{\boldsymbol{z}} + C_k \sigma \left(\nabla^2 \boldsymbol{u} + \frac{1}{3} \nabla (\nabla \cdot \boldsymbol{u}) \right) + \boldsymbol{F}, \tag{3.9}$$

$$\rho \frac{\partial \Theta}{\partial t} + \rho \nabla \cdot (\Theta \boldsymbol{u}) = -\rho(\gamma - 2)\Theta \nabla \cdot \boldsymbol{u} + \gamma C_k \nabla^2 \Theta + (\gamma - 1) C_k \sigma \Phi + (\gamma - 1) C_k \alpha \zeta (\nabla \times \boldsymbol{B})^2, \tag{3.10}$$

$$\frac{\partial \boldsymbol{B}}{\partial t} = \nabla \times (\boldsymbol{u} \times \boldsymbol{B}) + C_k \zeta \nabla^2 \boldsymbol{B}, \tag{3.11}$$

$$\nabla \cdot \boldsymbol{B} = 0, \tag{3.12}$$

$$P = \rho \Theta. \tag{3.13}$$

Equations (3.8)-(3.13) form a system of equations with seven dimensionless parameters, where the thermal conductivity, $\kappa = k/\rho_0 c_p$, is taken at the top of the layer, and shear viscosity μ, and the magnetic diffusivity η are taken to be constant. The dimensionless parameters are the Prandtl number, σ;

$$\sigma = \frac{\mu c_p}{\kappa}; \tag{3.14}$$

the ratio of the magnetic to thermal diffusivity at the top of the layer, ζ;

$$\zeta = \frac{\eta \rho_0 c_p}{\kappa}; \tag{3.15}$$

the dimensionless thermal diffusivity, C_k;

$$C_k = \frac{\kappa}{\rho_0 c_p d \sqrt{(c_p - c_v)\Theta_0}}; \tag{3.16}$$

the dimensionless magnetic field strength α (which is proportional to the plasma beta):

$$\alpha = \frac{B_0^2}{\mu_0 P_0}; \tag{3.17}$$

and $c_p/c_v = \gamma$, the ratio of specific heats. This set of non-dimensional parameters appear in groupings similar to those in Chapter 2. We write the more familiar dimensionless parameters — the magnetic and fluid Reynolds numbers, R_m, Re, the magnetic Prandtl number, P_m, and the Chandrasakhar number, Q — in terms of the parameters (3.14)-

(3.17). This yields the following relations

$$R_m = \frac{\mathcal{U}_0 d}{\eta} \sim \frac{1}{C_k \zeta}, \tag{3.18}$$

$$Re = \frac{\mathcal{U}_0 d}{\nu} \sim \frac{1}{C_k \sigma}, \tag{3.19}$$

$$P_m = \frac{R_m}{Re}, \tag{3.20}$$

$$Q = \frac{\alpha}{\zeta \sigma C_k^2}. \tag{3.21}$$

A full description of parameter values relevant to the solar tachocline can be found in Ossendrijver (2003): the parameter ranges given by Eqs (3.18)-(3.21) are

$$R_m \sim 10^6 - 10^{10}, \quad Re \sim 10^9 - 10^{13}, \quad P_m \sim 10^{-3} - 10^{-6}. \tag{3.22}$$

The parameter regimes given by Eq (3.22) are currently numerically inaccessible. However, numerical calculations are still possible with $R_m, Re \ll 1$ and $P_m < 1$, therefore allowing some insight into the characteristics of such instabilities in astrophysical contexts. Furthermore, it is useful to consider regimes where the balance of terms is consistent. This is achieved by ensuring the ratio of various terms in Eqs (3.1)-(3.7) are of similar orders of magnitude to that of the Sun.

3.2.2 The Model and Shear Forcing

Motivated by the solar tachocline, we consider an externally applied body forcing $\boldsymbol{F}$ defined by

$$\boldsymbol{F} = -\sigma C_k \frac{\mathrm{d}^2 U_0}{\mathrm{d}z^2} \hat{\boldsymbol{x}}, \tag{3.23}$$

and provided the flow is stable to the forcing, $\boldsymbol{F}$ will drive a target flow, $\boldsymbol{U}_0 = U_0(z)\hat{\boldsymbol{x}}$ in the absence of a vertical field. The geometry of the model is shown in Fig 3.1.

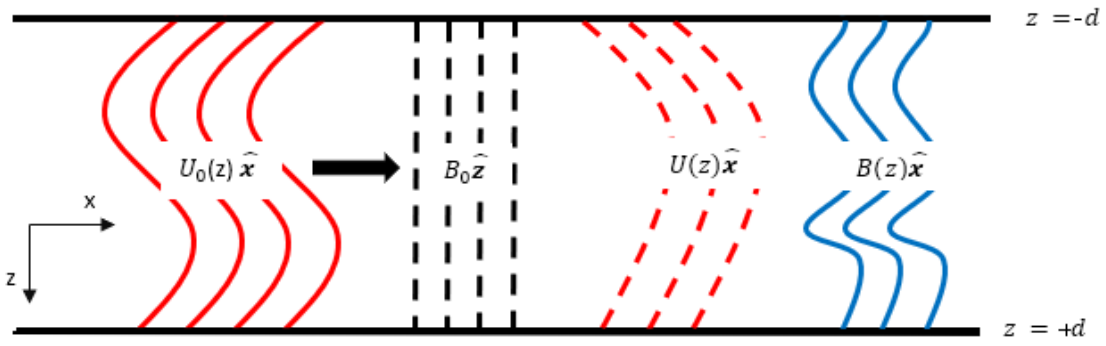

Figure 3.1: The domain is threaded with a vertical uniform magnetic field and is stretched in the x-direction by an imposed *target profile*, $U_0(z)$.

In Chapter 2, we considered two forms of target flow. Here, we restrict attention to the

hyperbolic tangent shear layer. In non-dimensional terms, this is given by,

$$U_0(z) = \mathcal{U}_0 \tanh(\lambda z). \tag{3.24}$$

The target flow is chosen such that the magnitude of the velocity is roughly constant within the upper region of the domain and has a different constant value within the lower region. Throughout the numerical calculations within this chapter, we set $\lambda = 10$. It is important to note that, in the absence of a magnetic field, this velocity forcing will balance viscous diffusion: the resultant basic flow will then be given by Eq (3.24). However, in the presence of magnetic fields, the resultant background flow will not be the target flow.

3.2.3 The Basic State

We consider a steady but non-trivial basic state where all state variables vary in the z-direction. The basic state is then given by solutions of the x- and z-component of the momentum equation, the x-component of the induction equation, and the temperature equation:

$$\sigma C_k \frac{\mathrm{d}^2 U_0}{\mathrm{d}z^2} - \alpha \frac{\mathrm{d}B}{\mathrm{d}z} = \sigma C_k \frac{\mathrm{d}^2 U}{\mathrm{d}z^2}, \tag{3.25}$$

$$\frac{\mathrm{d}U}{\mathrm{d}z} + \zeta C_k \frac{\mathrm{d}^2 B}{\mathrm{d}z^2} = 0, \tag{3.26}$$

$$\rho_0 \frac{\mathrm{d}T_0}{\mathrm{d}z} + T_0 \frac{\mathrm{d}\rho}{\mathrm{d}z} + \alpha B \frac{\mathrm{d}B}{\mathrm{d}z} = \theta(m+1)\rho_0, \tag{3.27}$$

$$\gamma C_k \frac{\mathrm{d}^2 T_0}{\mathrm{d}z^2} + C_k(\gamma - 1)\left(\sigma\left(\frac{\mathrm{d}U}{\mathrm{d}z}\right)^2 + \alpha\zeta\left(\frac{\mathrm{d}B}{\mathrm{d}z}\right)^2\right) = 0. \tag{3.28}$$

It can be seen from Eqs (3.25)-(3.26) that the velocity and magnetic field are independent of the density and temperature; therefore the basic state analysis in §2.2.2 still holds under the parameter transformations given by Eqs (3.18)-(3.21). We consider stress-free, zero horizontal magnetic field boundary conditions, where

$$\left.\frac{\mathrm{d}U}{\mathrm{d}z}\right|_{z=\pm\frac{1}{2}} = B\left(\pm\tfrac{1}{2}\right) = 0. \tag{3.29}$$

When $\alpha/C_k\sigma \gg \lambda^2$, it can be shown from the same analysis as in §2.2.2 that $B \sim U_0'$ — this will be useful when we look at local magnetic buoyancy instability criteria. The boundary conditions for the temperature are fixed such that

$$T_0\left(-\tfrac{1}{2}\right) = 1, \quad T_0\left(\tfrac{1}{2}\right) = 1 + \theta. \tag{3.30}$$

Owing to the choice of units, variation of the scaling parameters values would lead to changes in the density. To avoid this, it is helpful to define the mass of a layer of fluid

$$M_0(z) = \int_{-1/2}^{z} \rho_0(z)\mathrm{d}z. \tag{3.31}$$

Substitution of Eq (3.31) into Eq (3.27) leads to the mass equation

$$\frac{\mathrm{d}M_0}{\mathrm{d}z}\frac{\mathrm{d}T_0}{\mathrm{d}z} + T_0\frac{\mathrm{d}^2M_0}{\mathrm{d}z^2} + \alpha B\frac{\mathrm{d}B}{\mathrm{d}z} = \theta(m+1)\frac{\mathrm{d}M_0}{\mathrm{d}z}, \tag{3.32}$$

which is a second order Ordinary Differential Equation (ODE) and therefore requires two boundary conditions. It follows by construction that

$$M_0(-\tfrac{1}{2}) = 0. \tag{3.33}$$

We set the total mass within the layer to unity by imposing the other boundary condition

$$M_0\left(\tfrac{1}{2}\right) = 1. \tag{3.34}$$

Therefore, since the unit of mass is now fixed, so is the meaning of ρ_0. Numerical calculations show that within the parameter regimes we will investigate, the temperature and density profiles do not differ much from that of a linear temperature and a polytropic stratified atmosphere, i.e.,

$$T_0 \approx 1 + \theta(z+\tfrac{1}{2}), \tag{3.35}$$

$$\rho_0 \propto (1+\theta(z+\tfrac{1}{2})^m. \tag{3.36}$$

3.2.4 The Linear Equations and Computational Details

To analyse the stability of the basic state, we consider small perturbations of the form

$$\boldsymbol{u} = (U(z)+u, v, w), \quad \boldsymbol{B} = (B(z)+b_x, b_y, 1+b_z), \quad \rho = \rho_0(z)+\hat{\rho}, \quad \Theta = T_0(z)+\hat{T}. \tag{3.37}$$

We drop the hats and substitute Eq (3.37) into Eq (3.8)-(3.12), seeking solutions of the form

$$F(\boldsymbol{x}, t) = f(z)e^{ikx+ily+st}, \tag{3.38}$$

where s is the complex growth rate, and k and l are the horizontal wavenumbers. To ensure the magnetic field remains divergence-free, it is helpful to utilise the poloidal-toroidal decomposition given by Eq (2.55). The transformations are given by Eqs (C.10)-(C.12), but for clarity, they are given by

$$ik\frac{\partial h}{\partial z} + ilg = b_x, \tag{3.39}$$

$$il\frac{\partial h}{\partial z} - ikg = b_y, \tag{3.40}$$

$$(k^2+l^2)h = b_z. \tag{3.41}$$

The full linear perturbation equations are given by (A.6)-(A.15). They can be written as a generalised eigenvalue problem of the form

$$\mathcal{L}_1\boldsymbol{G} = s\mathcal{L}_2\boldsymbol{G}, \tag{3.42}$$

where $\mathcal{L}_{1,2}$ are linear differential operators and $\boldsymbol{G} = (\rho, u, v, w, T, g, h)^T$ is a state vector. To ensure numerical results are reliable, we consider two independent computational schemes: Chebyshev Spectral Methods (CSM) and uniform Finite Difference Methods (FDM). Each discrete grid is made up of $N+2$ points of coordinate z_i. The differentiation matrices can then be calculated using Chebyshev interpolant polynomials or second and fourth order finite difference stencils (FD2, FD4). To solve the eigenvalue problem, we use eigenvalue methods such as Singular Value Decomposition (SVD) and the generalised Schur decomposition. Full details can be found within the MATLAB and the `scipy` Python documentation.

Calculations can be made more efficient when using FDM, as the matrices $\mathcal{L}_{1,2}$ are sparse, whereas for CSM they are dense. Although, an alternative benefit of using spectral methods is their superior exponential convergence. For optimisation in (k, l) space we use the Nelder-Mead method, which is a direct search method useful for finding (non-)stationary points in multiple dimensions. One main benefit of the Nelder-Mead method is that analytic information of the gradient is not required. There are a few variations of this algorithm but, in the case when the gradient is known, the method is essentially described by the method of steepest descent. Accuracy of the numerical solvers is measured through obtaining known results within the literature. In addition to this, the convergence rates of the numerical solvers was found to be consistent with the theory.

For a given set of wavenumbers, we are only interested in the mode of maximum growth rate; therefore this problem is well suited to inverse iteration (also known as the inverse power method), which is an iterative eigenvalue algorithm. It is commonly used to find a very good approximation to an eigenvector when an approximation to the corresponding eigenvalue is already known. The inverse power iteration algorithm requires an initial eigenvalue and associated eigenvector, λ_0 and q_0 respectively. For a simple eigenvalue problem

$$\mathcal{A}\boldsymbol{q}_k = \lambda_k \boldsymbol{q}_k, \tag{3.43}$$

the method is described by the iterative scheme

$$\boldsymbol{q}_{k+1} = \frac{(\mathcal{A} - \lambda_k I)^{-1}\boldsymbol{q}_k}{A_k}, \tag{3.44}$$

where A_k is an arbitrary constant, which is usually chosen as the norm of the numerator in Eq (3.44). However, eigenvectors of the linear problem are defined up to a multiplicative constant, and so the choice of A_k is arbitrary. This method will be particularly useful as it allows efficient computation of the largest eigenvector without solving the full system. We use the Rayleigh Quotient Iteration (RQI), which is a combination of methods that obtain an eigenvalue estimate from an eigenvector estimate (inverse iteration), and an eigenvector estimate from an eigenvalue estimate (the Rayleigh quotient).

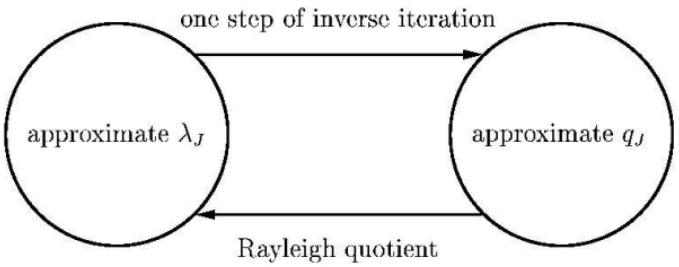

Figure 3.2: Schematic to demonstrate the RQI algorithm.

Figure 3.2 is an over simplified schematic of the RQI algorithm. The idea is to continually improve eigenvalue estimates to increase the rate of convergence of inverse iteration at every step. Inverse iteration can be extended to generalised eigenvalue problems (such as Eq (3.42)), of the form

$$\mathcal{A}\boldsymbol{q}_k = \lambda_k \mathcal{B}\boldsymbol{x}_k. \tag{3.45}$$

The analogue to Eq (3.44) then becomes

$$\boldsymbol{q}_{k+1} = (\mathcal{A} - \lambda_k \mathcal{B})^{-1}\mathcal{B}\boldsymbol{q}_k. \tag{3.46}$$

Again, inverse iteration is well suited to matrices with a banded structure, such as $\mathcal{L}_{1,2}$ for FD2 and FD4. It allows for more efficient calculations and can save storage. The main drawback of this method is that it provides only one eigenvector and associated eigenvalue. As we are only interested in the largest growth rate this does not seem like an issue, however it can present a problem when the most unstable eigenvalues are close together in complex space. All subsequent calculations will be checked using eigenvalue methods such as SVD and the generalised Schur decomposition which return the full spectrum of eigenvalues and associated eigenvectors.

3.3 Local Instability Criteria

An overview of the magnetic buoyancy instability and a literature review was given in §1.3.2. Here, we give a more detailed description of the magnetic buoyancy instability and outline the general mechanism for an ideal fluid (see Acheson, 1979). Consider a static atmosphere at equilibrium where the magnetic field acts in the x-direction and varies with height z. Under the influence of gravity, $\boldsymbol{g} = -g\hat{\boldsymbol{z}}$, the magnetohydrostatic balance between total pressure and gravity forces is given by

$$\frac{\mathrm{d}}{\mathrm{d}z}\left(p + \frac{B^2}{2\mu_0}\right) = -\rho g. \tag{3.47}$$

We take a fluid parcel at height z and raise it slowly to a height $z + \delta z$ in a manner in which magnetic field lines do not bend. The fluid properties inside and outside the tube will change. We will use 'δ' to refer to changes inside the tube and d to external

changes. We assume the parcel moves adiabatically, and therefore the specific entropy $p\rho^{-\gamma}$ is conserved to first order such that

$$\frac{p}{\rho^{\gamma}} = \frac{p+\delta p}{(\rho+\delta\rho)^{\gamma}} \implies \frac{\delta p}{p} = \gamma\frac{\delta\rho}{\rho}. \tag{3.48}$$

We also assume that the magnetic flux and mass are conserved as the parcel moves upwards, and thus B/ρ is conserved, i.e.,

$$\frac{\delta B}{B} = \frac{\delta\rho}{\rho}. \tag{3.49}$$

Finally, we assume the motion is slow compared to the sound speed and Alfvén speeds such that the parcel remains in total pressure equilibrium with its surroundings, such that

$$\mathrm{d}p + \frac{B\mathrm{d}B}{\mu_0} = \delta p + \frac{B\delta B}{\mu_0}. \tag{3.50}$$

Equations (3.48)-(3.49) are substituted into Eq (3.50), yielding

$$\delta\rho(c_s^2 - c_\alpha^2) = \mathrm{d}p + \frac{B\mathrm{d}B}{\mu_0}, \tag{3.51}$$

where c_α is the Alfvén speed and c_s is the sound speed defined by

$$c_\alpha^2 = \frac{B^2}{\rho\mu_0}, \quad c_s^2 = \frac{\gamma p}{\rho}. \tag{3.52}$$

Instability is guaranteed when the density of the parcel is smaller than that of its surroundings, i.e $\delta\rho < \mathrm{d}\rho$. Following from this, Eq (3.51) becomes

$$-\frac{gc_\alpha^2}{c_s^2}\frac{\mathrm{d}}{\mathrm{d}z}\ln\left(\frac{B}{\rho}\right) > N^2, \tag{3.53}$$

where N is the Brunt-Väsälä frequency given by

$$N^2 = -\frac{g}{\gamma}\frac{\mathrm{d}}{\mathrm{d}z}\ln\left(p\rho^{-\gamma}\right). \tag{3.54}$$

In the absence of a magnetic field, Eq (3.53) reduces to the Schwarzschild criterion for convective instability. Equation (3.53) essentially tells us that if B/ρ decreases rapidly with height, it can destabilise a convectively stable atmosphere. That is to say, a stratified layer such that $N^2 < 0$ can be unstable in the absence of a magnetic field.

The criteria given by Eq (3.53) is specific to interchange instabilities, i.e., 2D instabilities where $k = 0$. An obvious extension is to include 3D instabilities in which the magnetic field is allowed to bend. Naively, one would assume that doing work against the magnetic tension by bending fields would inhibit the instability mechanism. Newcomb (1961) was able to show that when $k \to 0$, the instability criteria for 3D instabilities is not as stringent compared to 2D interchange instabilities: this configuration was found to be unstable in

the fluid when

$$\frac{\mathrm{d}\rho}{\mathrm{d}z} > -\frac{\rho g}{c_s^2}. \tag{3.55}$$

On the surface, this looks similar to that of the hydrostatic (non-magnetic) criteria. The role of the magnetic field was made more obvious by Thomas and Nye (1975) by writing Eq (3.55) in the form

$$-\frac{g c_\alpha^2}{c_s^2}\frac{\mathrm{d}}{\mathrm{d}z}\ln(B) > N^2. \tag{3.56}$$

It can be seen from comparison of Eqs (3.53) and (3.56) that 3D modes are more easily destabilised — that is to say, interchange modes require a sufficiently rapid decrease of B/ρ in height (where, typically, ρ also decreases with height), whereas 3D modes are less stringent and depend only on a decrease of B in height. Equation (3.56) is a necessary but not sufficient criterion for instability and therefore there may be parameter regimes which result in equilibria which are unstable to undular modes but not interchange modes. Furthermore, it is important to note that the physical mechanisms for the interchange instability ($k = 0$) and the limiting case of an undular mode with $k \to 0$ are very different — this is fully detailed in Hughes and Cattaneo (1987).

3.3.1 The Influence of Diffusion

All investigations within this thesis are of diffusive systems. Acheson (1979) writes the instability criteria for an atmosphere with non-zero thermal and magnetic diffusion in the absence of viscosity by

$$-\frac{g c_\alpha^2}{c_s^2}\frac{\mathrm{d}}{\mathrm{d}z}\ln\left(\frac{B}{\rho}\right) > \frac{\eta}{\kappa}N^2 \qquad \text{(Interchange Modes)}, \tag{3.57}$$

$$-\frac{g c_\alpha^2}{c_s^2}\frac{\mathrm{d}}{\mathrm{d}z}\ln(B) > c_\alpha^2 k^2\left(1+\frac{m^2}{l^2}\right)+\frac{\eta}{\kappa}N^2 \qquad \text{(Undular Modes)}, \tag{3.58}$$

for interchange and undular modes respectively, where m here is the wavenumber in the z-direction, and the magnetic, η, and thermal, κ, diffusivity are assumed to be constant. It is important to note that Eqs (3.57)-(3.58) are based on a local approximation, which assumes the background state varies over a long spatial scale in comparison to the scales defined by m and l. It can be seen from comparison of Eqs (3.53),(3.56), (3.57), and Eq (3.58) that an equilibrium which is stable in the absence of diffusion can become unstable due to a reduced effect of N^2. In other words, $\eta/\kappa \ll 1$ helps the instability.

Diffusion can have various interesting effects on magnetic buoyancy instabilities. Gilman (1970) investigated the case where $\eta = \nu = 0$, but with $\kappa \to \infty$ in the asymptotic limit of small horizontal scale. Gilman (1970) concluded that there are modes which are able to rapidly exchange heat with their surroundings, which were susceptible to magnetic buoyancy instabilities. Magnetic buoyancy can also be regarded as a double-diffusive process. For example, it has been shown by Spiegel and Weiss (1982) that interchange instabilities in this context can be transformed into a form similar to that of thermohaline convection. A physical explanation for the preference of 3D modes to that of interchange

modes is offered in Hughes and Cattaneo (1987), and for further reading on the physical mechanisms, one should consult Hughes (1985a) and Hughes and Proctor (1988).

In the absence of diffusion, only direct modes of instability are possible — that is, the growth rate is purely real. Incorporating diffusion into the compressible MHD equations supports the existence of a type of instability referred to as overstability. Hughes (1985a) was able to derive instability criteria for interchange instabilities which demonstrated that overstability can occur in the presence of a bottom-heavy field gradient, i.e. with B/ρ increasing with height. Furthermore, Hughes (1985a) showed that it is possible to stabilise certain top-heavy field gradients, by making them more top-heavy. In general, the viscosity plays a stabilising role.

3.4 Magnetic Buoyancy Instability of a Linear Magnetic Field in the Absence of Forcing

First, it is helpful to consider the magnetic buoyancy instability within a simpler system — a horizontal linear magnetic field which varies with z in the absence of a shear flow and uniform vertical field. We will use this problem to validate numerical solvers by reproducing results in the literature and illustrate the nature of magnetic buoyancy instabilities in the absence of a velocity shear. In particular, we study the linear stability of a static, linear magnetic field in the presence of a stably stratified compressible atmosphere. This problem was studied in the nonlinear regime by Kersalé et al. (2007) and we will use the linear stability results therein to benchmark the numerical solver.

3.4.1 The Basic State

In the absence of flow and uniform vertical field, the basic state is given by the solution to Eq (3.26)-(3.27), where $U = 0$, $U_0 = 0$. To be consistent with Kersalé et al. (2007), we use the boundary conditions

$$B\left(-\tfrac{1}{2}\right) = 1, \quad B\left(\tfrac{1}{2}\right) = 1 + \Delta, \tag{3.59}$$

$$T_0\left(-\tfrac{1}{2}\right) = 1, \quad T_0\left(\tfrac{1}{2}\right) = 1 + \theta, \tag{3.60}$$

$$\rho_0\left(-\tfrac{1}{2}\right) = 1, \tag{3.61}$$

where Δ and θ are parameters that we are free to choose. We can solve for the basic magnetic field and temperature analytically, giving

$$B = 1 + \Delta\left(z + \frac{1}{2}\right), \tag{3.62}$$

$$T_0 = \frac{(1-\gamma)}{\gamma}\frac{\alpha\zeta\Delta^2}{2}\left(z^2 - \frac{1}{4}\right) + \theta\left(z + \frac{1}{2}\right) + 1, \tag{3.63}$$

however, we must calculate ρ_0 numerically. Equation (3.62) shows that the basic magnetic field is linear with gradient Δ. When $\alpha\zeta\Delta^2 \ll \theta$, Eq (3.63) shows that the temperature

is also linear — in the parameter regimes of interest we will see this is the case. In the absence of a magnetic field, the purely hydrostatic balance results in an atmosphere, with

$$T_0 = 1 + \theta\left(z + \tfrac{1}{2}\right), \tag{3.64}$$

$$\rho_0 = (1 + \theta\left(z + \tfrac{1}{2}\right))^m, \tag{3.65}$$

where m is the polytropic index, and θ is the temperature gradient.

3.4.2 Confirmation of Numerical Approach

To verify the numerical solver (and associated numerical techniques; FD2, FD4, and CSM) we reproduce the results in Kersalé et al. (2007) by solving Eq (A.6)-(A.15) where $\mathcal{U}_0$, $\delta = 0$. For consistency with Kersalé et al. (2007), the parameter values are $\sigma = \zeta = 2 \times 10^{-2}$, $C_k = 2.5 \times 10^{-2}$, $\Delta = 1$, $m = 1.6$, $\theta = 2$, and $\gamma = 5/3$ unless otherwise stated: we test two different values of $\alpha = 1/4$, 1. Calculation of the growth rate, s, over (k, l) space results in Fig 3.3.

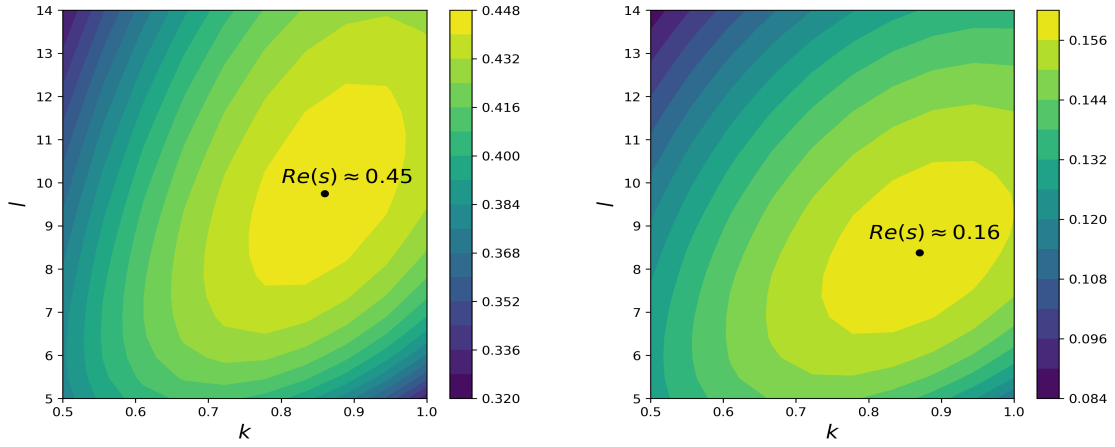

(a) (b)

Figure 3.3: Growth rate in (k, l) space for $\alpha = 1$ (left) and $\alpha = 1/4$ (right).

Figure 3.3 is the growth rate in (k, l) space. We calculate the local maximum, shown by the black dot through the optimising procedure described in §3.2.4.

α	k	l	FD2	FD4	CSM	Kersalé et al. (2007)
1/4	0.87	8.38	0.160352	0.160351	0.160351	0.16
1	0.86	9.75	0.445934	0.445933	0.445933	0.45

Table 3.1: Optimal growth rate calculated via 2D optimisation for FD ($N = 298$) and CSM ($N = 60$) and the true values shown in Kersalé et al. (2007) to 2 decimal place.

Table 3.1 illustrates that there is agreement across all three numerical schemes. It is expected that FD4 is more accurate than FD2, whereas spectral method on a Chebyshev grid illustrates greater accuracy at smaller values of N owing to the exponential convergence of the method. Furthermore, Fig 3.3 and Table 3.1 illustrate that the numerical scheme is

able to reproduce the results within Kersalé et al. (2007) to the decimal places given. We calculate the perturbed quantities and the basic state for both the optimal wavenumbers given in Table 3.1.

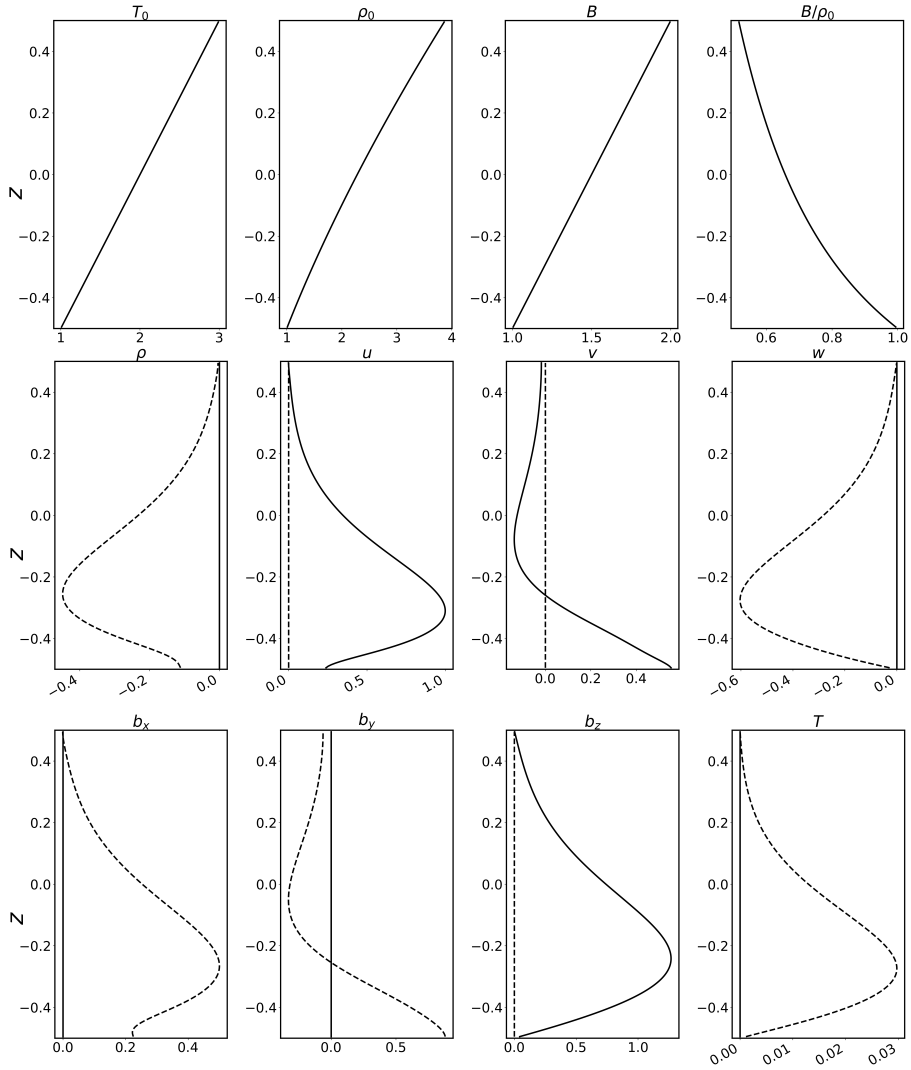

Figure 3.4: Basic state (top row) and linear eigenvectors (2nd and 3rd rows) for $\alpha = 1, k = 0.86$, and $l = 9.75$. The dashed and solid lines represent imaginary and real parts respectively.

Figures 3.4 shows the basic state and the real and imaginary components of the perturbed quantities for $k = 0.86$, $l = 9.75$, and $\alpha = 1$. It can be seen in Figs 3.4 that the perturbed quantities are all similar in form and are either purely real or imaginary. All of the disturbances are peaked in the upper half of the domain, i.e $z < 0$. The basic state temperature field is predominantly linear as the term $\alpha\zeta \ll 1$, and the density is essentially given by a polytrope. Figure 3.5 is analogous to Fig 3.4 but for $\alpha = 1/4$, with $k = 0.87$ and $l = 8.38$. Again, it can be seen in Fig 3.5 that the disturbances are all similar in form and are either purely real or imaginary. Comparison of Figs 3.4-3.5 shows that the basic state has changed very little — this is expected as α has only changed by a factor of 4.

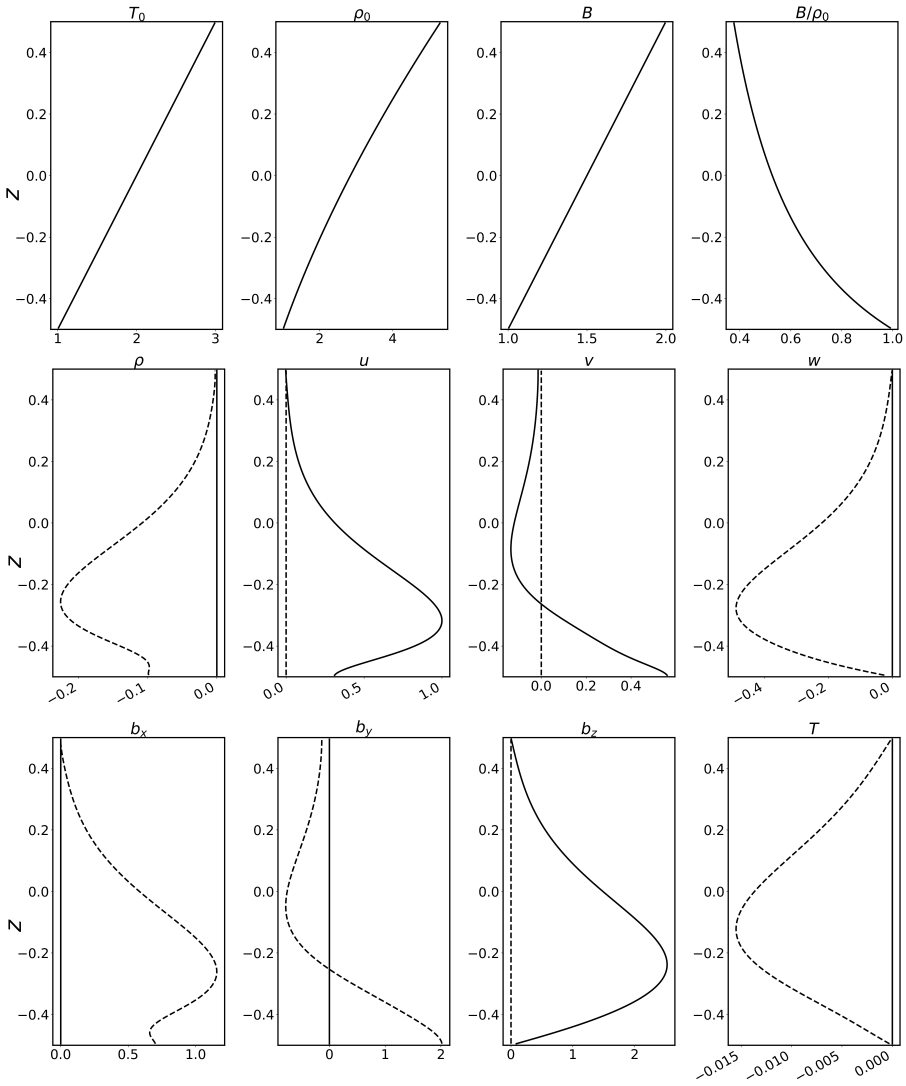

Figure 3.5: Basic state (top row) and linear eigenvectors (2^{nd} and 3^{rd} rows) for $\alpha = 1/4, k = 0.87$, and $l = 8.38$. The dashed and solid lines represent imaginary and real parts respectively.

3.5 Shear Generated Field

We will now investigate magnetic buoyancy instabilities in the presence of a velocity shear. First, we derive local instability criteria by using Eqs (3.57)-(3.58) based on the basic state analysis in §2.2.2, where it was described how the basic state magnetic field results from the background flow. We will then solve the eigenvalue problem to investigate how accurate our new instability criteria are at predicting instability. We will then explore the parameter space, illustrating the simultaneous existence of undular and interchange modes. The eigenfunctions of the optimal wavenumbers will then be discussed.

3.5.1 Predicting Instability in Terms of the Shear Flow

Local instability criteria are powerful tools in predicting instability of a basic state configuration. In the diffusive case, it is understood that Eqs (3.57)-(3.58) are an

approximation where variations across the layer are assumed to be small — for example, $B \sim B_0(1 + \varepsilon z/d)$ with $\varepsilon \ll 1$. In the case of no diffusion, regardless of the magnitude of variations, Eqs (3.53)-(3.56) are necessary and sufficient conditions for instability (see Newcomb, 1961). When $\alpha/C_k\sigma \ll \lambda^2$, we have shown that the magnetic field can be written in terms of the target flow, and therefore we wish to derive instability criteria in terms of the target flow, $U_0(z)$.

Equations (3.25)-(3.27) show that the flow and field are decoupled from the temperature and density. The basic state equations for the flow and field in dimensional form are given by

$$\frac{\mathcal{B}_0}{\mu_0}\frac{\mathrm{d}B}{\mathrm{d}z} + \mu\left(\frac{\mathrm{d}^2U}{\mathrm{d}z^2} - \frac{\mathrm{d}^2U_0}{\mathrm{d}z^2}\right) = 0, \tag{3.66}$$

$$\mathcal{B}_0\frac{\mathrm{d}U}{\mathrm{d}z} + \eta\frac{\mathrm{d}^2B}{\mathrm{d}z^2} = 0, \tag{3.67}$$

where μ_0 is the permittivity of free space, μ is the dynamic viscosity, and η is the magnetic diffusivity. It has been shown in §2.2.2 that the magnetic field is approximately equal to the derivative of the target flow when $\alpha/C_k\sigma \ll \lambda^2$. Integrating Eq (3.66) and substituting for $\mathrm{d}U/\mathrm{d}z$ into Eq (3.67) yields

$$\eta\frac{\mathrm{d}^2B}{\mathrm{d}z^2} - \frac{\mathcal{B}_0}{\mu_0\mu}B + \frac{\mathrm{d}U_0}{\mathrm{d}z} \approx 0, \tag{3.68}$$

where we have neglected the integration constant as it is approximately zero for a hyperbolic tangent target profile. It can be seen in Eqs (3.66)-(3.67) that when $\eta \ll 1$, the magnetic field is given approximately by

$$B \approx \frac{\mu\mu_0}{B_0}\frac{\mathrm{d}U_0}{\mathrm{d}z}. \tag{3.69}$$

Now, consider Eq (3.57)-(3.58), and remind the reader that due to the boundary layer in $U_0(z)$, and subsequently $B(z)$, that variations across the layer are not necessarily small. First, we substitute $c_a = B^2/\mu_0\rho$, $c_s^2 = \gamma P/\rho$ into Eq (3.57)-(3.58) and use the identity

$$B^2\frac{\mathrm{d}}{\mathrm{d}z}\ln B = \frac{\mathrm{d}}{\mathrm{d}z}\left(\frac{B^2}{2}\right) \tag{3.70}$$

to obtain

$$\frac{g}{\gamma P}\frac{\mathrm{d}}{\mathrm{d}z}\left(\frac{B^2}{2\mu_0}\right) - \frac{gB^2}{\gamma\mu_0 P}\frac{\mathrm{d}}{\mathrm{d}z}\ln\rho > \frac{\eta}{\kappa}N^2 \qquad \text{(Interchange Modes)}, \tag{3.71}$$

$$\frac{g}{\gamma P}\frac{\mathrm{d}}{\mathrm{d}z}\left(\frac{B^2}{2\mu_0}\right) > \frac{\eta}{\kappa}N^2 \qquad \text{(Undular Modes)}, \tag{3.72}$$

where we have assumed the wave number k is small in Eq (3.58). We remind the reader that Eqs (3.71)-(3.72) are instability criteria discussed in §3.3 in a different form. Furthermore, it is important to note that from now on, $B(z)$ is the result of shearing a uniform vertical

field. We take Eq (3.72) and substitute Eq (3.69) to obtain

$$\frac{g\mu^2\mu_0}{2B_0^2\gamma P}\frac{\mathrm{d}}{\mathrm{d}z}\left(\frac{\mathrm{d}U_0}{\mathrm{d}z}\right)^2 > \frac{\eta}{\kappa}N^2. \tag{3.73}$$

We then assume that the velocity varies on a scale such that $\mathrm{d}/\mathrm{d}z \sim 1/\Delta z$. We define the Richardson number by

$$Ri = \frac{N^2}{\left(\frac{\mathrm{d}U_0}{\mathrm{d}z}\right)^2}, \tag{3.74}$$

which measures the ratio of buoyancy to shear flow effects. We can manipulate Eq (3.73) to obtain

$$\frac{g\mu^2\mu_0}{2B_0^2\gamma P\Delta z} > \frac{\eta}{\kappa}Ri \quad \text{(Undular Modes)}. \tag{3.75}$$

Equation (3.75) represents magnetic buoyancy instability criteria for undular modes in terms of the forced shear flow. One can perform similar manipulations on Eq (3.71) to obtain

$$\frac{g\mu^2\mu_0}{2B_0^2\gamma P}\frac{\mathrm{d}}{\mathrm{d}z}\left(\frac{\mathrm{d}U_0}{\mathrm{d}z}\right)^2 - \frac{g\mu^2\mu_0}{B_0^2\gamma P}\left(\frac{\mathrm{d}U_0}{\mathrm{d}z}\right)^2\frac{\mathrm{d}}{\mathrm{d}z}\ln\rho > \frac{\eta}{\kappa}N^2 \quad \text{(Interchange Modes)}. \tag{3.76}$$

Equation (3.76) is analogous to Eq (3.75) but for interchange modes. Flow and magnetic field have little impact on the fluid stratification, and so we define the density scale height such that

$$H_\rho = \left(\frac{\mathrm{d}\ln\rho}{\mathrm{d}z}\right)^{-1}. \tag{3.77}$$

We then rewrite the two new instability criteria as

$$\frac{g\nu^2}{2(\Delta z)c_v^2c_s^2}\left(1-\frac{2\Delta z}{H_\rho}\right) > \frac{\eta}{\kappa}N^2 \quad \text{(Interchange Modes)}, \tag{3.78}$$

$$\frac{g\nu^2}{2(\Delta z)c_v^2c_s^2} > \frac{\eta}{\kappa}Ri \quad \text{(Undular Modes)}, \tag{3.79}$$

where $c_v = \mathcal{B}_0/\sqrt{\mu_0\rho_0}$ is the Alfvén speed for the vertical magnetic field, and $\nu = \mu/\rho_0$. Viscosity typically inhibits instability but it can be seen by Eqs (3.78)-(3.79) that, here, increasing the viscosity can lead to destabilisation of the basic state. This can be understood through the role of viscosity in generating the magnetic field whose amplitude increases linearly with ν. Since $\Delta z/H_\rho > 0$, the first instability to onset is undular. Equations (3.78)-(3.79) show that both modes of instability prefer $\Delta z \ll 1$ although, in this regime, local instability criteria may not be valid as the basic state variations across the domain are large. To investigate whether Eqs (3.78)-(3.79) are accurate, we first write them in non-dimensional form

$$\frac{\sigma^2C_k^2}{2\alpha\rho T}\left(\frac{\mathrm{d}}{\mathrm{d}z}\left(\frac{\mathrm{d}U_0}{\mathrm{d}z}\right)^2 - 2\left(\frac{\mathrm{d}U_0}{\mathrm{d}z}\right)^2\frac{\rho'}{\rho}\right) > -\zeta\frac{\mathrm{d}}{\mathrm{d}z}\ln\left(P\rho^{-\gamma}\right) \quad \text{(Interchange Mode)}, \tag{3.80}$$

$$\frac{\sigma^2C_k^2}{2\alpha\rho T}\frac{\mathrm{d}}{\mathrm{d}z}\left(\frac{\mathrm{d}U_0}{\mathrm{d}z}\right)^2 > -\zeta\frac{\mathrm{d}}{\mathrm{d}z}\ln\left(P\rho^{-\gamma}\right) \quad \text{(Undular Mode)}. \tag{3.81}$$

Equations (3.80)-(3.81) highlight the role of the Prandtl number, σ, in driving the instability. Increasing σ increases the amplitude of the basic magnetic field. This can be understood through the fact that, σ comes in through the forcing, and therefore, if viscosity increases, then so does the forcing. Instability sets in when both sides of Eqs (3.80)-(3.81) are equal. Therefore, we can find an approximate value of σ at which we would expect undular and interchange modes to become unstable. It is assumed that σ is a constant although both sides of Eq (3.80)-(3.81) are functions of z. We write the critical Prandtl number for undular and interchange modes as

$$\tilde{\sigma}_I^2 = \max\left[\frac{2\zeta\alpha\rho_0 T_0}{C_k^2}\left(\max\left(\frac{\mathrm{d}}{\mathrm{d}z}\left(\frac{\mathrm{d}U_0}{\mathrm{d}z}\right)^2 - 2\left(\frac{\mathrm{d}U_0}{\mathrm{d}z}\right)^2\frac{\rho_0'}{\rho_0}\right)\right)^{-1}\frac{\mathrm{d}}{\mathrm{d}z}\ln\left(P\rho_0^{-\gamma}\right)\right], \tag{3.82}$$

$$\tilde{\sigma}_U^2 = \max\left[\frac{2\zeta\alpha\rho_0 T_0}{C_k^2}\left(\max\left(\frac{\mathrm{d}}{\mathrm{d}z}\left(\frac{\mathrm{d}U_0}{\mathrm{d}z}\right)^2\right)\right)^{-1}\frac{\mathrm{d}}{\mathrm{d}z}\ln\left(P\rho_0^{-\gamma}\right)\right], \tag{3.83}$$

where subscript U, I denote undular and interchange respectively. Equations (3.82)-(3.83) are crude approximations since we take the maximum of both sides of Eqs (3.80)-(3.81). We are focusing on regions in which the basic state is marginally unstable, but it is expected that there will be regions of stability within the domain.

Parameter	C_k	ζ	α	θ	m	$\mathcal{U}_0$	γ	δ
Value	1/20	10^{-4}	1.25×10^{-4}	5	8/5	1/20	5/3	1

Table 3.2: Parameter values for testing the instability criteria (3.82)-(3.83).

For the parameters given in Table 3.2, Eqs (3.82)-(3.83) predict instability at

$$\sigma_U \approx 0.0022, \tag{3.84}$$

$$\sigma_I \approx 0.0028, \tag{3.85}$$

which means that the predicted stability boundary in Prandlt number space is higher for the interchange modes. Figure 3.6 shows the growth rate in (k, l) space for the parameter values within Table 3.2 and Prandtl numbers (3.84)-(3.85). It can be seen that Eqs (3.83)-(3.82) over-estimate the critical Prandtl number for undular and interchange modes. However, trial and error has shown that the actual stability boundary is of the same order of magnitude. Equations (3.79)-(3.78) are therefore reasonable approximations: recall that the instability criteria derived by Acheson (1979) assume small variations across the layer, which is not true for the parameter values given in Table 3.2, since $|B'| \approx 30$. Despite this, Eqs (3.79)-(3.78) work reasonably well to within an order of magnitude. Figure 3.6 also shows that modes are 2D undular at instability onset as $\sigma_U < \sigma_I$. Interestingly, this result illustrates that 2D undular modes are possible in this system — i.e. in the presence of a shear flow. However, in the absence of velocity shear, 2D undular modes are understood to be hard to destabilise (see Hughes and Cattaneo, 1987).

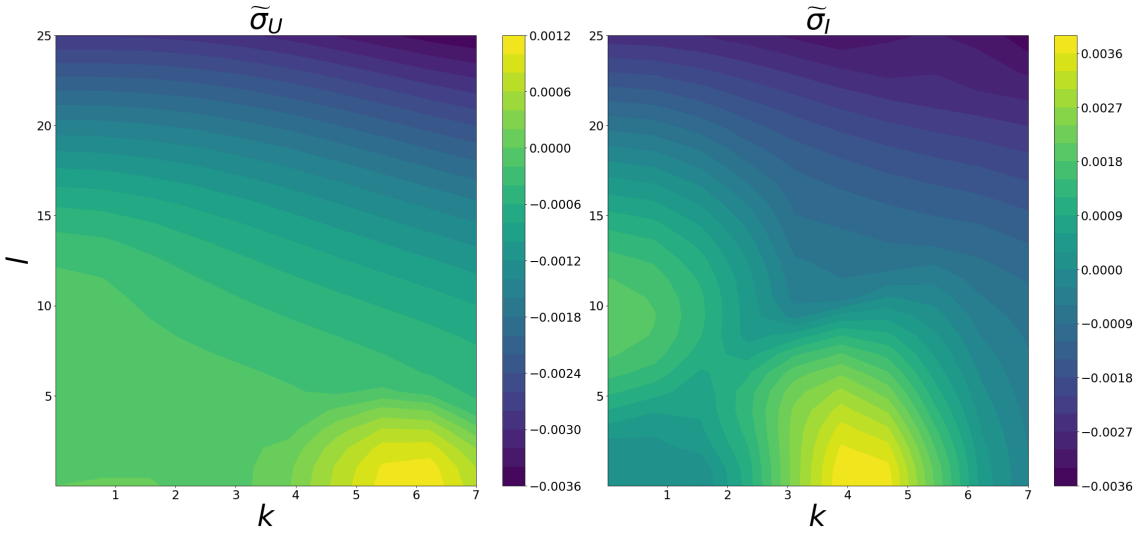

Figure 3.6: Growth rate in (k, l) space for the parameters given in Table 3.2 with σ_U (left) and σ_I (right).

3.5.2 Increasing the Prandtl Number, σ

In this section, we conduct a parameter survey by varying σ above the stability boundary defined by (3.84). Equations (A.6)-(A.15) are solved for the basic state given by Eqs (3.25)-(3.27). The remaining parameters are given in Table 3.2, unless otherwise stated.

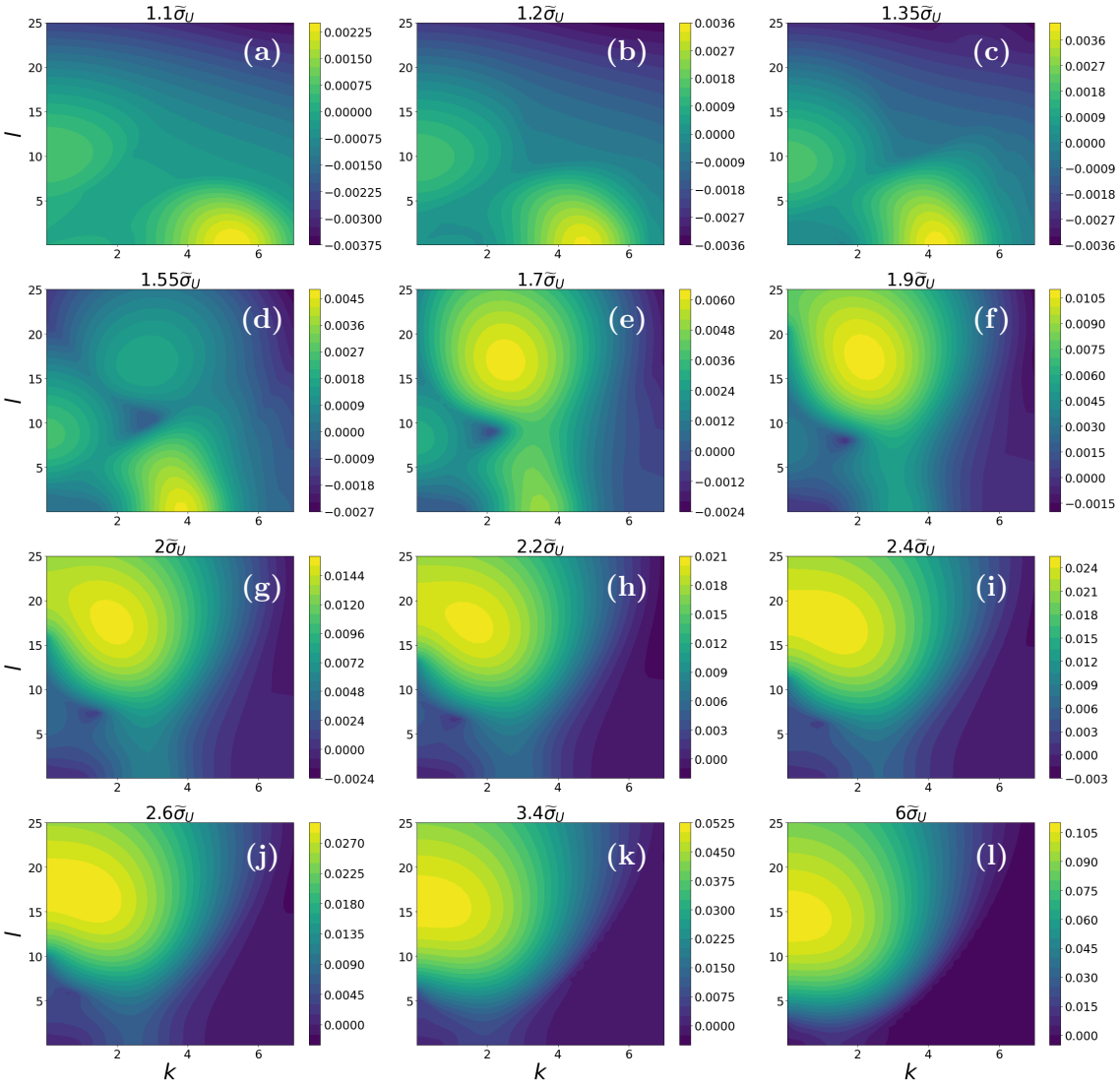

Figure 3.7: Growth rate in (k, l) space for varying σ. All other parameters are given in Table 3.2.

Figures 3.7 shows the growth rate in (k, l) space for various values of σ; the other parameter values are given in Table 3.2. It can be seen in Figs 3.7 that variation of σ can lead to a wide array of instabilities. Figures 3.7(a)-(c) show that there are two preferred modes of instability which are 2D; interchange ($k = 0$) and undular ($l = 0$), with undular being the dominant mode of instability, when $\sigma \leq 1.55\sigma_U$. It can be seen in Figs 3.7(a)-(c) that the optimal value of k is decreasing as σ is increasing. As σ is further increased, Figs 3.7(d)-(f) show that another local maximum appears with non-zero (k, l). It can be seen in Fig 3.7(e) that, at $\sigma = 1.7\tilde{\sigma}_U$, the preferred mode is a 3D undular mode. Comparison of Fig 3.7(a)-(f) illustrates that both the 2D undular and interchange mode

move to lower values of k and l respectively as σ is increased for $\sigma \geq 1.90\sigma_U$, and by Figs 3.7(f) are marginally unstable. Figures 3.7(g)-(i) show that as σ is further increased, the preferred instability becomes an interchange mode. Comparison of Figs 3.7(a) and (g) show two independent interchange modes — they occur at different values of l and both can be seen in Fig 3.7(g). By increasing σ further, it remains that there is only one local maximum, and the optimal mode of instability is an interchange mode (see Figs 3.7(j)-(l)).

It is important to note the limitations of the derived instability criteria. Increasing σ effectively increases the viscosity and this has been neglected to obtain Eq (3.56). Moreover, for larger values of σ, it is not the case that variations in the magnetic field across the layer are small. To show this, Figs 3.8 shows the magnetic field for two values of σ and compares it to the approximation $B \sim U_0'$. It can be seen in Figs 3.8 that for larger values of σ, the approximation for B is still reasonable, however we can see that the variations across the layer are large and not $\mathcal{O}(1)$. It would be unreasonable to assume that local instability criteria would be accurate.

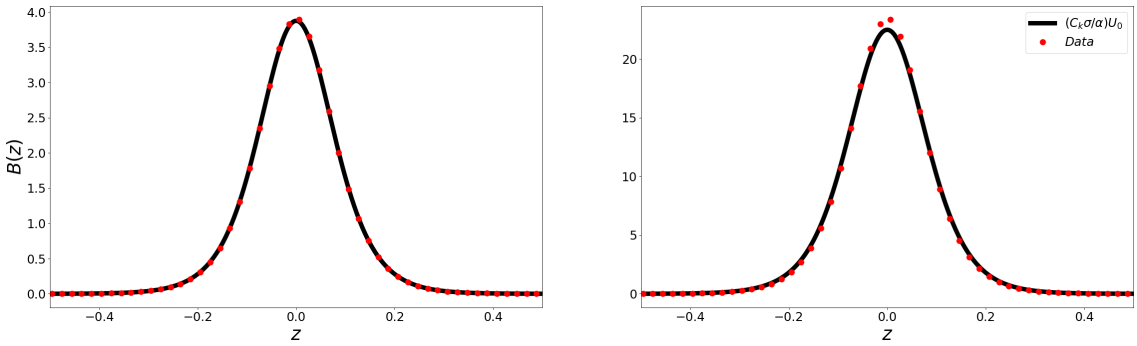

Figure 3.8: Numerical calculation of the magnetic field compared with U_0' for σ_U (left) and $6\sigma_U$ (right).

3.5.3 The Eigenfunctions

Here, we examine the eigenfunctions for the optimal instabilities shown in Figs 3.7(a),(e),(l). This involves optimising the growth rate $R(s)$ over (k, l) space to find the optimal wavenumbers for each local maximum. The optimal wavenumbers are shown in Table 3.3: note the existence of multiple local maxima for some values of σ. We will now show the associated eigenfunctions, which have been normalized by the maximum of $R(b_x)$.

σ	k_c	l_c	$R(s(k_c, l_c))$
$1.1\sigma_U$	5.33	0	0.00246
$1.7\sigma_U$	3.47	0	0.00257
$1.7\sigma_U$	2.52	16.87	0.00624
$1.7\sigma_U$	0	8.41	0.00450
$6\sigma_U$	0	14.17	0.108

Table 3.3: Optimal wavenumbers and growth rates for the local maxima shown in Figs 3.7 (a),(e), and (l) for the respective values of σ.

Figures 3.9-3.13 show the perturbed quantities for the optimum wavenumbers shown in Table 3.3. The corresponding local maxima are labelled in Figs 3.9-3.13 by black, blue, and red dots where appropriate. The three components of the magnetic field are computed by the transformations given by Eqs (3.39)-(3.41).

Figures 3.9 shows the eigenfunctions for the optimal 2D undular mode indicated by the black dot in the map of the growth rate. It is shown in Figs 3.9 that the perturbations of density and temperature are relatively small compared to the x-component of the magnetic field. Furthermore, it can be seen that the y-component of the velocity and magnetic field disturbances are zero as this is expected for 2D undular modes ($l = 0$). Figures 3.10 illustrates the eigenfunctions for the optimum value of (k, l) for the 2D undular mode illustrated by the black dot. Again, as expected, the y-component of the velocity and magnetic field disturbances are zero. Figures 3.11-3.13 are analogous to Figs 3.9-3.10. The 2D interchange mode in Figs 3.10-3.11 occur at similar values of l, and are understood through §3.3 to be magnetic buoyancy instabilities.

An interesting feature of Figs 3.12-3.13 is that the eigenfunctions are purely real or imaginary in comparison with the eigenfunctions shown for the other optimal modes of instability shown in Figs 3.9-3.11. All the eigenfunctions shown in Figs 3.9-3.13 show localisation around $z = 0$; however the general structure for the 2D interchange modes are much simpler in comparison. Figures 3.9-3.13 show that the density and temperature are relatively small compared to the x-component of the magnetic field. It is further shown in Figs 3.12-3.13 that the magnetic field perturbations are much larger relative to the x-component of the magnetic field, in comparison to the velocity — it can be seen, for example, in Figs 3.13, that the velocity components are at most $\mathcal{O}(10^{-4})$.

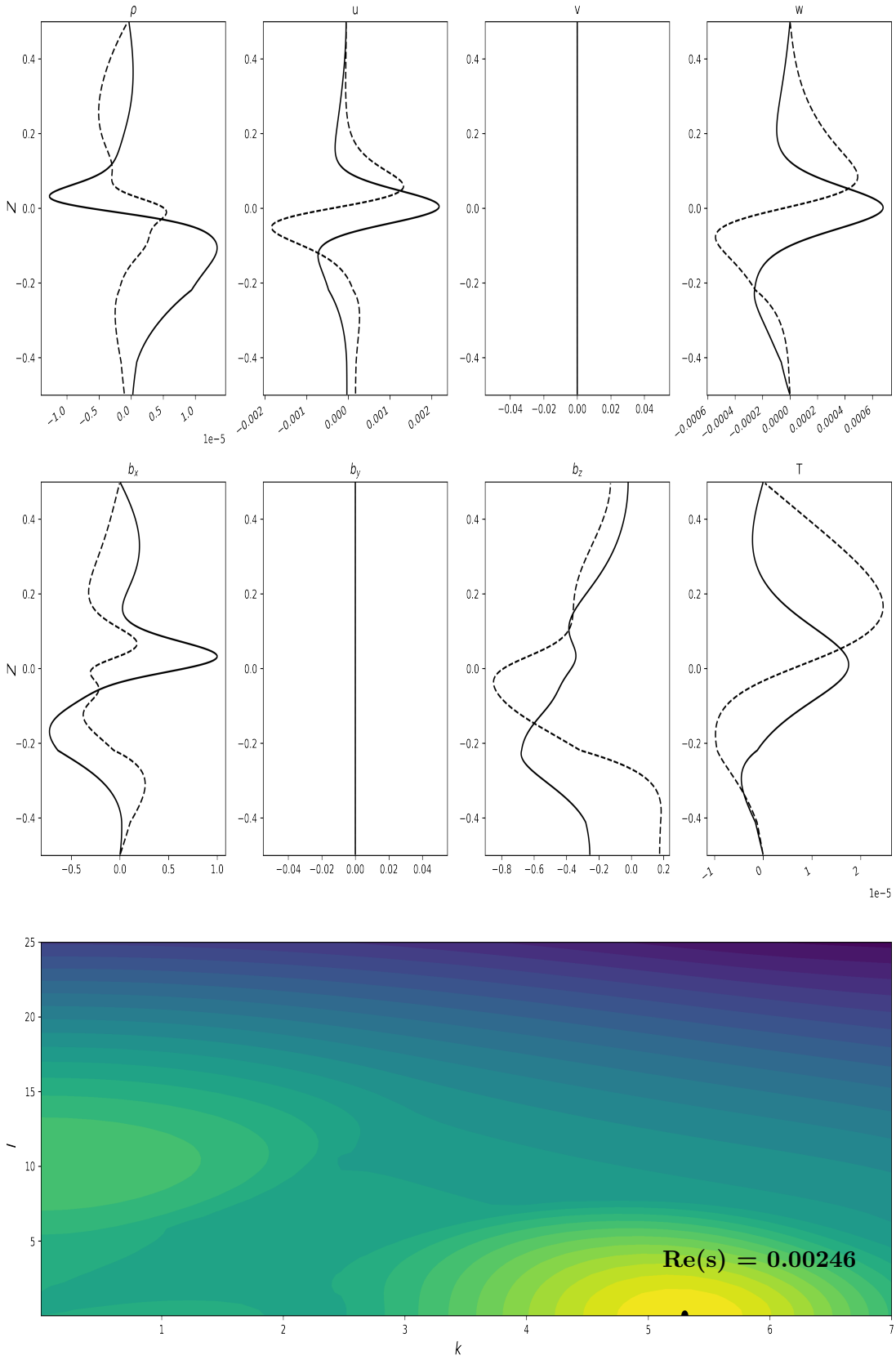

Figure 3.9: Perturbed quantities (top and middle) for $k = 5.33, l = 0$ (black dot) with the growth rate in (k, l) space (bottom panel). Solid and dashed lines represent real and imaginary components respectively. Parameters are defined in Table 3.2 and $\sigma = 1.1\tilde{\sigma}_U$.

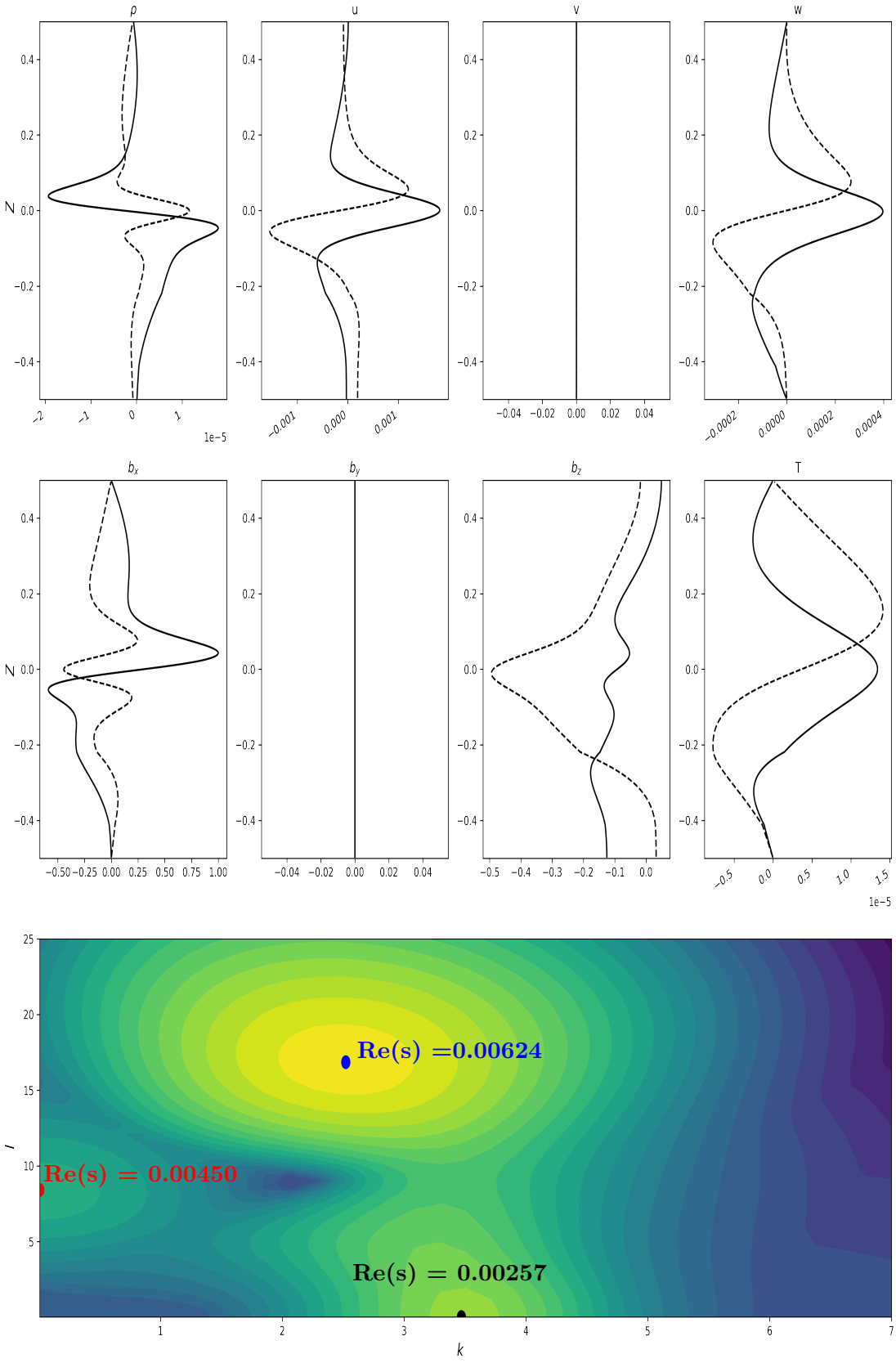

Figure 3.10: Perturbed quantities (top and middle) for $k = 3.47, l = 0$ (black dot) with the growth rate in (k, l) space (bottom panel). Solid and dashed lines represent real and imaginary components respectively. Parameters are defined in Table 3.2 and $\sigma = 1.7\tilde{\sigma}_U$.

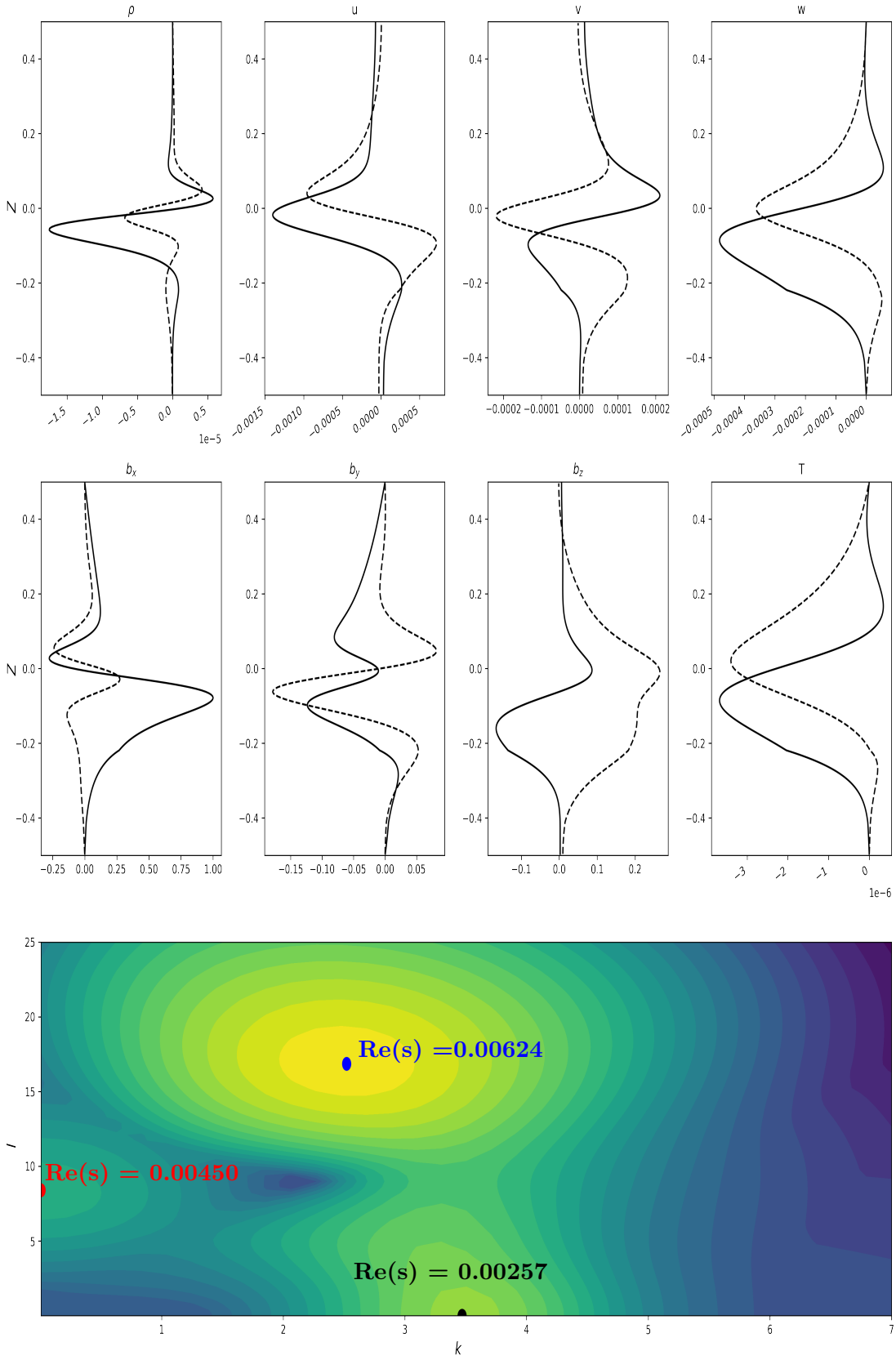

Figure 3.11: Perturbed quantities (top and middle) for $k = 2.52, l = 16.87$ (blue dot) with the growth rate in (k, l) space (bottom panel). Solid and dashed lines represent real and imaginary components respectively. Parameters are defined in Table 3.2 and $\sigma = 1.7\tilde{\sigma}_U$.

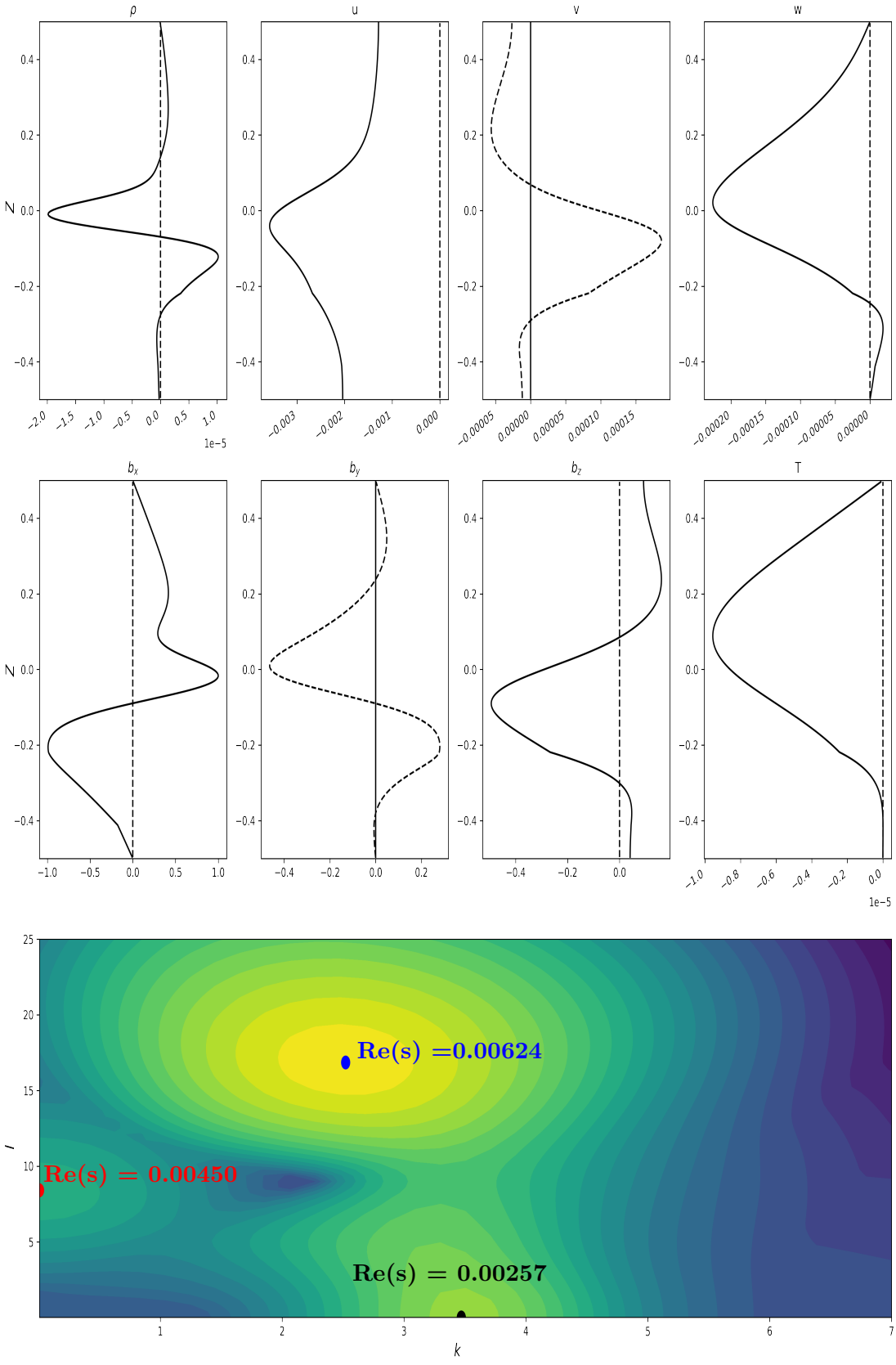

Figure 3.12: Perturbed quantities (top and middle) for $k = 0, l = 8.41$ (red dot) with the growth rate in (k, l) space (bottom panel). Solid and dashed lines represent real and imaginary components respectively. Parameters are defined in Table 3.2 and $\sigma = 1.7\tilde{\sigma}_U$.

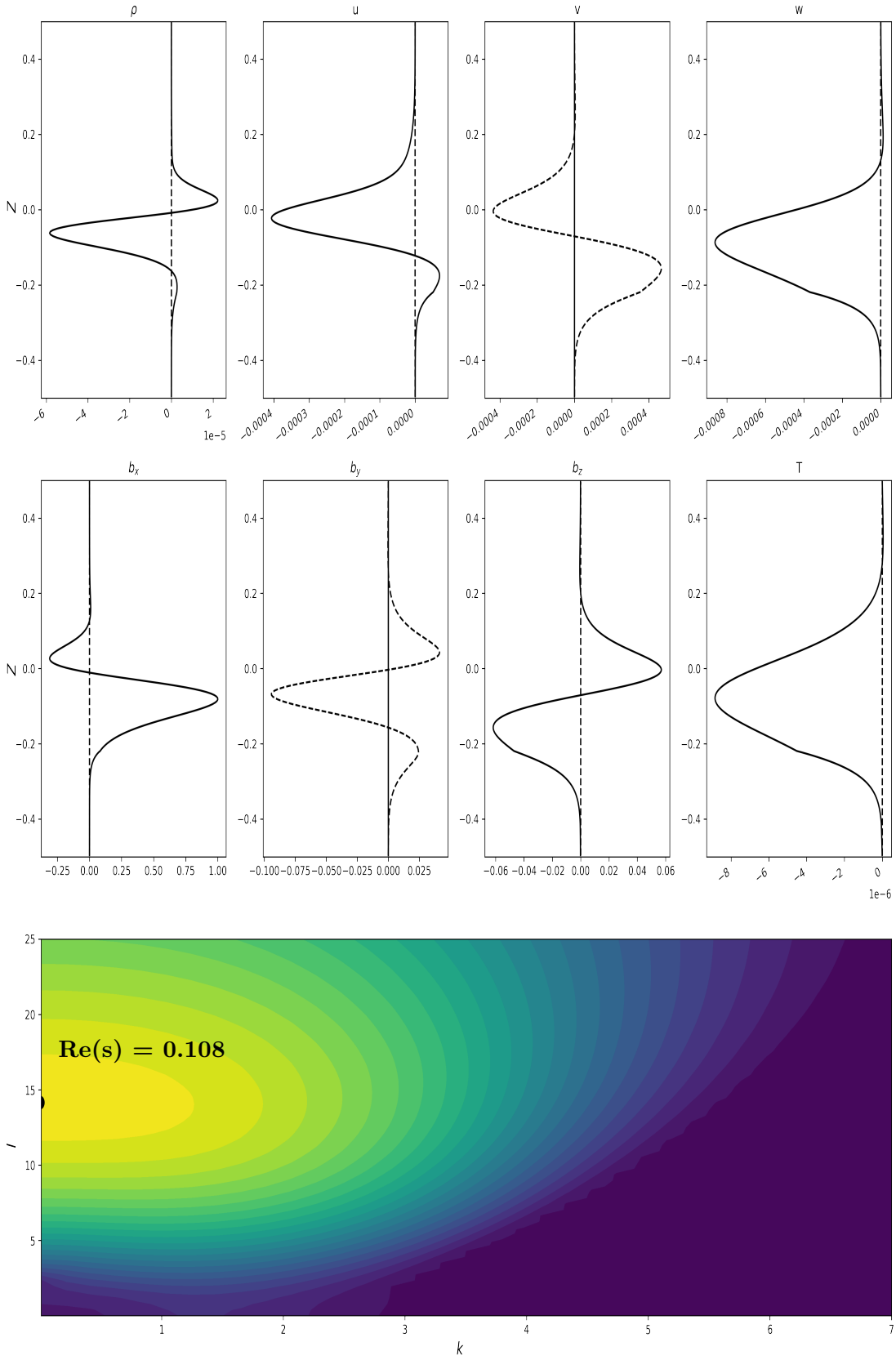

Figure 3.13: Perturbed quantities (top and middle) for $k = 0, l = 14.17$ (black dot) with the growth rate in (k, l) space (bottom panel). Solid and dashed lines represent real and imaginary components respectively. Parameters are defined in Table 3.2 and $\sigma = 6\tilde{\sigma}_U$.

3.6 Conclusions

In this chapter, we have considered the linear instability of a static MHD state generated from the shearing of a uniform magnetic field $\mathcal{B}_0\hat{\boldsymbol{z}}$: this process results in the field $\boldsymbol{B}_0 = (B(z), 0, \mathcal{B}_0)$ and flow $\boldsymbol{U}_0 = (U(z), 0, 0)$. We have combined our basic state analysis described in §2.2.2 with local instability criterion first introduced by Newcomb (1961), and have written a new instability criterion which predicts magnetic buoyancy instability in terms of the non-dimensional parameters and the prescribed target flow. Being able to predict instability from the basic state is of most importance for both linear and nonlinear computation. It is a useful result as it suggests that, as long as magnetic diffusion is weak, we are able to predict magnetic buoyancy instability purely in terms of the target flow. Even though variations in the basic state are not necessarily small, numerical calculations have shown the derived instability criteria can predict instability to within an order of magnitude. An interesting feature of this system is the role of Prandtl number, and hence viscosity. It has been shown that viscosity has a destabilising role, as it comes in through the magnetic field amplitude. It is important to note, however, that due to the large number of parameters, the role of viscosity is not so straightforward — increasing Prandtl number only means increasing the ratio ν/κ. It is important to note that, in our system, the forcing depends on viscosity explicitly.

Before we perform numerical calculations on the full compressible, shear flow MHD system, we study a simpler system: we consider the magnetic buoyancy instability of a stably stratified atmosphere embedded with a static linear magnetic field. Here, known results have allowed us to benchmark our complicated numerical solver. Once we have verified the numerical approach, we perform a parameter survey within the full shear flow problem. We have demonstrated that a wide range of instabilities are possible within the model described in §3.2, i.e., 2D undular and interchange modes as well as 3D undular modes. Furthermore, we have shown the existence of 2D undular modes, which in the absence of a shear flow are hard to destabilise.

A next step would be to use instability criteria that include viscosity, ν, explicitly before introducing our specific basic state. Such criteria are given in Acheson (1979) although we did not consider them here. For the parameter values shown in Table 3.2, the derived criteria predicted a stability boundary fairly accurately, and therefore the missing term due to viscosity is speculated to be small. However a complete analysis would be necessary to confirm this. Another extension to this work is to perform a complete parameter survey of important physical parameters, such as α. Moreover, the role of each parameter is not straightforward — changing the parameters leads to changes in the basic state as well as the linear system. The basic state is fairly well understood in parameter space and we have provided an analysis within §2.2.2.

An extension of this work is to investigate the magnetic buoyancy instability when the basic state is time-dependent — this will be the main topic of Chapter 5. It is a natural

extension to this work as the basic state within this chapter is the result of a dynamic process and the equilibrium state is reached through resistive and viscous processes — this will become clearer in Chapter 5. We will show that the relaxation of the basic state into a steady state given by Eqs (3.25)-(3.27) is a complicated process and depends heavily on the initial conditions. Therefore, the instability of the equilibrium state studied here is not always indicative of the stability of the transient state that preceded it.

Chapter 4

Linear Stability of Time-Dependent Rayleigh-Bénard Convection

4.1 Introduction

From this chapter onward, we analyse the linear stability of fluid systems where the basic state evolves in time, and therefore the eigenvalue approach used in Chapters 2-3 will not be applicable. Allowing the background state to be time-dependent adds another layer of complexity to the analysis and, therefore, it is instructive to begin with a relatively simple system — thermal instabilities in the context of the classical Rayleigh-Bénard Convection (RBC) problem with time-dependent basic states. Thermal instabilities arise when an adverse temperature gradient is created in a fluid layer. In general, if this fluid gradient is large enough, the stabilising effect of viscosity and thermal conductivity are overcome by the destabilising buoyancy, and an overturning instability results in convection. Convective instability was first described by Thomson (1882), but the first quantitative experiments were made by Bénard (1900). After Bénard's experiments, Rayleigh (1916) formulated the theory of convective instability of a layer of fluid confined between two horizontal planes. Rayleigh (1916) chose equations of motion and boundary conditions to model experiments, and derived the linear equations for normal modes. It was then shown that instability would occur only when the adverse temperature gradient was large enough so that the dimensionless parameter $g\alpha\beta d^4/\kappa\nu$ exceeded a certain critical value. Here g is the acceleration due to gravity, α the coefficient of thermal expansion of the fluid, $\beta = -\mathrm{d}T/\mathrm{d}z$ the magnitude of the vertical temperature gradient of the static background state, d the depth of the layer, κ the thermal diffusivity, and ν the kinematic viscosity. This dimensionless parameter is now called the *Rayleigh number*, which we denote *Ra*. The Rayleigh number is a characteristic ratio of the destabilising effect of buoyancy to the stabilizing effects of diffusion and dissipation.

After Bénard's experiments, up until at least the 1960s, the majority of work on convec-

tion focused on linear temperature profiles. On several occasions it has been observed experimentally that thermally induced instabilities occur under conditions which differ from theoretical predictions. Experiments by Graham (1933) suggested that a columnar mode of instability could be established at a smaller Rayleigh number than that predicted by linear theory, but no numerical data were reported. Experimental values obtained by Chandra (1938) and Sutton (1950) were considerably smaller than those predicted theoretically: it was suggested by Sutton (1950) that the non-uniform temperature gradient caused by rapid heating might be the cause of a columnar instability. Spangenberg and Rowland (1961) performed experiments studying the evaporative cooling of water and found that the temperature profile at the onset of instability was very different from that which was found once the instability had saturated. It was reported that the critical temperature difference was much greater than that predicted by the existing theory. The foregoing experiments were the first reported to establish that thermally induced instabilities may occur in fluids over a range of Rayleigh numbers, varying from slightly less than the theoretical value to several times the theoretical value. In short, the value depends on the rate of heating.

Alongside the experimental efforts to study the role of nonlinear temperature profiles in convective experiments was the research interest to establish a generalised analytic approach to understanding instabilities when the background states evolve in time. This problem is much more difficult than studying steady background states. The functional form of the time-dependence of perturbed quantities is no longer known, owing to source terms which vary in time: therefore, this precludes the use of an exponential growth rate, s. There has been multiple efforts to generalise linear stability theory for time-dependent basic states. One particular example relates to the linear stability of shear flows, i.e. attempts to derive integral criteria similar to that of Rayleigh's necessary condition for instability of inviscid flows — however, this approach is not helpful as these integral criteria involve the unknown eigenfunctions. Conrad and Criminale (1965) attempted to generalise the result of Squire (1933) for three-dimensional disturbances to apply to unsteady flows. However, they find that the time transformation does not allow the generalization to be a useful one. Conrad and Criminale (1965) also attempted to obtain a Rayleigh theorem for time-dependent flows. They assumed the eigenfunction $w(z,t)$ to have the form

$$w(z,t) = \sum_{n=1}^{N} a_n(t)\phi_n(z), \tag{4.1}$$

obtained a second-order differential equation for each of $\phi_n's$, and from that obtained the desired theorem. However, this result cannot be obtained from the equation for *each* individual ϕ_n, and must be arrived at by considering the *sum* given by Eq (4.1). Typically, in a linear stability analysis, the problem of stability reduces down to an eigenvalue problem in which the onset of instability manifests when the growth rate, s, changes sign. When the background states are evolving in time, the time dependence of the eigenfunctions is unclear, and the stability boundary is ill-defined — the importance

of this point cannot be overstated. Despite this, various time-dependent linear stability analyses have been investigated. In terms of RBC, three main studies of interest discussed in this thesis are the time-dependent thermal convection problems studied by Foster (1965), Venezian (1969), and Yih and Li (1972), who all investigated RBC with time-dependent heating at the fluid boundaries.

In this chapter, we first introduce the governing equations in Cartesian geometry, under the Boussinesq approximation. We then derive the set of linear equations that govern RBC. After that, we will look at three static background configurations with different temperature distributions. The first is an adverse linear temperature gradient which has been studied extensively — we will give an overview of analytic results and use these results to benchmark numerical solvers. The next two problems involve non-steady temperature fields: the result of linear cooling from below, and time-periodic heating at both boundaries. In both of these problems, we are able to reproduce known results in previous literature (Foster, 1965; Yih and Li, 1972), learn new techniques useful for performing a time-dependent linear analysis, and extend the results into unstudied asymptotic regimes.

4.2 The Equations of Motion

Here we introduce the relevant equations of motion within the Boussinesq limit, and the linearised equations of motion with a suitable non-dimensionalisation.

4.2.1 The Boussinesq Equations

Rayleigh (1916) applied the *Boussinesq approximation* to the governing equations of fluid dynamics, first derived by Oberbeck (1879) and Boussinesq (1901). The basis of the Boussinesq approximation is that there are flows in which the temperature, and therefore the density variations, are small, but the motion is nevertheless driven by buoyancy. The variation of density is neglected everywhere except for in the buoyancy term, and therefore, for a small temperature difference between the bottom and top layers of the fluid, the density can be written as

$$\rho = \rho_0(1 - \tilde{\alpha}(T - T_0)), \tag{4.2}$$

where ρ_0 is the density of the fluid at the temperature T_0, and $\tilde{\alpha}$ is the thermal expansion coefficient. One can approximate the thermodynamic variables as constants except for the pressure, temperature, and the density when multiplied by g. This approximation works well for flows with temperature differences of a few degrees or less, such as Bénard's experiments, and is formally justified by physical arguments (see Spiegel and Veronis, 1960) and asymptotic analysis (see Mihaljan, 1962). Without formal justification, the

Boussinesq equations are given by

$$\nabla \cdot \boldsymbol{U} = 0, \tag{4.3}$$

$$\frac{\partial \boldsymbol{U}}{\partial t} + \boldsymbol{U} \cdot \nabla \boldsymbol{U} = -\frac{1}{\rho_0}\nabla p + \frac{\rho}{\rho_0} g\hat{\boldsymbol{z}} + \nu \nabla^2 \boldsymbol{U}, \tag{4.4}$$

$$\frac{\partial T}{\partial t} + \boldsymbol{U} \cdot \nabla T = \kappa \nabla^2 T. \tag{4.5}$$

Here $\boldsymbol{U} = (U, V, W)$ is the fluid velocity, p is the pressure, ρ and T are the density and temperature, ν is the kinematic viscosity, and κ is the thermal diffusivity.

4.3 General Linear Stability Equations

As we have seen in Chapters 2-3, linear stability analysis involves first finding a basic state. We then consider small perturbations around this basic state and, in the governing equations, retain only terms that are linear in perturbed quantities. It is important to understand that the basic state temperature distribution can depend on time and space: we restrict attention to a temperature field which varies only in z but is not necessarily steady. We study separate cases: i) a linear and steady temperature field; ii) linear cooling at the boundary; and iii) periodic modulation of the boundary temperatures. Consider two horizontal plates at different temperatures (ΔT_0) and separated by a distance d in the z-direction. We will only perturb static basic states ($\boldsymbol{U_0} = 0$), with non-trivial basic temperature, density, and pressure, T_0, ρ_0, and P_0 respectively. Let $\boldsymbol{u}$, θ, p denote the velocity, temperature, and pressure perturbations respectively. Retaining only terms linear in perturbations yields the governing set of equations

$$\nabla \cdot \boldsymbol{u} = 0, \tag{4.6}$$

$$\frac{\partial \boldsymbol{u}}{\partial t} = -\frac{1}{\rho_0}\nabla p + \tilde{\alpha} g \theta \hat{\boldsymbol{z}} + \nu \nabla^2 \boldsymbol{u}, \tag{4.7}$$

$$\frac{\partial \theta}{\partial t} = -\frac{\mathrm{d}T_0}{\mathrm{d}z} w + \kappa \nabla^2 \theta. \tag{4.8}$$

We write Eqs (4.6)-(4.8) in dimensionless form, scaling lengths with d, times with the thermal relaxation time, d^2/κ, pressure with $\rho\kappa^2/d^2$, and temperature with ΔT_0. This yields the set of non-dimensional linear equations

$$\nabla \cdot \boldsymbol{u} = 0, \tag{4.9}$$

$$\frac{\partial \boldsymbol{u}}{\partial t} = \nabla p + RaPr\theta \hat{\boldsymbol{z}} + Pr \nabla^2 \boldsymbol{u}, \tag{4.10}$$

$$\frac{\partial \theta}{\partial t} = -\frac{\mathrm{d}T_0}{\mathrm{d}z} w + \nabla^2 \theta. \tag{4.11}$$

where the two non-dimensional parameters are the Rayleigh number, Ra, and the Prandtl number, Pr, defined

$$Ra = \frac{\tilde{\alpha} g d^2 \Delta T_0}{\nu \kappa}, \qquad Pr = \frac{\nu}{\kappa}. \tag{4.12}$$

where ΔT_0 is a suitable measure of the temperature difference across the plates.

We consider fixed temperature boundary conditions, and as such the temperature perturbation vanishes at the boundaries, i.e.

$$\theta = 0. \tag{4.13}$$

The impermeability condition states that fluid cannot penetrate the boundaries, and therefore the vertical velocity vanishes at the boundaries, $w = 0$. The horizontal velocity components depend on the nature of the plates, which leaves us with two cases: *stress-free* and *no-slip* boundary conditions. The no-slip condition is straightforward, it implies that the velocity must match the speed of the bounding surfaces at the interface and for stationary plates this states $\boldsymbol{u} = 0$. This condition must follow for all x, y and therefore Eq (4.9) implies that $\partial_z w = 0$ at the interface. The stress-free boundary condition is more involved — it states that the tangential stress must vanish on the boundary, which requires

$$\sigma_{xz} = \mu\left(\frac{\partial u}{\partial z} + \frac{\partial w}{\partial x}\right) = 0, \qquad \sigma_{yz} = \mu\left(\frac{\partial v}{\partial z} + \frac{\partial w}{\partial y}\right) = 0, \tag{4.14}$$

where σ_{ij} is the viscous stress tensor. Coupled with $w = 0$ at the interface, this implies that $\partial_z u = \partial_z v = 0$. Using Eq (4.9), it follows that $\partial_{zz} w = 0$. In the following sections, we will use either set of boundary conditions, specifying the particular case as stress-free or no-slip boundary conditions.

We seek to eliminate pressure in Eq (4.10) and consider two coupled stability equations in only w and θ. Taking the curl of Eq (4.10) yields

$$\frac{\partial \boldsymbol{\omega}}{\partial t} = RaPr(\nabla\theta \times \hat{\boldsymbol{z}}) + Pr\nabla^2\boldsymbol{\omega}, \tag{4.15}$$

where $\boldsymbol{\omega} = \nabla \times \boldsymbol{u}$ is the vorticity. Using the incompressibility condition, the curl of Eq (4.15) can be written in the form

$$\frac{\partial}{\partial t}\nabla^2\boldsymbol{u} = RaPr\left(\nabla^2\theta\hat{\boldsymbol{z}} - \nabla\frac{\partial\theta}{\partial z}\right) + Pr\nabla^4\boldsymbol{u}, \tag{4.16}$$

where, in particular, the z-component is given by

$$\frac{\partial}{\partial t}\nabla^2 w = RaPr\nabla_H^2\theta + Pr\nabla^4 w, \tag{4.17}$$

where $\nabla_H = \partial^2/\partial x^2 + \partial^2/\partial y^2$ is the horizontal Laplacian. The linear equations for the vertical velocity and temperature perturbations now read

$$\left(\frac{1}{Pr}\frac{\partial}{\partial t} - \nabla^2\right)\nabla^2 w = Ra\nabla_H^2\theta, \tag{4.18}$$

$$\left(\frac{\partial}{\partial t} - \nabla^2\right)\theta = w\frac{\partial T_0}{\partial z}, \tag{4.19}$$

where T_0 is the basic temperature field and is the solution to

$$\frac{\partial T_0}{\partial t} = \frac{\partial^2 T_0}{\partial z^2}, \tag{4.20}$$

for some boundary and initial conditions which will be specified later. We will now give a brief overview of steady Rayleigh-Bénard convection before investigating two different forms of time-dependent heating which have previously been studied in the literature.

4.4 A Steady and Linear Temperature Distribution

The problem of steady RBC is a classical problem of fluid dynamics which has been studied extensively. For an in-depth overview of Rayleigh-Bénvard convection, see Chandrasekhar (1961). Here, we will give a brief overview of the work therein, following this book closely. In classical RBC, the top and bottom plates are held at a constant temperature, with the bottom plate being hotter than the top. The basic temperature is then the solution to the equation

$$\frac{\mathrm{d}^2 T_0}{\mathrm{d}z^2} = 0 \qquad \text{with} \quad T_0(0) = 1, \quad T_0(1) = 0, \tag{4.21}$$

where the unit temperature, ΔT_0 is given by the difference across the plates. In this case, the basic temperature field is linear and is given by

$$T_0 = 1 - z. \tag{4.22}$$

We look for separable solutions to Eqs (4.18)-(4.19) of the form $F(t)X(x)Y(y)Z(z)$ and seek periodic solutions in the (x, y) plane. The velocity and temperature perturbations are then written in the form

$$w(\boldsymbol{x}, t) = W(z)\exp\{ikx + ily + st\}, \tag{4.23}$$

$$\theta(\boldsymbol{x}, t) = \Theta(z)\exp\{ikx + ily + st\}, \tag{4.24}$$

where $s = \sigma + i\omega$ is the (complex) growth rate and k, l are the horizontal wavenumbers. We substitute Eqs (4.23)-(4.24) into Eqs (4.18)-(4.19) to obtain

$$(\mathcal{D}^2 - \alpha^2)\left(\mathcal{D}^2 - \alpha^2 - \frac{s}{Pr}\right)W = \alpha^2 Ra\Theta, \tag{4.25}$$

$$(\mathcal{D}^2 - \alpha^2 - s)\Theta = -W, \tag{4.26}$$

where $\alpha^2 = k^2 + l^2$, $\mathcal{D} \equiv \mathrm{d}/\mathrm{d}z$, with the boundary conditions

$$w = \mathcal{D}w = \theta = 0 \quad \text{(no-slip)}, \quad \text{or} \tag{4.27}$$

$$w = \mathcal{D}^2 w = \theta = 0 \quad \text{(stress-free)}. \tag{4.28}$$

First, we give an overview of the analytic progress of standard RBC for no-slip and stress-free boundaries, where the numerical results will be used to develop a numerical solver. The free boundary problem is difficult to experimentally realise, but it allows the problem to

be simplified and renders Eqs (4.25)-(4.26) separable. We are interested in the marginal state: this allows the reduction of the problem to a characteristic value problem. The marginal state is the state in which there are zero growth or decay, i.e. $R(s) = 0$. We seek solutions to the equations

$$(\mathcal{D}^2 - \alpha^2)^2 W = \alpha^2 Ra\Theta, \tag{4.29}$$

$$(\mathcal{D}^2 - \alpha^2)\Theta = -W, \tag{4.30}$$

which can be written as the single equation,

$$(\mathcal{D}^2 - \alpha^2)^3 W = -\alpha^2 Ra W, \tag{4.31}$$

with the boundary conditions

$$W = \mathcal{D}W = (\mathcal{D}^2 - \alpha^2)^2 Q = 0 \qquad \text{(no-slip), or} \tag{4.32}$$

$$W = \mathcal{D}^2 W = \mathcal{D}^4 W = 0 \qquad \text{(stress-free).} \tag{4.33}$$

Analytically solving Eq (4.31) for no-slip boundary conditions is challenging. Progress is made by splitting W solutions of the form

$$W = e^{\pm qz}, \tag{4.34}$$

where q^2 is the root of the equation

$$(q^2 - \alpha^2)^3 = -\alpha^2 Ra. \tag{4.35}$$

To make analytic progress with Eq (4.35), the odd and even components of the vertical velocity perturbation W are written in terms of sinh and cosh. The boundary conditions are then used to obtain determinants which must vanish if the solution for W is to remain non-trivial. The determinants for the odd and even components of W result in transcendental equations, which relate α and Ra: the roots in (Ra, α) space can be calculated numerically. It is more straightforward to obtain an analytic solution to Eq (4.31) for stress-free boundary conditions. Since all even derivatives must vanish (see Eq (4.31) and Eq (4.33)), the solution to Eq (4.31) with Eq (4.33) must be of the form

$$W(z) = A \sin n\pi z, \qquad (n = 1, 2, \dots), \tag{4.36}$$

where A is a constant. Substituting Eq (4.36) into Eq (4.31) yields the characteristic equation

$$Ra = (n^2\pi^2 + \alpha^2)^3/\alpha^2. \tag{4.37}$$

It can be seen, by Eq (4.37), that the first mode to manifest instability is given by $n = 1$, and hence for a given α^2, the largest Ra which is marginally stable is given by

$$Ra = \frac{(\pi^2 + \alpha^2)^3}{\alpha^2}. \tag{4.38}$$

The critical values (Ra_c, α_c) are found by minimising Eq (4.38) with respect to α. The exact values are given by

$$Ra_c = \frac{27\pi^4}{4}, \qquad \alpha_c^2 = \frac{\pi^2}{2}. \tag{4.39}$$

Alternatively, substitution of Eq (4.36) into Eq (4.31) yields a quadratic equation in s of the form

$$(n^2\pi^2 + \alpha^2 + s)\left(n^2\pi^2 + \alpha^2 + \frac{s}{Pr}\right)(n^2\pi^2 + \alpha^2) = Ra\alpha^2. \tag{4.40}$$

We can then obtain Eq (4.39) by letting $s = 0$ and minimising over (Ra, α). It can be seen from Eq (4.40) that the stability boundary does not depend on the Prandtl number, i.e when $s = 0$, the Prandtl number drops out of Eq (4.40).

4.5 A Numerical Approach

The main focus of this chapter is to perform a linear stability analysis for time-dependent background states: it is therefore necessary to have a numerical scheme that time steps Eqs (4.18)-(4.19), and the problem of standard RBC will be used to validate the numerical approach outlined hereafter. We define the Laplacian, $\mathcal{L} = (\mathcal{D}^2 - \alpha^2)$, and use a Crank–Nicolson time stepping scheme, where $f(n\Delta t, z) = f^n$, is the function f evaluated at time $n\Delta t$ for a time step Δt. The time stepping scheme is given by

$$\left(\mathcal{L} - \frac{\Delta t Pr}{2}\mathcal{L}^2\right)\vec{w}^{n+1} + \frac{\Delta t\alpha^2 PrRa}{2}\vec{\theta}^{n+1} = \left(\mathcal{L} + \frac{\Delta t Pr}{2}\mathcal{L}^2\right)\vec{w}^{n} - \frac{\Delta t\alpha^2 PrRa}{2}\vec{\theta}^{n}. \tag{4.41}$$

$$\left(\mathcal{I} - \frac{\Delta t}{2}\mathcal{L}\right)\vec{\theta}^{n+1} - \frac{\Delta t}{2}\frac{\mathrm{d}}{\mathrm{d}z}\left(T_0^{n+1}\right)\mathcal{I}\vec{w}^{n+1} = \left(\mathcal{I} + \frac{\Delta t}{2}\mathcal{L}\right)\vec{\theta}^{n} + \frac{\Delta t}{2}\frac{\mathrm{d}}{\mathrm{d}z}\left(T_0^{n}\right)\mathcal{I}\vec{w}^{n}, \tag{4.42}$$

where $\mathcal{I}$ is the identity matrix. We discretise in space using a second order and fourth order spatial scheme and define the vector $\vec{G}^n = (w_1, ..., w_{N-1}, \theta_1, ..., \theta_{N-1})^T$. Equations (4.41)-(4.42) are then written as the matrix equation

$$\vec{G}^{n+1} = \mathcal{P}^{-1}\mathcal{M}\vec{G}^{n}, \tag{4.43}$$

where $\mathcal{P}$ and $\mathcal{M}$ are given by the block matrices

$$\mathcal{P} = \begin{pmatrix} \mathcal{L} - \frac{\Delta t Pr}{2}\mathcal{L}^2 & \frac{\alpha^2\Delta t PrRa}{2}\mathcal{I} \\ -\frac{\Delta t}{2}\frac{\mathrm{d}}{\mathrm{d}z}\left(T_0^{n+1}\right)\mathcal{I} & \mathcal{I} - \frac{\Delta t}{2}\mathcal{L} \end{pmatrix}, \tag{4.44}$$

$$\mathcal{M} = \begin{pmatrix} \mathcal{L} + \frac{\Delta t Pr}{2}\mathcal{L}^2 & -\frac{\Delta t\alpha^2 PrRa}{2}\mathcal{I} \\ \frac{\Delta t}{2}\frac{\mathrm{d}}{\mathrm{d}z}\left(T_0^{n}\right)\mathcal{I} & \mathbb{I} + \frac{\Delta t}{2}\mathcal{L} \end{pmatrix}. \tag{4.45}$$

Now we check the numerical methods against the special case of steady RBC. Equations (4.18)-(4.19) can be numerically solved as an eigenvalue problem for s upon substitution of $\partial/\partial t = s$, by using Finite Difference Methods (FDM) either on a spatially uniform or Chebyshev grid. We have seen in Chapters 2-3 that this approach is standard for steady background states: one would look for roots to the eigenvalue problem, $f(s; Ra, \alpha) = 0$ and optimise over (Ra, α) to determine the critical parameter values.

However, solving Eq (4.43) leads to a solution of the form $F(z,t)$, and since there is no inhomogeneous time-dependent forcing terms in Eq (4.41)-(4.42) we can make use of the fact that the solutions must be of the form $F(z,t) = e^{st}f(z)$. We define some measure on the velocity $\langle w^2 \rangle_z$,

$$\langle w^2 \rangle_z = e^{2st} \int_0^1 W^2(z) \mathrm{d}z. \tag{4.46}$$

Taking the logarithm of both sides of Eq (4.46) yields

$$\ln\langle w^2 \rangle_z = 2st + \ln \int_0^1 W^2(z) \mathrm{d}z. \tag{4.47}$$

It can be seen from Eq (4.47) that the growth rate varies linearly in time. We can determine the growth rate as half of the gradient of the line. To verify the numerical method, we solve Eq (4.43) and fit a straight line to $\ln\langle w^2 \rangle$ vs. t for stable and unstable Rayleigh numbers for $Pr = 1$, with the wavenumber $\alpha = \pi/\sqrt{2}$: the gradient is then compared to the analytic fundamental ($n = 1$) solution to Eq (4.40).

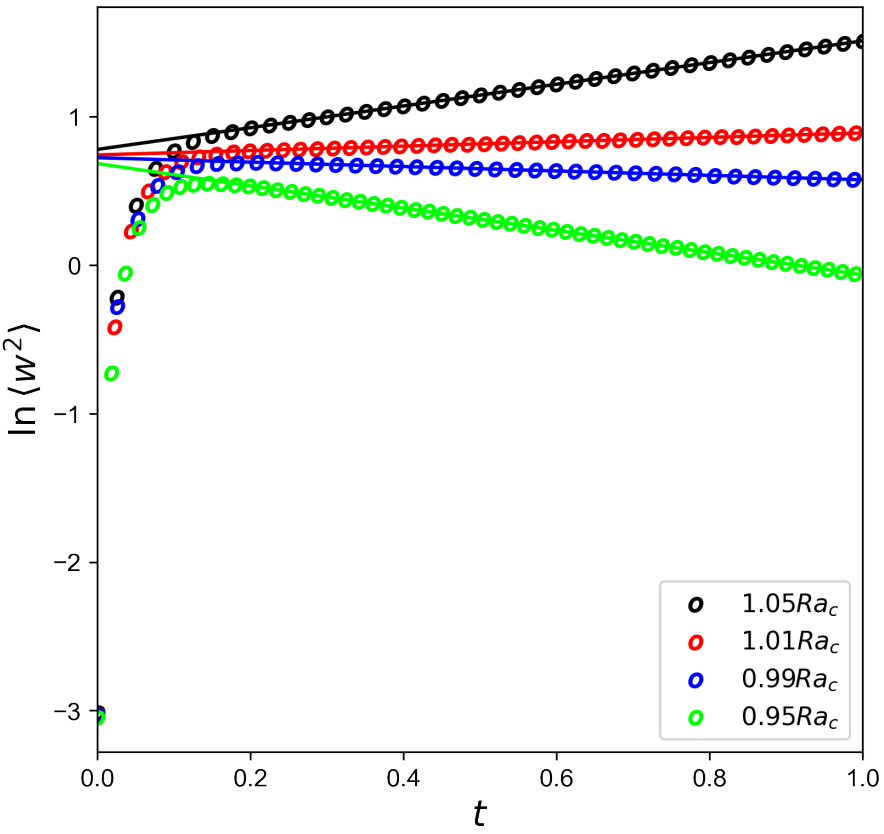

Figure 4.1: The natural logarithm of the average kinetic energy versus time for various Ra with stress-free boundary conditions. The solid lines represent theoretical results. Here $Pr = 1, \alpha = \pi/\sqrt{2}$.

Figure 4.1 compares the numerical kinetic energy in time against lines determined by Eq (4.47), with $R(s)$ given by Eq (4.40). It can be seen that the growth rate can be calculated through the kinetic energy given by Eq (4.47) is within excellent agreement of

the analytical theory given by Eq (4.40). Note the initial jump in growth before $t \approx 0.2$ — this is an important feature. It is well known that the numerical solution projects onto *all* the normal modes, however, it takes a finite time before the most unstable mode emerges. Therefore, we must wait a finite time before we calculate the gradient and therefore the growth (this is an important point for Chapter 5). To illustrate this, we time-step Eqs (4.41)-(4.42) for four initial conditions and calculate the kinetic energy.

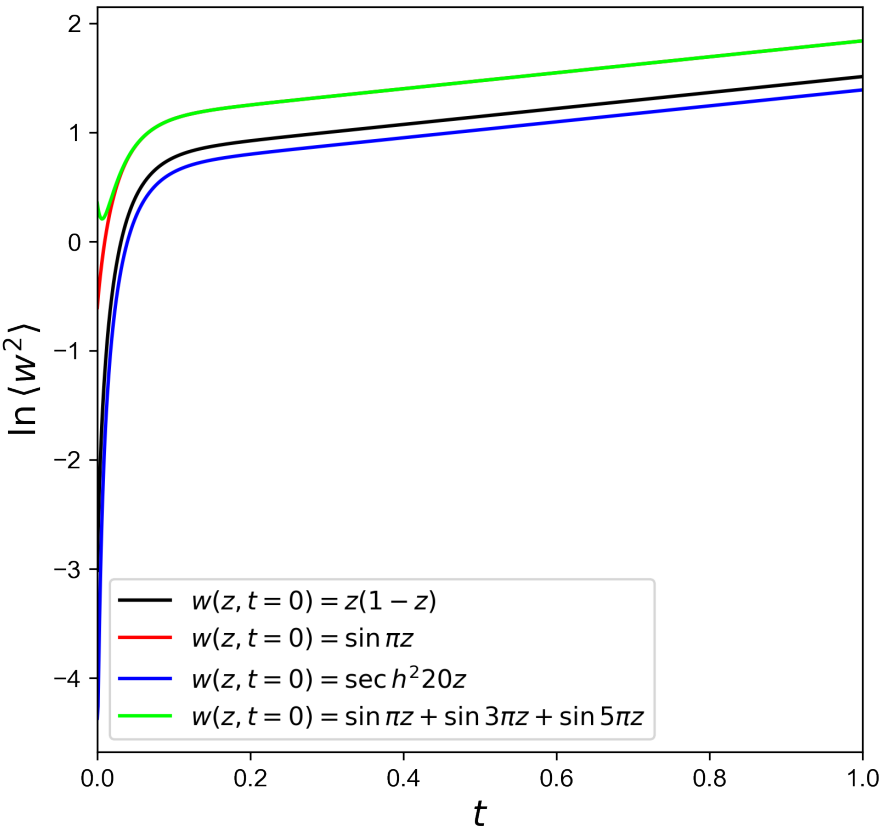

Figure 4.2: The natural logarithm of the average kinetic energy against time for various initial conditions. $Ra = \frac{27\pi^4}{4}$ and $Pr = 1$, and $\alpha = \pi/\sqrt{2}$.

Figure 4.2 demonstrates that, after a finite time, the numerical solution to Eqs (4.41)-(4.42) is independent of the initial conditions. It can be seen in Fig 4.2 that there is an initial transient behaviour that is dependent on the initial conditions. After some finite time the projection of the initial conditions onto the most unstable (least stable) eigenmode will dominate the solution, which will subsequently grow/decay exponentially with a rate determined by Eq (4.40).

4.6 Decreasing the Temperature at the Top Plate in Time

In this section we investigate the case of time-dependent heating, where the top plate is cooled linearly in time. This problem was investigated by Foster (1965) who also considered the linear stability of a sudden temperature decrease at the top plate. The problem of linear

cooling is easily realisable in an experimental setting and occurs in nature and engineering settings such as in buildings (for example thermal comfort by using floor heating or ceiling cooling). It is important to note that no new work is developed in this chapter: here, we are interested in giving an overview of a time-dependent linear stability analysis. We closely follow the work of Foster (1965) and reproduce the results therein to validate the time-dependent numerical approach. This subsection will therefore serve to illustrate the nature of time-dependent linear stability problems. There are multiple lines of enquiry one can consider in a time-dependent linear stability analysis. The two empirical aspects of this dynamic linear stability analysis that are subject to refinement are: 1) the initial condition for the perturbation; 2) the criterion for the determination of the time at which convection is onset. First, we will solve the heat equation given by Eq (4.20) for the basic state temperature. Here, we will be able to show that certain characteristics of the basic state temperature allow us to define a suitable stability boundary. We will then discuss a suitable measure of stability which is useful in the context of this basic temperature profile and then reproduce the linear stability results of Foster (1965).

4.6.1 The Basic Temperature Profile

To be consistent with Foster (1965), we define the z-direction to be vertically downwards and so the top plate is located at $z = 0$ and the bottom plate at $z = 1$ — note that this will require a change of sign of the buoyancy term in Eqs (4.18)-(4.19). We consider the case where the top surface temperature (in dimensional units) is cooled by an amount βt starting at a time $t = 0$. In dimensionless quantities, we must therefore solve

$$\begin{aligned} \frac{\partial T_0}{\partial t} &= \frac{\partial^2 T_0}{\partial z^2}, \\ T_0(0) = -t, \quad T_0(1) = 0, \quad &\text{for} \quad t \geq 0, \end{aligned} \tag{4.48}$$

where the temperature scale factor is taken to be

$$\Delta T_0 = \beta h^2/\kappa. \tag{4.49}$$

Using the method of eigenfunction expansion, the solution to Eq (4.48) is

$$T_0 = (z-1)t + \frac{2}{\pi^3}\sum_{n=1}^{\infty}\frac{\sin(n\pi z)}{n^3}(1 - e^{-n^2\pi^2 t}), \tag{4.50}$$

with temperature gradient

$$\frac{\partial T_0}{\partial z} = t + \frac{2}{\pi^2}\sum_{n=1}^{\infty}\frac{\cos(n\pi z)}{n^2}(1 - e^{-n^2\pi^2 t}). \tag{4.51}$$

The background temperature gradient is important as it appears in Eq (4.19) as $(w\partial T_0/\partial z)$. It can be seen by Eq (4.51) that the temperature gradient is linearly divergent in time. In the long time limit, the temperature and temperature gradient

become

$$\lim_{t\to\infty} T_0 \approx (z-1)t, \tag{4.52}$$

$$\lim_{t\to\infty} \frac{\partial T_0}{\partial t} \approx t. \tag{4.53}$$

It can be seen in Eqs (4.52)-(4.53) that when $t \to \infty$, the temperature is dominated by a linear profile with a gradient that increases linearly in time.

4.6.2 Suitable Measure of Instability

Since Eqs (4.59)-(4.60) cannot be written as an eigenvalue problem, there is no natural stability boundary. That is to say, there is no obvious way to separate growing and decaying solutions, similar to the steady case where the stability boundary is characterised by the line $R(s) = 0$. Therefore, we must define an alternative stability boundary. Furthermore, the increasing adverse temperature gradient given by Eq (4.51) leads to an unconditionally unstable system, in which all non-zero parameter values will lead to super-exponentially growing solutions to Eqs (4.18)-(4.19). Some initial conditions and parameter values will be optimal for growth, that is, certain parameters and initial conditions will lead to faster growing solutions. To be able to conclude which parameters are optimal, it is essential to be able to measure the amplification in the disturbed quantities. Foster (1965) suggests that the onset time be marked as the time at which the magnitude of the disturbance grows by an order of magnitude relative to its initial value: this criterion for marking the time when convection onsets is satisfactory, and assumes that before these times, the onset of disturbances are small enough to justify the linearisation approximation. In particular, Foster (1965) defines the growth of disturbances to be

$$\bar{w} = \left(\frac{\int_0^1 w(z,t)^2 dz}{\int_0^1 w(z,0)^2 dz} \right)^{\frac{1}{2}}. \tag{4.54}$$

The denominator is a measure of the total kinetic energy in the initial condition, whereas the numerator is a measure of the total instantaneous kinetic energy. Furthermore, Eq (4.54) is a measure of the amplification in the velocity disturbance compared to the initial state.

4.6.3 Optimal Initial Conditions

As briefly mentioned in §4.6.2, the growth of the disturbances governed by Eqs (4.18)-(4.19) depends heavily on the initial conditions. It is therefore essential to investigate various initial conditions within the linear stability analysis. Foster (1965) eliminates the temperature disturbance, θ, and seeks solutions of a 6^{th} order equation for w, in the form of a Fourier sine series with time-dependent coefficients,

$$w(z,t) = \sum_{m=1}^{\infty} A_m(t) \sin(m\pi z), \tag{4.55}$$

such that the boundary conditions are automatically satisfied. After some manipulation, the resultant system of ordinary differential equations solved by Foster (1965) are integrated using a Runge-Kutta-Gill method. Foster (1965) considers various initial conditions such as

$$w_N(z,0) = A\sin(N\pi z), \quad \dot{w}(z,0) = 0, \tag{4.56}$$

and 'white-noise', defined as

$$w(z,0) = A\sum_{N=1}^{12} w_N, \quad \dot{w}(z,0) = 0. \tag{4.57}$$

The constant A is determined through normalising the initial growth to unity, and N characterises a particular Fourier mode. We seek perturbations of the form

$$f(x,y,z;t) = \hat{f}(z,t)e^{ikx+ily}, \tag{4.58}$$

which yields the system of linear equations for the vertical velocity, w, and the temperature, θ;

$$\left(\frac{1}{Pr}\frac{\partial}{\partial t} - (\mathcal{D}^2 - \alpha^2)\right)(\mathcal{D}^2 - \alpha^2)w = -Ra\nabla_H^2\theta, \tag{4.59}$$

$$\left(\frac{\partial}{\partial t} - (\mathcal{D}^2 - \alpha^2)\right)\theta = -w\frac{\mathrm{d}T_0}{\mathrm{d}z}, \tag{4.60}$$

where we note the change of sign on the right hand side of Eq (4.19) due to the orientation of z, $\alpha^2 = k^2 + l^2$, and $\Delta_H^2 = \partial_{xx} + \partial_{yy}$ is the horizontal Laplacian. Initial conditions are required on both w and θ, and so substituting Eqs (4.56)-(4.57) in Eq (4.60) yields equivalent initial conditions on the temperature as:

$$\theta_N(z,0) = -A\left(\frac{N^4\pi^4}{\alpha^2} + 2\pi^2N^2 + \alpha^2\right)\sin(N\pi z), \tag{4.61}$$

for a single Fourier mode and, in the case of white noise,

$$\theta(z,0) = \sum_{N=1}^{12}\theta_N(z,0). \tag{4.62}$$

We time-step Eqs (4.59)-(4.60), starting with single Fourier modes, for fixed Rayleigh, Prandtl, wave numbers, and calculate the amplification given by Eq (4.54).

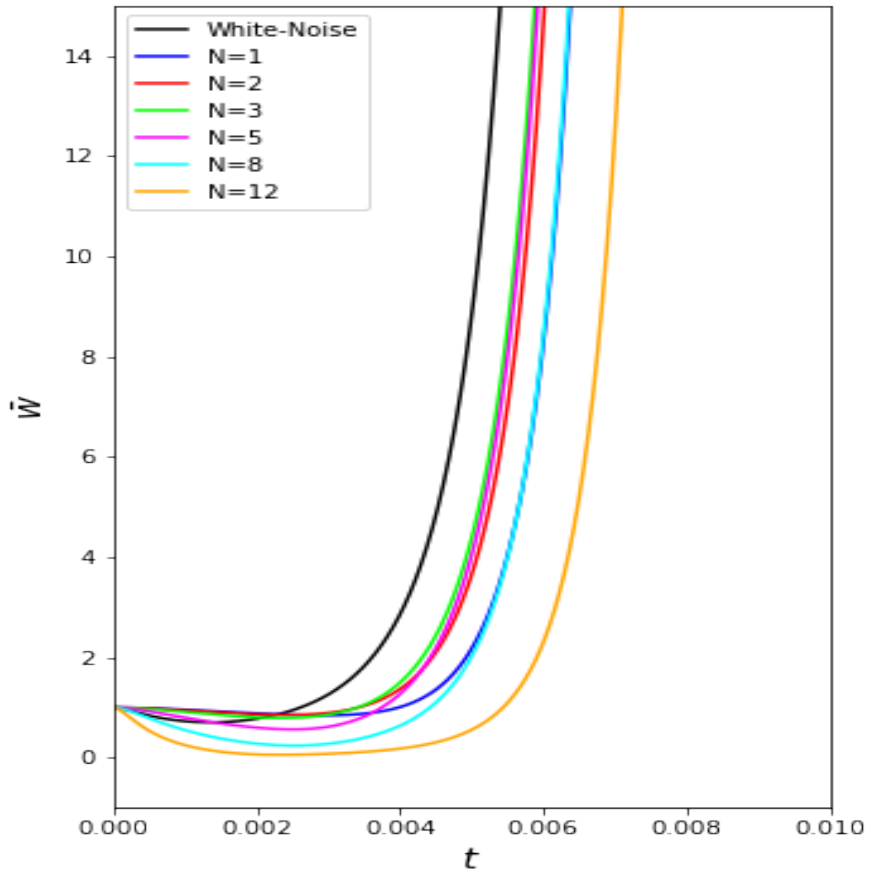

Figure 4.3: $\bar{w}$ versus time for a series of Fourier modes and 'white-noise' initial condition. Here, $Ra = 10^8, Pr = 7$, and $\alpha = 11$.

Figure 4.3 shows the growth of disturbances in time, for a series of initial conditions defined by Eqs (4.56)-(4.57) and Eqs (4.61)-(4.62). It can be seen that there are a preferred set of initial conditions, resulting in optimal growth. Across all the initial conditions in Fig 4.3, it is shown that there is some small transient decay when t is small. 'White-noise' is manifest by growth before all the other Fourier modes and is therefore the optimal initial condition considered here: however, it is understood that 'white-noise' will not be the optimal initial condition overall. We can see in Fig 4.3 that by $t \approx 5 \times 10^{-3}$ growth is present across all initial conditions. It is important to note that 'white-noise' will not be the optimal initial condition in general, but in the case of a temperature profile that is linear when $t \to \infty$ one might expect that the fastest growing mode is sinusoidal. This is because when $t \to \infty$, the temperature profile is essentially linear with an infinitely large temperature gradient across the layer. We have described this problem earlier, and it is understood that sinusoidal disturbances grow the fastest. Foster (1965) also claims that 'white-noise' is the most reasonable assumption for an arbitrary initial disturbance and therefore 'white-noise' will be used in all succeeding calculations.

4.6.4 Defining an Instability Boundary in an Unconditionally Unstable System

It has been shown that, in a time-dependent linear stability analysis, the form of the initial conditions has a significant effect on the subsequent growth of the disturbances. We have deduced that 'white-noise' is a reasonable initial condition to proceed with as it leads to optimal growth compared to all initial conditions with individual Fourier modes.

Since all modes will grow at a super exponential rate, Foster (1965) assumes that the onset of instability can be characterised by the time when the averaged velocity disturbance has increased by factors between one and three orders of magnitude. Therefore, we define the nominal critical time, t_c, as the time for the average velocity growth to increase by a factor, $1, 10, 100$ or 1000.

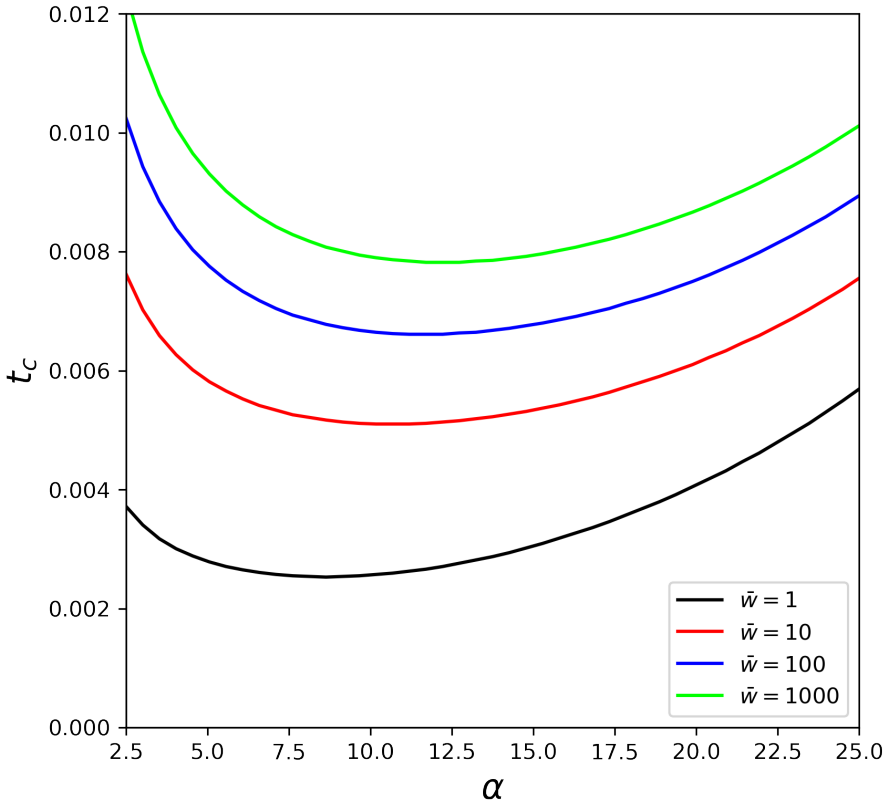

Figure 4.4: Critical time, t_c, versus wavenumber, α, for $Pr = 7, Ra = 10^8$.

Figure 4.4 shows the nominal critical time, t_c, versus wavenumber, α, for various amplification factors — the Rayleigh number and Prandtl number are fixed. It can be inferred from the minimum in t_c that there are optimal wavenumbers where convective instability sets in earliest. From Fig 4.4 we conclude that the minimum does not have a strong dependence on the amplification factor as the variation in the minimum, i.e., $\min(t_c)$ is insignificant as $\bar{w}$ is increased. As Foster (1965) points out, the theory predicts that, for a particular Rayleigh number, there is a particular wavenumber which will amplify the fastest; however it is shown in Fig 4.4 that the minima are not sharply defined. As such,

a range of wavenumbers will most likely be excited in an experimental setting. Nevertheless, Fig 4.4 demonstrates that the nominal critical time, t_c, is a reasonable measure of instability.

4.6.5 Ra Scaling with Critical Time t_c

Here we investigate the dependence of the Rayleigh number on the nominal critical time t_c. For a series of Rayleigh numbers, we solve Eqs (4.59)-(4.60), for fixed Prandtl and wavenumbers and calculate the critical time, t_c.

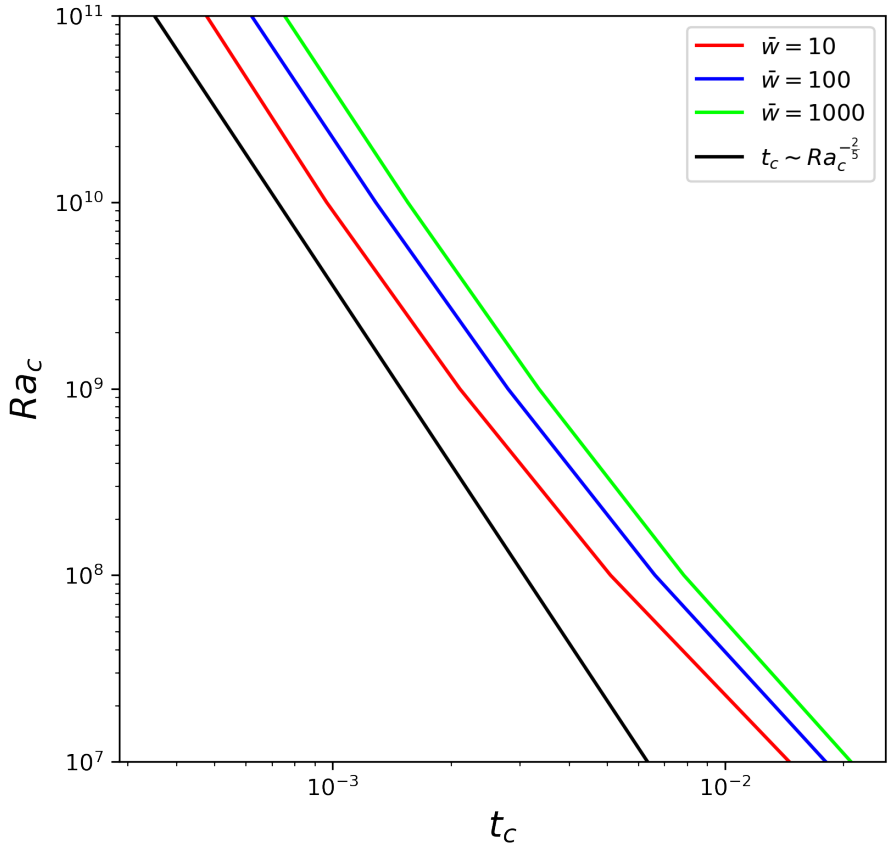

Figure 4.5: Ra versus t_c with $Pr = 7, \alpha = 11$. The nominal critical time is taken as the time taken for disturbances to grow by a factor of $1, 10, 100$, and 1000.

Figure 4.5 shows Ra_c as a function of t_c, plotted on logarithmic axes. For $Ra \gg 1$, $Ra_c \sim t_c^{-2/5}$ (illustrated by the solid black line). It can be seen in Fig (4.5) by the solid black line the Rayleigh number scales with the nominal critical time to the power $-\frac{2}{5}$. Foster (1965) observes that since time is non-dimensionalised with the thermal diffusive time, d^2/κ, and the effective Rayleigh number is proportional to d^5 (due to the definition of β), then in the limit of $Ra \gg 1$, the nominal critical time observed is independent of the plate separation.

4.7 Periodic Heating of the Basic State Temperature Distribution From Above and Below

Here, we investigate the linear stability of a more complicated time-dependent background temperature profile. We will consider a basic state temperature that is time-periodic, due to the periodic heating of the top and bottom boundaries. Numerous stability problems in mechanics involve oscillation of the basic state. Oscillation of the basic state has been found to have both a stabilising, and sometimes destabilising effect: the latter often being associated with the reduction of the problem to Mathieu's equation. Some pertinent references in the field of fluid mechanics are Benjamin and Ursell (1954), Roppo et al. (1984), Yih (1963), and the experimental works of Donnelly (1964). This section concerns RBC under the action of periodically modulated temperature boundaries. Similar problems have been considered previously by

- Venezian (1969), who studied small amplitude modulation using asymptotic methods;
- Rosenblat and Herbert (1970), who studied the linear stability where the modulation frequency is small, and the amplitude is finite;
- Rosenblat and Tanaka (1971) and Yih and Li (1972) who investigated the linear stability of a time-periodic temperature distribution that has finite amplitude and frequency.

In this section, we utilise the approach of Yih and Li (1972). We first validate and reproduce their results, then we extend the problem to unstudied asymptotic parameter regimes and study the linear stability through a combination of analytic and numerical techniques. We also further validate the results of Venezian (1969) through solving the linear system of equations numerically, in the regime where the modulation frequency is large.

4.7.1 The Basic Temperature Profile

We first introduce the basic state temperature profile. To be consistent with Yih and Li (1972) we consider a fluid layer between two fixed plates at $z = \pm d/2$. The temperature of the upper plate (at $z = d/2$) is maintained at $T_2 + T_3 \cos \omega^* t$ and the bottom plate (at $z = -d/2$) is maintained at $T_1 - T_3 \cos \omega^* t$, where ω^* is a frequency. We scale distances with d and time with d^2/κ, and the modulation frequency is scaled such that $\omega = \omega^* \kappa / d^2$. The representative temperature scale is chosen such that $T_0(z) = (\bar{T} - T_2)/(T_1 - T_2)$, where $\bar{T}$ is the dimensional temperature. In these units, the basic temperature satisfies

$$\frac{\partial T_0}{\partial t} = \frac{\partial^2 T_0}{\partial z^2}, \tag{4.63}$$

$$T_0\left(-\tfrac{1}{2}, t\right) = 1 - b \cos \omega t, \tag{4.64}$$

$$T_0\left(\tfrac{1}{2}, t\right) = b \cos \omega t, \tag{4.65}$$

where $b = T_3/(T_1 - T_2)$. The solution to Eqs (4.63)-(4.65) is given by

$$T_0(z,t) = \frac{1}{2} - z + bF(z,t), \tag{4.66}$$

where

$$F(z,t) = (B\cos\omega t - C\sin\omega t)\sinh\beta z\cos\beta z - (C\cos\omega t + B\sin\omega t)\cosh\beta z\sin\beta z, \tag{4.67}$$

with

$$B = -\sin\beta'\cos\beta'/(\sinh^2\beta' + \sin^2\beta'), \quad C = -B\tan\beta'\coth\beta', \tag{4.68}$$

$$\beta = \left(\frac{\omega}{2}\right)^{1/2}, \quad \beta' = \frac{1}{2}\beta. \tag{4.69}$$

4.7.2 The Linear System of Equations

In a similar vein to §4.4, we consider a modal linear stability analysis. Equations (4.18)-(4.19) given Eqs (4.66)-(4.69) yield

$$\left(\frac{1}{Pr}\frac{\partial}{\partial t} - (\mathcal{D}^2 - \alpha^2)\right)(\mathcal{D}^2 - \alpha^2)w = -Ra\alpha^2\theta, \tag{4.70}$$

$$\left(\frac{\partial}{\partial t} - (\mathcal{D}^2 - \alpha^2)\right)\theta = (1 + bF'(z,t))w, y \tag{4.71}$$

where $\alpha^2 = l^2 + k^2$, $\mathcal{D} = \partial/\partial z$, $F'(z,t) \equiv \partial F/\partial z$, and where the Rayleigh number is now scaled with the average temperature difference between the plates, i.e $Ra = g\alpha(T_0 - T_1)d^3/\kappa\nu$. We will consider both stress-free and no-slip boundary conditions, whereas Yih and Li (1972) consider only no-slip, fixed temperature boundaries. The time-periodic component of the basic temperature profile, $F(z,t)$ is spatially odd and therefore the z-derivative is even. The form of Eqs (4.70)-(4.71) allows for the solution to be split into odd and even categories. Yih and Li (1972) investigate the stability of even eigenfunctions only, with the justification that previous studies of classical, time-independent RBC have demonstrated that disturbances corresponding to even eigenfuctions (and hence odd cell numbers) are more unstable — the single-celled disturbance being the most unstable. While this is true in the case of steady RBC, when the basic temperature field evolves in time, this is not necessarily guaranteed. For completeness, we will also consider the linear stability of odd eigenfunctions, confirming whether odd eigenfunctions are more stable than their even counterparts.

4.7.3 Even Eigenfunctions for No-Slip Boundary Conditions

We first focus on even eigenfunctions and no-slip boundary conditions. It is helpful to introduce the expansions for w and θ

$$w = \sum_{n=0}^{\infty} A_n(t)\phi_n, \tag{4.72}$$

$$\theta = \sum_{n=0}^{\infty} B_n(t)\cos(2n+1)\pi z, \tag{4.73}$$

where ϕ_n is determined by the solution to the equation

$$(\mathcal{D}^2 - \alpha^2)\phi_n = \cos(2n+1)\pi z, \tag{4.74}$$

$$\phi_n\left(\pm\tfrac{1}{2}\right) = \mathcal{D}\phi_n\left(\pm\tfrac{1}{2}\right) = 0, \tag{4.75}$$

which results from substitution of Eqs (4.72)-(4.73) into Eq (4.70). The solution to Eqs (4.74)-(4.75) is

$$\phi_n = P_n\cosh\alpha z + Q_n z\sinh\alpha z + c_n^2\cos(2n+1)\pi z, \tag{4.76}$$

where

$$P_n = -(-1)^n((2n+1)\pi c_n^2\sinh\left(\tfrac{1}{2}\alpha\right))/(\alpha+\sinh\alpha), \tag{4.77}$$

$$Q_n = 2(-1)^n((2n+1)\pi c_n^2\cosh\left(\tfrac{1}{2}\alpha\right))/(\alpha+\sinh\alpha), \tag{4.78}$$

$$c_n = \frac{1}{(2n+1)^2\pi^2+\alpha^2}. \tag{4.79}$$

We then substitute Eqs (4.72)-(4.73) into Eqs (4.70)-(4.71), multiply each equation by $\cos(2m+1)\pi z$, and integrate over z to obtain an infinite set of coupled first order ODEs given by

$$\frac{2}{Pr}\sum_{n=0}^{\infty}\zeta_{mn}A_n'(t) - A_m(t) = -\alpha^2 RaB_m(t), \tag{4.80}$$

$$B_m'(t) + \frac{1}{c_m}B_m(t) = -2\sum_{n=0}^{\infty}(c_m\zeta_{mn} + b\lambda_{mn}\cos\omega t + b\xi_{mn}\sin\omega t)A_n(t), \tag{4.81}$$

where $m \in \mathbb{N}$ and

$$\zeta_{mn} = 8\alpha(-1)^{m+n}(2n+1)(2m+1)\pi^2 c_n^2 c_m\cosh^2\left(\tfrac{1}{2}\alpha\right)/(\alpha+\sinh\alpha) - \frac{1}{2}c_n\delta_{mn}, \tag{4.82}$$

where δ_{mn} is the Kronecker delta and λ_{mn}, ξ_{mn} are the solution to

$$\lambda_{mn}\cos\omega t + \xi_{mn}\sin\omega t = -\int_{-\frac{1}{2}}^{\frac{1}{2}} F'(z,t)\phi_n(z)\cos(2m+1)\pi z\mathrm{d}z. \tag{4.83}$$

Eqs (4.80)-(4.83) form an infinite system of linear ODEs which we will truncate at some

finite m and n in order to perform a linear stability analysis. The coefficients of Eqs (4.80)-(4.81) are either time-periodic or constant, and so we can make analytic progress with Floquet theory.

4.7.4 Floquet Theory and Defining A Stability Boundary

In a time-dependent linear stability analysis we can no longer perform an eigenmode analysis, and therefore one of the first hurdles we must overcome is to define a suitable stability boundary that is mathematically meaningful: this is often problem specific. In §4.6, the divergent basic temperature profile resulted in unconditional instability of the linear system: this leads to the natural choice of measuring the time taken for disturbances to be amplified by a suitable factor relative to the initial state. This is not the case for Eqs (4.80)-(4.83), which form a set of ODEs where the coefficients are either periodic or constant.

Since Floquet theory is involved heavily in the linear stability analysis, an overview is given, along with useful definitions. For a more in-depth discussion one should consult Coddington (1955); Grimshaw (1993); Ince (1927). Floquet theory is a powerful tool for solving ODEs in the particular form

$$\boldsymbol{x}' = \boldsymbol{A}(t)\boldsymbol{x}, \tag{4.84}$$

where $\boldsymbol{A}(t)$ is τ-periodic, and Eq (4.84) is a system of n equations. Then $\boldsymbol{x}$ takes the form

$$\boldsymbol{x}(t) \sim e^{\mu t}\boldsymbol{p}(t), \tag{4.85}$$

where $\boldsymbol{p}(t)$ is periodic with period τ. Additionally, there are n such μ, namely $\mu_1, \ldots, \mu_n$ which satisfy

$$e^{\mu_1 \tau} e^{\mu_2 \tau} \ldots e^{\mu_n \tau} = \exp\left\{\int_0^\tau \mathrm{Tr}(\boldsymbol{A}(s))\mathrm{d}s\right\}, \tag{4.86}$$

where Tr is defined as the trace. Now, we list a set of definitions and theorems which are necessary to proceed with the linear stability problem.

Definition (Fundamental Matrix): Let $\boldsymbol{x}^1(t), \ldots, \boldsymbol{x}^n(t)$ be n solutions of Eq (4.84). We define the matrix

$$\boldsymbol{X}(t) = \left[\left[\boldsymbol{x}^1\right], \ldots, \left[\boldsymbol{x}^n\right]\right], \tag{4.87}$$

where $\boldsymbol{X}$ satisfies $\boldsymbol{X}' = \boldsymbol{A}\boldsymbol{X}$. If $\boldsymbol{x}^1(t), \ldots, \boldsymbol{x}^n(t)$ are linearly independent, then $\boldsymbol{X}$ is non-singular and is called the *Fundamental Matrix*.

Lemma. We define the Wronskian $W(t)$ of $\boldsymbol{X}(t)$ as the determinant of $\boldsymbol{X}(t)$, and it is given by

$$W(t) = W(t_0)\exp\left\{\int_{t_0}^t \mathrm{Tr}(\boldsymbol{A}(s))\mathrm{d}s\right\}. \tag{4.88}$$

Theorem. Let $\boldsymbol{A}(t)$ be a τ-periodic matrix. If $\boldsymbol{X}(t)$ is a Fundamental Matrix, then so is

$\boldsymbol{X}(t+\tau)$ and there exists a non-singular constant matrix $\boldsymbol{B}$ such that

1. $\boldsymbol{X}(t+\tau) = \boldsymbol{X}(t)\boldsymbol{B}$ for all t;
2. $\det(\boldsymbol{B}) = \exp\{\int_0^\tau \mathrm{Tr}(\boldsymbol{A}(s))\mathrm{d}s\}$.

Definition (Characteristic Multipliers and Exponents): The eigenvalues $\rho_1, \ldots, \rho_n$ of $\boldsymbol{B}$ are called the characteristic multipliers for $\boldsymbol{X}' = \boldsymbol{A}\boldsymbol{X}$. The characteristic exponents (or Floquet multipliers) are $\mu_1, \ldots, \mu_n$ which satisfy

$$\rho_1 = e^{\mu_1 \tau}, \quad \rho_2 = e^{\mu_2 \tau}, \quad \ldots, \quad \rho_n = e^{\mu_n \tau}, \tag{4.89}$$

where μ_j may be complex. Furthermore, we know that

$$\boldsymbol{X}(t+\tau) = \rho_i \boldsymbol{X}(t) \quad \text{for } i = 1, \ldots, n. \tag{4.90}$$

The characteristic multipliers have the interesting properties:

- It is convenient to calculate the constant matrix $\boldsymbol{B}$ as $\boldsymbol{B} = \boldsymbol{B}\boldsymbol{X}(0)$ if $\boldsymbol{X}(0) = \mathcal{I}$, however, the product of the characteristic multipliers is equal to $\det(\boldsymbol{B}) = \Pi_i \rho_i$ always;
- The trace of $\boldsymbol{B}$ is the sum of the eigenvalues;
- The complex part of the characteristic exponents are not unique, since we can add any integer multiple of $2i\pi/\tau$;
- The characteristic multipliers ρ_i are an intrinsic property of the equation and do not depend on the choice of fundamental matrix.

Each characteristic multiplier will fall into one of the following categories

1. If $|\rho| < 1$ then $Re < 0$ and so $\boldsymbol{x}(t) \to 0$ as $t \to \infty$
2. If $|\rho| = 1$ then $R(\mu) = 0$ and so the solution is quasi-periodic
3. If $|\rho| > 1$, then $R(\mu) > 0$ and so $\boldsymbol{x}(t) \to \infty$ as $t \to \infty$

and hence a key point is that the solution to Eq (4.84) is stable if $|\rho_j| \leq 1$ for all j.

To relate this back to the linear system of equations, it is helpful to point out that Eqs (4.80)-(4.83) can be written in the form of Eq (4.84), and therefore, the Floquet exponents can be used to define a suitable stability boundary, which will separate exponentially growing and decaying periodic solutions. We truncate the series (4.72)-(4.73) to $M+1$ terms, yielding a total of $2M$ equations given by Eqs (4.80)-(4.81). The resultant $2M$ equations can be combined into one $2M$-th order ODE with $2M$ linearly independent solutions, which we denote by $G_n(t)$, where $n = 1, \ldots, 2M$. To be consistent with Yih

and Li (1972), we use the initial condition

$$G_n^{(k-1)}(0) = \delta_{nk},, \quad n,k = 1,\ldots,2M \tag{4.91}$$

$$\text{where} \quad G_n^{(k)}(t) = \frac{\mathrm{d}^k G_n}{\mathrm{d}t^k} \quad n = 1,\ldots,2M \quad k = 0,\ldots,2M. \tag{4.92}$$

We then generate a set of solutions at $t+\tau$ from the basis set of solutions which satisfy Eq (4.91), i.e. $\{G_1,\ldots,G_{2M}\}$, such that

$$G_n(t+\tau) = \sum_{m=1}^{2M} a_{mn} G_m(t), \tag{4.93}$$

where, from Eq (4.91),

$$a_{mn} = G_n^{(m-1)}(\tau). \tag{4.94}$$

Since the coefficients of Eqs (4.80)-(4.81) are periodic, we can use Floquet theory and therefore seek solutions of the form

$$U(t+\tau) = \rho U(t). \tag{4.95}$$

The solution $U(t)$ may be expressed as a linear combination of G_n, as the initial condition given by Eqs (4.91)-(4.92) ensures G_n are linearly independent. Then using the method described above, we then obtain the secular equation

$$\det\{G_n^{(k-1)}(\tau) - \rho\delta_{nk}\} = 0. \tag{4.96}$$

where ρ is the Floquet multiplier. Hence we can determine the Floquet exponents through $\rho = e^{\mu\tau}$.

4.7.5 Numerical Approach

Here, we give an overview of the numerical approach necessary for solving Eqs (4.80)-(4.83). We truncate Eqs (4.80)-(4.81) to $n = M+1$ and define the following vectors, $\boldsymbol{A} = (A_0, A_1, \ldots, A_{M+1})^T, \boldsymbol{B} = (B_0, B_1, \ldots, B_{M+1})^T$, such that

$$\boldsymbol{A}' = \frac{Pr}{2}\boldsymbol{\zeta A} - \frac{\alpha^2 RaPr}{2}\boldsymbol{\zeta B}, \tag{4.97}$$

$$\boldsymbol{B}' = -\boldsymbol{CB} - 2\boldsymbol{qA}, \tag{4.98}$$

where

$$\boldsymbol{\zeta} = \begin{pmatrix} \zeta_{0,0}^{-1} & \zeta_{0,1}^{-1} & \cdots & \zeta_{0,M+1}^{-1} \\ \zeta_{1,0}^{-1} & \zeta_{1,1}^{-1} & \cdots & \zeta_{1,M+1}^{-1} \\ \vdots & \vdots & \ddots & \vdots \\ \zeta_{M+1,0}^{-1} & \zeta_{M+1,1}^{-1} & \cdots & \zeta_{M+1,M+1}^{-1}, \end{pmatrix}, \; \boldsymbol{q}(t) = \begin{pmatrix} q_{0,0} & q_{0,1} & \cdots & q_{0,M+1} \\ q_{1,0} & q_{1,1} & \cdots & q_{1,M+1} \\ \vdots & \vdots & \ddots & \vdots \\ q_{M+1,0} & q_{M+1,1} & \cdots & q_{M+1,M+1} \end{pmatrix}, \tag{4.99}$$

$$\boldsymbol{C} = \begin{pmatrix} \frac{1}{c_0} & 0 & \cdots & 0 \\ 0 & \frac{1}{c_1} & \cdots & 0 \\ \vdots & \vdots & \ddots & \vdots \\ 0 & 0 & \cdots & \frac{1}{c_{M+1}} \end{pmatrix}, \tag{4.100}$$

where the elements q_{mn} are given by,

$$q_{mn}(t) = c_m \zeta_{mn} + b\lambda_{mn} \cos \omega t + b\xi_{mn} \sin \omega t, \tag{4.101}$$

with ζ_{mn}, ξ_{mn}, and λ_{mn} given by Eqs (4.82)-(4.83). We define the solution vector $\boldsymbol{G} = (A_0, \ldots, A_N, B_0, \ldots B_{M+1})^T$, and then from this construct the system

$$\boldsymbol{G}' = \mathcal{P}\boldsymbol{G}, \tag{4.102}$$

where $\mathcal{P}$ is a time-periodic matrix such that

$$\mathcal{P} = \begin{pmatrix} \frac{Pr}{2}\boldsymbol{\zeta} & -\frac{\alpha^2 RaPr}{2}\boldsymbol{\zeta} \\ -2\boldsymbol{q} & \boldsymbol{M} \end{pmatrix}. \tag{4.103}$$

To calculate the Floquet multipliers we must calculate a Fundamental Matrix. Using the Theorem detailed in §4.7.4, we know that

$$\boldsymbol{G}(t+\tau) = \boldsymbol{G}(t)\boldsymbol{B}, \tag{4.104}$$

where the eigenvalues of $\boldsymbol{B}$ are the Floquet multipliers. We calculate $\boldsymbol{B}$ through

$$\boldsymbol{B} = \boldsymbol{G}^{-1}(0)\boldsymbol{G}(\tau), \tag{4.105}$$

where the initial conditions given by Eqs (4.91)-(4.92) are chosen such that

$$\boldsymbol{G}^{-1}(0) = \boldsymbol{G}(0) = \mathcal{I}, \tag{4.106}$$

where $\mathcal{I}$ is the identity. It can be seen from Eqs (4.105)-(4.106) that only the solution at $t = \tau$ is needed. To ensure we have a set of linearly independent solutions, we integrate Eq (4.102) subject to the set of initial conditions

$$\boldsymbol{G}(0) = \{(1, 0, \ldots, 0), (0, 1, \ldots, 0), (0, 0, \ldots, 1)\}, \tag{4.107}$$

using a fourth-order Runge-Kutta iteration scheme. At the onset of instability, we know $\rho = \pm 1$, where the sign is decided by $\mu_i = 0, \pm i\pi$. To calculate neutral stability curves, we seek solutions to

$$|R\{\rho(Ra, \alpha, Pr, \omega, b)\}| - 1 = 0, \tag{4.108}$$

using Newton's method. To find the critical parameter values, we will use the Nelder-Mead method.

4.7.6 The First Truncation Limit and the Relation to the Mathieu Equation

The damped Mathieu equation is a particular case of a more general periodic ODE named Hills equation, and is given by

$$\frac{d^2x}{dt^2} + c\frac{dx}{dt} + (\delta + \varepsilon\cos t)x(t) = 0, \tag{4.109}$$

where c is a damping coefficient, δ an amplitude, and ε a small perturbation. Although it is not always possible to reduce the linear system with periodic coefficients to the Mathieu/Hill equation, it is often the case. That is to say, it is not unusual for stability problems in mechanics, where the basic state oscillates in time, to be associated with a reduction to the Mathieu equation (Yih and Li, 1972). Yih and Li (1972) did not relate any characteristics of their results to the Mathieu equation. However we shall see that this problem shares many similarities with, and to a first approximation, reduces exactly down to Mathieu's equation. In the truncated system (4.80)-(4.81) (to a first approximation, i.e., $M = 0$) substitution of $B_0'(t)$, $B_0(t)$ in terms of $A_0''(t)$, $A_0'(t)$, and $A_0(t)$ leads to the second order ODE

$$A_0''(t) - \left(\frac{\sigma}{2\zeta_{00}} - \frac{1}{c_0}\right)A_0'(t) \\ - \frac{\sigma}{\zeta_{00}}\left(\frac{1}{2c_0} + \alpha^2 Ra(c_0\xi_{00} + b\lambda_{00}\cos(\omega t) + b\xi_{00}\sin(\omega t)\right)A_0(t) = 0, \tag{4.110}$$

which is analogous to the damped Mathieu equation (4.109) with the transformations

$$c = -\left(\frac{Pr}{2\zeta_{00}} - \frac{1}{c_0}\right), \tag{4.111}$$

$$\delta = -\left(\frac{Pr}{2c_0\zeta_{00}} + Pr\alpha^2 Rac_0\right), \tag{4.112}$$

$$\varepsilon = -\frac{Pr}{\zeta_{00}}\alpha^2 Rab\sqrt{\lambda_{00}^2 + \xi_{00}^2}\cos(\omega t - \alpha), \tag{4.113}$$

$$\alpha = \arctan\left(\frac{\lambda_{00}}{\xi_{00}}\right), \tag{4.114}$$

The (damped) Mathieu equation has been studied extensively both analytically and numerically, and its associated stability properties are well documented (see Kovacic et al.,

2018). An interesting result which is relevant to this work is the existence of Arnold tongues in phase space (see Ecke et al., 1989). Arnold tongues are neutral stability curves: solutions to the Mathieu equation are unstable when the parameters lie above these curves. To determine the Arnold tongues, we numerically solve the Mathieu equation for a series of damping coefficients, and produce neutral stability curves in (δ, ε) space.

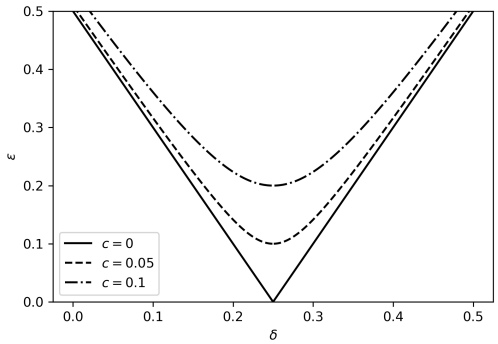

(a) Analytic approximations to the leading order transition curve for Mathieu's equation for three different values of damping. This approximation is valid in the regime where $c = \mathcal{O}(\varepsilon)$.

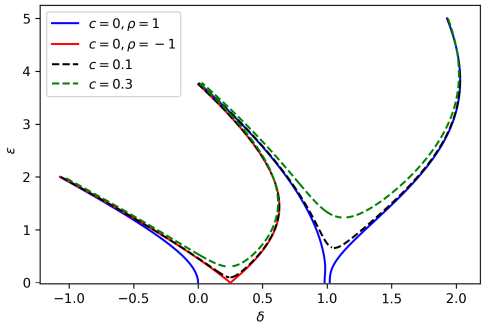

(b) The first few transition curves for various values of damping. The red and blue lines correspond to solutions with periods of 4π and 2π respectively.

Figure 4.6

Figure 4.6 illustrates the nature of these tongues. Figure 4.6a compares marginal stability curves for multiple values of c, the damping coefficient. These marginal stability curves were obtained through an asymptotic analysis of the Mathieu equation, for $\varepsilon \ll 1$ which is shown in Appendix B. Figure 4.6b compares multiple neutral stability curves for various damping coefficients, in a regime where asymptotic analysis to leading order is not valid, and therefore they are obtained numerically: here, multiple neutral stability curves are shown to illustrate the previously mentioned Arnold tongues. It can be seen in Figs 4.6 that when the damping coefficient is non-zero, the tongues become detached from the x-axis. The red curve shown in Fig 4.6b is the same as the solid black curve shown in Fig 4.6a: the difference in appearance is a matter of scale, as the asymptotic analysis is only valid when $c = \mathcal{O}(\varepsilon)$. It is possible to analytically produce the curves shown in Fig 4.6a, however one would need to include higher order terms in the asymptotic analysis. It is important to note that even though Fig 4.6b shows only two Arnold tongues, infinitely many are possible, with the pattern extending throughout phase space. Since to a first approximation (we only include A_0, B_0, i.e., $M = 0$) Eqs (4.80)-(4.83) can be reduced to the Mathieu equation, we would expect to see similar patterns. Despite being unable to reduce higher order approximations (truncating the series (4.72)-(4.73) to $M > 1$) to a series of 'Mathieu-like' equations, we are able to see Arnold tongues even for higher approximations. We know that the onset of stability occurs when $\rho = \pm 1$ and so we fix b, ω, and Pr, and study how the Floquet multipliers vary when we change Ra and α.

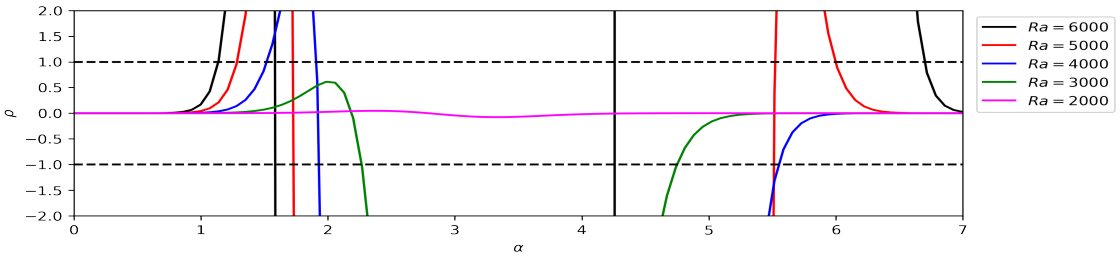

Figure 4.7: The largest Floquet multiplier as a function of α for a series of Rayleigh numbers. Here $b = 0.62, Pr = 0.75$, $\omega = 5$, and we consider the second approximation, i.e., $M = 2$.

Figure 4.7 shows the behaviour of the largest Floquet multiplier as a function of wavenumber. It can be seen that there are multiple instances when the Floquet multipliers are equal to ± 1. This means there are multiple values of wavenumber which are marginally stable. The multiple roots to Eq (4.108) shown in Fig 4.7 are indicative of Arnold tongues. The magenta curve in Fig 4.7 show that for Ra sufficiently small, the modulus of the Floquet multipliers, $|\rho|$ remains less than unity for $0 \leq \alpha \leq 7$ — this implies that, for example, all wavenumbers in this range are stable for $Ra = 2000$.

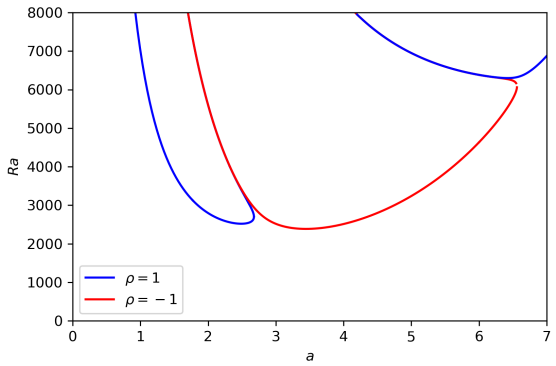

(a) $b = 0.60$

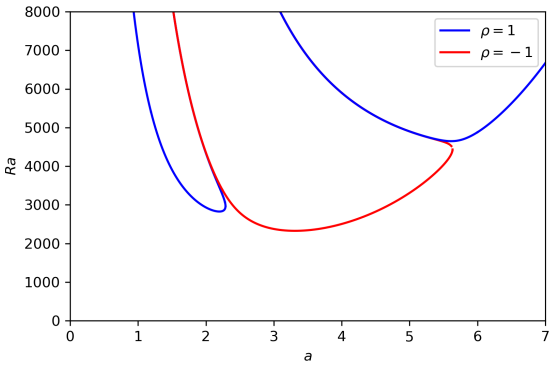

(b) $b = 0.62$

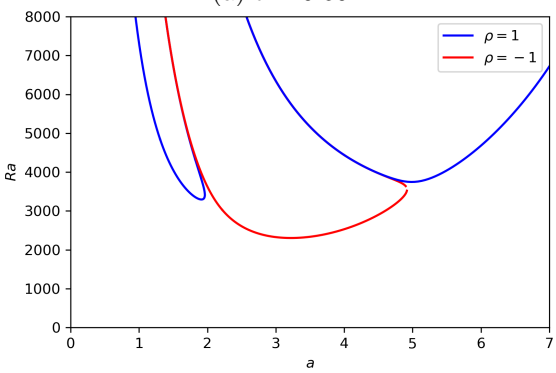

(c) $b = 0.64$

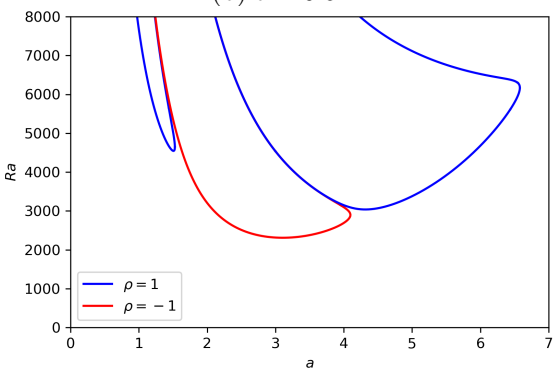

(d) $b = 0.67$

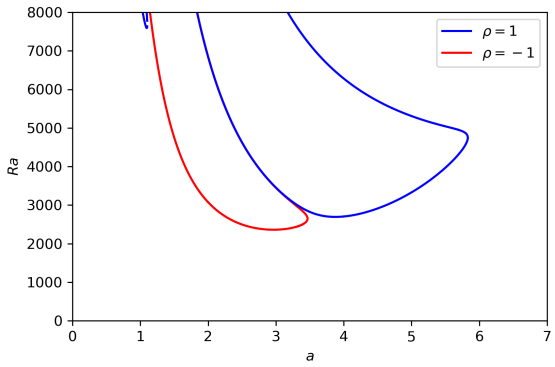

(e) $b = 0.70$

Figure 4.8: Neutral stability curves in (Ra, α) space for various values of b; red curves have $\rho = -1$ and blue curves have $\rho = 1$. Here $Pr = 0.73, \omega = 5$.

Figure 4.8 shows neutral stability curves in (Ra, α) space for various values of b: the blue curve corresponding to roots where $\rho = 1$ and red curves corresponding to $\rho = -1$. It is important to note that Fig 4.8 shows only the first three tongues; this pattern continues as $\alpha \to \infty$. An important feature of Fig 4.8 is that the two branches $\rho = \pm 1$ approach an asymptotic limit in which they do not touch — in between the red and blue curves are thin regions of stability. Comparison of Figs 4.8a, 4.8e shows that when b is increased, the region of instability moves to higher Rayleigh numbers and becomes narrower. Furthermore, it is shown in Fig 4.8 that there are multiple local minima. It can be discerned from the variation in the local minima relative to one another, that eventually, the global minimum will lie on the blue curve. The existence of multiple neutral stability curves therefore presents several challenges in calculating the critical parameter values. We employ a

combination of numerical continuation and multiple direct searches to ensure convergence to the global minimum. Finally, it is important to note that when $\rho = 1$, the disturbances are synchronous (S): that is to say, the perturbation has the same period as the time-dependent part of the temperature field. When $\rho = -1$, the perturbations are half-synchronous (H) with half the period of the temperature field.

4.7.7 Increasing the Order of Approximation

Possibly because of computational resources available at the time, Yih and Li (1972) investigated only up to a second approximation — i.e., they truncate the linear system at $M = 0$ and therefore solve four 1^{st} order ODEs. Yih and Li (1972) show that the first approximation provides results that are different to the second approximation, thus concluding the first approximation is not sufficient. Here, we will calculate the critical Rayleigh number as we vary b for a fixed Prandtl number, Pr, and frequency, ω. We will reproduce the results of Yih and Li (1972) and go a step further, truncating at higher values of M to determine whether the second approximation is sufficiently converged.

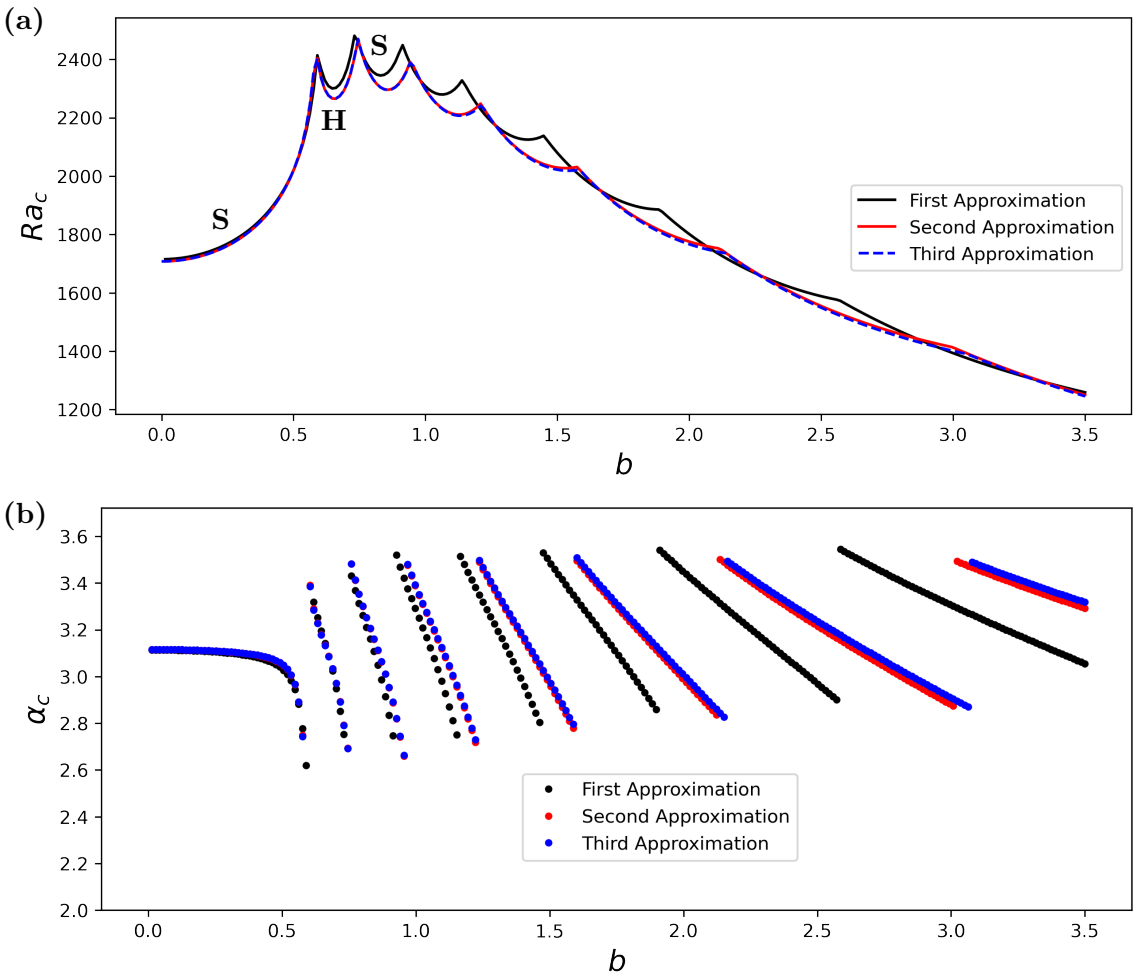

Figure 4.9: (a) The critical Rayleigh number and (b) the critical wavenumber as functions of the forcing amplitude b. Here $\omega = 5, Pr = 0.73$, S (Synchronous) and H (Half-Synchronous) correspond to the global minimum existing on the $\rho = 1, -1$ branch respectively, and alternate.

Figure 4.9 shows the critical Rayleigh number and wavenumber against b for multiple levels of approximation (various M). It can be seen that the second approximation ($M = 1$) for this range of forcing amplitude is sufficient. There is very little difference between the critical Rayleigh and wavenumbers between the second ($M = 1$) and third ($M = 2$)

approximations. An important feature of Fig 4.9 is the alternate overlapping of periodic (S) and half periodic (H) cusps described in §4.7.6. It is important to note that these cusps are independent curves and continue after they intersect; that is to say when periodic disturbances are unstable, solutions which are half-periodic can be stable or unstable and vice versa. The exchange of global minima can be seen by the discontinuous curves in Fig 4.9(b) — this switching is a consequence of the Arnold tongues moving through (Ra, α) space as b is varied. When $b = 0$ we just have a steady linear temperature gradient between the plates and therefore we expect to recover the result for the classical no-slip RBC problem discussed in Chandrasekhar (1961). Table 4.1 is a comparison of the theoretical value to numerical calculations for varying levels of approximation.

Approximation	Ra_c
First	1715.1
Second	1707.9
Third	1707.8

Table 4.1: The critical Rayleigh number in the classical limit when $b = 0, Pr = 0.73$ for varying levels of approximation. The theoretical value is 1707.8 (Chandrasekhar, 1961).

Table 4.1 shows that as the order of approximation is increased, the numerical calculation tends towards the classical result for a linear temperature field. It is found that, by the third approximation, there is agreement to the first decimal place. Figure 4.9(a) shows that for $b < 0.6$, increasing b leads to a more stable background temperature distribution as the critical Rayleigh number increases. However, increasing b above $b = 0.6$ generally leads to a destabilising effect as the critical Rayleigh number becomes smaller. It can be seen in Fig 4.9(a) that at a certain value of $b \approx 2$, the temperature distribution becomes more unstable than the classical case ($b = 0$). Figure 4.9(b) illustrates that the critical wavenumber generally exists within the range $2.6 \leq \alpha_c \leq 3.6$, with this range of critical wavenumber remaining roughly constant with increasing b.

4.7.8 Odd Eigenmodes for No-Slip Boundary Conditions

Yih and Li (1972) consider only even eigenfunctions with the justification that in classical RBC, single cell disturbances exhibit instability at a lower Rayleigh number than disturbances with more cells. While this is true in classical RBC, in the case of temperature modulation, and in the more general case of a time-dependent temperature profile, we are far from classical RBC and so there is no evidence to suggest this is still true. We briefly consider odd eigenfunctions and determine if they behave qualitatively the same as their even counterparts and if they become unstable for larger values of Ra. We follow a similar

procedure as in §4.7.2; however, we expand θ and w as follows:

$$\theta = \sum_{n=0}^{\infty} B_n(t)\sin((2n+2)\pi z), \tag{4.115}$$

$$w = \sum_{n=0}^{\infty} A_n(t)\phi_n(z), \tag{4.116}$$

where ϕ_n is determined by the solution to the equation

$$(\mathcal{D}^2 - \alpha^2)^2\phi_n = \sin(2(n+1)\pi z), \tag{4.117}$$

$$\phi(\pm\tfrac{1}{2}) = 0, \quad \mathcal{D}\phi(\tfrac{1}{2}) = 0, \tag{4.118}$$

which results from substitution of Eqs (4.115)-(4.116) into Eq (4.70). The solution to Eqs (4.117)-(4.118) are

$$\phi_n = P_n\sinh(\alpha z) + Q_n z\cosh(\alpha z) + c_n^2\sin((2n+2)\pi z), \tag{4.119}$$

$$\text{where} \quad P_n = -2(-1)^{n+1}(n+1)\pi c_n^2\cosh(\alpha/2)/(\alpha - \sinh(\alpha)), \tag{4.120}$$

$$Q_n = 4(-1)^{n+1}(n+1)\pi c_n^2\sinh(\alpha/2)/(\alpha - \sinh(\alpha)), \tag{4.121}$$

$$\text{and} \quad c_n = \frac{1}{4(n+1)^2\pi^2 + \alpha^2}. \tag{4.122}$$

We substitute Eqs (4.115)-(4.116) into Eqs (4.70)-(4.71), multiply the resulting equations by $\sin((2m+2)\pi z)$, and integrate over z. This results in the infinite set of equations:

$$\frac{2}{Pr}\sum_{n=0}^{\infty}\zeta_{mn}A_n'(t) - A_m(t) = -\alpha^2 Ra B_m(t), \tag{4.123}$$

$$B_m'(t) + \frac{1}{c_m}B_m(t) = -2\sum_{n=0}^{\infty} q_{mn}(t)A_n(t), \tag{4.124}$$

where $m \in \mathbb{N}$ and,

$$q_{mn}(t) = c_m\zeta_{mn} + b\psi_{mn}\cos(\omega t) + b\gamma_{mn}\sin(\omega t), \tag{4.125}$$

with

$$\zeta_{mn} = (-1)^{m+n+1}32\alpha(n+1)(m+1)\pi^2 c_n^2 c_m\frac{\sinh^2(a/2)}{(a-\sinh(a))} - \frac{1}{2}c_n\delta_{mn}; \tag{4.126}$$

δ_{mn} is the Kronecker delta, and ψ_{mn} and γ_{mn} are defined by

$$\psi_{mn}\cos(\omega t) + \gamma_{mn}\sin(\omega t) = \int_{-\frac{1}{2}}^{\frac{1}{2}} F'(z,t)\sin[(2m+2)\pi z]\phi_n(z)\mathrm{d}z. \tag{4.127}$$

Again, we use Floquet theory and look for the critical Rayleigh number and wavenumbers for a fixed Prandtl and frequency as we vary the forcing amplitude.
Figure 4.10 shows that odd disturbances lead to patterns similar to those shown in Fig 4.9,

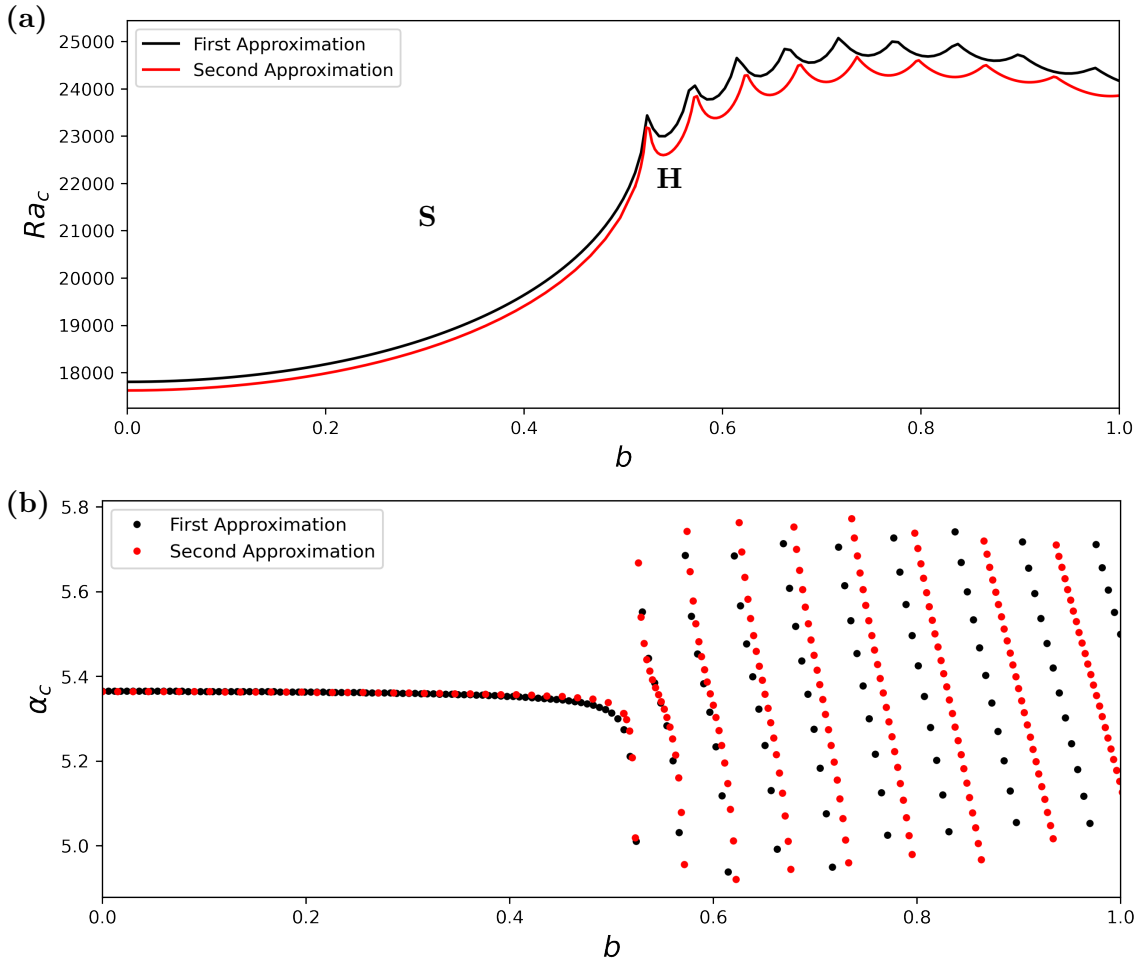

Figure 4.10: (a) The critical Rayleigh number and (b) the critical wavenumber as a function of forcing amplitude, b. Here $\omega = 5, Pr = 0.73$, S (Synchronous) and H (Half-Synchronous) correspond to the global minimum existing on the $\rho = 1, -1$ branch respectively.

however it is shown that the second approximation is quite different to the first approximation even for $b = 0$ — the black and red curves deviate from one another for all b and, for larger values of b, become almost out of phase with one another. Figure 4.10 illustrates that the alternating cusps are more frequent. Again, we see an initially destabilising effect as the amplitude is increased. As the amplitude is increased further, the effect of the temperature modulation starts to inhibit stability. Table 4.2 compares the classical value of Ra_c from Chandrasekhar (1961) to the numerical calculations in Fig 4.10 for $b = 0$.

Approximation	Ra_c
First	17803.24
Second	17621.74
Third	17611.84
Fourth	17610.68
Fifth	17610.47

Table 4.2: The critical Rayleigh number in the classical limit when $b = 0, Pr = 0.73$ for varying levels of approximation. The theoretical value for odd-disturbances is given by 17610.39 (Chandrasekhar, 1961).

Table 4.2 shows that when $b = 0$ we recover the classical results of RBC: there is excellent agreement with that of Chandrasekhar (1961) for the classical case of RBC for odd solutions for a high level of approximation. Figure 4.10(a) shows that, as b is increased, the critical Rayleigh number becomes significantly larger than that of the even disturbances shown in Fig 4.10(a). Comparison of Figs 4.9(a), 4.10(b) illustrates that even disturbances are more susceptible to instability. In this case, they are the preferred mode of instability when compared with odd disturbances, consistent with the claim of Yih and Li (1972).

4.7.9 Even Eigenfunctions for Stress-Free Boundary Conditions

Yih and Li (1972) consider only the case of no-slip, fixed temperature boundary conditions for the perturbed quantities. For completeness, we perform a brief analysis using the same methods in §4.7.2 but for stress-free, fixed temperature boundary conditions,

$$w = \frac{\mathrm{d}^2 w}{\mathrm{d}z^2} = \theta = 0. \tag{4.128}$$

The boundary conditions suggest that we can seek solutions of the form

$$w_n, \theta_n \sim \cos(2n+1)\pi z. \tag{4.129}$$

We therefore perform a modal expansion on w and θ, where

$$w(z,t) = \sum_{n=0}^{\infty} A_n(t) c_n^2 \cos(2n+1)\pi z, \tag{4.130}$$

$$\theta(z,t) = \sum_{n=0}^{\infty} B_n(t) \cos(2n+1)\pi z, \tag{4.131}$$

where $c_n = 1/((2n+1)^2\pi^2 + \alpha^2)$. We substitute Eqs (4.130)-(4.131) into Eqs (4.70)-(4.71), multiply by $\cos(2m+1)\pi z$, and integrate between $z = \pm 1/2$, which yields the infinite set

of ODEs:

$$\frac{c_m}{Pr}A'_m(t) + A_m(t) = -\alpha^2 Ra B_m(t), \tag{4.132}$$

$$B'_m(t) + \frac{1}{c_m}B_m(t) = c_m^2 A_m(t) - 2\sum_{n=0}^{\infty}(b\psi_{mn}\sin\omega t + b\lambda_{mn}\cos\omega t)A_n(t), \tag{4.133}$$

where $m \in \mathbb{N}$ with

$$\psi_{mn}\cos(\omega t) + \gamma_{mn}\sin(\omega t) = \int_{-1/2}^{1/2} F'(z,t)\cos((2m+2)\pi z)\phi_n(z)\mathrm{d}z. \tag{4.134}$$

We utilise Floquet theory and the numerical methods outlined in §4.7.5 to solve Eqs (4.132) - (4.133) for a fixed Pr, ω, and determine the critical Rayleigh number and wavenumbers for varying forcing amplitude. Figure 4.11 is analogous to Figs 4.9 and

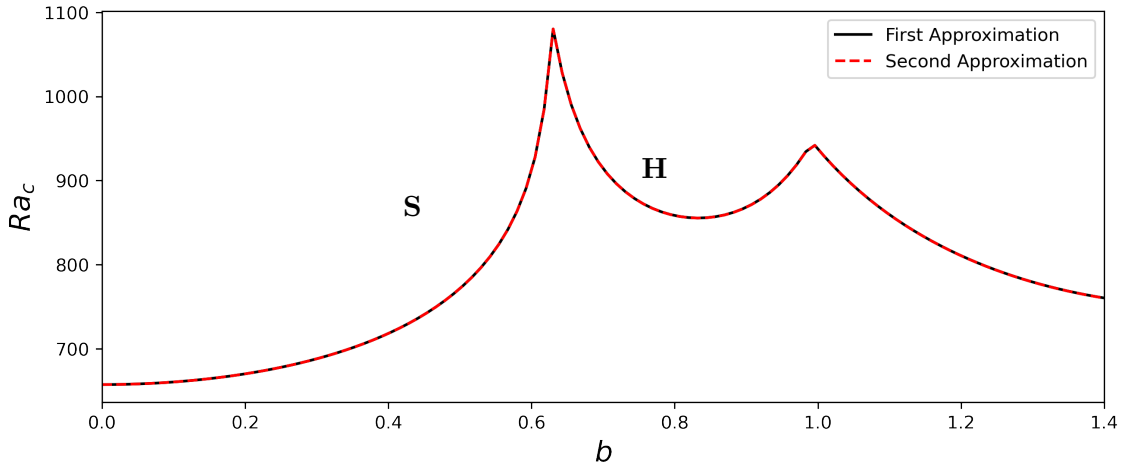

Figure 4.11: (a) The critical Rayleigh number and (b) the critical wavenumber as a function of forcing amplitude, b. Here $\omega = 5$, $Pr = 0.73$; S (Synchronous) and H (Half-Synchronous) correspond to the global minimum existing on the $\rho = 1, -1$ branch respectively.

4.10. When $b = 0$ we expect to recover the classical limit, and we compare the values from numerical calculations for various approximations to the results of Chandrasekhar (1961).

Approximation	Ra_c
First	657.5113644795164
Second	657.5113644795163

Table 4.3: The critical Rayleigh number in the classical limit when $b = 0, Pr = 0.73$ for varying levels of approximation. The theoretical value for stress-free boundary conditions $Ra_c \approx 657.5113644795163$ (Chandrasekhar, 1961).

It is shown in Table 4.3 that the first approximation is excellent and is sufficient in reproducing the theoretical value of Ra_c. It is clear that there is good agreement between this

system when $b = 0$ and the classical theory.

4.7.10 The Regime $b \gg 1$, the Large Forcing Limit for No-slip Boundary Conditions

In the previous subsections of §4.7, the parameters b, ω, and Pr have all been assumed to be moderate values of order unity. Here, we consider the limit when $b \gg 1$, which is an unexplored asymptotic regime in the context of this problem. When $b \to \infty$, the amplitude of the temperature modulation is dominant, and the effect of the steady linear component of negligible. Therefore, when $b \gg 1$, the basic state temperature distribution can be approximated by

$$T(z,t) \approx bF(z,t), \tag{4.135}$$

where $F(z,t)$ is given by Eqs (4.66)-(4.69). Equations (4.70)-(4.66) become

$$\left(\frac{1}{Pr}\frac{\partial}{\partial t} - (\mathcal{D}^2 - \alpha^2)\right)(\mathcal{D}^2 - \alpha^2)w = -\alpha^2 Ra\theta, \tag{4.136}$$

$$\left(\frac{\partial}{\partial t} - (\mathcal{D}^2 - \alpha^2)\right)\theta = -bF'(z,t)w. \tag{4.137}$$

Using the scaling:

$$Ra = \widetilde{Ra}/b, \tag{4.138}$$

$$w = \widetilde{w}, \tag{4.139}$$

$$\theta = b\widetilde{\theta}, \tag{4.140}$$

Eqs (4.136)-(4.137) become

$$\left(\frac{1}{Pr}\frac{\partial}{\partial t} - (\mathcal{D}^2 - \alpha^2)\right)(\mathcal{D}^2 - \alpha^2)\widetilde{w} = -\alpha^2\widetilde{\theta}\widetilde{Ra}, \tag{4.141}$$

$$\left(\frac{\partial}{\partial t} - (\mathcal{D}^2 - \alpha^2)\right)\widetilde{\theta} = -F'(z,t)\widetilde{w}, \tag{4.142}$$

which are independent of b. If we fix the Prandtl number and frequency, then we can solve Eqs (4.141)-(4.142) for the critical Rayleigh number and wavenumber in the new scaling. This should be equivalent to solving the full system given by Eqs (4.70)-(4.71) when $b \gg 1$. From Eq (4.138), the critical Rayleigh number calculated from Eqs (4.70)-(4.71) should scale with $1/b$.

To test this hypothesis, we fix the Prandtl number such that $Pr = 0.73$ and solve Eqs (4.141)-(4.142) for two values of ω and determine the critical Rayleigh number in the new scaling, $\widetilde{Ra}_c$. We then calculate the critical Rayleigh number in the old scaling (i.e., for Eqs (4.70)-(4.71)) for a range of $b \gg 1$. We then compare the numerical results from Eqs (4.70)-(4.71) to the prediction given by Eq (4.138).

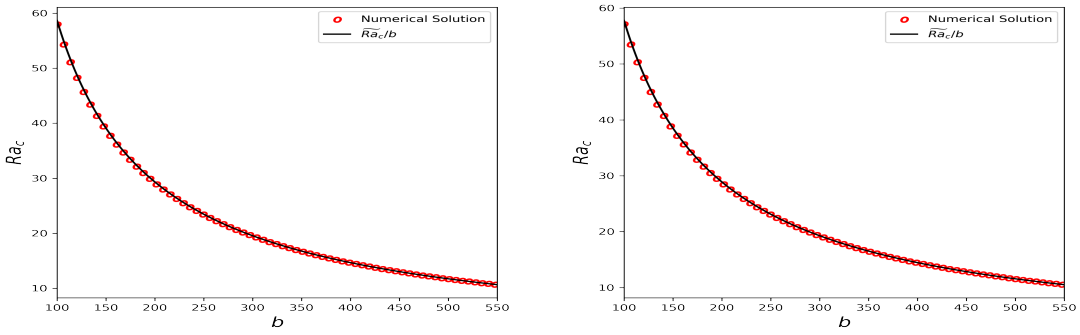

(a) (b)

Figure 4.12: Critical Rayleigh number versus b for (a) $\omega = 7$, $\widetilde{Ra} \approx 5867.4$, and (b) $\omega = 12$, $\widetilde{Ra} \approx 5779.5$; Here $Pr = 0.73$.

Figures 4.12 compares the neutral stability curves for the full linear problem to the scaling predicted by Eqs (4.138)-(4.140). It can be seen that the scaling predicted by Eqs (4.138)-(4.140) is accurate. More precisely, we can see in Fig 4.12 that, when $b \gg 1$, $Ra_c = \widetilde{Ra}_c/b$, where $\widetilde{Ra}_c$ is determined by optimising over α for a fixed frequency and Prandtl number in the re-scaled problem given by Eqs (4.141)-(4.142). From a computational perspective, this is an important result. It means that, in the regime where $b \gg 1$, it is not necessary to optimise over (Ra, α) for a given b, which as we have seen, can be an involved process which involves optimising across multiple local minima in which the global minimum switches position. Instead, we solve the re-scaled problem for a given Prandtl number and frequency, and therefore determine the critical Rayleigh number. From a physical perspective, this result demonstrates that any system can be destabilised if the periodic heating is sufficiently strong since $Ra_c \to 0$ as $b \to \infty$ for all finite Pr and ω.

4.7.11 Varying Frequency and the Regime $\omega \to \infty$ for No-slip Boundary Conditions

The last piece of this puzzle we will consider is varying the frequency, ω, for a fixed b. Here, we perform a brief parameter survey in ω by calculating the critical Rayleigh number as a function of b for multiple values of ω.

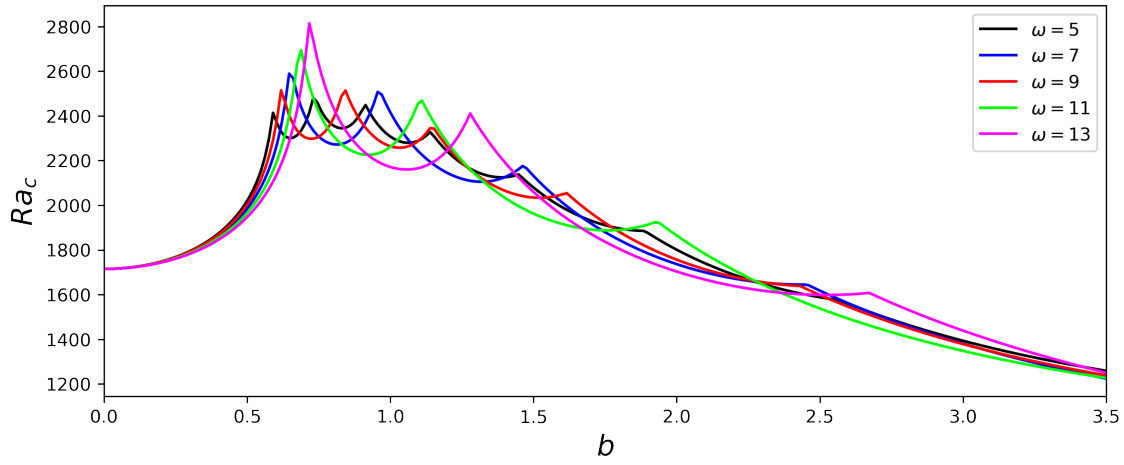

(a)

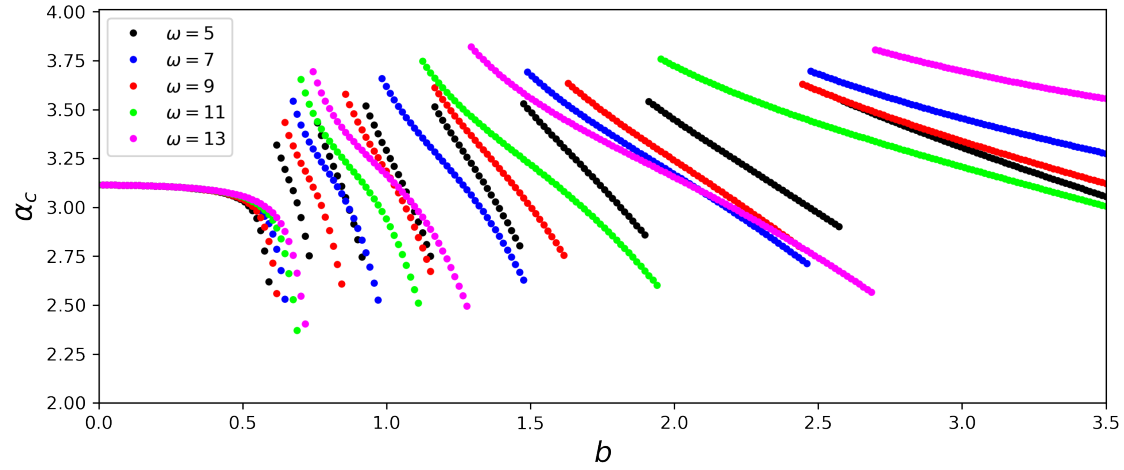

(b)

Figure 4.13: (a) The critical Rayleigh number and (b) the critical wavenumber as a function of b, for multiple values of ω; here $Pr = 0.73$, S (Synchronous) and H (Half-Synchronous) correspond to the global minimum existing on the $\rho = 1, -1$ branch respectively.

Figure 4.13b illustrates that despite the range of wave numbers not changing significantly, increasing the frequency increases the amount of intersections between periodic and half-periodic branches, i.e the amount of cusps shown in Fig 4.13a. Comparison of the black and magenta lines in Fig 4.13a shows that for $\omega = 5$ there are eight exchanges between (H) and (S) branches, while for $\omega = 13$ there are only four, for the range of b considered.

Now we consider in the regime where $\omega \gg 1$ for order unity values of Pr and b. Venezian

(1969) explored this parameter regime for an arbitrarily small forcing amplitude using asymptotic methods. He performed a series expansion around the classical critical Rayleigh number and was able to show that when $\omega \gg 1$ the second order correction to the classical Rayleigh number ($Ra_c^{(2)}$) tends to zero as the frequency tends to infinity, i.e. $\lim_{\omega\to\infty} Ra_c^{(2)} = 0$. Venezian (1969) states that when $\omega \gg 1$, the diffusion equation admits a boundary layer near the top and bottom plates at $z = \pm 1/2$. To illustrate this boundary layer, we separate $T(z,t)$ into a steady and a time-dependent part, i.e. $T(z,t) = T_0(z) + T_1(z,t)$. The steady part is the solution to

$$\frac{\mathrm{d}^2 T_0}{\mathrm{d}z^2} = 0, \tag{4.143}$$

$$T_0\left(-\tfrac{1}{2}\right) = 1, \quad T_0\left(\tfrac{1}{2}\right) = 0, \tag{4.144}$$

which has solution $T_0(z) = \frac{1}{2} - z$. The non-steady part is the solution to

$$\frac{\partial T_1}{\partial t} = \frac{\partial^2 T_1}{\partial z^2}, \tag{4.145}$$

$$T_1\left(-\tfrac{1}{2}, t\right) = -b\cos\omega t, \quad T_1\left(\tfrac{1}{2}\right) = b\cos\omega t. \tag{4.146}$$

We define a new timescale $\tau = \omega t$. Then, using $\Theta_1(z,\tau) = T_1(z,t)$, Eqs (4.145)-(4.146) become

$$\frac{\partial \Theta_1}{\partial \tau} = \epsilon \frac{\partial^2 \Theta_1}{\partial z^2}, \tag{4.147}$$

$$\Theta_1\left(-\tfrac{1}{2}, \tau\right) = -b\cos\tau, \quad \Theta_1\left(\tfrac{1}{2}, \tau\right) = b\cos\tau, \tag{4.148}$$

where $\epsilon = 1/\omega$. This is a typical boundary value problem if $\varepsilon \ll 1$, and, by rescaling in z and using Van-Dykes principle of least degeneracy (see Dyke, 1975), one can show that there is a boundary layer of width $\mathcal{O}(1/\sqrt{\omega})$, which is consistent with Venezian (1969). When $\omega \gg 1$, the basic state temperature is generally linear throughout the bulk of the fluid layer with a boundary layer of width $\omega^{-\frac{1}{2}}$ at $z = \pm\frac{1}{2}$. From this, we conclude that, for $\omega \to \infty$, the linear stability reduces to the classical problem, except for the boundary layers: that is to say, in the large frequency limit, modulation has little to no effect on the critical Rayleigh number for classical Rayleigh-Bénard convection. With this in mind, we fix the forcing amplitude, $b = 1$, and the Prandtl number, $Pr = 0.73$, and calculate neutral stability curves in (Ra, α) space for increasing values of ω. We also calculate the critical Rayleigh number as b is increased from zero to unity to illustrate that, as the frequency increases, the effect of the temperature modulation is negligible.

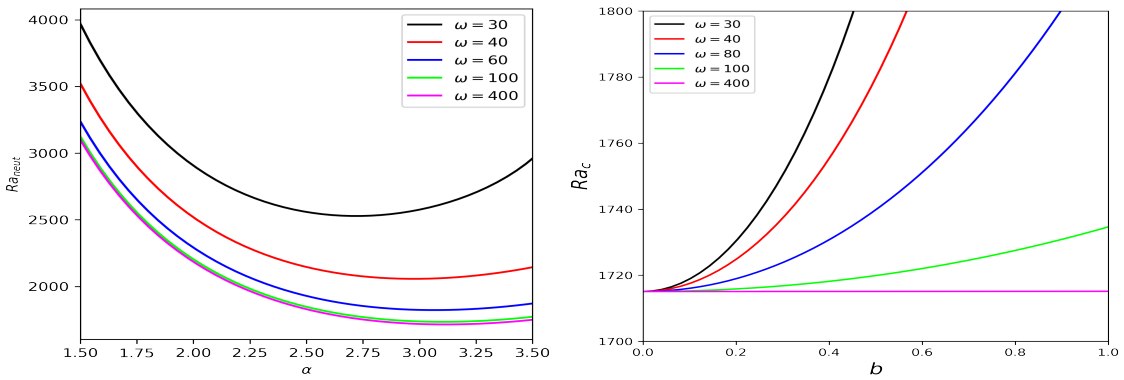

(a) (b)

Figure 4.14: (a) Neutral stability curves for $b = 1$ for a range of ω (b) Critical Rayleigh number as a function of b, for a range of ω. Here, $Pr = 0.73$ and we consider no-slip, fixed temperature boundary conditions.

Figure 4.14a illustrates that, as the frequency is increased for a fixed forcing amplitude, the neutral stability curves tend towards an asymptotic limit. It can be inferred from Fig 4.14a that the rate at which the neutral stability curve approaches the classical limit is not linear in ω. Figure 4.14b illustrates that, as b is increased for a series of increasingly large ω, the effect of the temperature modulation becomes weaker — at $\omega = 400$ it is shown by the purple line that increasing b has little to no effect on the critical Rayleigh number, as Ra_c remains at the classical value of $Ra_c \approx 1707.8$. To further confirm this asymptotic limit, we fix $b = 1$ and $Pr = 0.73$ and show in Fig **??** that the critical Rayleigh number tends towards the classical limit indicated by the dashed back line, as ω is increased by three orders of magnitude.

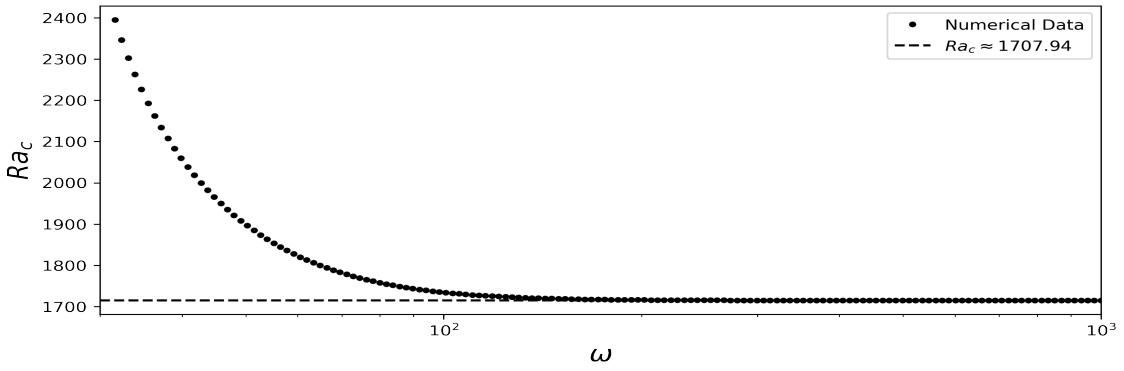

Figure 4.15: The critical Rayleigh number for $b = 1$ and $Pr = 0.73$ as $\omega \to \infty$. The dashed black line represents the value from the classical theory in Chandrasekhar (1961)

We have shown two very different asymptotic limits in §4.7.10 and §4.7.11: for a fixed ω (however large), then we have shown $Ra_c \to 0$ as $b \to \infty$; whereas for a fixed b (order unity), $Ra_c \to 1707.8$ as $\omega \to \infty$. This suggests an interesting dual limit, where $b, \omega \to \infty$.

4.8 Discussion & Considerations

Prior to this chapter, we have tackled a class of linear stability problems in which the basic states are steady. In this chapter, we have considered a more complicated class of stability problems where the basic state evolves with time. The overall aim of this chapter was therefore to consider a problem which does not include magnetic fields, and had already been partially investigated — the classical problem of RBC. Considering a time-varying basic state is not as straight-forward as the linear stability for a steady configuration, as the problem is no longer a typical eigenvalue problem.

In §4.6, we achieved the aim to gain insight into performing a time-dependent linear stability analysis, and we were able to reproduce numerical results within the literature. We then considered another previously investigated problem — the time-periodic forcing of the basic state temperature. In this problem we reproduced and validated the results within the literature, and we extended this work to unstudied asymptotic parameter regimes. We have shown that the modulation of the basic state temperature distribution can be both destabilising and stabilising and we have found a physical system that exhibits patterns which are well studied in oscillation problems, showing an intimate link with the Mathieu and Hill equations. A natural extension to this problem would be to consider a non-zero phase between the temperatures at the top and bottom plates.

More generally, the overall aim of this chapter was to illustrate the complex nature of time-dependent linear stability analysis and to equip ourselves with techniques that we could apply to study the linear stability of a compressible MHD system. We have shown in §4.6 that the choice of initial conditions is an important one. Varying the initial conditions affects the evolution of the disturbances in the linear stability analysis, suggesting there are a set of optimal initial conditions. While Foster (1965) was not concerned with generally finding the optimal initial conditions, a method for this is outlined in Kerr and Gumm (2017) where the authors find an optimal 'seed' by solving for a transfer matrix.

We have also shown through considering two time-dependent problems that defining a stability boundary is problem-specific. In a case similar to that of Foster (1965), we were able to look at the time taken for disturbances to amplify by an arbitrary amount — this can always be done in general, but it was particularly useful as that system was unconditionally unstable. However, in the case of periodic temperature modulation, we were able to exploit the nature of the linear system to define a clear stability boundary through Floquet theory. However, we have shown that, regardless of a natural stability boundary, we are able to find optimal parameters, and in the case of conditional stability, produce neutral stability curves in a phase-space of interest.

Chapter 5

Linear Instability of a Time-Varying Magnetic Field Generated by Velocity Shear

5.1 Introduction

In this chapter we study the magnetic buoyancy instability of a time-varying magnetic field. The model considered here is motivated by the solar tachocline and is an extension to the model analysed in Chapter 3 (see 3.1). The general idea is to consider the linear stability of an evolving magnetic layer that is generated from the shearing of a vertical uniform magnetic field. The work in Chapter 3 can be understood as the linear stability analysis of the equilibrium steady state that results from this dynamic shearing process. The inclusion of time-dependence is important: the shearing of a poloidal field within the tachocline is an inherently time-dependent process. Therefore, studying the instabilities associated with an evolving basic state will help to bridge the gap between the linear stability analysis of a steady state and nonlinear simulations.

As already discussed, the linear stability for steady states is performed through a normal-mode analysis to determine which disturbances grow/decay exponentially in time. In general, for unstable configurations, disturbances will become large enough for nonlinearity to become important. In the steady case, the main focus has been to obtain neutral stability curves which describe the onset of instability. The problem of interest here however, is when the background state evolves, and therefore, the governing system of linear equations will feature source terms that vary in time. This can result in disturbances which may grow and decay algebraically in time. What we will see here, is that we must consider more than growth: we must consider how much the instability grows in a given time. If the transient state has insufficient total growth, then the disturbances may decay away unnoticed when compared to the background state. As seen in §4.6.2, we have some freedom in defining a stability boundary, and hence what condition is necessary for a background configuration to be considered 'unstable'. We will see in this chapter

that this problem is not as straightforward. The basic state does not grow forever, and eventually reaches a steady state. Therefore, the disturbances will not unconditionally grow in time, and hence, just considering the time taken for disturbances to grow by a set amount is not sufficient. In an experimental or physical setting, there are always small background disturbances to the fluid, for example, fluctuations due to ambient noise. In practice, the order of magnitude of these variations is hard to estimate, and therefore the growth required for instability to manifest is poorly defined. We discuss multiple ways to describe instability, and show that the method used in eq. (4.54), i.e., the definition of a critical time is not sufficient on its own. We will show that wavenumbers that correspond to disturbances that amplify the most in the early stages are not necessarily the optimal wavenumbers for long term amplification. That is to say, certain wavenumbers can amplify perturbations by orders of magnitude in the initial stages of growth before decaying. For example, if one was to suggest instability is manifest when disturbances amplify by a factor of 10^3 relative to the initial conditions (similar to the nominal critical time in Eq (4.54)), then one would reach the wrong conclusion, as this mode may decay away at longer times, and furthermore, not become large enough for nonlinearity to become important. This is a well-documented phenomenon for non-normal operators; for example Trefethen et al. (1993) have shown that when background states are steady, it is possible to observe significant transient growth before decay. Furthermore, we have shown the importance of the initial configuration of disturbances, even for steady background states in §4.5, showing that various initial disturbances lead to different transient evolution.

Throughout this chapter, we will use the non-dimensional equations governing the motion of compressible magnetised fluids, given by Eq (3.8)-(3.13). First, we will discuss the evolution of the basic state which depends heavily on the initial conditions, exploring two cases studied by Vasil and Brummell (2008, 2009). We will then discuss the short and long term behaviour of the basic state, and demonstrate that the final state is independent of the initial conditions. Equipped with the knowledge from basic state investigations, we will study discrepancies between Vasil and Brummell (2008) and Silvers et al. (2009). In particular, we will demonstrate that the great difference in the numerical solutions described by Vasil and Brummell (2008) and Silvers et al. (2009) arises from the difference in initial conditions and not, as claimed by Silvers et al. (2009), to double-diffusive behaviour.

The next step in this chapter is to perform a quasi-static stability analysis. The quasi-static analysis can be understood as bridging the gap between a steady and a non-steady linear stability analysis. This type of analysis is useful because it allows us to gain insight into the linear stability of the time-dependent state at a sequence of fixed times without needing to define an alternative stability boundary. To perform a quasi-static analysis, first one evolves the basic state according to its governing equations. One then considers 'snapshots' of the background state at a series of times, t^*. A linear stability analysis is then performed in terms of normal modes, for each 'snapshot' of the basic state (assumed steady), where perturbations are therefore given by exponentially growing/decaying

waves. We will perform a quasi-static analysis for two types of initial conditions in the background flow (fluid initially static or not) and demonstrate that, in the case of an initially static configuration, the equilibrium analysis given in Chapter 3 is indicative of the linear stability of the evolving basic state that results in the steady equilibrium state. That is to say, the linear stability of the steady basic state is representative of the linear stability of the basic state that proceeded it, and one should not concern themselves with the complexities of defining a stability boundary. The results of this type of analysis will then be used to inform parameter choices in the full time-dependent analysis.

Finally, we consider the full time-dependent analysis where we introduce the full system of linear equations. Here, the techniques discussed in Chapter 4 will become useful: we will discuss the problem of defining a suitable stability boundary. After that, it will be necessary to discuss the multiple lines of enquiry for the time-dependent analysis, e.g. parameter choices, wavenumbers, and initial conditions for the disturbances. We will discuss a range of initial conditions for the disturbances, illustrating that certain initial conditions are optimal for amplification of the perturbations. We will then conclude by discussing natural extensions of this work.

5.2 Governing Equations

We consider a box in Cartesian geometry (x, y, z) which is infinite in x and y and has height d in the z-direction. The box is filled with a compressible and conducting fluid, threaded by a uniform vertical magnetic field, $\mathcal{B}_0\hat{\boldsymbol{z}}$, and is subject to a horizontal forcing, $F\hat{\boldsymbol{x}}$, which is conceptualised as the second derivative of a target flow, $U_0(z)$. We scale magnetic field, pressure, density, and temperature with the scales $\mathcal{B}_0$, P_0, ρ_0 and Θ_0, where Θ_0 is the temperature at the top boundary, and ρ_0 is proportional to the total mass within the domain. The z-direction is chosen to point in the same direction as gravity. With this scaling, the equations of compressible Magnetohydrodynamics (MHD) are

$$\frac{\partial \rho}{\partial t} + \nabla \cdot (\rho \boldsymbol{u}) = 0, \tag{5.1}$$

$$\begin{aligned}\frac{\partial (\rho \boldsymbol{u})}{\partial t} + \nabla \cdot (\boldsymbol{u}\boldsymbol{u} - \alpha \boldsymbol{B}\boldsymbol{B}) = -\nabla \left(\rho\Theta + \alpha \frac{B^2}{2} \right) + \theta(m+1)\rho\hat{\boldsymbol{z}} \\ + C_k \sigma \left(\nabla^2 \boldsymbol{u} + \frac{1}{3}\nabla(\nabla \cdot \boldsymbol{u}) \right) + \boldsymbol{F},\end{aligned} \tag{5.2}$$

$$\begin{aligned}\rho \frac{\partial \Theta}{\partial t} + \rho \nabla \cdot (\Theta \boldsymbol{u}) = -\rho(\gamma - 2)\Theta \nabla \cdot \boldsymbol{u} + \gamma C_k \nabla^2 \Theta + (\gamma - 1) C_k \sigma \Phi \\ + (\gamma - 1) C_k \alpha \zeta (\nabla \times \boldsymbol{B})^2,\end{aligned} \tag{5.3}$$

$$\frac{\partial \boldsymbol{B}}{\partial t} = \nabla \times (\boldsymbol{u} \times \boldsymbol{B}) + C_k \zeta \nabla^2 \boldsymbol{B}, \tag{5.4}$$

$$P = \rho\Theta, \tag{5.5}$$

$$\nabla \cdot \boldsymbol{B} = 0, \tag{5.6}$$

where the non-dimensional groupings are the same as in Chapter 3 and are given by Eqs (3.14)-(3.17). and $\boldsymbol{F}$ is a body forcing. As discussed in §3.2.2, we will consider a forcing modelled after the second derivative of a target flow, such that

$$\boldsymbol{F} = -C_k \sigma \frac{\mathrm{d}^2 U_0}{\mathrm{d}z^2} \hat{\boldsymbol{x}}, \tag{5.7}$$

where the target flow is $\boldsymbol{U}_0 = U_0(z)\hat{\boldsymbol{x}}$.

5.3 The Basic State

5.3.1 Evolution Equations

The basic state for the time-dependent system is much more complicated than the steady equilibrium state. The evolution of mass density is dictated by vertical motions governed by the vertical component of the momentum equation, which includes a pressure term governed in parts by the heat equation. The basic state is therefore governed by

$$\frac{\partial \rho_0}{\partial t} = -W\frac{\partial \rho_0}{\partial z} + \rho \frac{\partial W}{\partial z}, \tag{5.8}$$

$$\frac{\partial U}{\partial t} = -W\frac{\partial U}{\partial z} + \frac{\alpha}{\rho_0}\frac{\partial B}{\partial z} + \frac{C_k \sigma}{\rho_0}\left(\frac{\partial^2 U}{\partial z^2} - \frac{\mathrm{d}^2 U_0}{\mathrm{d}z^2}\right), \tag{5.9}$$

$$\frac{\partial W}{\partial t} = -W\frac{\partial W}{\partial z} - \frac{1}{\rho_0}\left(\frac{\partial(\rho_0 T_0)}{\partial z} - \theta(m+1)\rho_0\right) - \frac{\alpha}{\rho_0}B\frac{\partial B}{\partial z} + \frac{C_k\sigma}{\rho_0}\frac{\partial^2 W}{\partial z^2}, \tag{5.10}$$

$$\frac{\partial B}{\partial t} = \frac{\partial U}{\partial z} - B\frac{\partial W}{\partial z} - W\frac{\partial B}{\partial z} + C_k \zeta \frac{\partial^2 B}{\partial z^2}, \tag{5.11}$$

$$\frac{\partial T_0}{\partial t} = -W\frac{\partial T_0}{\partial z} - (\gamma-1)T_0\frac{\partial W}{\partial z} + (\gamma-1)\frac{C_k\sigma}{\rho_0}\left[\frac{4}{3}\left(\frac{\partial W}{\partial z}\right)^2 + \left(\frac{\partial U}{\partial z}\right)^2\right] + \frac{\gamma C_k}{\rho_0}\frac{\partial^2 T_0}{\partial z^2} + (\gamma-1)\frac{C_k\alpha\zeta}{\rho_0}\left(\frac{\partial B}{\partial z}\right)^2, \tag{5.12}$$

which are the mass conservation equation, the $x-$ and $z-$ component of the momentum equation, the x-component of the induction equation, and the temperature equation. Throughout this chapter, attention is restricted to a target flow of the form

$$U_0(z) = \mathcal{U}_0 \tanh 10z. \tag{5.13}$$

As a result of the vertical motion permitted in the time-dependent basic state, Eqs (5.8)-(5.12) are nonlinear. Throughout this chapter, we will consider zero field, stress-free, fixed temperature boundary conditions, such that

$$B\left(\pm\tfrac{1}{2}\right) = \left.\frac{\mathrm{d}U}{\mathrm{d}z}\right|_{\pm\frac{1}{2}} = W\left(\pm\tfrac{1}{2}\right) = 0, \tag{5.14}$$

$$T_0\left(-\tfrac{1}{2}\right) = 1, \quad T_0\left(\tfrac{1}{2}\right) = 1+\theta. \tag{5.15}$$

The initial conditions for temperature, density, field, and vertical flow are that of a polytrope, given by

$$T_0(z,0) = 1 + \theta\left(\tfrac{1}{2} + z\right), \tag{5.16}$$

$$\rho_0(z,0) = \left(1 + \theta\left(\tfrac{1}{2} + z\right)\right)^m, \tag{5.17}$$

$$B(z,0) = W(z,0) = 0. \tag{5.18}$$

We will then consider two different initial conditions for the horizontal flow, either

$$U(z,0) = 0 \quad \text{(initial condition is zero flow)}, \tag{5.19}$$

$$\text{or} \quad U(z,0) = U_0(z) \quad \text{(initial condition is the target flow)}. \tag{5.20}$$

The choice of initial conditions for the horizontal flow proves important, as it has significant impacts on the transient evolution of the magnetic field and flow.

5.3.2 Numerical Methods

Equations (5.8)-(5.12) form a set of nonlinear partial differential equations in time and space, and therefore previous techniques such as eigenvalue methods will not be applicable. In this section, we outline the numerical methods that will be useful to solve Eqs (5.8)-(5.12). We will still make use of the spatial discretisation schemes used previously, i.e. FD2 and FD4 (see Chapter 3), and so this discussion will focus on the necessary time-stepping schemes. We use a combination of two second-order schemes, one implicit and the other explicit. To illustrate this, consider the nonlinear equation

$$\frac{\partial X}{\partial t} = \mathcal{N}(X) + \mathcal{L}(X), \tag{5.21}$$

where $X(t,z)$ is a function of time and space, and $\mathcal{N}, \mathcal{L}$ are nonlinear and linear differential operators. To handle the linear components, we use the Crank-Nicolson (CN) method. The CN scheme is based on the trapezoidal rule and is essentially an implicit midpoint method, which is a combination of the forward and backward Euler schemes. The evolution of the linear operator $\mathcal{L}$ is given by

$$\Delta\mathcal{L}^{n+1} = \bar{X}^{n+1} - X^n = \frac{\delta t}{2}\left(\mathcal{L}(X^{n+1}) - \mathcal{L}(X^n)\right), \tag{5.22}$$

where superscript n denotes $t^n = n\Delta t$ for some positive integer n. There are various time-stepping schemes for handling nonlinear terms: we choose between Runge-Kutta (RK) or Adams-Bashforth (AB) methods. Adams-Bashforth and Runge-Kutta are explicit multi-step methods which allow increasing orders of accuracy by using information from multiple previous time steps. Runge-Kutta methods are different to AB, in that they are a single-step method which requires multiple evaluations of $\mathcal{N}$ per time step. The choice of multi-step or single-step is not straightforward. On the one hand, higher order schemes using an RK stencil are obtained by increasing the number of evaluations of $\mathcal{N}$ per time step. However, multi-step methods increase their accuracy by using more data

from previous time steps, and can achieve a similar accuracy as RK methods with fewer calculations. It is important to note that both RK and AB methods allow a straightforward implementation of adaptive time-stepping, which can dramatically speed up computation, especially when the stability condition associated with the whole scheme is restrictive. Using a second-order Adams-Bashforth (AB2) stencil, the nonlinear evolution is given by

$$\Delta N^{n+1} = \tilde{X}^{n+1} - X^n = \delta t \left(\frac{3}{2}\mathcal{N}(X^n) - \frac{1}{2}\mathcal{N}(X^{n-1}) \right). \tag{5.23}$$

The next step in the iteration of X is found by combining Eqs (5.22)-(5.23), yielding

$$X^{n+1} = X^n + \Delta\mathcal{N}^{n+1} + \Delta\mathcal{L}^{n+1}, \tag{5.24}$$

which can be written as

$$\left(1 - \frac{\delta t}{2}\mathcal{L}\right) X^{n+1} = \delta t \left[\frac{3}{2}\mathcal{N}(X^n) - \frac{1}{2}\mathcal{N}(X^{n-1}) \right] + \left(1 + \frac{\delta t}{2}\mathcal{L}\right) X^n. \tag{5.25}$$

For eigenvalue problems and underlying optimisation procedures involved, we continue to use the algorithms discussed in §3.2.4.

5.3.3 Initial Condition: Zero Flow

Here, we solve Eqs (5.8)-(5.12) with Boundary Conditions (BCs) (5.14)-(5.15) with initial conditions Eq (5.16)-(5.18) with initial horizontal flow given by Eq (5.19). Figure 5.1 shows the numerical solutions up to $t = 20$, for the parameters given in the caption. It can be seen that the density and temperature do not deviate much from the initial

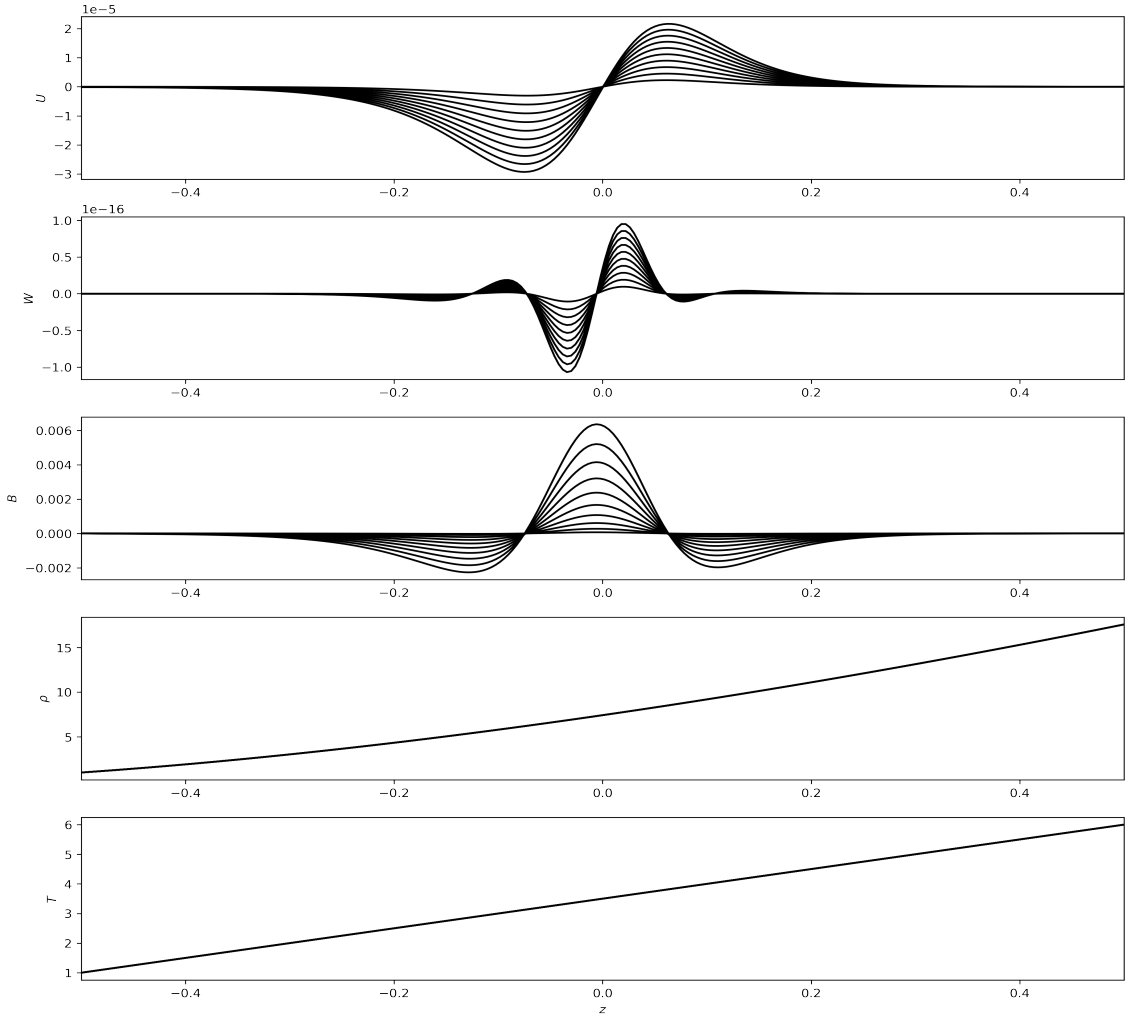

Figure 5.1: Evolution of the basic state for $C_k = 0.01, \sigma = 2.5 \times 10^{-4}, \zeta = 5.0 \times 10^{-4}, m = 1.6$, $\mathcal{U}_0 = 1/20$, and $\alpha = 1.25 \times 10^{-5}$. The black lines are snapshots of the solution at 2 time-unit intervals up to $t = 20$.

distributions. This results from the fact that the magnitude of the vertical velocity, $W(z,t)$, remains small, and therefore does not contribute much to changing the density distribution (see Eq (5.8)). Furthermore, Fig 5.1 illustrates that, at least for the parameter values considered, the x-component of the flow, $U(z,t)$, is small compared to the sound speed but nevertheless much larger than $W(z,t)$. Figure 5.1 also shows that the magnetic field grows in time and two negative lobes that travel outwards are observed. We will show in §5.3.5 that these negative lobes are Alfvén waves that travel outwards, and are inverted and reflected at the boundaries.

5.3.4 Initial Condition: Target Flow

Here, we solve Eqs (5.8)-(5.12) again, with the same BCs and initial conditions as in the previous section, except that now, the initial horizontal flow is given by Eq (5.20). Numerical solutions are shown in Fig 5.2 up to $t = 20$, for the parameters given in the caption (which are the same as in the previous section). Figure 5.2 shows that the

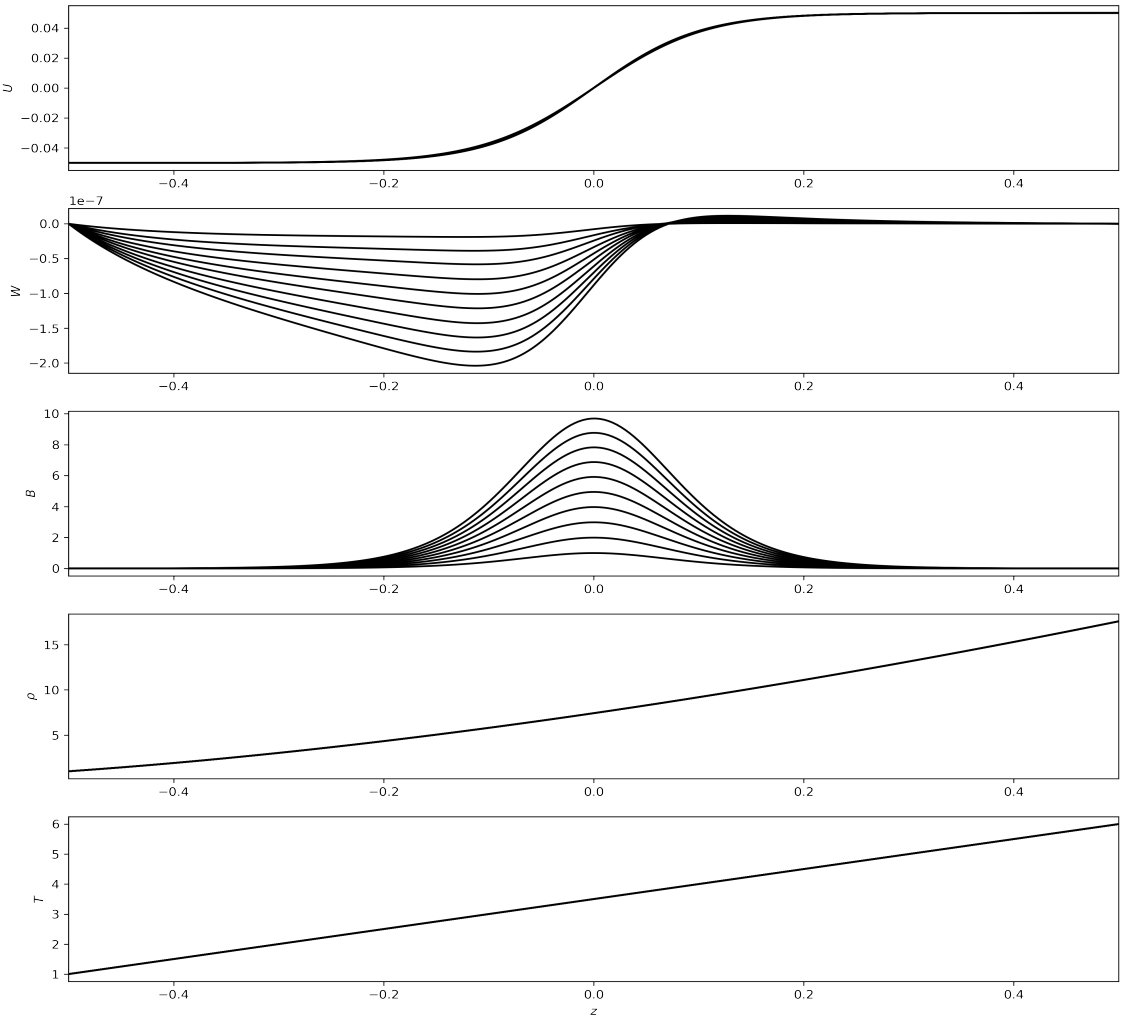

Figure 5.2: Evolution of the basic state for $C_k = 0.01, \sigma = 2.5 \times 10^{-4}, \zeta = 5.0 \times 10^{-4}, m = 1.6$, $\mathcal{U}_0 = 1/20$, and $\alpha = 1.25 \times 10^{-5}$. The black lines are snapshots of the solution at 2 time-unit intervals up to $t = 20$.

vertical velocity component remains small. This is not surprising as it is shown that the temperature and density do not deviate from the initial linear and polytrope distribution. This is expected since the dominant vertical force balance (for the parameters chosen) is between pressure and gravity, and therefore, the system remains close to hydrostatic equilibrium. It is shown in §3.2.3 that the final equilibrium state does not include a vertical velocity, and so it must diffuse away to zero. It can be seen in Fig 5.2 that the x-component of the velocity remains similar to the target flow up to $t = 20$. Furthermore, Fig 5.2 illustrates that, in contrast with Fig 5.1, the magnetic field is amplified to a strength of ten times the imposed vertical field. We will show that this magnetic field continues

to grow and reach a maximal value before diffusive processes set in. Furthermore, it can be seen by comparison of Figs 5.1-5.2, that the amplitude of the magnetic field depends critically on the initial condition for $U(z,t)$; for example, by $t = 20$, the difference in the magnetic field is approximately four orders of magnitude. This difference will be crucial in the linear stability analysis, as the basic state configurations are so different, and so we expect very different stability properties.

5.3.5 The Role of Alfvén Waves

In this section, we study the evolution of the magnetic and velocity fields over a longer period of time. We timestep Eqs (5.8)-(5.12) subject to the BCs (5.14)-(5.15) with initial conditions given by Eqs (5.19)-(5.20) up to $t = 1500$ and show contour maps of the magnetic and velocity fields as functions of time and space. We wish to illustrate three main points: (1) depending on the initial conditions, the magnetic field undergoes a reversal, oscillating with positive and negative amplitudes; (2) Alfvén waves travel along magnetic field lines due to a competition between inertia and a restoring force, i.e., magnetic tension; (3) to reiterate the importance of initial conditions for the amplification of the basic magnetic field.

Figures 5.3 and 5.4 show contour maps of $B(z,t)$ and $U(z,t)$ as functions of time and space, for an initial target flow and zero initial flow, respectively. It is shown in Fig 5.3

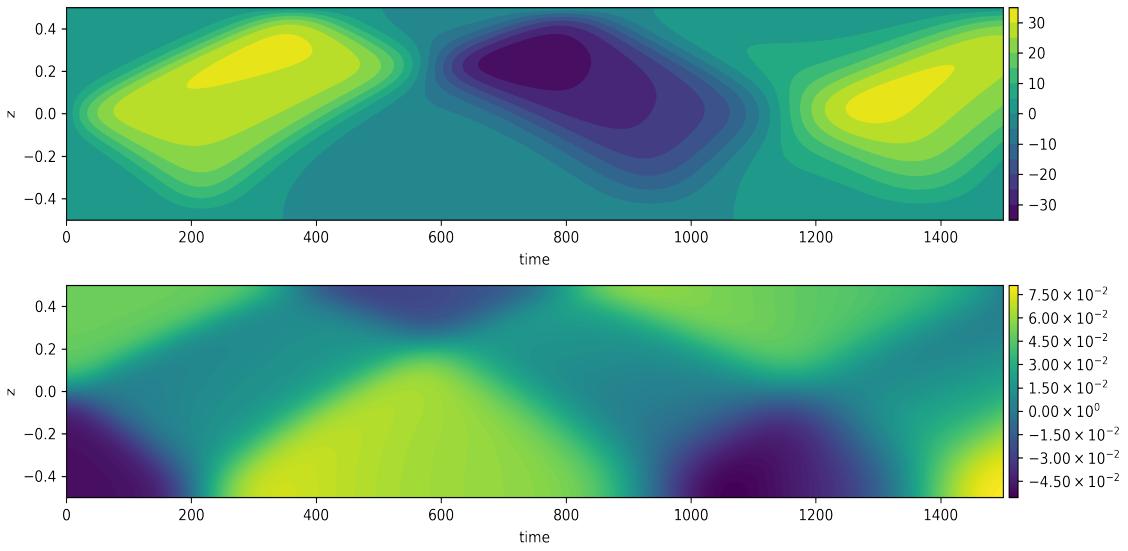

Figure 5.3: Magnetic field, $B(z,t)$ (top) and velocity field, $U(z,t)$ (bottom) in (t,z) space with the initial flow as the target shear flow. Here $C_k = 0.01$, $\sigma = 2.5 \times 10^{-4}$, $\zeta = 5.0 \times 10^{-4}$, $m = 1.6$, $\mathcal{U}_0 = 1/20$, and $\alpha = 1.25 \times 10^{-5}$.

that the magnetic field initially grows to an amplitude of $|B| \approx 35$ before reversing at approximately $t = 600$, subsequently propagating throughout the layer. Furthermore, it is shown in Fig 5.3 that the maximal value of the magnetic field is skewed towards the lower-half of the domain. This is due to the Alfvén speed being smaller in the lower half of the domain owing to an increased density. It is shown, in the bottom panel of Fig 5.3

that the velocity pattern is generally anti-symmetric, with a propagating component corresponding to Alfvén waves. Furthermore, the bottom panel of Fig 5.3 shows that in the case of an initial target flow, the subsequent resultant flow can be larger than the maximum of the target flow, i.e. $\mathcal{U}_0 = 1/20$. This is due to the motion of Alfvén waves adding to the background flow.

Figure 5.4 shows the basic field and horizontal velocity field in space and time for the case of zero initial flow. In contrast with Fig 5.3, the top panel of Fig 5.4 demonstrates that the global maximum of the magnetic field remains at $z = 0$. Furthermore, the negative lobes shown in Fig 5.1 can be seen in Fig 5.4: these negative lobes propagate outwards as Alfvén waves, and then invert at the boundaries due to energy conservation. It can be seen in the top panel of Fig 5.4 that the magnetic field performs small oscillations around $|B| \approx 0.1$, and the Alfvén waves decay away as diffusive processes inhibit the evolution. These Alfvén waves, although transient, are indicative of strong Alfvénic responses within the basic state. The bottom panel of Fig 5.4 shows that the velocity remains much smaller than the target flow. It is typically anti-symmetric, and is inhibited by Alfvén waves which propagate throughout the domain. Comparison of Figs 5.3 and 5.4 illustrates

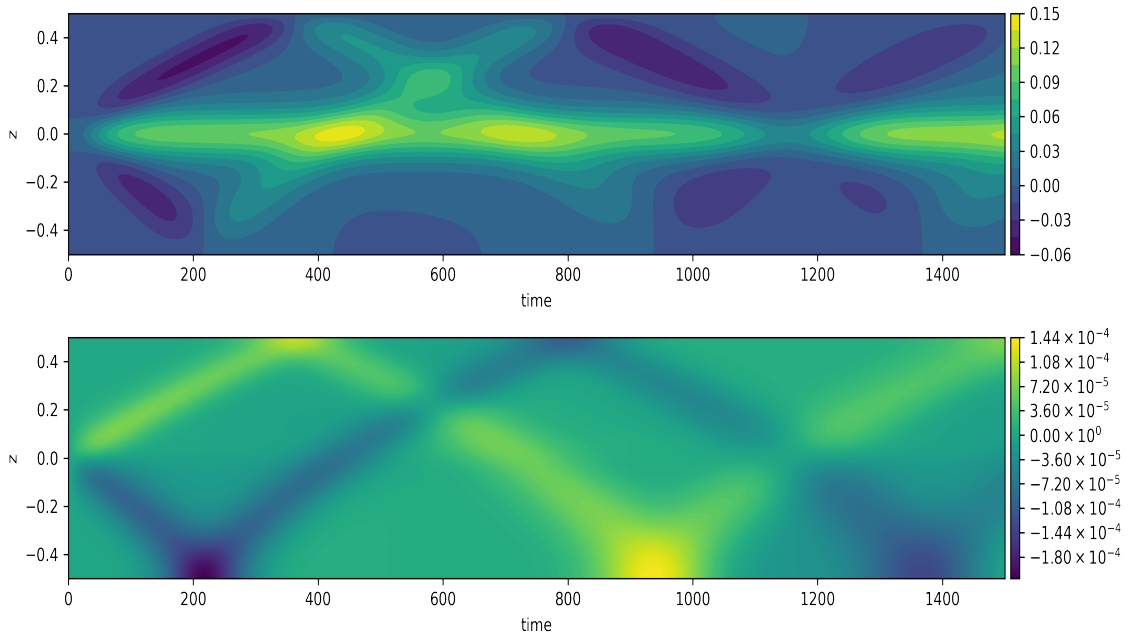

Figure 5.4: Magnetic field (top) and velocity field (bottom) in (t, z) space for zero initial flow. Here $C_k = 0.01$, $\sigma = 2.5 \times 10^{-4}$, $\zeta = 5.0 \times 10^{-4}$, $m = 1.6$, $\mathcal{U}_0 = 1/20$, and $\alpha = 1.25 \times 10^{-5}$.

that the evolution of the magnetic field and flow depend heavily on the initial conditions. It can be seen that, for the same parameters, the maximum magnetic field generated from an initial shear flow is four orders of magnitude larger than that produced from zero initial flow. Figure 5.4 illustrates that the magnetic field and velocity do not vary much after a certain time and therefore the equilibrium basic state in, for example, chapter 3, is a good representative of the transient evolution in the case of an initially static atmosphere.

5.3.6 Short and Long Term Behaviour

It is of interest to examine the evolution of the flow and magnetic field for $t \ll 1$ and for $t \gg 1$. We can make analytic progress with Eqs (5.8)-(5.12) by inferring a simpler system from the results shown in Figs 5.1-5.2. We have shown that the temperature and density do not vary significantly in time and, for at least up to $t = 20$, the vertical component of the velocity field remains small. Therefore, for $t \ll 1$, Eqs (5.8)-(5.12) can be approximated by

$$\frac{\partial U}{\partial t} \approx \frac{\alpha}{\rho_0}\frac{\partial B}{\partial z} + \frac{C_k\sigma}{\rho_0}\left(\frac{\partial^2 U}{\partial z^2} - \frac{\mathrm{d}^2 U_0}{\mathrm{d}z^2}\right), \tag{5.26}$$

$$\frac{\partial B}{\partial t} \approx \frac{\partial U}{\partial z} + C_k\zeta\frac{\partial^2 B}{\partial z^2}, \tag{5.27}$$

$$W \approx 0, \tag{5.28}$$

$$\rho_0(z) \approx \left(1 + \theta\left(\tfrac{1}{2} + z\right)\right)^m, \tag{5.29}$$

$$T_0(z) \approx 1 + \theta\left(\tfrac{1}{2} + z\right), \tag{5.30}$$

where the form of W, ρ_0, and T_0 follow from the initial conditions (5.16)-(5.18). We will now consider the two initial conditions for the velocity given by Eqs (5.19)-(5.20), and manipulate Eqs (5.26)-(5.30) to study analytically the early evolution of flow and field.

Analytic Evolution of Field and Flow for Zero Initial Flow when $t \ll 1$

Consider first the case of zero initial target flow. When coupled with zero initial horizontal magnetic field, this means that, if $t \ll 1$, then $|U|, |B| \ll \mathcal{U}_0$ and therefore Eqs (5.26)-(5.27) can be accurately approximated by

$$\frac{\partial U}{\partial t} \approx \frac{C_k\sigma}{\rho_0}\frac{\mathrm{d}^2 U_0}{\mathrm{d}z^2}, \tag{5.31}$$

$$\frac{\partial B}{\partial t} = \frac{\partial U}{\partial z} + C_k\zeta\frac{\partial^2 B}{\partial z^2}. \tag{5.32}$$

The evolution of the flow at short time can therefore be calculated analytically by integrating Eq (5.31) in time, yielding

$$U(z,t) \approx -t\frac{C_k\sigma}{\rho_0}\frac{\mathrm{d}^2 U_0}{\mathrm{d}z^2}. \tag{5.33}$$

We then substitute Eq (5.33) into Eq (5.32), neglecting the diffusion term, and integrate in time. This admits the time-dependent magnetic field

$$B(z,t) \approx -t^2\frac{C_k\sigma}{2\rho_0}\frac{\mathrm{d}^3 U_0}{\mathrm{d}z^3}. \tag{5.34}$$

The comparison of Eqs (5.33)-(5.34) to the numerical solutions to Eqs (5.9)-(5.11), presented in Fig 5.5, shows that there is reasonable agreement between the analytic approximations and the full numerical solution. It can also be seen that there is better agreement for the velocity field than for the magnetic field. The slight disagreement between the

numerical and analytic approximation for the magnetic field occurs at the larger times and is most likely due to neglecting the diffusion term. For $t \ll 1$ it is reasonable to assume that the magnetic diffusion is negligible, however.

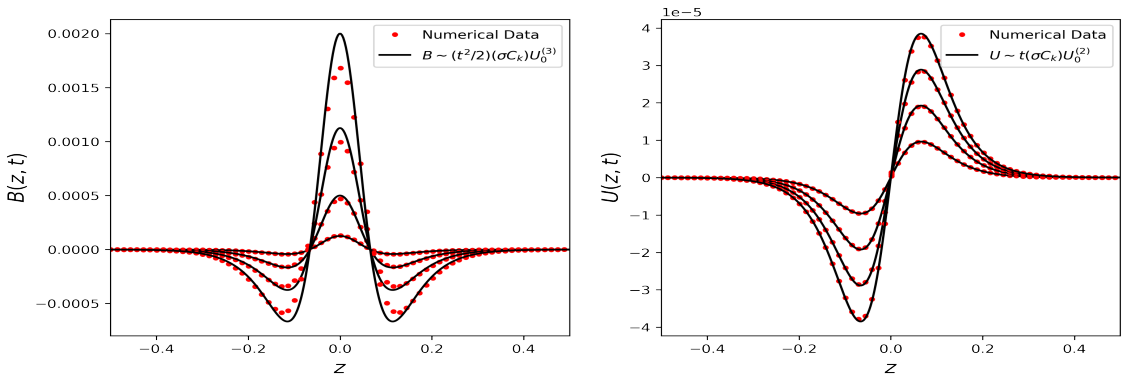

Figure 5.5: Comparison of the magnetic field (left) and velocity (right) obtained numerically and expressions (5.33)-(5.34) for $t \ll 1$ with zero initial horizontal flow. Here $C_k = 0.01$, $\sigma = 2.5 \times 10^{-4}$, $\zeta = 5.0 \times 10^{-4}$, $m = 1.6$, $\mathcal{U}_0 = 1/20$, and $\alpha = 1.25 \times 10^{-5}$.

Analytic Evolution of Field and Flow for Initial Target Flow when $t \ll 1$

We now perform a similar analysis for the case were the initial flow is the target flow. It is shown in Fig 5.2 that, for an initial target flow, the resultant flow remains similar to the target flow up to $t = 20$. From this, we conclude that the flow is approximated by

$$U(z,t) \approx U_0(z). \tag{5.35}$$

Substituting Eq (5.35) into Eq (5.27), neglecting diffusion, and integrating in time, results in the approximation for the evolution of the magnetic field,

$$B(z,t) \approx t\frac{\mathrm{d}U_0}{\mathrm{d}z}. \tag{5.36}$$

Comparison of Eqs (5.35)-(5.36) to the numerical solutions of Eqs (5.9)-(5.11) from an initial target flow are shown in Fig 5.6. It can be seen that there is again good agreement

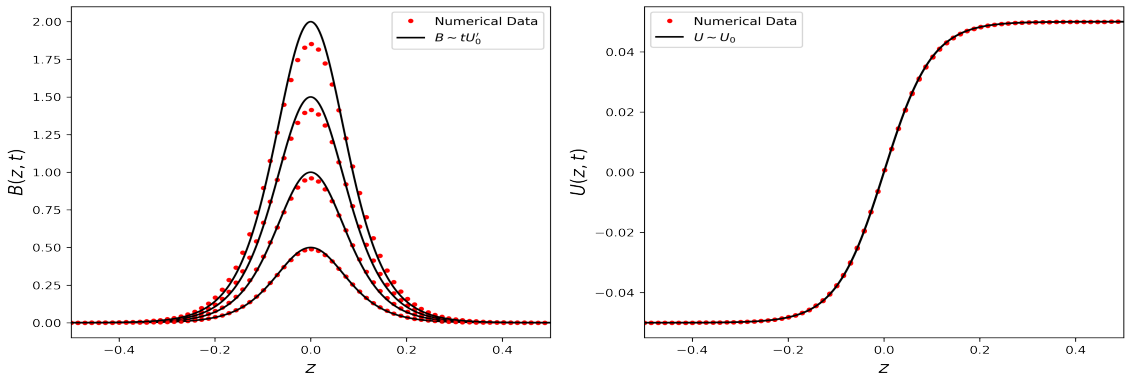

Figure 5.6: Comparison of the magnetic field (left) and velocity (right) obtained numerically and Eqs (5.33)-(5.34) for $t \ll 1$ with the initial flow as the target shear flow. Here $C_k = 0.01$, $\sigma = 2.5 \times 10^{-4}$, $\zeta = 5.0 \times 10^{-4}$, $m = 1.6$, $\mathcal{U}_0 = 1/20$, and $\alpha = 1.25 \times 10^{-5}$.

between the analytic approximation and the full numerical solutions. Equations (5.33)-(5.34) and Eqs (5.35)-(5.36) are helpful analytic results, as they determine the transient behaviour of the magnetic field and flow in terms of the target flow, the density, C_k, and the Prandtl number. It can be seen by comparison of Eqs (5.34) and (5.36) that the magnetic field generated from zero initial flow grows quadraticly in time, in contrast with that generated from an initial target flow, which grows linearly in time, and hence, faster in the regime where $t \ll 1$.

The Evolution of the Magnetic Field for Long Times

We now consider the long-time regime, with $t \gg 1$. If we assume that $W(z,t)$ remains small, and that the temperature and density remain static throughout the evolution of the field and flow, then the governing evolution equations (see Eqs (5.26)-(5.27)) are linear advection-diffusion equations. This means that the solution in the regime where $t \to \infty$ is independent of the initial conditions. We evolve (5.8) – (5.12) for both initial conditions given by expressions (5.19) and (5.20). At each time step we calculate the maximum

amplitude of the absolute magnetic field (see Fig 5.7).

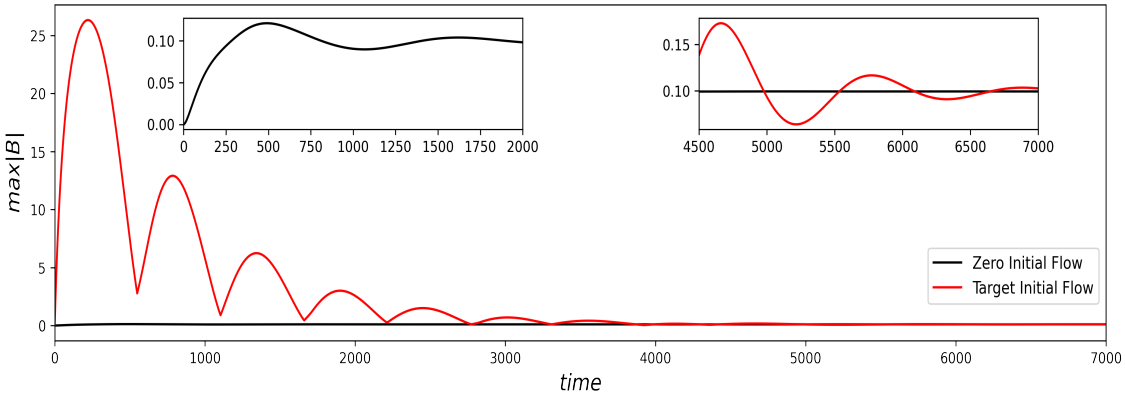

Figure 5.7: Amplitude of the magnetic field generated from: zero initial horizontal flow (black); an initial horizontal target flow (red).

Figure 5.7 reinforces that in the early stages of evolution, the difference in magnetic field amplitudes between the two cases with different initial flows is significant — the amplitude of the magnetic field generated from an initially static atmosphere can not even be seen on the same scale as that generated from an initial target flow. It is shown in the two sub-figures in Fig 5.7 that, when $t \gg 1$, both configurations lead to oscillations about a constant amplitude (in this case $|B| \approx 0.1$). It is clear that it takes much longer for the magnetic field generated from an initial flow to decay away.

Regardless of choice of initial conditions, diffusion will eventually balance advection and other source terms, and therefore the magnetic field (and other basic state variables) tend towards an equilibrium state that is governed by Eqs (5.8)-(5.12) with $\partial_t \equiv 0$. We solve the resultant boundary value problem, as in §3.2.3, for the equilibrium magnetic field and compare this to the long term magnetic fields resulting from both initial flows (Eqs (5.19)-(5.20)). It can be seen in Fig 5.8 that there is excellent agreement between the time-dependent magnetic field for both initial flow configurations and the equilibrium magnetic field.

5.4 The Decisive Role of an Initial Flow

Equipped with a better understanding of the role of initial conditions in the basic flow, it is time to discuss a significant discrepancy between the results of Vasil and Brummell (2008) and Silvers et al. (2009). As discussed in §1.3.2, Vasil and Brummell (2008, 2009) and Silvers et al. (2009) performed nonlinear simulations to further understand magnetic buoyancy instabilities, for the framework shown in §3.2. It is understood that for magnetic structures to become buoyant, the shear flow must transfer enough energy into the toroidal magnetic field; so much so, that it can overcome the background stratification. Vasil and Brummell (2008) concluded that for magnetic buoyancy to ensue, the conditions on the target profile were quite demanding: their conclusion was that for magnetic layers to rise, the target shearing velocity needed to be of the order of Mach 15 (15 times

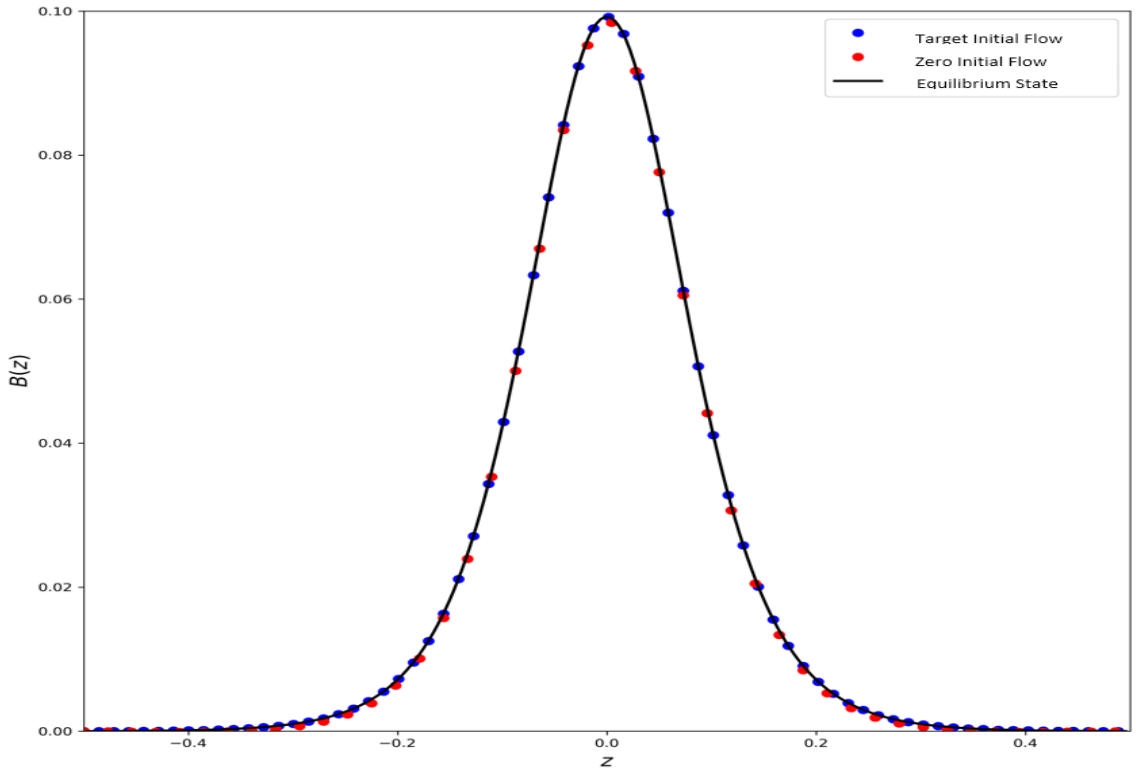

Figure 5.8: Comparison of the equilibrium magnetic field with the non-steady magnetic field at $t = 7000$ for both initial conditions given by Eqs (5.19)-(5.20).

the sound speed). This is an exceedingly large velocity amplitude, however, the resultant nonlinear flow is highly turbulent and susceptible to hydrodynamic instabilities such as the Kelvin-Helmholtz instability: these instabilities lead to a flow with speed $\simeq 0.7$ Ma. In short, Vasil and Brummell (2008) concluded that magnetic buoyancy could only occur if the velocity shear is hydrodynamically unstable, and if the background flow is hydrodynamically stable then it is difficult for the resultant magnetic field to overcome the constraints of stratification: that is to say, Vasil and Brummell (2008) required a very fast flow with a drastically large forcing. A year later, Silvers et al. (2009) studied an ostensibly similar problem and were able to observe buoyant magnetic structures. However, the key difference is that Silvers et al. (2009) observed the onset of magnetic buoyancy for shear flows which are a small fraction of the sound speed, i.e. 0.05 Ma. Silvers et al. (2009) concluded that the significant reduction in the shear flow velocity could be ascribed to double-diffusive effects — in particular the small value of $\eta/\kappa = \zeta$. However, the parameters in Vasil and Brummell (2008) and Silvers et al. (2009) are not very different: as shown in Table 5.1.

Parameter	Vasil and Brummell (2008)	Silvers et al. (2009)
α	1.25×10^{-5}	7.2×10^{-4}
C_k	1.0×10^{-2}	1.0×10^{-2}
σ	5.0×10^{-3}	2.5×10^{-4}
ζ	8.0×10^{-3}	5.0×10^{-4}
Q	1.8×10^{5}	1.0×10^{6}
$\mathcal{U}_0$	7.5	0.05

Table 5.1: Simulation parameters.

The important parameter for double-diffusive instabilities, ζ, is shown in Table 5.1 and we can see that in both papers ζ is much smaller than unity. Both papers contain numerical results for the evolution of the magnetic field that is governed by Eqs (5.8)-(5.12): comparison of the resultant magnetic field shows that they attain similar amplitudes, but on very different time scales. We will show here that the crucial difference between these two papers is the initial conditions for the basic horizontal flow. This overlooked dependence is an important one, as we are able to describe from the basic state alone why Vasil and Brummell (2008) could not observe magnetic buoyancy without an exceedingly large shear amplitude. To demonstrate this difference, we will reproduce the basic magnetic field from Silvers et al. (2009); Vasil and Brummell (2008).

To confirm the initial conditions of Vasil and Brummell (2008) and Silvers et al. (2009) we solve Eqs (5.8)-(5.12) for both sets of parameters shown in Table 5.1. First, we start with the parameters shown in Vasil and Brummell (2008) and, as they did, consider zero initial shear flow.

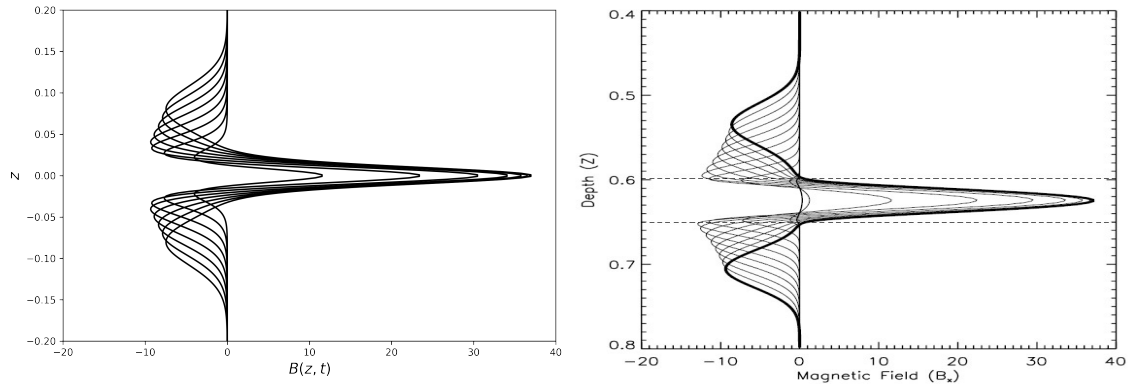

(a) (b)

Figure 5.9: Evolution of the horizontal magnetic field from our numerical solver (left) and from Vasil and Brummell (2008) (right), up to $t \approx 3.4$. Lines represent every 0.4 time units. Parameters are listed in Table 5.1.

Figure 5.9 shows the numerical solution for the horizontal magnetic field that we calculate (left) and that calculated by Vasil and Brummell (2008) (right). Comparison of Fig 5.9(a) and (b) shows that there is good agreement between our numerical results and the basic

magnetic field within Vasil and Brummell (2008): we conclude that the initial conditions in that paper must have been zero initial target flow. If we consider the same parameter values and solve Eqs (5.8)-(5.12) for an initial target flow, the magnetic field amplitude is significantly larger. Figure 5.10 shows the magnetic field generated from an initial

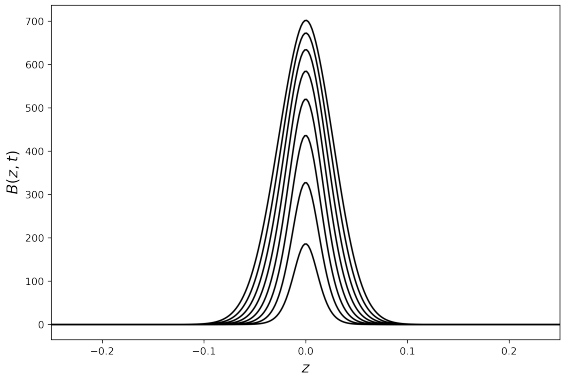

Figure 5.10: Magnetic field for the parameters within Vasil and Brummell (2008) for an initial target flow.

target flow with the parameters used by Vasil and Brummell (2008). It can be seen from comparison of Figs 5.9-5.10 that starting with an initially established flow would result in a magnetic field several orders of magnitude larger than that which is generated from zero initial target flow. Again, it is seen in Fig 5.10 that an initial target flow results in an initially growing magnetic field; however there are no negative lobes that travel outwards. We can infer from Fig 5.3 that if Vasil and Brummell (2008) had started with an initial target flow, the resultant horizontal velocity would be similar to the target flow, and therefore would be highly supersonic: this resultant flow would have been unstable, and inhibited by hydrodynamic instabilities.

We now perform a similar analysis for the parameters of Silvers et al. (2009). The resultant horizontal magnetic field from an initially established target flow is shown in Fig 5.11.

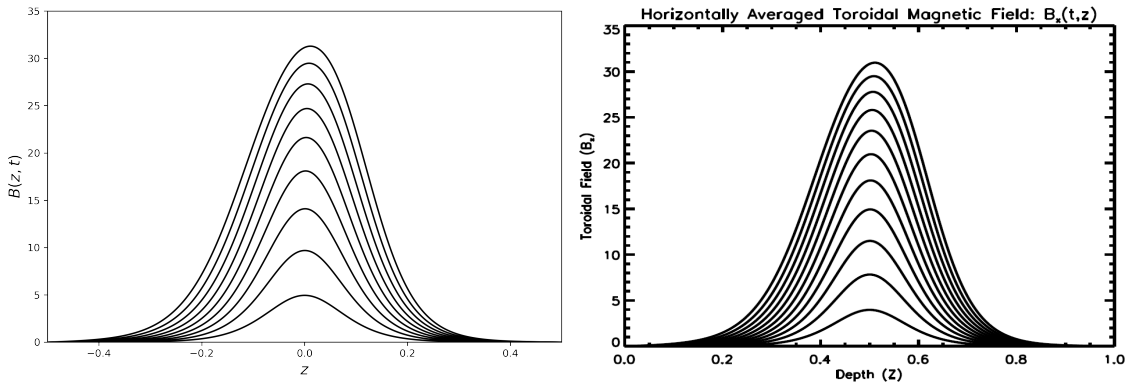

(a) (b)

Figure 5.11: Evolution of the horizontal magnetic field from our numerical solver (left) and from Silvers et al. (2009) (right), up to $t \approx 90$. Lines represent every 10 time units. Parameters are listed in Table 5.1.

It can be seen in Fig 5.11 that there is good agreement between our numerical results and the background magnetic field calculated by Silvers et al. (2009), and therefore we conclude that the authors considered an initial target flow. We also consider the evolution of the magnetic field if Silvers et al. (2009) were to consider zero initial target flow: the evolution of the magnetic field is shown below in Fig 5.12. It is clear from Figs 5.9-5.12

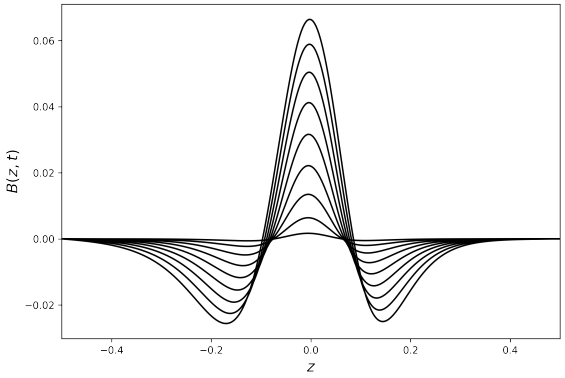

Figure 5.12: Magnetic field for the parameters within Silvers et al. (2009) for zero initial flow.

that the choice of initial horizontal flow is a dominant factor in the subsequent evolution of the horizontal magnetic field. We conclude that the initial conditions are different between the two papers, and can infer from comparison of Figs 5.9 and 5.11 that if Vasil and Brummell (2008) had considered an initial target flow, such stringent conditions on the amplitude of the shear forcing would not have been observed. It is clear that an initial target flow leads to a 'healthier' growth of the magnetic field regardless of forcing amplitude. Throughout the remainder of this chapter, we will use the parameters given in Table 5.1 of Silvers et al. (2009) unless otherwise stated.

5.5 Quasi-Static Linear Stability Analysis

In this section, we will perform a quasi-static linear stability analysis for both initial conditions given by Eqs (5.19)-(5.20). Since the background state in this section are steady, the numerical methods from §3.2.4 are applicable, and so any discussion of the numerical approach will be brief. We will show that for zero initial flow, performing a quasi-static (and subsequently a time-dependent) linear stability analysis is not necessary: the linear stability of the equilibrium state described in Chapter 3 is representative of the transient stability.

5.5.1 Discussion of the Quasi-Static Analysis and Solution Method

As mentioned in §5.1, the quasi-static analysis is an important next step towards a full time-dependent linear stability analysis. It has been shown in §5.3 that the transient evolution of the basic state depends heavily on the initial conditions. Furthermore, the equilibrium state that results from the long-term evolution of the basic state can be

very different to that of the transient state that proceeded it. Therefore, the type of analysis performed in Chapters 2-3 is not sufficient to study the linear stability of what is, ultimately, a time-dependent process. However, it was shown in Chapter 4 that including time-dependence is not straightforward.

The quasi-static analysis is more complicated than that of an equilibrium analysis as knowledge of how the basic state evolves in time is essential. However, a quasi-static analysis is simpler than the full time-dependent linear calculation, as the evolution of the basic state in the linear equations can be ignored, and an instantaneous stability analysis is carried out. This allows a normal-mode analysis to be performed. As we will show, performing this frozen-in-time linear stability analysis at various times in the evolution of the basic state can provide insight into what instabilities might be present at given times. Of course, in the fully time-dependent case, the time-dependence of the disturbances is not necessarily exponential, and so performing a quasi-static analysis provides mostly a qualitative description of the instabilities. Nevertheless, we will show that this approach can be used to inform the full time-dependent analysis.

The fundamental approach to the quasi-static analysis is the same as for the steady case described in Chapter 2-3: however, for completeness, we describe the approach here. We perform small perturbations to the basic state, at a given time t^*,

$$\boldsymbol{U} = (U(z,t^*) + u, v, W(z,t^*) + w), \tag{5.37}$$

$$\boldsymbol{B} = (B(z,t^*) + b_x, b_y, 1 + b_z), \tag{5.38}$$

$$\Theta = T_0(z,t^*) + \hat{T}, \tag{5.39}$$

$$\rho = \rho_0(z,t^*) + \hat{\rho}. \tag{5.40}$$

We substitute Eqs (5.37)-(5.40) into Eqs (5.1)-(5.6), retaining terms linear in perturbed quantities. It is then useful to perform a poloidal-toroidal decomposition (see Eqs (2.55)) to ensure the solonoidal condition on the magnetic field is satisfied for all times. We then perform a normal mode analysis, and look for solutions of the form

$$f(\boldsymbol{x},t) = \hat{f}(z)\exp\{ikx + ily + st\} + \text{c.c.}, \tag{5.41}$$

where s is the complex growth rate and (k,l) are the horizontal wavenumbers. Owing to the size of the system of linear equations they are expressed fully in Appendix C. We recast the linear equations in the form

$$\mathcal{L}_1\boldsymbol{G} = s\mathcal{L}_2\boldsymbol{G}, \tag{5.42}$$

where $\mathcal{L}_1$ and $\mathcal{L}_2$ are linear differential operators, containing the basic state at time t^*, and $\boldsymbol{G} = (\rho, u, v, w, h, g, T)^T$. We consider stress-free and zero temperature boundary conditions such that

$$\frac{\partial u}{\partial z} = \frac{\partial v}{\partial z} = w = T = 0 \quad \text{on} \quad z = \pm\tfrac{1}{2}. \tag{5.43}$$

We consider zero current magnetic boundary conditions, such that

$$\frac{\partial h}{\partial z} = g = 0 \quad \text{on} \quad z = \pm\tfrac{1}{2}, \tag{5.44}$$

which is equivalent to

$$b_x = b_y = \frac{\partial b_z}{\partial z} = 0 \quad \text{on} \quad z = \pm\tfrac{1}{2}. \tag{5.45}$$

Using the numerical schemes discussed in §3.2.4, we can then solve Eq (5.42) subject to Eqs (5.43)-(5.44) as an eigenvalue problem in s, given a basic state configuration at time t^*. Now we are equipped to perform quasi-static analysis for both horizontal flow initial conditions given by Eqs (5.19)-(5.20).

5.5.2 Initial Target Flow in the Basic State

First, we consider the quasi-static linear stability of a magnetic field generated from an initial target flow. We first evolve the basic state according to Eqs (5.8)-(5.12) up to a time $t = 200$. It has already been shown that density and temperature are generally static, and the magnitude of the vertical velocity remains small: for this reason, we will only show the evolution of the horizontal magnetic field and flow. Furthermore, throughout the following calculations, it will be understood that any reference to the basic-state means the solution to Eqs (5.8)-(5.12); however, we will discuss only the field, B, and the flow U. It can be seen in Fig 5.13 that the magnetic field grows in time before saturating

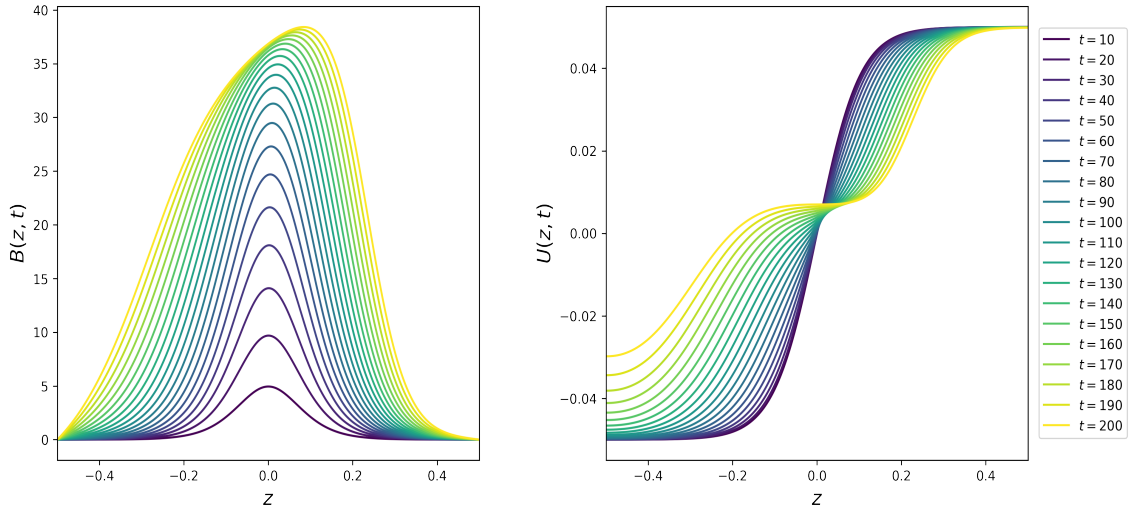

Figure 5.13: The magnetic field (left) and horizontal flow (right) generated from an initial target flow. Lines indicate the evolution every 10 time units up to $t = 200$.

at a maximum. Furthermore, it can be seen that the magnetic field begins to skew to the lower half of the domain due to an increased density: this results from Alfv́en waves propagating slower. It can be seen in Figs 5.13 that the velocity begins to spread out in the center of the domain, with the the absolute magnitude becoming smaller at the upper boundary, while the velocity at the lower boundary generally remains constant. The density and temperature field do not evolve significantly from the initial conditions

given by Eqs (5.16)-(5.17). We solve the linear system given by Eqs (C.6)-(C.15) for the frozen-in-time basic state for a series of times, in (k, l) space.

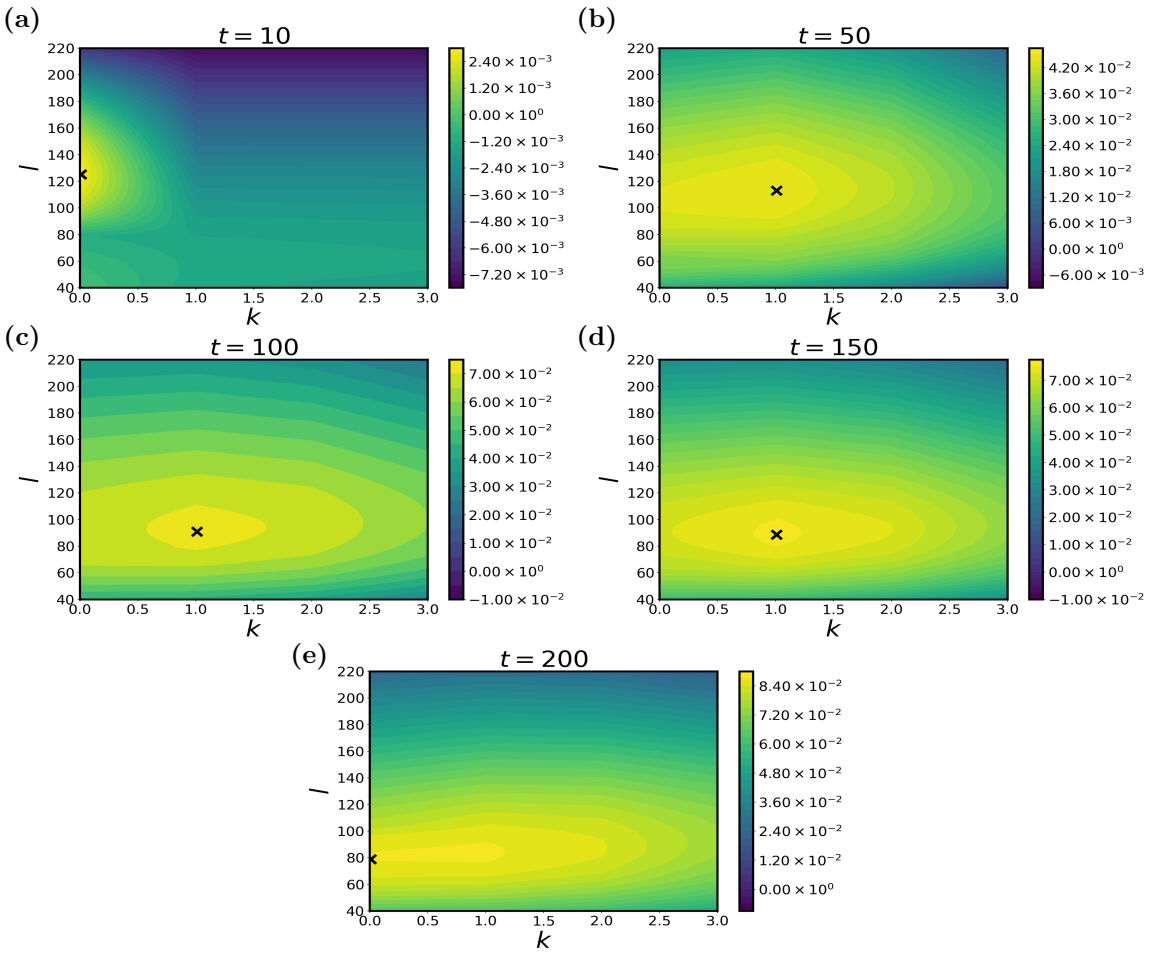

Figure 5.14: The growth rate at various times in (k, l) space for the 'frozen-in' basic state generated from an initial horizontal target flow. The times are; (a) $t = 10$, (b) $t = 50$, (c) $t = 100$, (d) $t = 150$, (e) $t = 200$.

Figure 5.14 demonstrates the linear stability for the basic state in (k, l) space for a series of times. It is shown in Fig 5.14(a) that by $t = 10$ instability is present and the optimal mode of instability is an interchange instability (i.e. $k = 0$). It is shown by Fig 5.14(b)-(d) that further evolution of the basic state results in more wavenumbers becoming unstable, that is to say, there are very few regions of stability shown for $0 \leq k \leq 3$ and $40 \leq l \leq 220$. Interestingly, it can be seen from Figs 5.14(b)-(d) that for $50 < t \leq 150$ the optimal mode of instability is given by a 3D undular mode. It is further shown in Fig 5.14(e) that evolving the basic state further until $t = 200$ results in an optimal mode of instability in the form of an interchange. Figures 5.14 show that as the basic state evolves, the optimal mode of instability is very different physically. Furthermore, it is clear from Figs 5.14 that up until $t = 200$ the growth rate increases; i.e., the basic state becomes more susceptible to instabilities in time. Furthermore, while the optimal mode of instability is an interchange at $t = 200$, we can see that there will be multiple 3D undular instabilities onset at this time, of a similar growth rate — this can be seen by the largest contour,

which is narrow and extends to $k \approx 1$.

To further investigate the instabilities present in Figs 5.14, we restrict our attention to the l-axis and set $k = 0$, and consider interchange instabilities. Analogous to taking cross-sections of Figs 5.14 along the l-axis, we solve Eqs (C.6)-(C.15) for increasing l, for the series of basic configurations shown in Figs 5.13. Interestingly, the bottom panel of

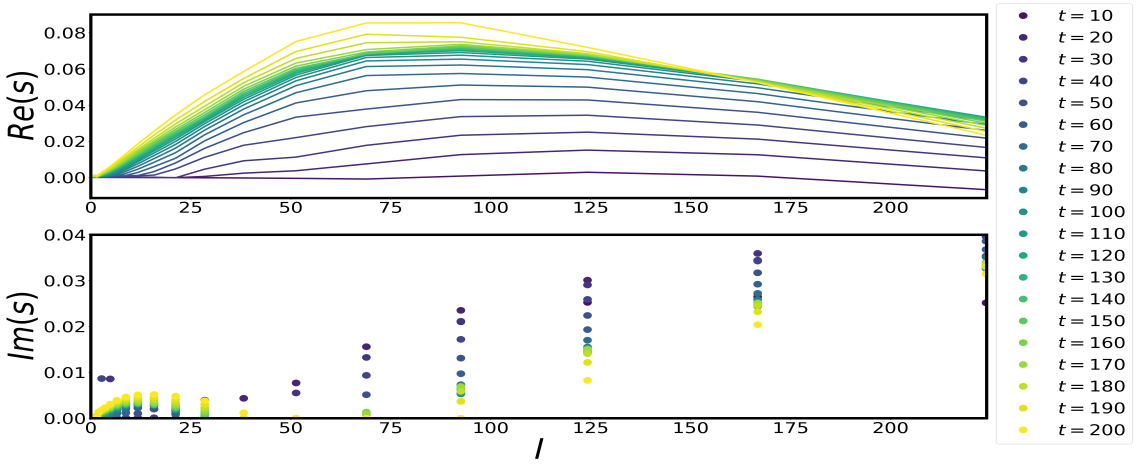

Figure 5.15: The growth rate (top) and frequency (bottom) vs. l for various times in the evolution of the basic state generated from an initial horizontal target flow. Here $k = 0$.

Figs 5.15 shows that instabilities can be either oscillatory or stationary: it is clear that in the earlier stages of the evolution of the basic state, the optimal instability along the l-axis is travelling, and therefore has non-zero frequency. It is important to note that the travelling solutions appear as a complex pair and the oscillatory waves travel in opposite directions: these travelling interchanges are a result of the shear flow as they are not present in the magnetic buoyancy problem in the absence of flow. The yellow-most line in Figs 5.15 demonstrates however, that by $t = 200$, the dominant mode is stationary and has zero frequency. Furthermore, it can be seen in Figs 5.15 that the optimal wavenumber for interchange instability is generally smaller at later times than for earlier times. To illustrate this further, we can discern a path through $l - t$ space for the optimal growth and wavenumber, equivalent to optimising the curves shown in Figs 5.15 over the l-axis: this is shown in Fig 5.16. The maximal growth rate and associated wavenumber for a given time is shown in Fig 5.16. It can be seen in Fig 5.16 that the maximal growth increases in time: it is shown that that maximal growth increases generally linearly in time for $t \leq 75$, and then slows down, plateauing, until the growth rate rapidly increases in time again at $t \geq 175$. Figure 5.16 shows the variation of the optimal wavenumber in time. The optimal wavenumber generally decreases before rapidly falling off at $t \approx 60$. After that, the optimum wavenumber slightly increases with time until $t \approx 150$, after which it generally decreases. Overall, it is shown in Fig 5.16 that the optimal wavenumber is smaller at larger times than it is initially.

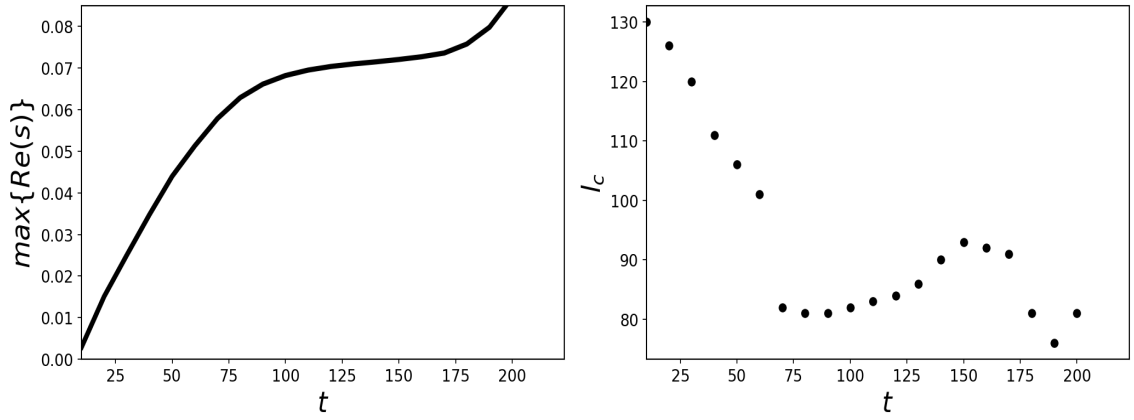

Figure 5.16: Maximum growth rate (left) and associated optimal wavenumber (right) as a function of time, for an initial horizontal target flow.

5.5.3 Zero Initial Flow in the Basic State

We now perform an analysis analogous to that in §5.5.2, but for the initial condition of zero horizontal velocity. We have shown in §5.3 that the basic state generated from zero initial flow is not very different to that of the final state, and this final state (for the parameters in Table 5.1) was found to be stable. Again, the density and temperature variations do not deviate significantly from the initial conditions and so in Figs 5.17 we just show the basic state field and flow.

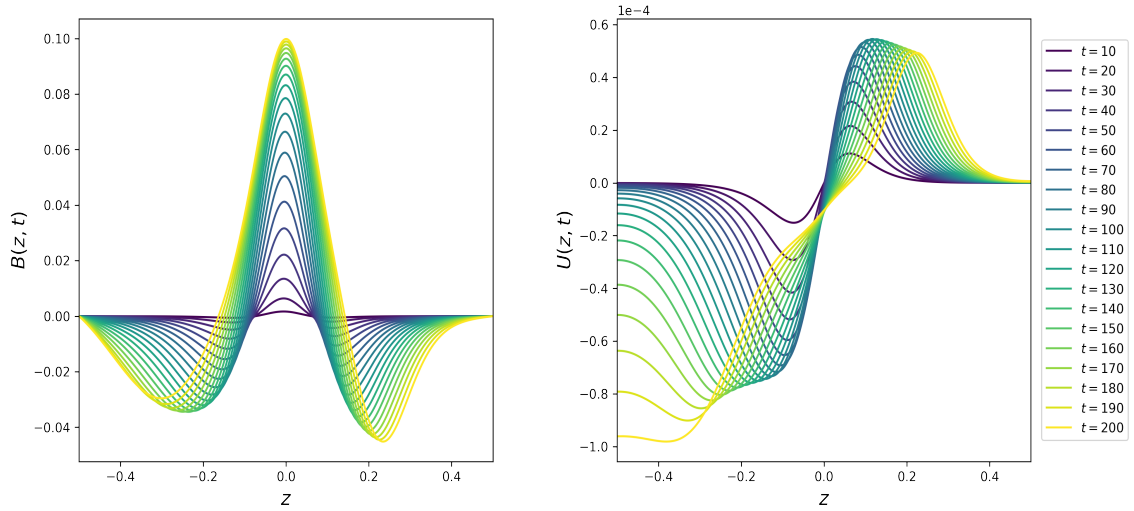

Figure 5.17: The horizontal magnetic field (left) and horizontal flow (right) generated from zero initial flow. Lines indicate the evolution every 10 time units up to $t = 200$.

We have already discussed the evolution of the basic state in great detail; however Figs 5.17 shows that the basic field and flow initially grow, before reaching an optimum value and being inhibited by Alfvén waves. We perform a quasi-static analysis for a series of times in (k, l), with the results for the largest growth rate and associated frequency being shown in Figs 5.18. It is shown in Figs 5.18 that instability is not onset throughout the evolution of this basic state. Figure 5.7 illustrates that for the case of zero initial horizontal velocity,

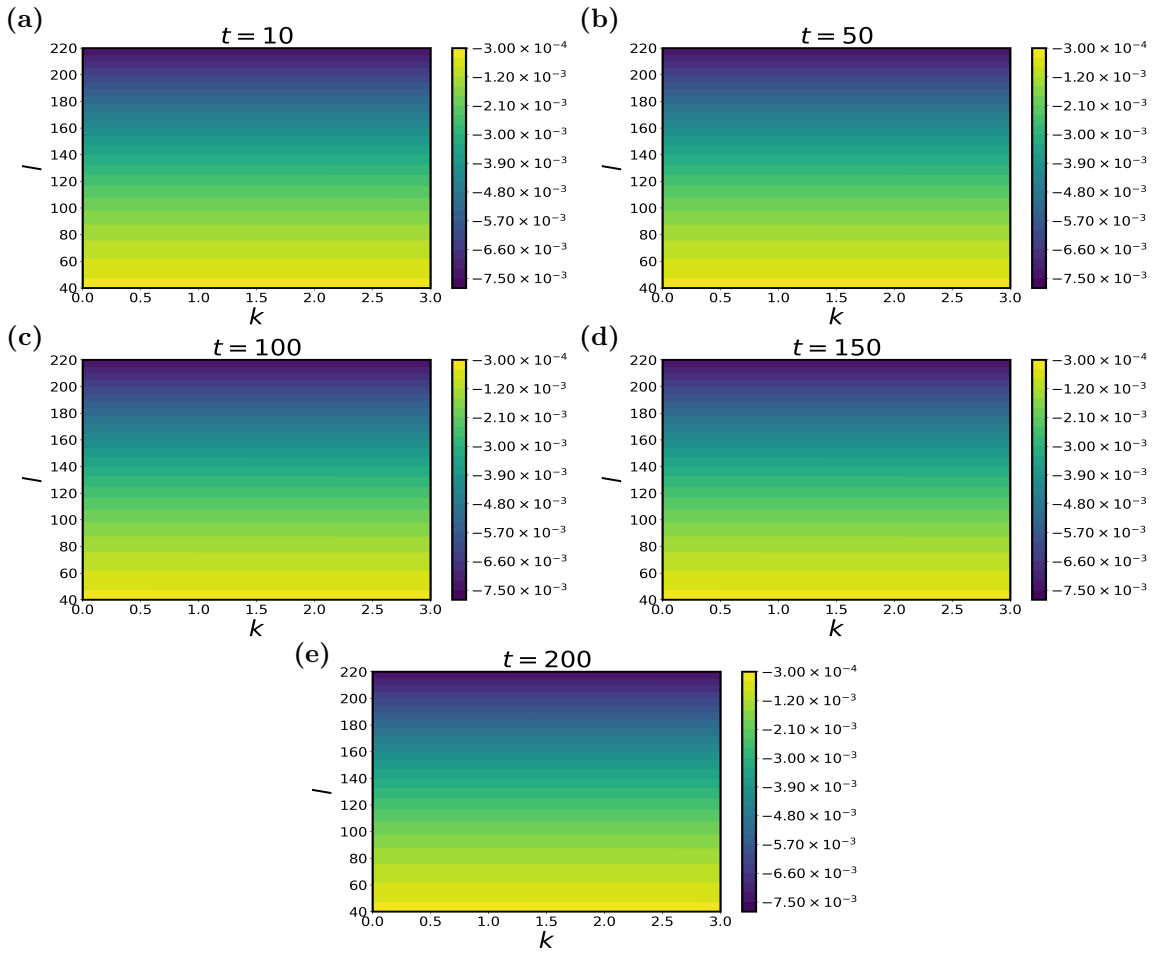

Figure 5.18: The growth rate at various times in (k, l) space for the 'frozen-in' basic state generated from zero initial horizontal flow. The times are; (a) $t = 10$, (b) $t = 50$, (c) $t = 100$, (d) $t = 150$, (e) $t = 200$.

the maximum value of the magnetic field does not vary significantly in time, and therefore we conclude that any subsequent basic state evolution does not result in instability. Figures 5.18 further justifies the conclusion that the final-state analysis described in Chapter 3 is indicative of the time-dependent linear stability, at least for the parameters used here. For completeness, we take cross-sections of Figs 5.18 at $k = 0$, for a series of times, and plot the resultant growth and frequency in Figs 5.19.

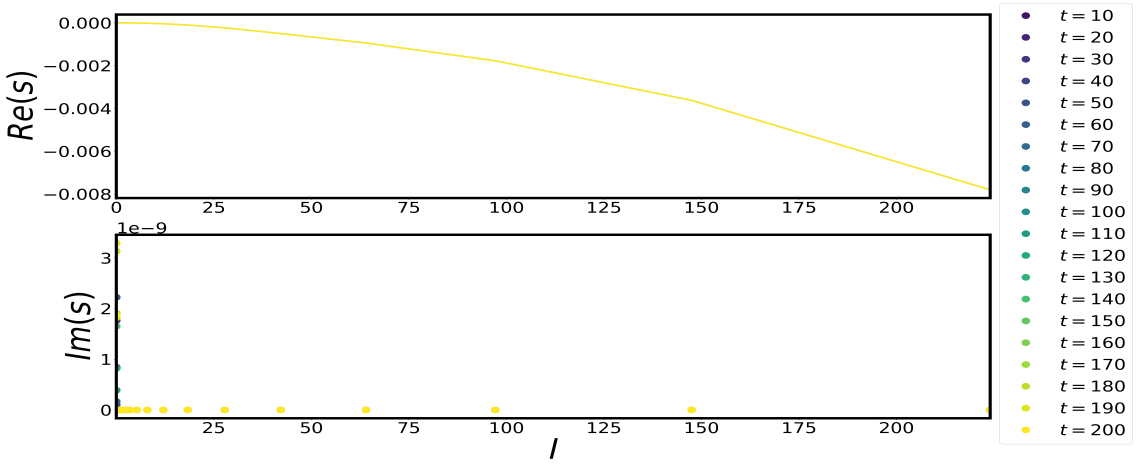

Figure 5.19: The growth rate (top) and frequency (bottom) vs. l for various times in the evolution of the basic state generated from zero initial flow. Here $k = 0$.

Figures 5.19 is analogous to Figs 5.15, and it is clear in Figs 5.19 that all values of l, in the range $0 \leq l \leq 220$ are stable, and the mode with the largest growth rate has zero frequency.

5.5.4 Field Reversal

In this section, we perform an analogous analysis to §5.5.2 but for longer times, i.e. $t \geq 900$. This is an interesting regime, as we have shown in Fig 5.3 that at approximately $t = 700$, the magnetic field undergoes a reversal, and changes sign. When the horizontal magnetic field reverses, it increases in magnitude until reaching a local minimum. This leads us to consider whether this configuration is more unstable than its positive counterpart. To investigate the evolution of the instability described in §5.5.2, we evolve the basic state up to $t = 900$, and then solve Eqs (C.6)-(C.15) for a series of times, in (k, l) space. The horizontal magnetic field and flow are shown in Figs 5.20. It can be seen that the resultant flow initially deviates from the target profile, by spreading out in the centre of the domain, leading to a shear region larger than the target, i.e. $\Delta z \sim 1/\lambda$. Comparison of the field and flow in Fig 5.20 shows that the flow 'reverses' before the magnetic field, and at some times has a larger magnitude than that of the target profile.

To gain insight into the structure of the resultant instabilities due to the field reversal, we solve Eqs (C.6)-(C.15) in (k, l) space for $t = 700$ and $t = 900$. The motivation for choosing these times is that at $t = 700$ the magnetic field is close to reversing and changing sign. We have seen in Figs 5.14 that at $t = 200$ the preferred mode of instability was an interchange: we wish to see if this is still the case when the magnetic field amplitude has decreased before reversal. The time $t = 900$ is interesting because this is the time at which the magnetic field has achieved a local minimum. Figure 5.21(a) shows that at $t = 700$, even when the magnetic field is small (see Fig 5.20), there is still instability. It is shown in Fig 5.21(a) that the dominant mode of instability is an interchange. We cannot conclude from Figs 5.14 and Fig 5.21(a) that the dominant mode of instability between

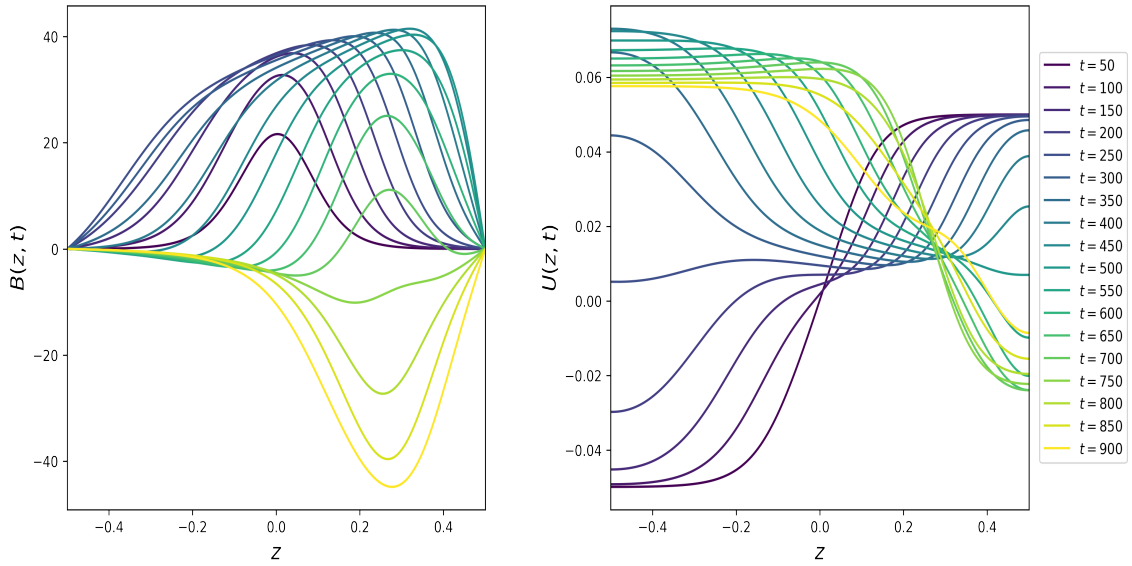

Figure 5.20: The horizontal magnetic field (left) and horizontal flow (right) generated from an initial target flow. Lines indicate the evolution every 50 time units up to $t = 900$.

$t = 200$ and $t = 700$ is an interchange mode. However, comparison of Figs 5.14 and 5.21(a) shows that the resultant interchange mode at $t = 700$ has a larger wavenumber, and is more stable; the interchange mode at $t = 200$ has a growth rate an order of magnitude larger. Although at $t = 700$, the horizontal magnetic field is about to undergo reversal and is small in amplitude, it is still sufficient to drive instability.

Figure 5.21(b) shows the largest growth rate in (k, l) space at $t = 900$. At this time, the magnetic field has fully reversed and has reached a local minimum with amplitude -40. It is shown in Fig 5.21(b) that this negative magnetic field is sufficient to drive instability, with the preferred mode of instability being a 3D undular. The growth rate of the 3D undular mode at $t = 900$ is larger in magnitude than the interchange instability at $t = 700$; however, comparison of Figs 5.21(b) and 5.14(c) -(d) shows that the preferred 3D undular mode at $t = 100, 150$ has a larger growth rate. Figure 5.20 shows that the horizontal magnetic field at $t = 100, 150$ is smaller in magnitude than that at $t = 900$; however, from numerical results shown in Figs 5.21(b) and 5.14(c) -(d), we conclude that the magnetic field after reversal is more stable than prior to the reversal.

We now restrict attention to the evolution of interchange instabilities for $50 \leq t \leq 900$ and solve Eqs (C.6)-(C.15) with $k = 0$, and vary l. Figures 5.22 shows the growth rate and frequency as a function of l for various basic state configurations. It can be seen that the basic state for $50 \leq t \leq 900$ results in instability, and that there exists an optimal wavenumber which results in maximal growth rate. Generally, we can see from the bottom panel of Fig 5.22 that the optimal instability is oscillatory. Although, we note the existence of multiple modes: we can see from the 'kinks' in the lines, for example at $t = 250$, that the instabilities at lower wavenumbers tend to be steady with zero imaginary component. The important point of Fig 5.22 is that the yellow-most line corresponding to a basic state

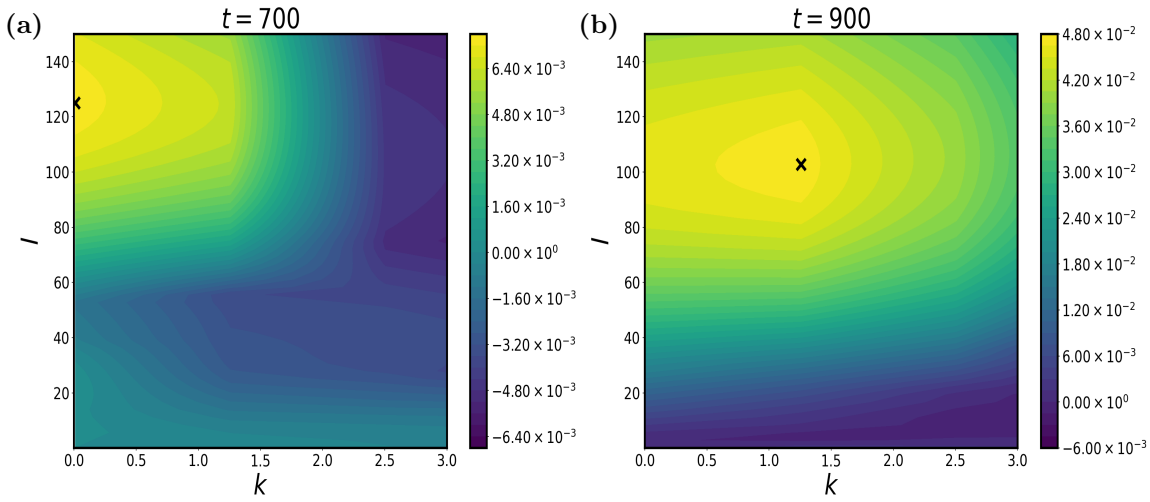

Figure 5.21: The growth rate at various times in (k, l) space for the 'frozen-in' basic state generated from zero initial horizontal flow. The times are; (a) $t = 700$, (b) $t = 900$.

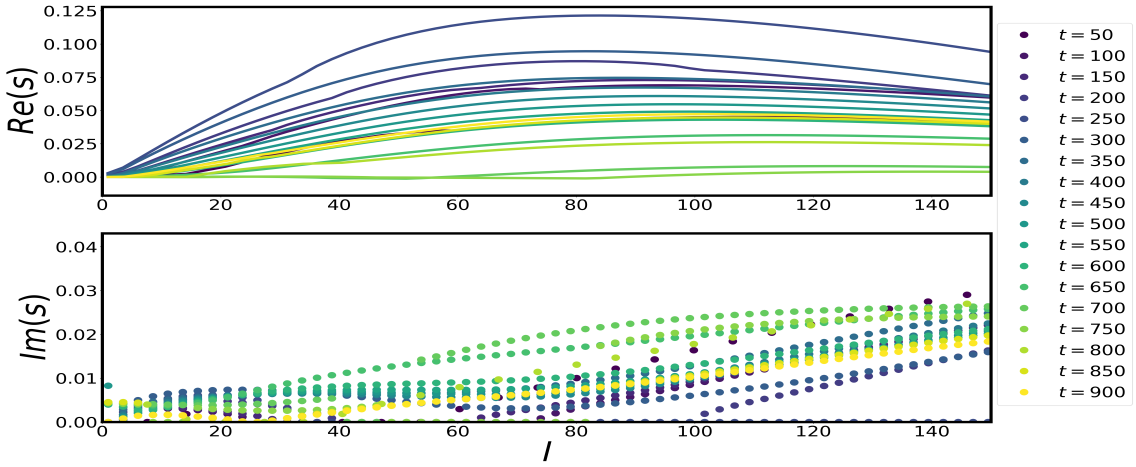

Figure 5.22: The growth rate (top) and frequency (bottom) vs. l for various times in the evolution of the basic state generated from an initial horizontal target flow. Here $k = 0$.

at $t = 900$ is less unstable than the configuration at $t \approx 300$. To illustrate this point more clearly, we calculate the maximal growth rate in time and the associated wavenumber: this is shown in Fig 5.23. It is shown in Figs 5.23 that the maximal growth rate is achieved by the basic state configuration at $t = 250$. Furthermore, the right panel of Figs 5.23 illustrates that the largest growth rates that occur at earlier times have smaller optimal wavenumbers than the less unstable instabilities present at later times. Interestingly, Figs 5.23 shows a local minimum in the range $700 \leq t \leq 750$. The curve corresponding to this time shown in Fig 5.20 shows that in between $t = 700$ and $t = 750$ the magnetic field undergoes its field reversal, and therefore has a small magnitude. Because of this, it is not surprising that the magnetic field within this time interval has the smallest growth rate. Furthermore, the right panel of Figs 5.23 shows that the local minimum in the growth rate corresponds to the largest wavenumber.

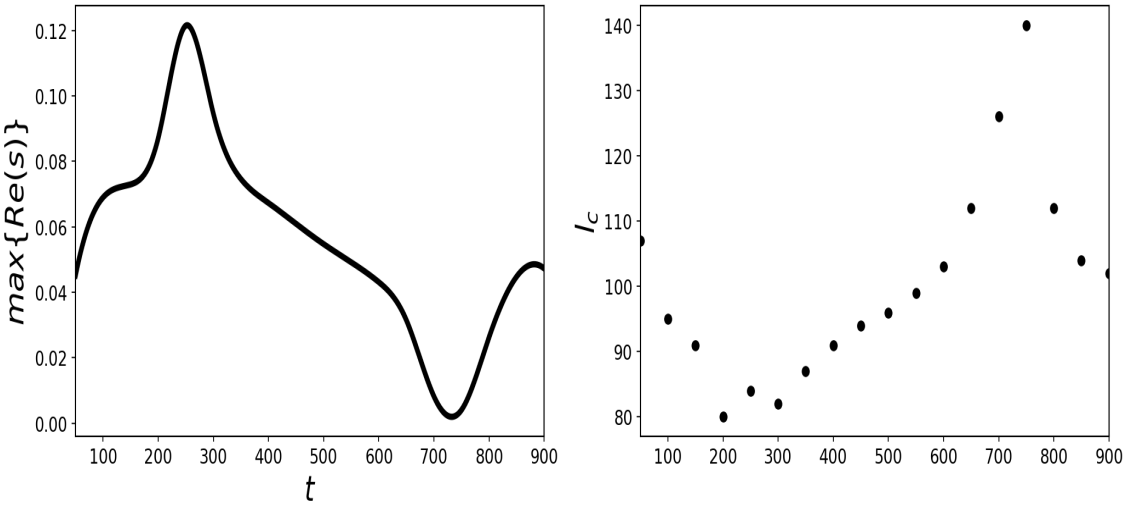

Figure 5.23: Maximum growth rate (left) and associated optimal wavenumber (right) as a function of time, for an initial horizontal target flow, up to $t = 900$.

5.6 Time-Dependent Linear Stability Analysis

In this penultimate section of the Thesis, we discuss the final problem of the linear stability of a time-dependent magnetic field generated from a shear flow. After a thorough discussion of the basic state in §5.3, and the quasi-static linear stability analysis in §5.5, we are equipped to solve this problem. One way to approach this investigation of the stability of an evolving state is to impose a low-level background noise, evolve the perturbations in time, and then to look at the evolution of the linear perturbations. Kerr and Gumm (2017) were interested in a more general approach in their investigation of the thermal instability of a time-dependent basic state, similar to that in §4.6. Kerr and Gumm (2017) were interested in finding the set of initial conditions for the disturbances that lead to the fastest growth. This approach involved following the evolution of all linear instabilities from an initial time, t_0, to some later time, t_1. Then, from a measure of the amplitude (see §4.6.2), they were able to calculate a set of optimal initial conditions through a transfer matrix. The approach of Foster (1965) can now be explained as a less general approach than that of Kerr and Gumm (2017): Foster (1965) chose to measure the kinetic energy relative to the initial conditions (i.e. $t_0 = 0$), and only studied a limited set of initial perturbations to the linear states.

Since we are studying a more complicated system than RBC, we also use a limited approach similar to that of Foster (1965). First, we will derive the set of time-dependent linear equations, which are now much different to the quasi-static system given by Eqs (C.6)-(C.15). We will then provide a brief recap of the numerical methods necessary to evolve the linear equations. We will then motivate our choice of initial conditions for the perturbations, and define a suitable measure of growth. We will show that from this definition of growth, the approach of Foster (1965), i.e. defining a nominal critical time, can lead to incorrect conclusions in this system, since the basic state is not divergent in

time.

We restrict ourselves to the parameters used by Silvers et al. (2009) and using information from §5.5.2, we will consider only interchange modes, i.e. $k = 0$ throughout. However, it is to be understood that the optimal mode of instability is not necessarily an interchange mode at all times. We will now be equipped to evolve the basic state for a variety of initial conditions. We will show that in the case of a zero initial shear flow, the magnetic field that is generated can lead to significant transient growth, although all perturbations decay away for longer times. This is expected, as §5.5.3 shows that the basic state for times up to $t = 200$ are stable in (k, l) space. We will then restrict our attention to the case where the initial horizontal velocity is given by the target flow. Here, we will show that the magnetic and kinetic energies will grow at an algebraic rate: that is to say that the perturbations do not grow exponentially in time. We will show that certain characteristics of the initial conditions are optimal for growth, and that there are particular wavenumbers that are also optimal for growth. Before we conclude, we will motivate our parameter choices, i.e. setting $k = 0$, and choices concerning the initial conditions. We will then discuss the limitations of this approach, and discuss natural extensions of this work.

5.6.1 The Time-Dependent Linear Equations and Numerical Methods

The framework for deriving the set of linear equations is not modified due to the time-dependence of the basic state. We perform small perturbations to the basic state, such that

$$\boldsymbol{U} = (U(z,t), 0, W(z,t)) + \boldsymbol{u}, \tag{5.46}$$

$$\boldsymbol{B} = (B(z,t), 0, 1) + \boldsymbol{b}, \tag{5.47}$$

$$\Theta = T_0(z,t) + \hat{T}, \tag{5.48}$$

$$\rho = \rho_0(z,t) + \hat{\rho}, \tag{5.49}$$

where $\boldsymbol{u} = (u, v, w)$ and $\boldsymbol{b} = (b_x, b_y, b_z)$. We substitute Eqs (5.46)-(5.49) into Eqs (5.1)-(5.6), retaining terms linear in perturbed quantities. It is then useful to perform a poloidal-toroidal decomposition (see Eqs (2.55)) to ensure the solenoidal condition on the magnetic field is satisfied for all times. We then perform a normal-mode analysis, and look for solutions of the form

$$f(\boldsymbol{x}, t) = \hat{f}(z,t)\exp\{ikx + ily\} + \text{c.c.}, \tag{5.50}$$

where (k, l) are the horizontal wavenumbers. Owing to the size of the system of linear equations they are written out fully in Appendix C. We recast Eqs (C.6)-(C.15) in the form

$$\frac{\partial \boldsymbol{G}}{\partial t} = \mathcal{L}_1(t, \boldsymbol{x})\boldsymbol{G}(t, \boldsymbol{x}), \tag{5.51}$$

where $\boldsymbol{G} = (\rho, u, v, w, h, g, T)^T$ and $\mathcal{L}_1(t)$ is a linear differential operator containing the basic state and its associated derivatives at time t. We consider stress-free and fixed

temperature boundary conditions such that

$$\frac{\partial u}{\partial z} = \frac{\partial v}{\partial z} = w = T = 0 \quad \text{on} \quad z = \pm\tfrac{1}{2}. \tag{5.52}$$

We consider zero current magnetic boundary conditions, such that

$$\frac{\partial h}{\partial z} = g = 0 \quad \text{on} \quad z = \pm\tfrac{1}{2}, \tag{5.53}$$

which is equivalent to

$$b_x = b_y = \frac{\partial b_z}{\partial z} = 0 \quad \text{on} \quad z = \pm\tfrac{1}{2}. \tag{5.54}$$

By construction, Eqs (C.6)-(C.15) are linear, and therefore we use a fully implicit time-stepping scheme. To be consistent with the basic state time-stepping scheme, we utilise the Crank-Nicolson method, which is second order in time. We define the time step Δt as the time elapsed between iterations, and the time at the i-th iteration is given by $i\Delta t$. Equation (5.51) written in the Crank-Nicolson stencil is given by

$$\frac{\boldsymbol{G}(t^{i+1}, \boldsymbol{x}) - \boldsymbol{G}(t^{i}, \boldsymbol{x})}{\Delta t} = \frac{1}{2}\Big(\mathcal{L}_1(t^{i+1}, \boldsymbol{x})\boldsymbol{G}(t^{i+1}, \boldsymbol{x}) + \mathcal{L}_1(t^{i}, \boldsymbol{x})\boldsymbol{G}(t^{i}, \boldsymbol{x})\Big). \tag{5.55}$$

After performing a spatial discritisation in space using FD2 or FD4, the differential operator given by $\mathcal{L}_1$ will be sparse, and therefore we can utilise this to make the numerical approach more efficient. We solve Eq (5.55) for $\boldsymbol{G}(t^{i+1}, \boldsymbol{x})$ through LU-factorisation of a sparse matrix.

5.6.2 Choosing A Measure of Growth of the Disturbances

Here, we will motivate how we decide to measure the growth of disturbances, and therefore classify instability. Foster (1965) chooses to measure the growth of the vertical velocity disturbance by calculating the kinetic energy as a function of time, relative to the kinetic energy of the initial conditions: this expression is given by Eq (4.54). Kerr and Gumm (2017) consider a semi-infinite domain, i.e., where $z \in (0, \infty]$, and allow for the initial conditions for the perturbations to be applied at t_0, after the start of heating. The growth is monitored through a 'generalized' energy, of the form

$$E(t) = \frac{1}{2P}\int_0^{\infty}\int_0^{P} \left(|\boldsymbol{u}|^2 + \Lambda T^2\right) \mathrm{d}x\mathrm{d}z, \tag{5.56}$$

where P is the horizontal periodicity of the disturbances, T is their temperature perturbation, $\boldsymbol{u}$ is the velocity perturbation, and Λ is a positive parameter specific to their approach. They consider a semi-infinite domain, and hence $0 \leq z < \infty$. Other measures could be used, for example the enstrophy. Nevertheless, it is clear that there is no strict rule when choosing a suitable measure of growth, and, as such, we have some freedom. Since we consider a compressible MHD system, we have perturbations for the density, temperature, velocity, and magnetic field, and so in a similar vein to Foster (1965) and Kerr and Gumm (2017) we consider a 'generalized' energy. Using an approach similar to

Foster (1965), we consider energies of the form

$$E_X(t) = \frac{\int_{-1/2}^{1/2} |X(z,t)|^2 \mathrm{d}z}{\int_{-1/2}^{1/2} |X(z,0)|^2 \mathrm{d}z}, \tag{5.57}$$

for some quantity, X. For example, X may represent the disturbance to the velocity, temperature, magnetic field, or a linear combination of all state variables. As we will see in the next section, there is a lot of parameter choice in this problem, and so we restrict our attention to the kinetic and magnetic energies, defined by

$$E_K(t) = \frac{\int_{-1/2}^{1/2} |\hat{\boldsymbol{u}}(z,t)|^2 \mathrm{d}z}{\int_{-1/2}^{1/2} |\hat{\boldsymbol{u}}(z,0)|^2 \mathrm{d}z}, \tag{5.58}$$

$$E_B(t) = \frac{\int_{-1/2}^{1/2} |\hat{\boldsymbol{b}}(z,t)|^2 \mathrm{d}z}{\int_{-1/2}^{1/2} |\hat{\boldsymbol{b}}(z,0)|^2 \mathrm{d}z}, \tag{5.59}$$

where hats denote the time-varying, and z-dependent component of the perturbations given by Eq (5.50). All the components of the energy are measured relative to the initial perturbations, and in the case where the initial condition is zero, the numerator is set to unity.

5.6.3 Initial Conditions for the Disturbances and Parameter Choices

There are several lines of enquiry for this problem: there are multiple non-dimensional parameters, a choice of initial condition in the basic state, the choice of measuring the growth of perturbations, and the choice of initial conditions in the perturbed quantities. As discussed in §5.1, the line of enquiry taken by Kerr and Gumm (2017) bypasses the need to chose initial conditions for the perturbations, as they are interested in finding the optimal initial conditions through solving a self-adjoint system. We take a more specific approach and consider a set of initial conditions, similar to the approach of Foster (1965). While this approach is less general than that of Kerr and Gumm (2017), we consider a set of functions for the initial conditions that are from a 'family' of functions, with the hopes that we can draw meaningful conclusions about the perturbations.

The two sets of initial conditions we consider are given by

$$f(z) = \sin n\pi z \quad \text{(Neumann)}, \quad g(z) = \cos N\pi z, \quad \text{(Dirichlet)}, \tag{5.60}$$

$$f(z) = \operatorname{sech}^2 \beta z \quad \text{(Neumann and Dirichlet)}, \tag{5.61}$$

where n and β are positive numbers, Dirichlet corresponds to perturbation quantities which are zero at the boundaries, and Neumann corresponds to perturbation quantities with zero derivative at the boundaries. Therefore, only one function is required for initial conditions of the form given by Eq (5.61) as this function has approximately zero value and derivative at $z = \pm\frac{1}{2}$ for large β. Equations (5.60)-(5.61) are chosen because, similar to Foster (1965),

we will be able to vary either the frequency or width of the initial perturbation, and show how this effects the growth of perturbations. To be more exact, monitoring the transient growth from Eq (5.60)-(5.61), will allow us to conclude whether, for example, the fastest growing mode prefers a higher localisation in z (large β, n). We are free initially to perturb any state quantity, but we will restrict our attention to perturbing only the velocity or magnetic field components with the initial temperature and density perturbations set to zero. In terms of parameters we restrict our attention to those of Silvers et al. (2009), shown in Table 5.1. Finally, we reiterate that in all the following calculations, $k = 0$ unless otherwise stated. We will later show brief numerical results which motivated the choice of $k = 0$, but we reiterate that the preferred mode of instability at any given time may be 3D, i.e. k, $l \neq 0$.

5.6.4 Transient Growth: A Red Herring in Non-modal Stability Theory

Throughout this subsection, we will make clear two problems associated with the initial transient growth of the disturbances; in particular, using the nominal critical time, similar to Foster (1965), can lead to an incorrect conclusion of (optimal) instability. The main purpose of this section is to illustrate the first problem, namely that disturbances which decay away in the long term, can exhibit significant transient growth. This point was touched upon in §5.1; however we will demonstrate this through calculations. We have already shown that the transient basic state that arises from zero initial horizontal flow is not very different to the long term solution. From this, we performed a quasi-static analysis for a series of times in the evolution, and showed that this configuration is stable. To illustrate this point further, one can perform a comprehensive linear stability of the long term equilibrium state. To complement the quasi-static results shown in §5.5.3 we will show that, if we consider a non-modal analysis and time-step Eqs (C.6)-(C.15), the basic state that arises from zero initial horizontal flow is not sufficient enough to result in long term growth of the perturbations. However, as will become clear, the basic state can drive significant initial growth in the perturbations, which will later decay away.

It is stressed that within this subsection, we consider zero initial horizontal flow in the basic state. The remaining initial conditions are defined by Eqs (5.16)-(5.18) unless otherwise stated. To illustrate the transient growth, we will consider initial perturbations only to the magnetic field disturbances. We consider initial magnetic disturbances of the form given by Eq (5.60), and evolve Eqs (C.6)-(C.15), calculating the kinetic and magnetic energy given by Eqs (5.58)-(5.59).

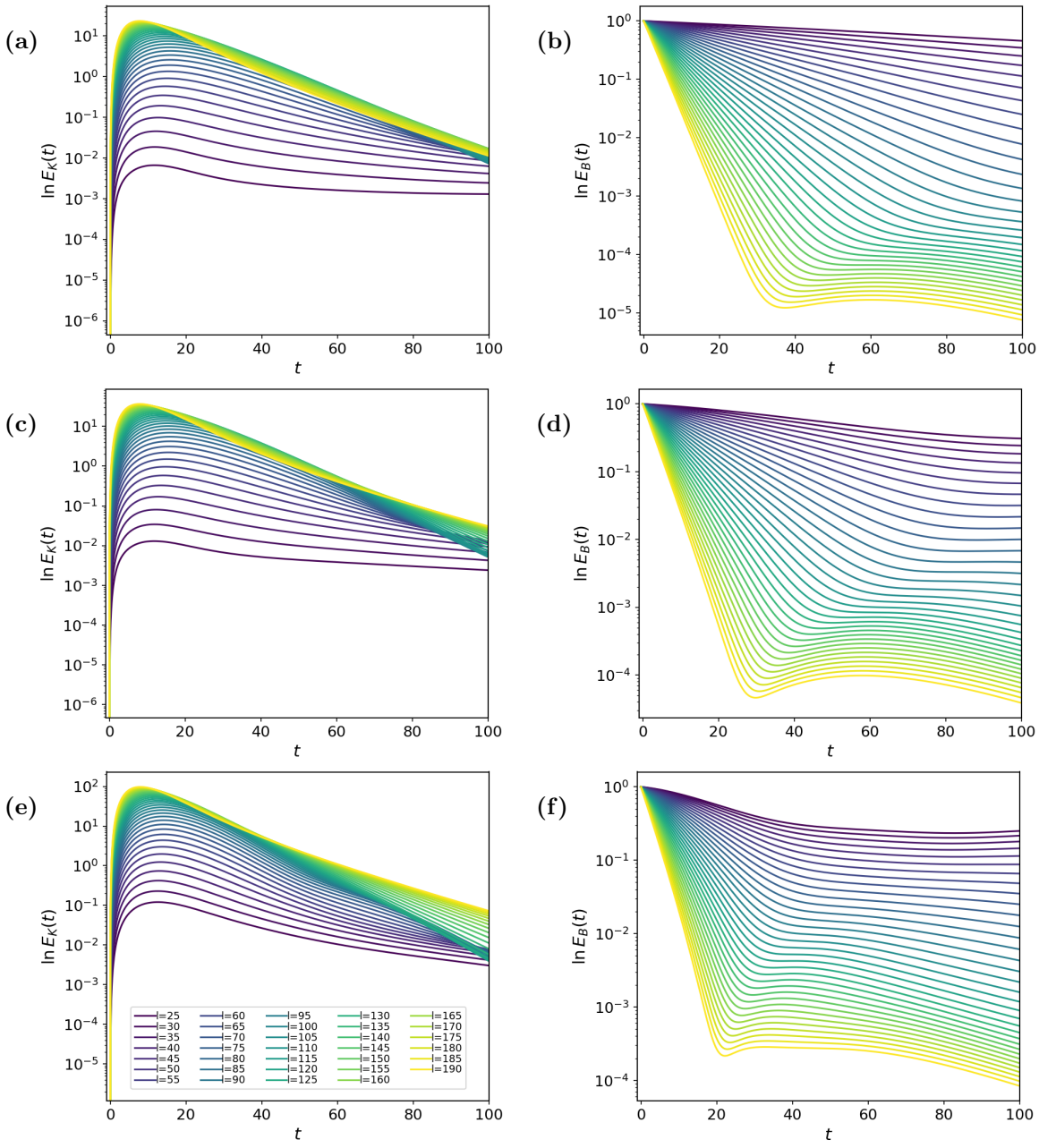

Figure 5.24: The natural logarithm of the kinetic (left) and magnetic (right) energy as a function of time, for an initial Fourier mode perturbation to the magnetic field; (a)-(b) $n = 1$; (c)-(d) $n = 3$; (e)-(f) $n = 7$.

The left and right columns of Fig 5.24 show the kinetic and magnetic energy for three different Fourier modes: $n = 1, 3$, and 7. It can be seen from the right column of Fig 5.24 that the magnetic energy decays in time. From comparison of Figs 5.24(b),(f) it can be seen that increasing the value of n leads to a faster decaying magnetic energy. Furthermore, the right column of Fig 5.24 shows that the largest wavenumber considered, i.e. $l = 190$, decays away the fastest, while the solution with the shortest wavenumber decays the slowest. On the other hand, the left column of Fig 5.24 shows that the kinetic energy of the perturbations increases rapidly before decaying away. It can be seen from Fig 5.24(e) that the modes with larger wavenumbers lead to the largest increase

in kinetic energy before decaying, whereas the solutions with the smallest wavenumbers decay quicker. Again, comparison of Figs 5.24(a) and (e) illustrates that the disturbances achieve a larger transient growth for $n = 7$ than they do for $n = 1$.

The significant increase in the kinetic energy shown in Fig 5.24(e) is a manifestation of transient growth in the velocity disturbances. It can be seen that the kinetic energy grows to $\mathcal{O}(10^2)$. If we were to consider a nominal critical time, similar to Foster (1965), then we might conclude that when the kinetic energy of the disturbance was one or two orders of magnitude larger than the initial condition, that instability has set in. However, as we have shown, this is incorrect, as the disturbances decay, and by $t = 100$, the magnetic and kinetic energy are smaller than those of the initial configuration. To further illustrate the decay of the perturbations, we show the evolution of the modulus of the components of the disturbances responsible for the growth in Figs 5.24(e),(f) . We focus on the modes given by $l = 25$ and $l = 190$.

Figure 5.25 shows the evolution of the disturbances for $l = 25$. Comparison of Figs 5.24 (e), (f) and Fig 5.25 illustrates that both v and w have decayed significantly by $t = 100$ compared with $t \approx 15$. It can be seen in Fig 5.25 that u is the largest velocity component and has not decreased significantly, but this is expected as we can still see in Fig 5.24(e) that the kinetic energy is still $\mathcal{O}(10^{-1})$. Figure 5.25 shows that the magnetic field disturbances, g and h, have not decayed significantly by $t = 100$, but are smaller in magnitude compared to the initial state. This is expected as Fig 5.24(f) illustrates that the mode corresponding to $l = 25$ decays at the slowest rate.

Figure 5.26 is analogous to Fig 5.25 but for $l = 190$. We can see in Fig 5.26 that all the velocity components are much smaller at $t = 100$ than at $t \approx 15$. This is expected, as we can see in Fig 5.24(e) that there is a clear maximum in the kinetic energy at $t \approx 15$; this peak in kinetic energy is $\mathcal{O}(10^2)$ and by $t = 100$ the kinetic energy is $\mathcal{O}(10^{-1})$. Interestingly, the vertical component of the velocity in Fig 5.26 is approximately an order of magnitude larger than the horizontal components, u and v. This shows that the vertical velocity plays an important role in the initial transient growth of the kinetic energy. Figure 5.24(f) shows that the magnetic energy of disturbances with $l = 190$ decay the quickest. This decay is shown in Fig 5.26 and it can be seen that by $t = 20$, the variation in h and g cannot be seen on this scale: it is clear that the magnetic perturbations have significantly decayed by $t = 100$.

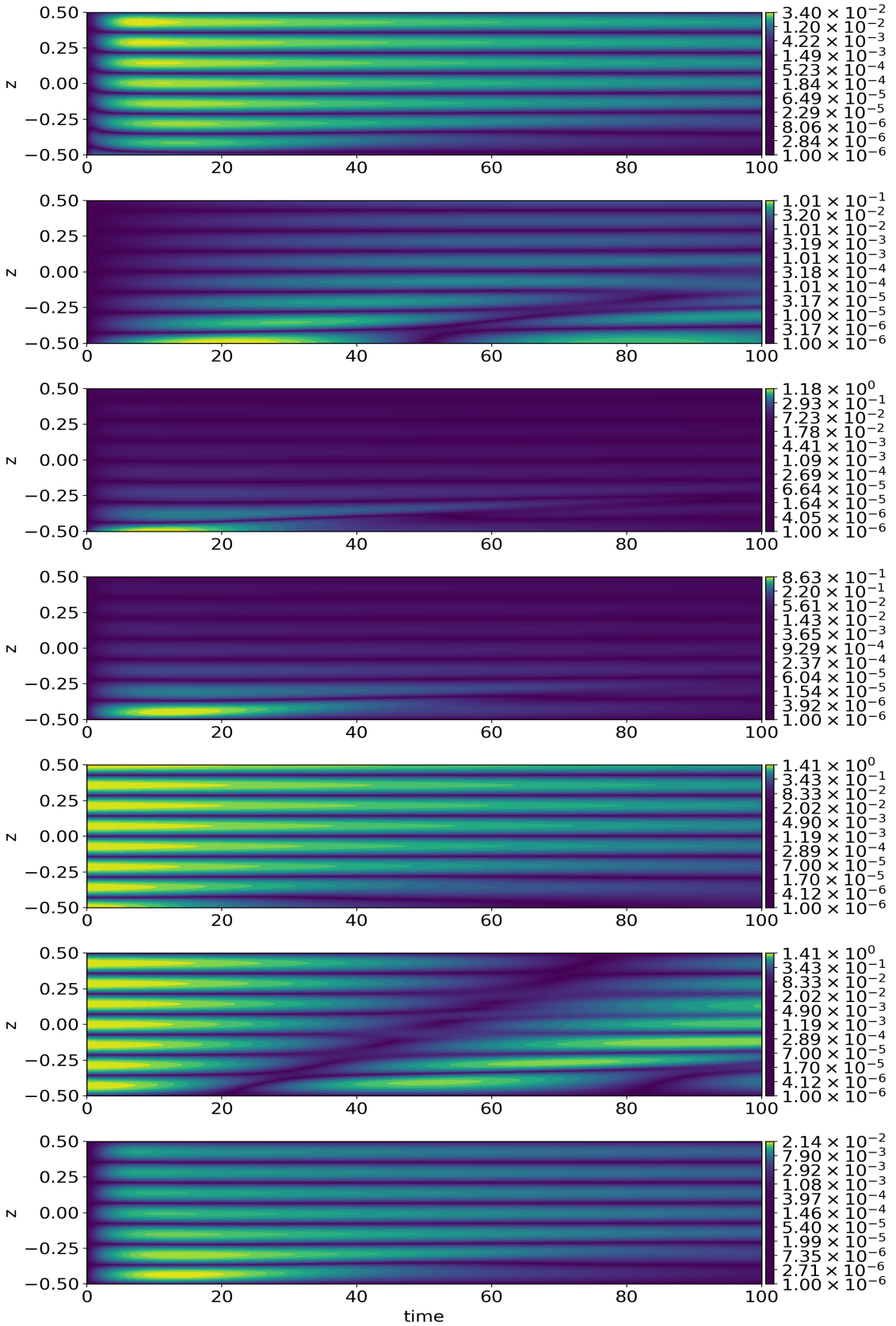

Figure 5.25: Evolution, from top to bottom, of ρ, u, v, w, h, g, T. Here, $k = 0$, $l = 25$, and $n = 7$.

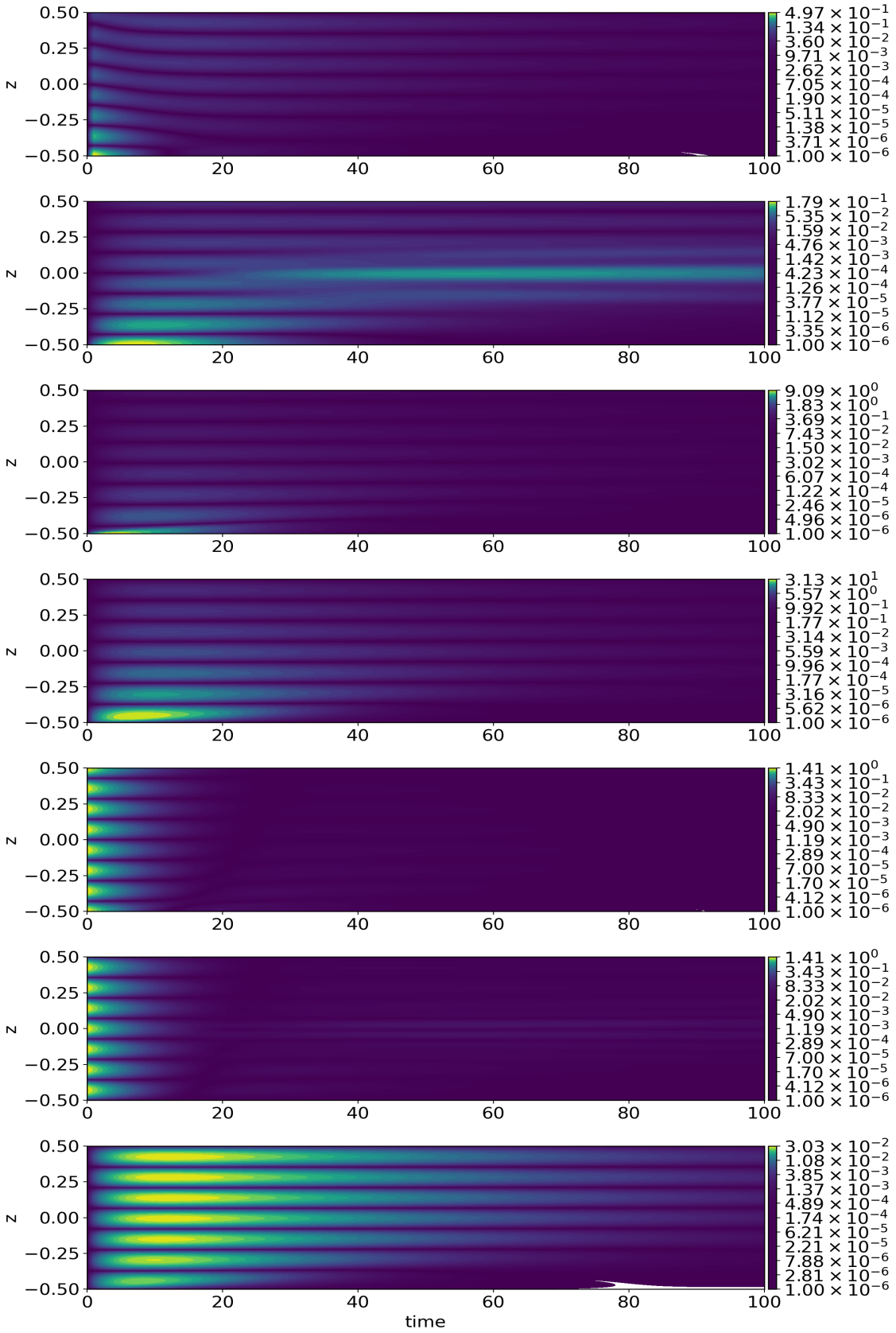

Figure 5.26: Evolution, from top to bottom, of ρ, u, v, w, h, g, T. Here, $k = 0$, $l = 190$, and $n = 7$.

5.6.5 Initial Disturbance: Fourier Mode

We have shown in §5.5.3 and §5.6.4 that the initial condition of zero flow is not sufficient to drive a basic state that can result in long term instability. Therefore, in the remaining sections of this chapter, we will only consider disturbances that result from a basic state generated from an initial target flow. We again consider the parameters given in Table 5.1 by Silvers et al. (2009) and consider interchange instabilities only. The initial conditions for the disturbances are given by Eqs (5.60)-(5.61).

In this subsection, we consider an initial disturbance for either the magnetic field or velocity of the form given by Eq (5.60). We will consider the three Fourier modes given by $n = 1, 3, 7$, and show the subsequent evolution of the disturbances and the associated kinetic and magnetic energy. We consider two cases: first, we initially perturb only the magnetic field components, h and g; second, we initially perturb only the velocity components, u, v, and w.

Initially Perturbing Magnetic Quantities Only

First, we consider a non-zero initial magnetic disturbance. The initial conditions for the disturbances are therefore given by

$$\rho(z,0) = u(z,0) = v(z,0) = w(z,0) = T(z,0) = 0, \tag{5.62}$$

$$h(z,0) = \sin(n\pi z), \quad g(z,0) = \cos(n\pi z). \tag{5.63}$$

We now evolve Eqs (C.6)-(C.15) subject to the initial conditions given by Eqs (5.62)-(5.63), for a series of l such that $25 \leq l \leq 190$. Figure 5.27 shows the kinetic and magnetic energy in time, for a series of wavenumbers and is analogous to Fig 5.24. It can be seen in Figs 5.27(a), (c), (e) that the kinetic energy significantly amplifies in the early stages of the evolution, before the growth of velocity perturbations slows down. It can be seen in Fig 5.27 that the modes with the largest wavenumbers show the most significant transient growth in both kinetic and magnetic energies. However, it is later seen, that at $t = 100$, that $l = 190$ is not the preferred wavenumber for growth. We can see in Figs 5.27(b), (d), (f) that the magnetic energy initially increases rapidly, before decreasing by an order of magnitude. After that, the magnetic energy increases exponentially in time. This illustrates again the issues that would arise if we considered a nominal critical time similar to Foster (1965): the wavenumber that reaches a kinetic energy of $\mathcal{O}(10^3)$ first is not the mode that leads to the largest growth in the long term, and the notion of a nominal critical time, in the sense of Foster (1965), would lead us to conclude that larger wavenumbers are the most unstable.

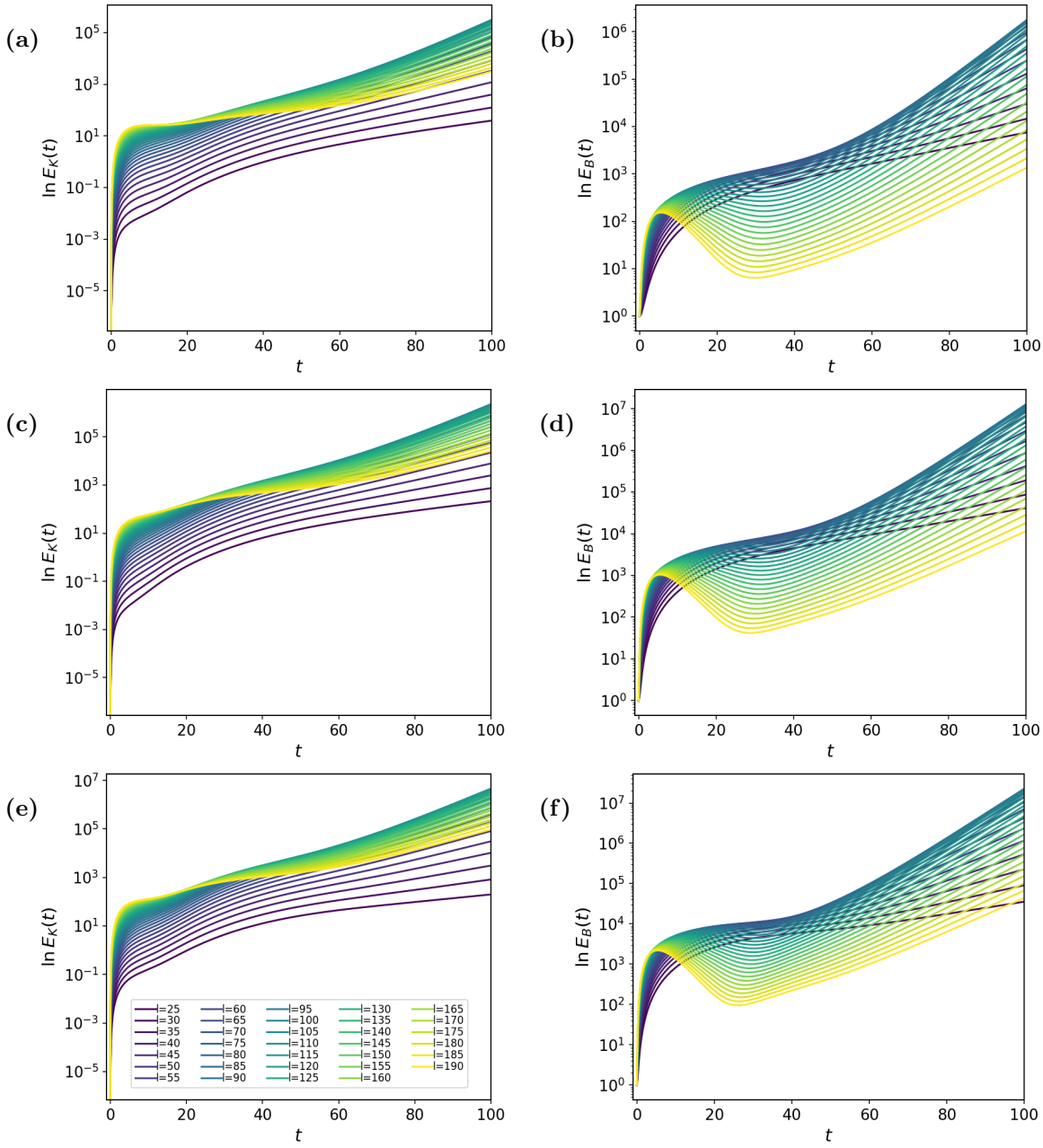

Figure 5.27: The natural logarithm of the kinetic (left) and magnetic (right) energy as a function of time, for an initial Fourier mode perturbation to the magnetic field; (a)-(b) $n = 1$; (c)-(d) $n = 3$; (e)-(f) $n = 7$.

To discern an optimal wavenumber for long term growth of the disturbances, we consider the kinetic and magnetic energies at $t = 100$ and plot these as functions of wavenumber (see Fig 5.28). We can see from Fig 5.28 that the wavenumbers for optimal magnetic and kinetic growth respectively are different; however they are both in the range $75 \leq l \leq 100$. This is consistent with the quasi-static results shown in Fig 5.16, which show that for $t \geq 50$, the wavenumbers responsible for maximal exponential growth exist within this range. Furthermore, we conclude from Fig 5.28 that when we initially perturb the magnetic field only, optimal growth is achieved for an initial condition with more structure in z — this is inferred from the fact that the largest magnetic and kinetic energies are achieved for an

initial Fourier mode with $n = 7$.

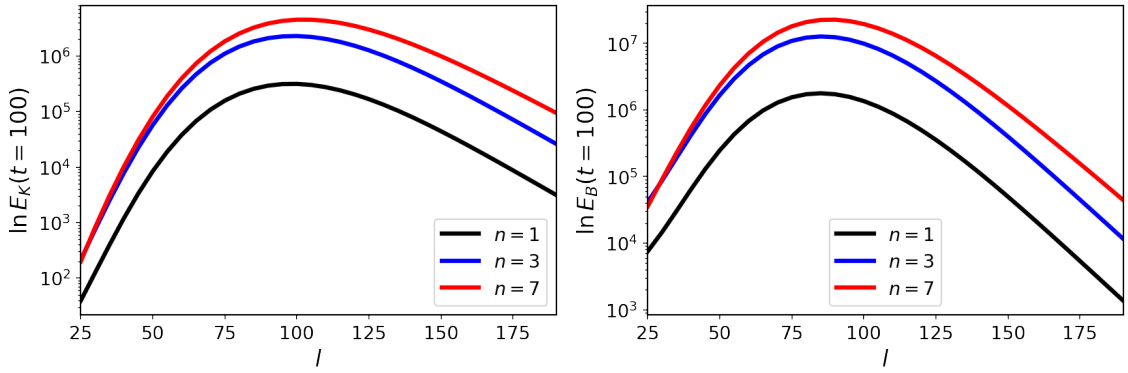

(a) (b)

Figure 5.28: Kinetic energy (left) and magnetic energy (right) at $t = 100$ as a function of l. Here, the initial conditions are Fourier modes in the magnetic field quantities only.

We will now show the evolution of the disturbances for an initial magnetic field configuration corresponding to $n = 7$ with $l = 90$. To capture the full evolution of the perturbations, we show this in three stages: the initial transient growth up to $t = 10$; the evolution up to $t = 50$; and finally, the evolution up to $t = 100$. The motivation for this will be clear later, but it is essentially owing to the scale of the perturbations: the amplitudes increase rapidly in time, and by $t = 100$ the magnitude of the perturbations is significant compared with the early time. Therefore, we cannot see any structure in the transient evolution on this scale.

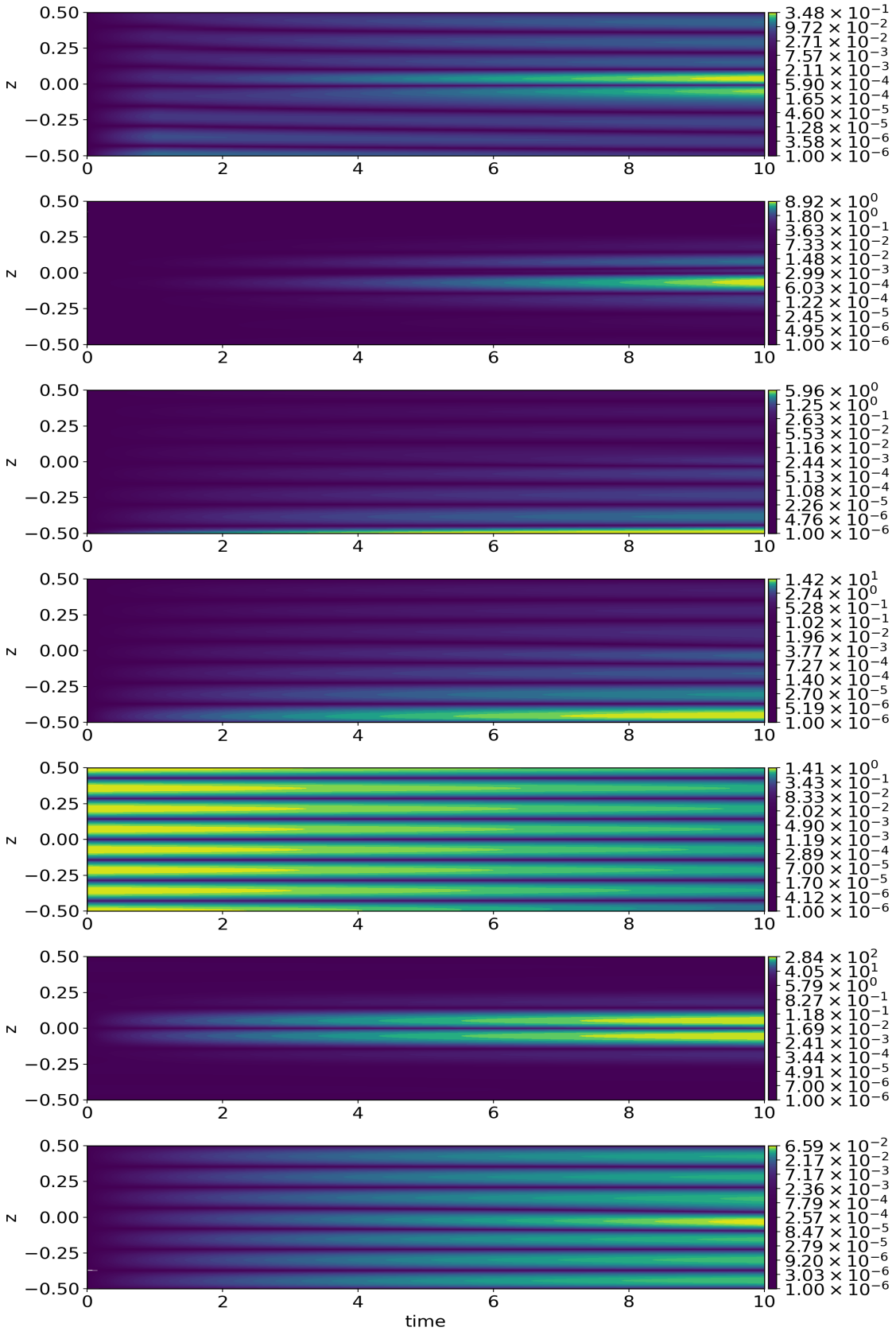

Figure 5.29: Evolution, from top to bottom, of ρ, u, v, w, h, g, T up to $t = 10$. Here, $k = 0$, $l = 90$, and $n = 7$.

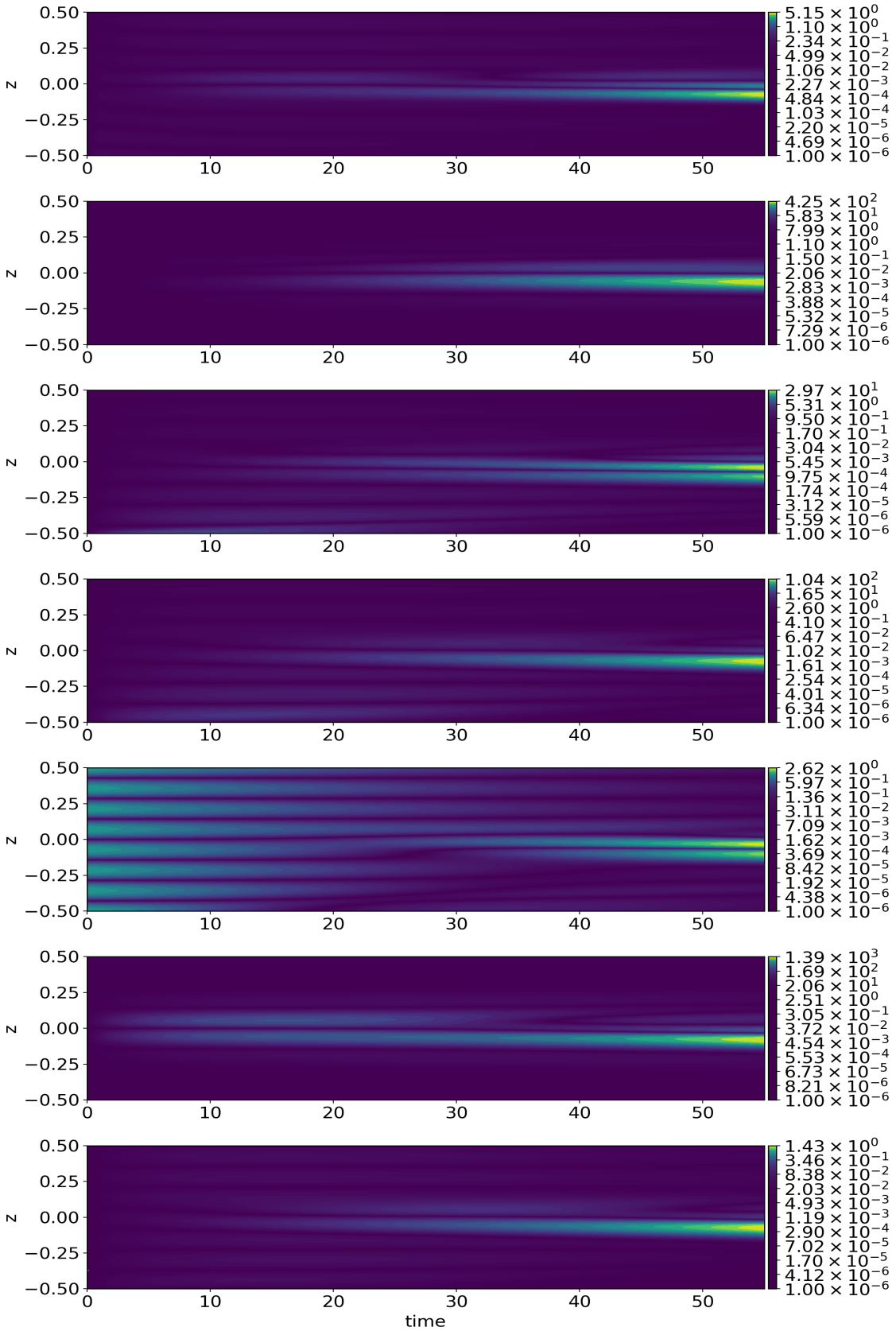

Figure 5.30: Evolution, from top to bottom, of ρ, u, v, w, h, g, T up to $t = 55$. Here, $k = 0$, $l = 90$, and $n = 7$.

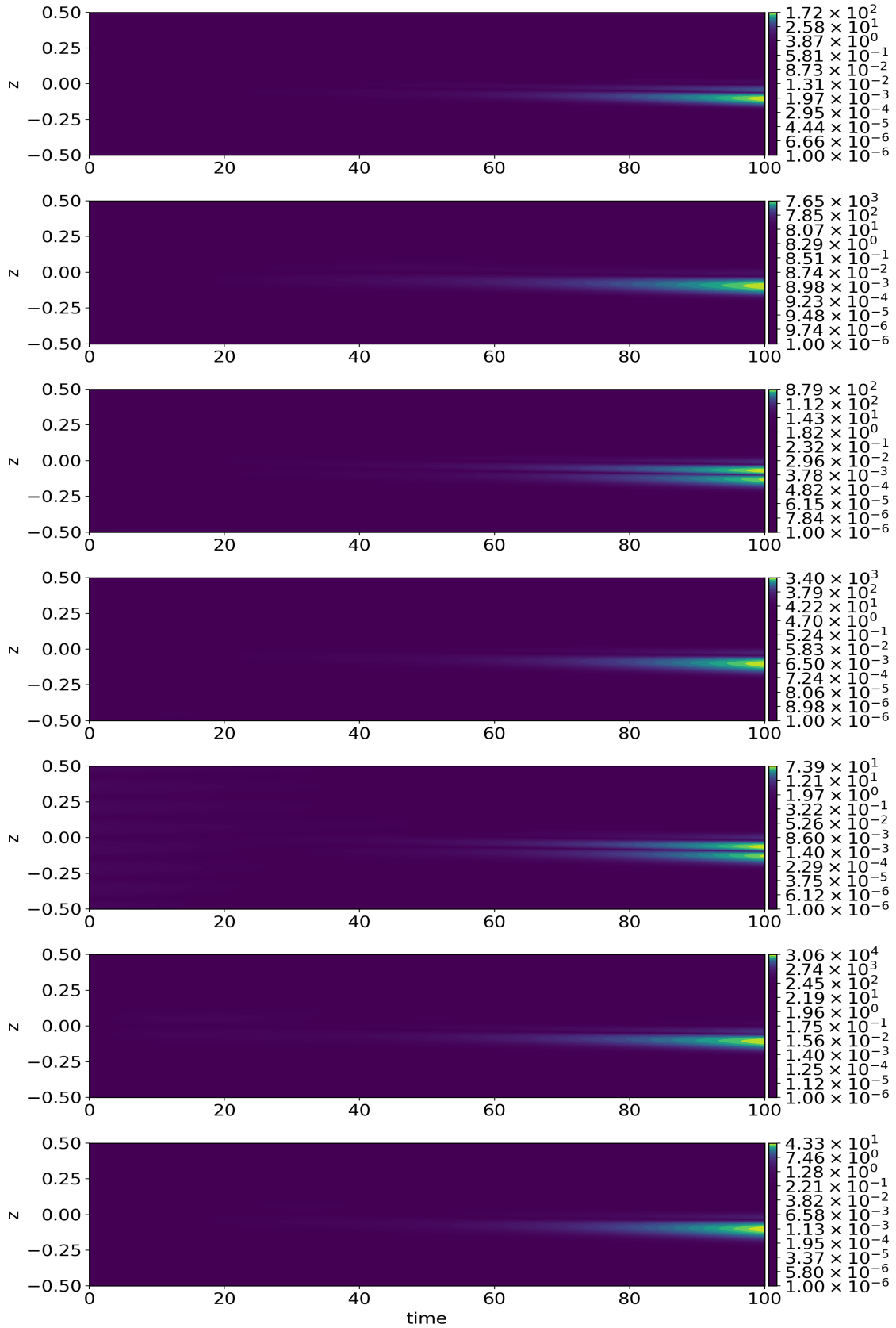

Figure 5.31: Evolution, from top to bottom, of ρ, u, v, w, h, g, T up to $t = 100$. Here, $k = 0$, $l = 90$, and $n = 7$.

It can be seen in Fig 5.29 that all the disturbances become large compared to the initial conditions. In addition, it is shown that by $t = 10$ all of the disturbances show a complicated structure in z. In the transient stages of the evolution, ρ, u, g, and T show a local maximum at or near the centre of the domain. Furthermore, v and w show a strong maximum near the top boundary at $z = -0.5$. Additionally, it is clear that h has not changed much in the earlier stages, this is shown by the 'rays' illustrated in Fig 5.29. After evolving up to $t = 55$, it can be seen that the complicated structure in z has decayed and the preferred eigenmode becomes clear at $t \approx 35$ on this scale: this is particularly clear in the magnetic field component h. We can clearly see that around $t = 30$, this disturbance does not resemble the initial condition, and begins to show localisation around $z = 0$.

Figure 5.31 shows the evolution of the disturbances up to $t = 100$. It is shown in Fig 5.28 that the kinetic and magnetic energies for $l = 90$ have increased significantly by $t = 100$. This is illustrated by the magnitude of the perturbations shown in Fig 5.31. Comparison of Figs 5.30-5.31 shows that the disturbances at $t = 55$ and $t = 100$ are quite similar in terms of z-structure, but have very different amplitudes: this is an indication that instability has manifest in the disturbances, and we would expect the perturbed quantities to continue to grow past $t = 100$, although further calculations would be needed to confirm this.

Initially Perturbing Velocity Components Only

Here, we perform an analysis analogous to §5.6.5, for an initial perturbation in the velocity components only. We consider a non-zero initial velocity disturbance, with the initial conditions for the disturbances given by

$$\rho(z,0) = h(z,0) = g(z,0) = T(z,0) = 0, \tag{5.64}$$

$$u(z,0) = v(z,0) = \sin(n\pi z), \quad w(z,0) = \cos(n\pi z). \tag{5.65}$$

We now evolve Eqs (C.6)-(C.15) subject to the initial conditions given by Eqs (5.64)-(5.65), for a series of l in the range $25 \leq l \leq 190$.

Figure 5.32 shows the kinetic and magnetic energy in time, for a series of wavenumbers. It can be seen in Figs 5.32(a),(c),(e) that the kinetic energy initially decreases, before increasing. Again, it can be seen that disturbances with larger wavenumbers grow the fastest up to $t \approx 40$ before being over-taken by perturbations with smaller wavenumbers. It is shown in Figs 5.32(b),(d),(f) that the magnetic energy initially increases rapidly across all wavenumbers.

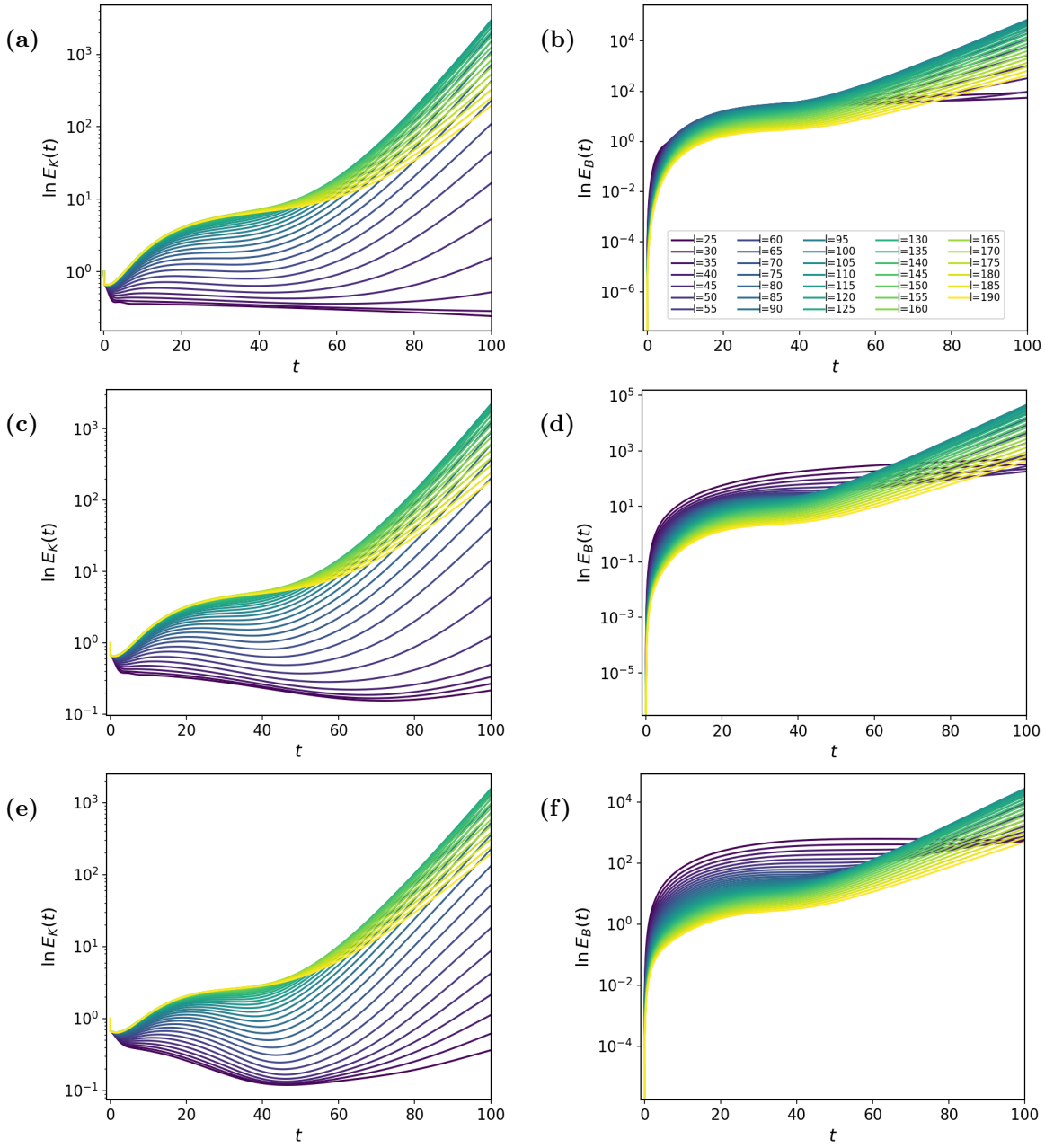

Figure 5.32: The natural logarithm of the kinetic (left) and magnetic (right) energy as a function of time, for an initial Fourier mode perturbation to the velocity field; (a)-(b) $n = 1$; (c)-(d) $n = 3$; (e)-(f) $n = 7$.

Figure 5.32 clearly shows that the smaller wavenumbers lead to a larger increase in the initial magnetic energy compared to the larger wavenumbers. Moreover, the blue-most lines in Fig 5.32 shows that the rate at which magnetic energy increases is approximately equal. Comparison of Figs 5.27 and 5.32 demonstrates that initially perturbing the magnetic field leads to faster growing disturbances, compared to initially perturbing only the velocity: this is most clear at $t = 100$. We can see that initially perturbing the magnetic field leads to growth in the kinetic and magnetic energies by $t = 100$ in the range $10^5 - 10^7$, whereas initially perturbing the velocity leads to growth in the range $10^4 - 10^5$.

To detect an optimal wavenumber for long term growth of the disturbances, we consider the kinetic and magnetic energies at $t = 100$ and plot these as a function of wavenumber (see Fig 5.33). We can see from Fig 5.33 that the wavenumbers responsible for optimal growth are in the range $75 \leq l \leq 125$. This is consistent with the quasi-static results shown in Fig 5.16, which show, that, for $t \geq 50$, the wavenumbers responsible for maximal exponential growth occur within this range. We can see from Fig 5.33 that there is no preference in initial Fourier mode for disturbances with larger wavenumbers. However, an interesting feature of Fig 5.33 is that when we initially perturb the velocity components, the fastest growing disturbances result from initial perturbations with less structure in z: this can be seen by the black curve ($n = 1$). This is to be compared with Fig 5.28; which shows that if the initial magnetic disturbances only are non-zero, then optimal growth is achieved for $n = 7$. Additionally, comparison of Figs 5.28 and 5.33 shows that regardless of the value of n, starting from a non-zero initial magnetic disturbance is preferential for growth compared to starting from a non-zero initial velocity disturbance.

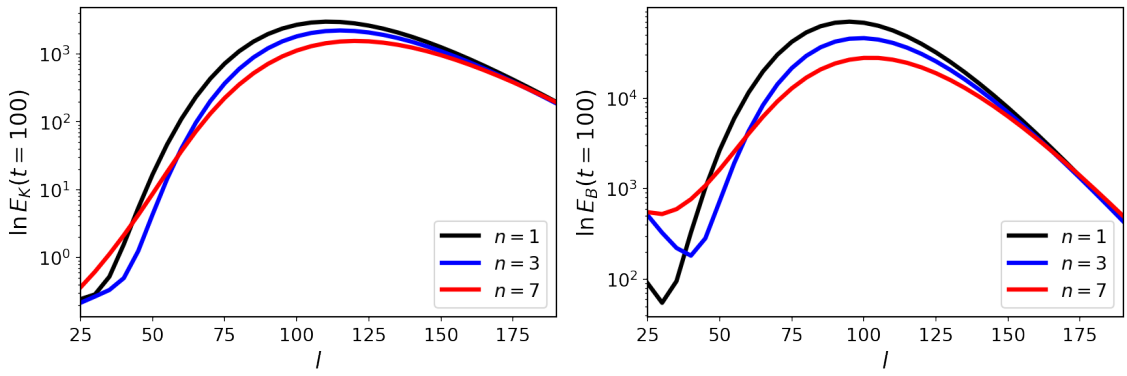

(a) (b)

Figure 5.33: Kinetic energy (left) and magnetic energy (right) at $t = 100$ as a function of l. Here, the initial conditions are Fourier modes only in the velocity.

Analogous to §5.6.5, we will show the evolution of the mode corresponding to $l = 100$ with $n = 1$, up to three separate times; $t = 5$, 35, and 100.

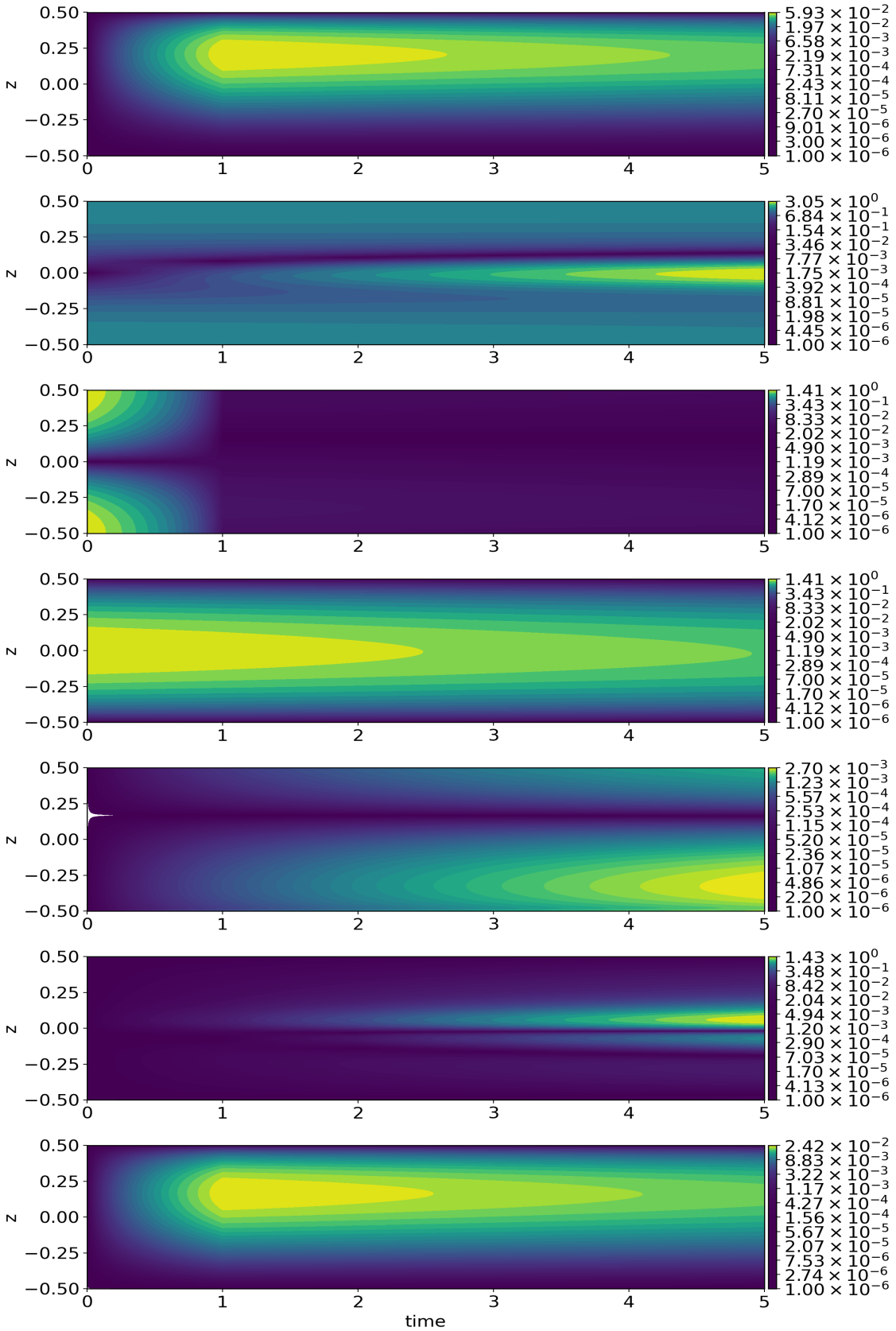

Figure 5.34: Evolution, from top to bottom, of ρ, u, v, w, h, g, T up to $t = 5$. Here, $k = 0$, $l = 100$, and $n = 1$.

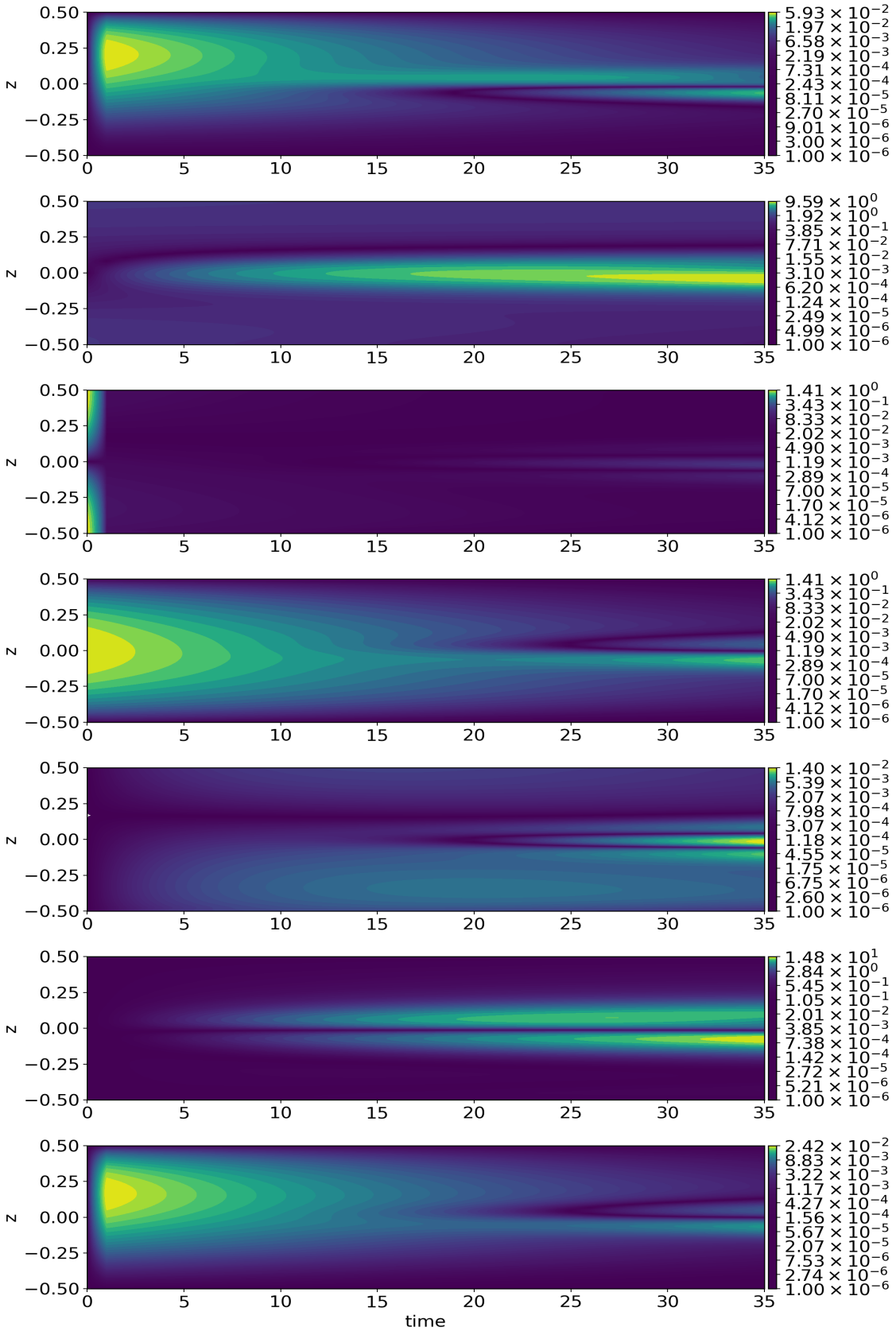

Figure 5.35: Evolution, from top to bottom, of ρ, u, v, w, h, g, T up to $t = 35$. Here, $k = 0$, $l = 100$, and $n = 1$.

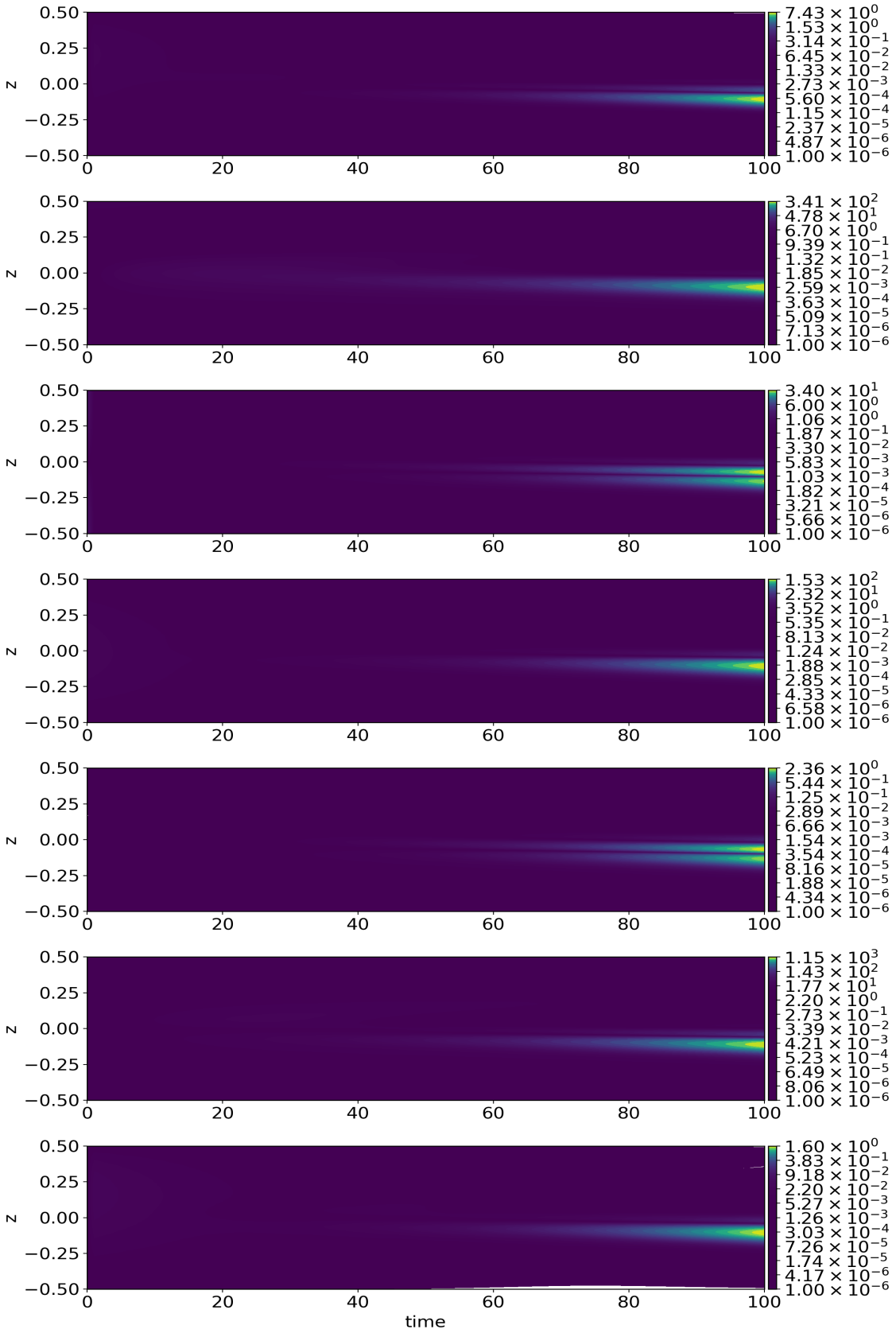

Figure 5.36: Evolution, from top to bottom, of ρ, u, v, w, h, g, T up to $t = 100$. Here, $k = 0$, $l = 100$, and $n = 1$.

Figure 5.34 illustrates that the velocity components v and w initially decay, with little to no structure in z developing in the early stages; this is consistent with the dip in kinetic energy shown in Figs 5.32(a),(c),(e). However, it is shown that u begins to develop a maximum at $z = 0$, which grows in time. It is shown in Fig 5.34 that the temperature and density perturbations are similar in terms of structure, and both are peaked in the upper half of the domain. The magnetic components start to increase in amplitude in the initial stages, with g beginning to develop a central maximum which increases in amplitude with time.

Figure 5.35 depicts the evolution of the perturbations up to $t = 35$. Here, it can be seen that the structure of g in z has not changed appreciably, and similar to Figs 5.29-5.31, the other quantities begin to project onto the preferred eigenmodes. It is evident in Fig 5.35 that all the quantities besides g have a different structure in space than that shown shown in the initial stages. Figure 5.36 shows that again, by $t = 100$, the perturbed quantities do not change much in z, and all contain one or two peaks near the origin. It is clear from Figs 5.35-5.36 that once the perturbed quantities have projected onto the localized functions shown at $t \approx 35$, they begin to rapidly increase in amplitude. Comparison of Figs 5.31 and 5.36 shows that by $t = 100$, the disturbances have the same spatial structure regardless of initial conditions in the perturbed quantities. This is not surprising, since Eqs (C.6)-(C.15) are linear, and therefore the long term solution should be independent of initial conditions. What is surprising, is that despite the preferred eigenmodes being similar in z-structure, the preferential initial condition for the velocity perturbations is less structure in z ($n = 1$), compared with the case of an initial magnetic perturbation only ($n = 7$).

5.6.6 The Initial Disturbance is a Jet

Here, we consider an initial disturbance for either the magnetic or velocity disturbances of the form Eq (5.61). We consider three widths in the initial conditions; $\beta = 10$, 15, and 25, and show the subsequent evolution of the disturbances and the associated kinetic and magnetic energy. We consider two cases: first, we initially perturb only the magnetic field components, h and g; second, initially perturb only the velocity components, u, v, and w.

Initially Perturbing Magnetic Quantities Only

First, we consider a non-zero initial magnetic disturbance. The initial conditions for the disturbances here are therefore given by

$$\rho(z,0) = u(z,0) = v(z,0) = w(z,0) = T(z,0) = 0, \tag{5.66}$$

$$h(z,0) = g(z,0) = \operatorname{sech}^2 \beta z. \tag{5.67}$$

We now evolve Eqs (C.6)-(C.15) subject to the initial conditions given by Eqs (5.66)-(5.67), for a series of l in the range $25 \leq l \leq 190$.

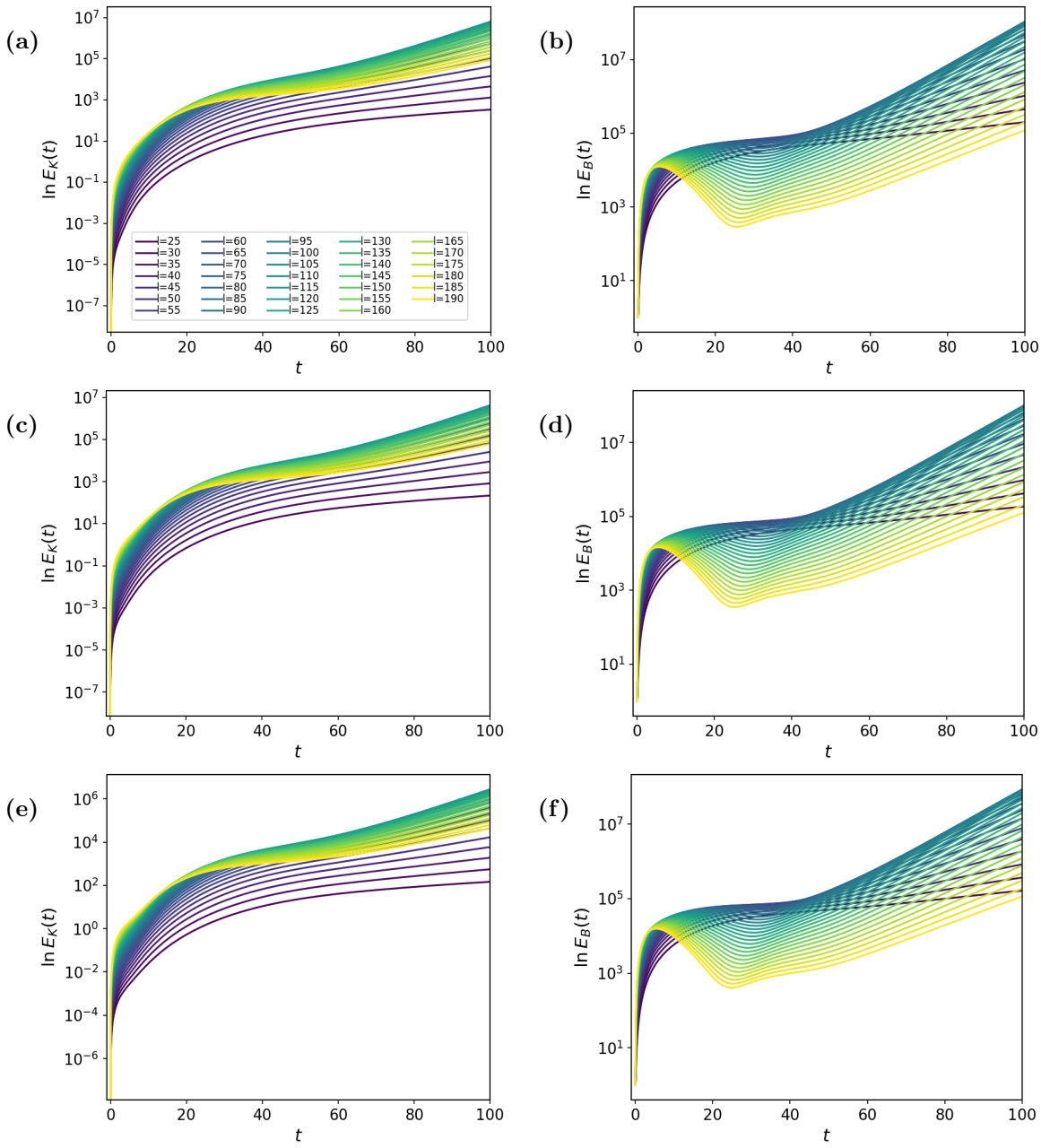

Figure 5.37: The natural logarithm of the kinetic (left) and magnetic (right) energy as a function of time, for an initially peaked perturbation to the magnetic field; (a)-(b) $\beta = 10$; (c)-(d) $\beta = 15$; (e)-(f) $\beta = 20$.

Figure 5.37 is analogous to Fig 5.27 and illustrates the kinetic and magnetic energy as a function of time, for a series of wavenumbers. A key point to take from Figs 5.37(a),(c),(e) is that the kinetic energy significantly amplifies in the early stages of the evolution, before the growth of velocity perturbations slows down. It can be seen in Fig 5.37 that the modes with the largest wavenumbers show the most significant transient growth in both kinetic and magnetic energies; however, it is seen that by $t = 100$ that $l = 190$ is not the wavenumber that leads to the largest long term growth. We can see in Fig 5.37(b),(d),(f) that the magnetic energy initially increases rapidly, before decreasing by an order of magnitude.

To calculate the optimal wavenumber for long term growth of the disturbances, we consider the kinetic and magnetic energies at $t = 100$ and plot these as a function of wavenumber (see Fig 5.38).

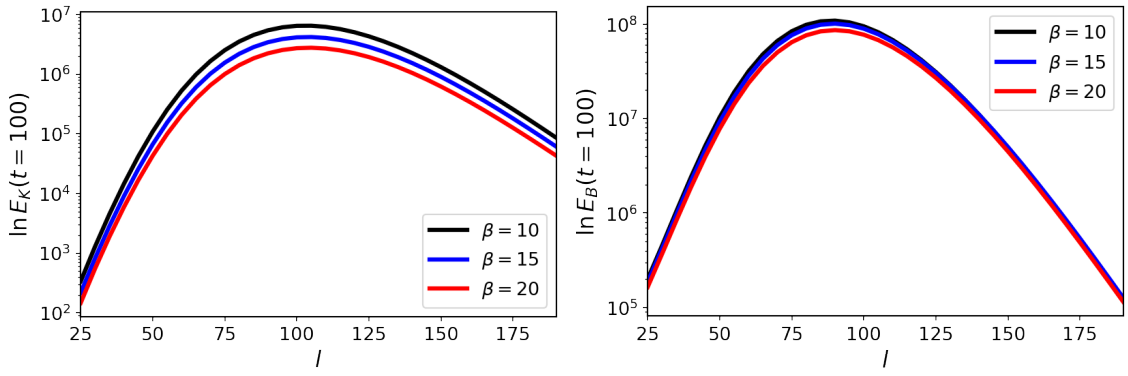

(a) (b)

Figure 5.38: Kinetic energy (left) and magnetic energy (right) at $t = 100$ as a function of l. Here, the initial conditions are given by jets in the magnetic field quantities only.

We can see from Fig 5.38 that the wavenumbers for optimal magnetic and kinetic growth respectively, are both in the range $75 \leq l \leq 100$. This is consistent with the quasi-static results shown in Fig 5.16, which show, that, for $t \geq 50$, the wavenumbers responsible for maximal exponential growth occur within this range. It is shown in Fig 5.38 that initial magnetic perturbations for which the jet is wider at $z = 0$ are preferential for instability compared to narrow distributions, i.e. width increasing with decreasing β. However, it is clear that this preference is weak. From comparison of Figs 5.28 and 5.38 we conclude that initially perturbing the magnetic field only with a centrally localized function leads to growth in the magnetic and kinetic energies orders of magnitude larger than when the initial magnetic perturbation is a Fourier mode. This is not surprising, as we have already seen that the preferred eigenmodes, for example in Fig 5.31, are composed of one or two localised peaks close to the origin.

In a similar manner to the previous section, we will show the evolution of the disturbances for the wavenumber $l = 95$, and the optimal width $\beta = 10$. Again, to show the evolution on a clear scale, we show it in three stages: up to $t = 5, 55$, and 100 respectively.

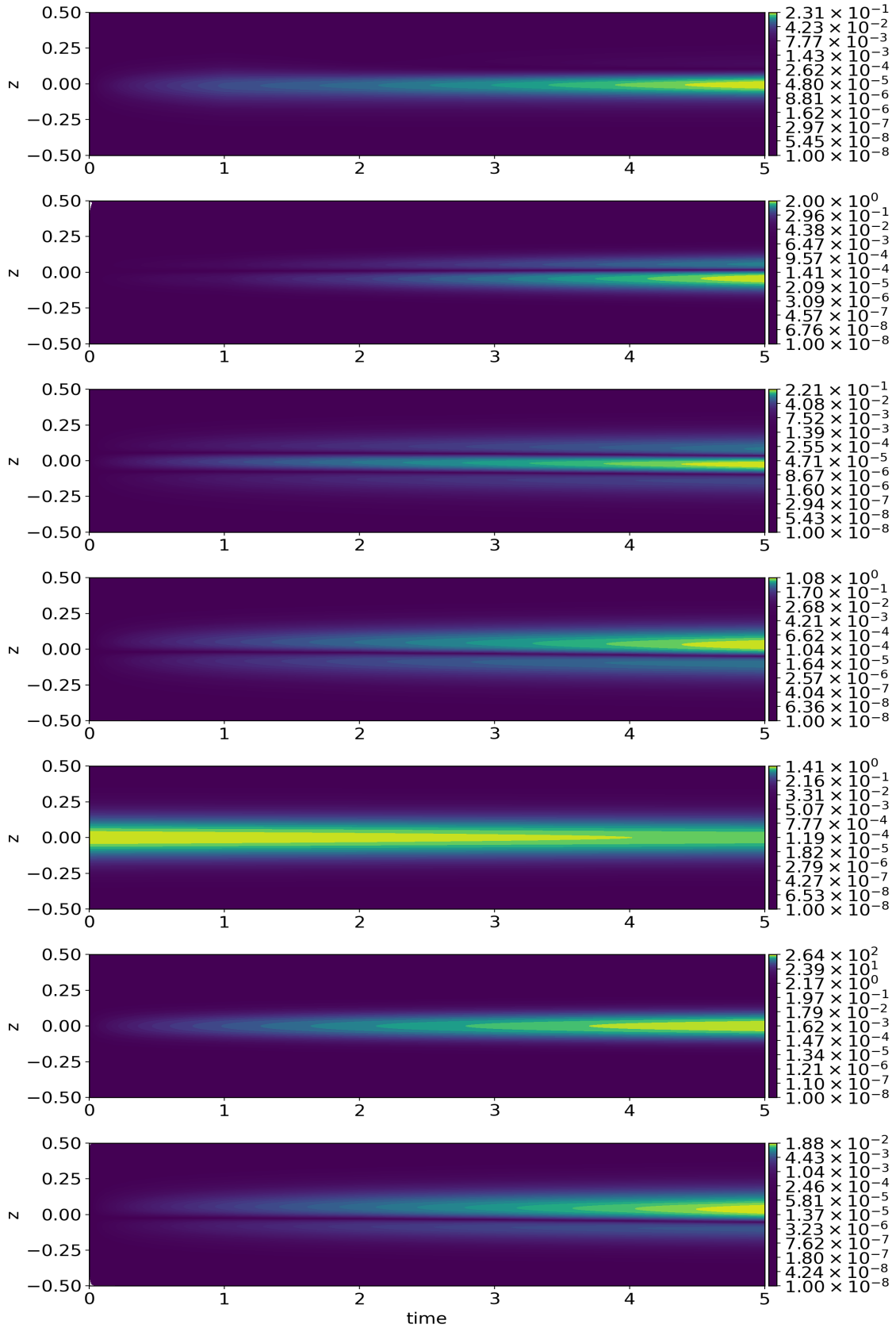

Figure 5.39: Evolution, from top to bottom, of ρ, u, v, w, h, g, T up to $t = 5$. Here, $k = 0$, $l = 95$, and $\beta = 10$.

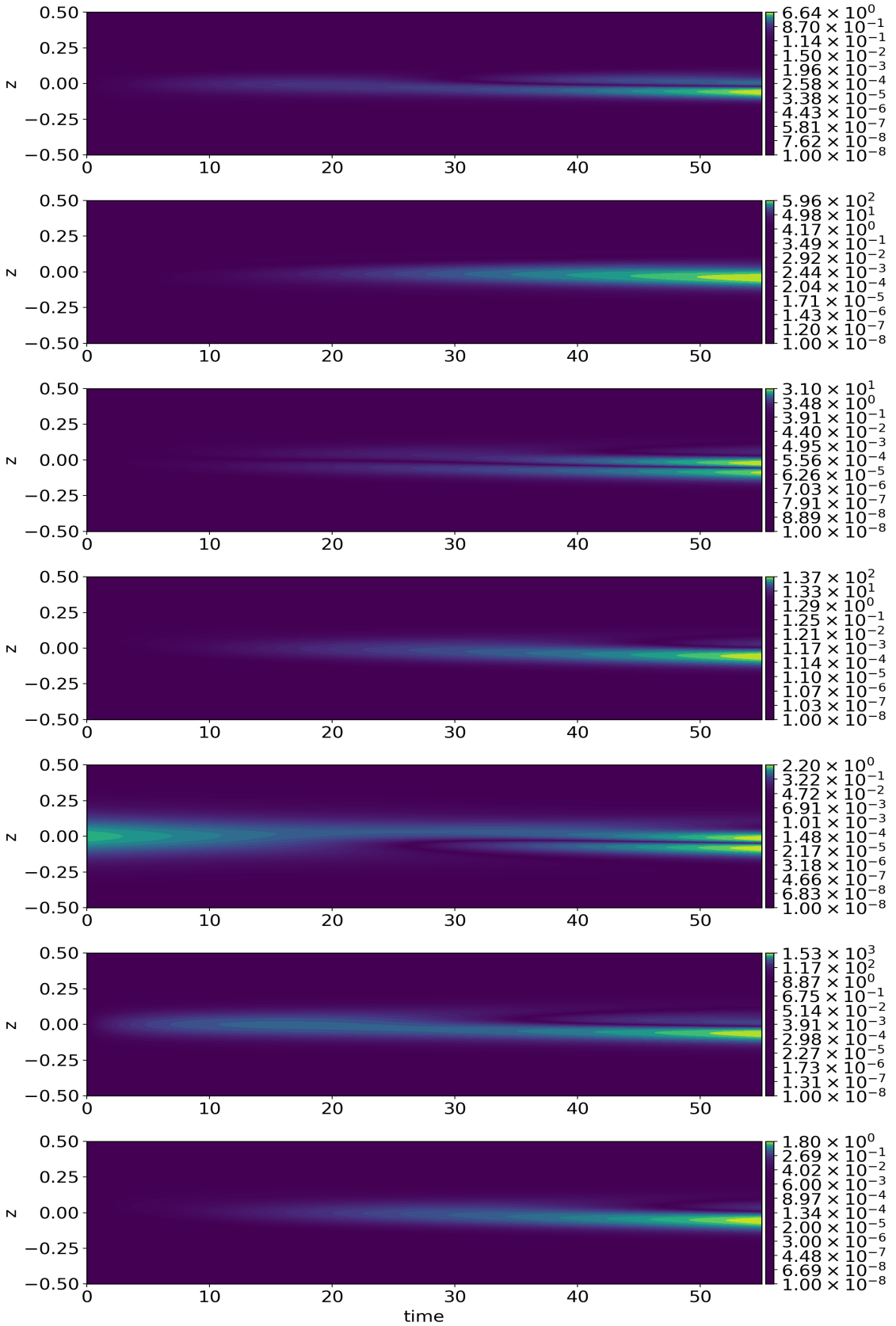

Figure 5.40: Evolution, from top to bottom, of ρ, u, v, w, h, g, T up to $t = 55$. Here, $k = 0$, $l = 95$, and $\beta = 10$.

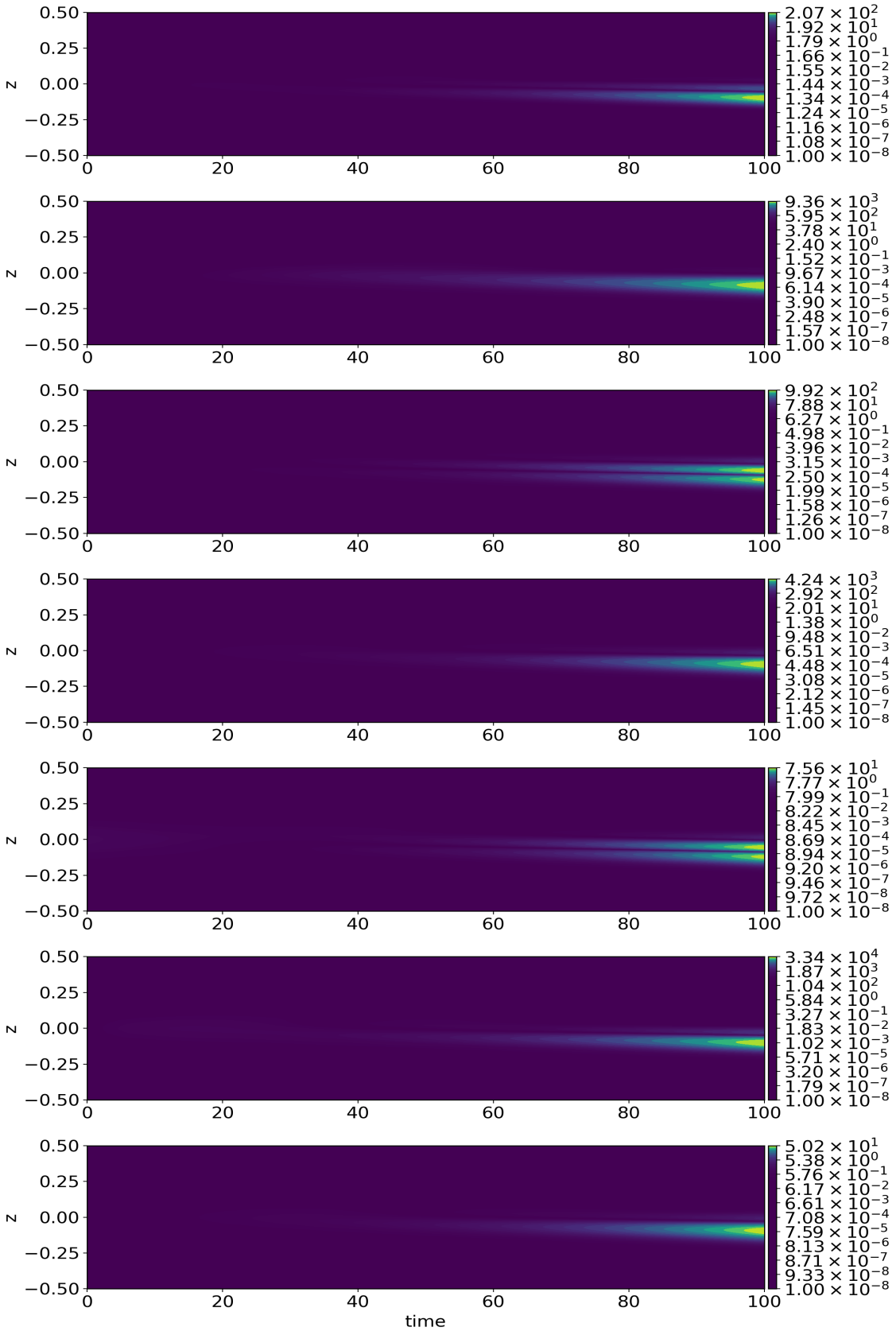

Figure 5.41: Evolution, from top to bottom, of ρ, u, v, w, h, g, T up to $t = 100$. Here, $k = 0$, $l = 95$, and $\beta = 10$.

Figure 5.39 demonstrates that the transient evolution of the disturbances that result from an initially peaked magnetic field perturbation are generally localised around $z = 0$, with the central maximum increasing in amplitude with time. It can be seen in Fig 5.40 that after the initial transient stages, the perturbations begin to project onto the preferred eigenmode. While the initial disturbances are generally localized in z, the perturbations do not project rapidly onto the eigenmodes — this can be seen by comparison of the structure in z at earlier and later times, i.e. $t = 5$ and $t = 55$. Figure 5.41 confirm that by $t = 100$ the disturbances match that shown in the other cases illustrated in Figs 5.31 and 5.36. This is not surprising, as Eqs (C.6)-(C.15) are linear equations and so we expect the long term behaviour to be independent of the initial conditions.

Initially Perturbing Velocity Components Only

Here, we consider the last iteration in this time-dependent linear analysis. We consider an initially peaked velocity disturbance with all other initial perturbations set to zero. The initial conditions for the disturbances are therefore given by

$$\rho(z,0) = h(z,0) = g(z,0) = T(z,0) = 0, \tag{5.68}$$

$$u(z,0) = v(z,0) = w(z,0) = \mathrm{sech}^2\,\beta z. \tag{5.69}$$

We now evolve Eqs (C.6)-(C.15) subject to the initial conditions given by Eqs (5.68)-(5.69), for a series of l in the range $25 \leq l \leq 190$.

Figure 5.42 is analogous to Fig 5.27 and illustrates the kinetic and magnetic energy as a function of time, for a series of wavenumbers. The main features shown in Figs 5.42(a),(c),(e) are that the kinetic energy initially decreases, before the growth of velocity perturbations turns around and rapidly increases, before slowing down. The modes with the largest wavenumbers show the most significant transient growth in kinetic energy; however modes with larger wavenumbers grow the slowest in the initial stages. It can be seen in Figs 5.42(b),(d),(f) that the magnetic energy initially increases rapidly, and for larger wavenumbers it can be seen that there is an initial local maximum in the magnetic energy after which there is a small decrease, before the magnetic energy begins to increase.

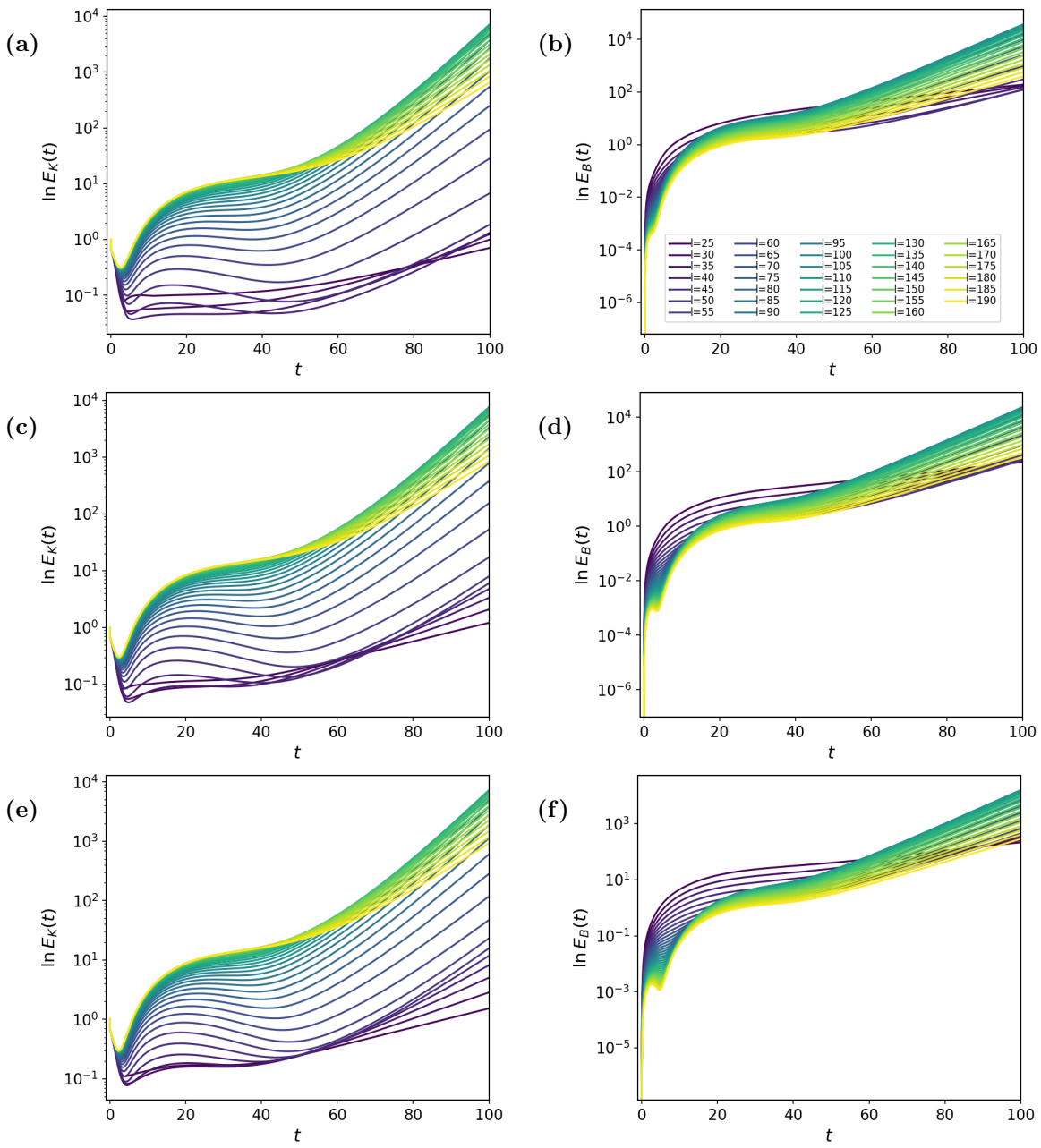

Figure 5.42: The natural logarithm of the kinetic (left) and magnetic (right) energy as a function of time, for an initially peaked perturbation to the velocity components; (a)-(b) $\beta = 10$; (c)-(d) $\beta = 15$; (e)-(f) $\beta = 20$.

To calculate the optimal wavenumber for long term growth of the disturbances, we consider the kinetic and magnetic energies at $t = 100$ and plot these as a function of wavenumber (see Fig 5.43). It is shown in Fig 5.43a that increasing β does not enhance nor inhibit growth in kinetic energy: the optimal wavenumber for amplification in kinetic energy appears to be the same across all values of β and is given by approximately $l \approx 110$. However, it can be seen in Fig 5.43b that there is a preference for β for growth in the magnetic energy. Initial perturbations in the velocity only prefer a larger width, i.e. smaller β for preferential growth in the magnetic energy. It can be seen that the optimal wavenumber for maximal growth in the magnetic energy increases slightly with β. The

optimal wavenumbers shown in Fig 5.43 are consistent with the optimal wavenumbers in the quasi-static analysis shown in Fig 5.16.

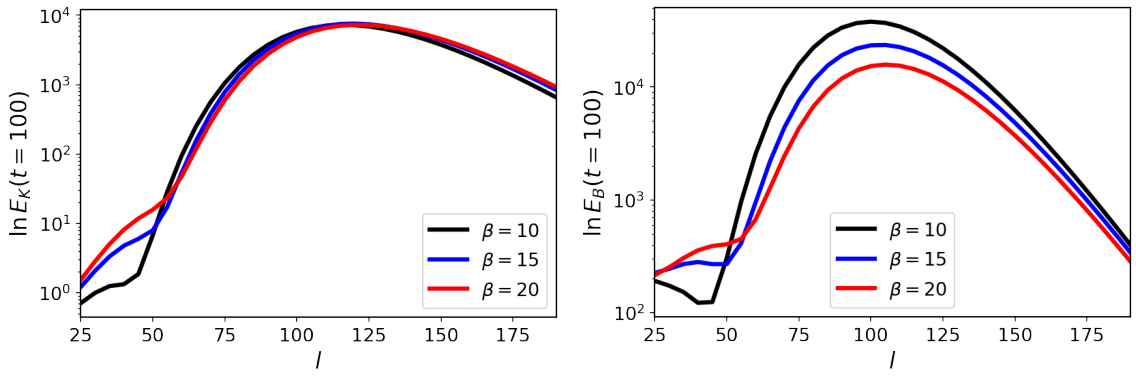

(a) (b)

Figure 5.43: Kinetic energy (left) and magnetic energy (right) at $t = 100$ as a function of l. Here, the initial conditions are given by jets in the velocity field quantities only.

Comparison of Figs 5.38 and 5.43 shows that whether it is only the initial magnetic or velocity disturbances that are non-zero, then subsequent growth is maximized for smaller β, and therefore wider distributions. Additionally, we have shown that if we only consider non-zero initial conditions in the velocity, then there is a dependence on β for maximal growth in the magnetic energy; the same is true for initial conditions in the magnetic field and the kinetic energy.

5.6.7 Motivation for Wavenumber Choices and Initial Conditions

Before we conclude this chapter, we provide some brief numerical results which were used to inform our choice of parameters and initial conditions. The time-dependent linear analysis of a compressible MHD system is complicated, and multiple lines of enquiry are possible. To make meaningful conclusions, given the finite time to conduct this study, we restricted ourselves to interchange modes, a set of parameter values given by Silvers et al. (2009), and two sets of initial conditions.

It is clear from §5.5.2 that various instabilities are possible as the basic state evolves in time: interchange and 3D instabilities are both present. In the time-dependent linear analysis, we decided to restrict attention to the case where $k = 0$, and consider growth of interchange instabilities only. This choice was made because evolving both a nonlinear basic state, and large system of linear equations in time for multiple wavenumbers is computationally costly. To justify this choice, we also performed calculations of the magnetic and kinetic energy, for various values of k as we varied l.

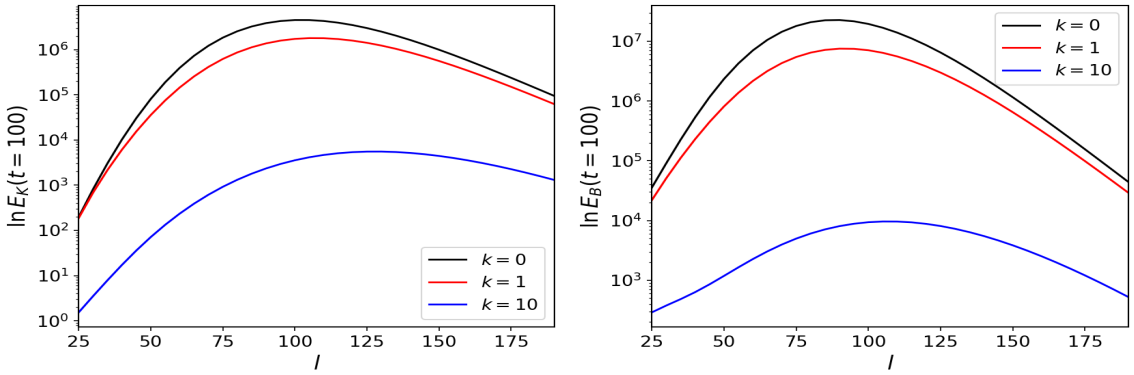

(a) (b)

Figure 5.44: Kinetic energy (left) and magnetic energy (right) at $t = 100$ as a function of l, for various values of k. The initial conditions are a Fourier mode with $n = 7$ in the initial magnetic field perturbations.

Figure 5.44 shows the kinetic and magnetic energies at $t = 100$ as a function of l for various values of k. To produce Fig 5.44 we solved Eqs (C.6)-(C.15) subject to an initial magnetic disturbance given by Eq (5.60) with $n = 7$: however, we did perform a few other calculations with different initial conditions. Fig 5.44 shows that disturbances with $k = 0$ reach a larger magnetic and kinetic energy by $t = 100$, compared to disturbances with larger values of k; the optimal value of l does not change significantly as k is increased. This is consistent with the quasi-static analysis, as it is shown in Figs 5.14(a)-(d) that the preferred interchange and 3D undular modes occur at similar values of l. Given Fig 5.44, we decided to restrict attention to $k = 0$ and to only vary l in the numerical analysis.

Another restriction we would like to address is the subset of Fourier modes we considered, i.e. $n = 1$, 3, and 7. We have shown that between $n = 1, 3, 7$ there is a preferred Fourier mode, which depends on whether we perturb the initial velocity or magnetic disturbances. In the case of an initially non-zero magnetic configuration, Fig 5.28 illustrates that initial configurations with more structure in z, i.e. $n = 7$ lead to preferential growth in the magnetic and kinetic energies. However, at some point, increasing n further would lead to inhibiting the long term growth. To motivate restricting attention to $n = 1$, 3, and 7, we show numerical calculations for a wider range of Fourier modes. We solve Eqs (C.6)-(C.15), and consider a non-zero initial magnetic field, and non-zero velocity field respectively, i.e., $g, h \neq 0$ or $u, v, w \neq 0$. In the example below, we fix $l = 95$ and $k = 0$ and consider the magnetic energy as a function of time.

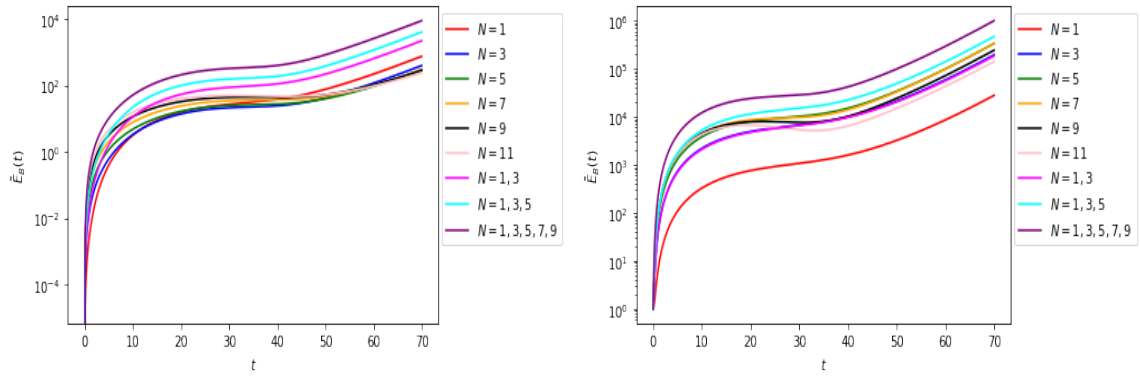

(a) (b)

Figure 5.45: The magnetic energy in time for multiple initial Fourier modes. (left) non-zero initial conditions in the velocity field only; (right) non-zero initial conditions in the magnetic field only.

Figure 5.45 shows the magnetic energy as a function of time, for $l = 95$ and $k = 0$ for the two initial configurations described above. Where multiple values of n are shown in the legend, we have considered a linear combination of Fourier modes. It can be seen in Fig 5.45a that when the initial condition is non-zero only in the velocity field, then preferential growth is achieved for a linear combination of odd Fourier modes. However, for single Fourier modes, we can see that varying n makes very little difference. Figure 5.45b shows that when we consider a non-zero magnetic field perturbation only, the preferential initial condition is a linear combination of odd Fourier modes from $n = 1$ to $n = 9$. It is shown in Fig 5.45b that $n = 1$ is the least optimal Fourier mode for growth in the magnetic energy. Additionally, from considering the magnetic energy at $t = 75$ in Fig 5.45b, we can see for single Fourier modes, increasing the structure in the initial conditions, i.e. $n = 1$ to $n = 7$, leads to more optimal growth in the magnetic field — this is what we have shown earlier. However, increasing n further to $n = 9$ leads to a decrease in the magnetic energy at $t = 75$ compared to $n = 7$. For this reason, we considered $n = 1, 3, 7$. The results in Fig 5.45 make it clear that the trend shown in Fig 5.28 does not necessarily continue past $n = 7$, and further increasing the structure in z for the initial configuration can lead to inhibiting growth in the perturbations.

5.7 Discussion of Results and Future Work

Considering the time-dependent linear stability of a system as complicated as compressible MHD is not necessarily straightforward. First, we have shown that the evolution of the basic state is complicated and a full understanding of its evolution provides invaluable insight for the linear stability analysis. Crucially, we have shown in §5.3 that the basic state configuration depends heavily on the initial conditions. We have shown that depending on the initial conditions, the magnetic field can reverse and change signs, and the transient evolution is not clear in the case of an initial target flow. Purely from the basic state analysis, we have cleared up a significant difference between the results of Silvers et al. (2009) and Vasil and Brummell (2008). The difference rests mostly on the

initial conditions, and that the nature of double-diffusion is a slight red-herring.

We have performed a quasi-static analysis on the evolving basic state, and shown that when the initial condition is zero horizontal flow, then the equilibrium analysis in Chapter 3 is a good indicator of whether instability is possible in the time-dependent evolution of the basic state. When the evolution of the basic state is significantly different compared with the equilibrium state, performing a quasi-static analysis is an essential first step. We have shown the existence of multiple instabilities in the evolution of the basic state, namely interchange and 3D undular modes. We have shown that the preferred mode of instability changes in the evolution of the basic state. The reversal of the magnetic field leads to instability, but despite the amplitude of the negative magnetic field being similar to its positive counterpart, the negative configuration is less unstable, and when the magnetic field reverses polarity, the preferred mode of instability is a 3D undular mode.

We then performed a time-dependent linear analysis. Here, we discussed multiple lines of enquiry, and highlighted the multiple choices one can make. To make progress with this system, we made choices for the parameters and initial conditions, which we later justified. Here, we were able to show that the growth of disturbances is not necessarily exponential, and the time dependence of the perturbations is complicated. We considered a variety of initial conditions, and showed that: 1) the structure of the initial conditions can drastically affect the transient growth of perturbations; 2) the choice of initial perturbation affects the growth of perturbations, and changes the time-dependent evolution of the perturbations.

A natural extension of this work is to consider a more in-depth analysis of wavenumber space and perform extensive calculations for various values of k. A further extension would be to consider evolving the perturbations for longer times. We have shown in §5.3 that it can take a long time for the magnetic field to diffuse; however, the form of the basic magnetic field changes significantly after $t = 100$. Furthermore, the quasi-static analysis has shown that the structure of instabilities can change significantly after $t = 100$. Therefore, it would be interesting to see whether the perturbations subsequently decay. However, despite not knowing whether the perturbations decay after $t = 100$, the results up to this time are still important: even if the perturbations do decay slightly or significantly after $t = 100$, we have shown that by $t = 100$, the magnitude of disturbances reach $\mathcal{O}(10^3)$, and therefore nonlinearity would become important. The ultimate extension of this work is to derive the optimal initial condition for the perturbed quantities for instability, in the manner of Kerr and Gumm (2017).

Chapter 6

Conclusions

6.1 Summary

The interaction of shear flow, magnetic field, and convection is extremely important in many astrophysical contexts. Much of the work of this thesis has been motivated by the Solar Tachocline, a thin region in which shear flow and magnetic field interact. The Solar Tachocline is understood to be the source of the solar cycle, which in turn allows us to observe the solar magnetic field indirectly through surface features such as solar flares and sunspots. Dynamo theory is used to explain the generation of large scale magnetic fields within the tachocline. While the specific details of the solar dynamo are widely debated, the common feature of these arguments is that the magnetic field is predominantly a strong toroidal, owing to the strong velocity shear which separates the radiation and convection zones. The resultant toroidal magnetic field subsequently escapes to the solar surface through magnetic buoyancy instabilities.

There has been a long-standing effort to understand the solar magnetic field and the Sun's interior both from an observational and theoretical perspective. The two main areas discussed in Chapter 1 are solar observations and modelling the solar interior. As described in Chapter 1, there have been extensive simulations of the solar interior. While valuable, large global simulations are computationally costly, and more so, the results can be hard to interpret. The overall aim of this thesis was to investigate the magnetic buoyancy instability, in the linear regime, of a magnetic field generated through the shearing of a uniform transverse magnetic field. This model is motivated by the Solar Tachocline has been studied by Vasil and Brummell (2008) and Silvers et al. (2009) within the non-linear regime; however, there are many interesting questions to be answered via a linear stability analysis. Additionally, the shearing of a uniform vertical magnetic field is inherently a time-dependent process and so we endeavoured to perform a time-dependent stability analysis. Performing a time-dependent linear analysis is not as straight-forward as the static counterpart, as the time-dependence of perturbations is unknown, and therefore there is no natural stability boundary. To equip us with the tools for performing a linear stability analysis of a time-varying state, we studied multiple linear stability problems all with a common feature: the background state is

either non-trivial or time-dependent.

Chapter 2 describes the most straight-forward problem we consider: the joint instability of a magnetic layer generated from a shear flow in the absence of gravity. There have been numerous studies of the combined instability of an aligned shear flow and magnetic field in the absence of diffusion. Moreover, the prescription of shear and magnetic field are arbitrary. In Chapter 2 we considered a flow and magnetic field that are related self-consistently. Under a suitable non-dimensionalisation, we found that the linear stability was governed by three parameters: the Chandrasekhar number, and the viscous and magnetic Reynolds numbers. It is shown in §2.2 that, in certain parameter regimes, the basic state can be understood analytically through asymptotic methods. Before studying the combined instability of the resultant shear flow and magnetic field, we had to return to studying the classical instability problems for flow and field respectively: the Orr–Sommerfeld equation and the current sheet problem. In a similar style to Drazin (1961), we studied the linear stability of a hyperbolic tangent shear layer in a finite domain. In the case of an infinite domain, Drazin (1961) shows that when $k \ll 1$, the critical wavenumber scales linearly with the Reynolds number. However, in the case of a finite domain, we have shown that when $k \ll 1$, the critical Reynolds number scales with $1/k$. Comparison of the asymptotic scaling to numerical results shows good agreement. We then studied the current sheet problem in a similar manner to Dahlburg et al. (1983). Here, we observe oscillatory instabilities for a jet magnetic field, instabilities which were not observed in the case considered by Dahlburg et al. (1983).

From §2.6 we begin to study the combined instability. We introduce a set of artificial but helpful sub-problems and in §2.7, §2.8 provide invaluable insights into understanding the dominant mechanisms in the resultant instabilities. By considering the set of sub-problems described in §2.6 we have shown the role of each individual component of the basic state. Comparison of linear stability results from the full linear system and the reduced sub-problems shows that there is a strong correlation between the Orr-Sommerfeld and the current sheet problems in the regimes of weak field and flow respectively: i.e., in these regimes, the dominant instabilities are essentially either purely hydrodynamic or purely magnetic. It is clear in §2.7, §2.8 that increasing the magnetic Reynolds number first inhibits the purely hydrodynamic instability, until it becomes large enough to drive a tearing instability. Inclusion of a basic flow in the current sheet problem shows that while the flow is hydrodynamically stable, it can enhance the tearing mode instability and increase the growth rate. Finally, we considered the role of non-zero magnetic flux, H, in the basic state. Inclusion of a non-zero magnetic flux leads to a vertical shift of the basic state horizontal magnetic by a value $H/2$. For sufficiently large H, the hydrodynamic instability is completely suppressed. For a fixed H, increasing R_m leads to an increase in the gradient of the basic state magnetic field; this basic state magnetic field still stabilises the resultant hydrodynamic instabilities, but significantly less than when the horizontal field is approximately uniform. Here, we have shown that

instability can ensue due to a combined effect of flow and field.

In Chapter 3 we performed our first investigations into magnetic buoyancy instabilities. Here, the basic state is steady, and the process which generates the magnetic field and flow is the same as in Chapter 2, namely through a forced target flow. However, this shearing takes place in the presence of a stably-stratified and compressible atmosphere. Before performing any numerical calculations on the compressible MHD system in the presence of shear, the computational approach was verified through reproducing numerical results within the literature for a simpler problem — the magnetic buoyancy instabilities of a static, linear magnetic field in the presence of a stably stratified atmosphere. We performed a basic state analysis, and demonstrated parameter regimes in which the magnetic field can be written purely in terms of input parameters, i.e. non-dimensional parameters and the target velocity shear profile. From this, we used the criteria first introduced by Newcomb (1961) to obtain instability criteria in terms of the Richardson number. Numerical calculation has shown that the instability criteria do a reasonable job at approximating the onset of interchange and undular instability.

In Chapter 3 we found that the instability criteria for interchange and undular (see Eqs (3.80)-(3.81)) depend linearly on the Prandtl number and have shown that 2D undular modes are present within this system. This is interesting, because it is understood that 2D undular modes are typically hard to destabilise in the absence of shear flows, whereas here, with a shear flow, they are relatively easy to destabilise. Moreover, the Prandtl number is typically thought to be stabilising, whereas increasing the Prandtl number in this full system further destabilises both 2D undular and interchange modes. This is understood through the basic state analysis, which demonstrates that the amplitude of the magnetic field increases with Prandtl number. This is due to the fact that increasing the Prandtl number, increases the forcing, even though the target profile is the same. A parameter survey has shown that multiple instabilities can simultaneously exist within this system. For example, when the Prandtl number is increased, we have shown that the optimal mode of instability changes between undular and interchange modes. As the Prandtl number is increased further, the effects of the magnetic field are significant and result in tearing modes which were discussed in Chapter 2.

Owing to the complexity of a time-dependent stability analysis of magnetic buoyancy instabilities, it is helpful first to consider a simpler problem. Therefore, in Chapter 4, we perform a linear stability analysis of the classical problem of Rayleigh-Bénard convection for different time-dependent primary temperature distributions. To familiarise the reader with Rayleigh-Bénard convection, we have given an overview of the analytic progress for the case of a static, linear temperature profile. The known classical results within Chandrasekhar (1961) were then used to benchmark the time-stepping scheme for the perturbation equations before studying the case of time-dependent heating.

The first problem we studied in Chapter 4 was investigated by Foster (1965) who considered convection in which the bottom plate is linearly cooled in time. We have shown that this results in a primary temperature distribution that has a time-divergent temperature gradient. This divergent temperature gradient appears as a forcing in the linear system, and therefore all disturbances are unconditionally unstable. We use a measure of kinetic energy defined by Foster (1965) to show that we can define a suitable stability boundary that is characterised by the time taken for disturbances to grow by a prescribed factor, t_c. From this, we first consider a set of initial conditions: the set of Fourier modes. Here, we show that there is an optimal initial configuration for the perturbed quantities. We have then shown that certain wavenumbers are optimal for instability, although it can be seen that instability will be onset for multiple wavenumbers; this is shown in §4.6.3 as the global minimum of the curves in (t_c, k) space are not sharply defined.

We then studied the time-dependent linear stability of a time-periodic temperature distribution. We consider a periodic modulation of the basic state temperature through the boundaries, with an amplitude, b, and frequency, ω. We have shown the resultant basic temperature profile has a steady linear component and a periodic component with an amplitude b. We use the approach of Yih and Li (1972) and write the linear system of equations as an infinite set of Ordinary Differential Equations (ODE) in time by expanding the perturbations and integrating in space. The resultant linear system is a set of time-periodic ordinary differential equations and so Floquet theory can be applied. We have shown that when only one term is included in the perturbation expansion (first approximation), the linear equations are analogous to the Mathieu equation, an equation which often appears in mechanical systems involving the oscillation of the equilibrium state. We have shown a relationship between the first approximation to the linear system and the Mathieu equations, showing the existence of Arnold tongues. Yih and Li (1972) did not study expansions with more than two terms, presumably owing to limited computational resources at the time: we have shown that approximations which include three or more terms are unnecessary and the neutral stability curves in multiple parameter spaces are reasonably approximated by two term expansions in the perturbed quantities (second approximation).

In the case of steady Rayleigh-Bénard convection, odd-cell numbered disturbances are the easiest to destabilise. We have shown that even in the case where the basic state is time-dependent, disturbances with odd cell numbers are more readily destabilised, with the disturbances with even cell numbers being much harder to destabilise. We have shown through asymptotic analysis that when the forcing amplitude of the modulation is large i.e. $b \gg 1$, the non-dimensional parameters within the full linear system can be re-scaled, eliminating b from the problem. This asymptotic scaling has been shown to be in agreement with numerical calculation. One benefit of this asymptotic analysis is computational. Due to the presence of local minima, finding the global minimum is computationally expensive, even with numerical continuation. Therefore, being able to

produce neutral stability curves in (Ra, b) with just one numerical calculation in the re-scaled system. Furthermore, this scaling shows that the system becomes unconditionally unstable when $b \to \infty$. Finally, we consider the case of large modulation frequency, i.e. $\omega \gg 1$. Here, we have shown that when the modulation frequency is large, the primary temperature distribution exhibits boundary layers at the edges of the domain, with the bulk temperature distribution being governed by a linear temperature profile. Therefore, increasing the modulation frequency inhibits the effect due to the time-dependence, and the critical Rayleigh number is given by the classical value (see Chandrasekhar, 1961) — this analysis is in agreement with Venezian (1969).

After Chapter 4, we were equipped with the tools necessary to study the more complicated problem of magnetic buoyancy instabilities of a time-varying magnetic field — Chapter 5. First, we performed an extensive analysis of the time-dependent basic state. We considered two initial conditions for the horizontal flow: i) zero horizontal initial velocity; ii) the horizontal flow is given by the target velocity. We have shown that the transient behaviour of the generated magnetic field depends heavily on the initial conditions. From this, we have made clear the source of the discrepancy between the papers of Vasil and Brummell (2008) and Silvers et al. (2009). This conclusion is an important one, as we have been able to show that the difference — which is significant — boils down to a difference of initial condition in the basic state.

In the case of zero initial flow, we have shown that the generated magnetic field is not very different to the equilibrium state studied in Chapter 3 — through performing a quasi-static linear stability analysis we show that performing a time-dependent linear stability analysis is not necessary: the equilibrium state is representative of the transient basic state, and therefore a steady linear stability is adequate. However, results from the quasi-static linear stability analysis have shown that in the case of an initial horizontal target flow, the basic state can drive instability in the form of both undular and interchange modes even when the equilibrium state is stable in (k, l) space. Furthermore, we have performed a quasi-static analysis of the magnetic field as it undergoes a reversal in polarity: here, we have shown that while the magnetic field grows to an equal but opposite amplitude, it is more stable than its positive counterpart.

Quasi-static linear stability results were used to justify parameter choices in the full time-dependent linear stability analysis. We restrict attention to interchange modes, i.e. $k = 0$, and in a similar fashion to Foster (1965), we consider a set of initial conditions for the velocity and magnetic perturbations: Fourier modes and jets of different width. We consider initially perturbing only the magnetic field or velocity disturbances, and show that perturbing only the magnetic components is optimal for growth of the kinetic and magnetic energy. We have shown that when we initially perturb only the magnetic field components, then there is a preference for initial conditions with more vertical structure: the Fourier mode preferential for growth is given by $n = 7$. Alternatively, when we perturb

only the velocity components, then the resultant disturbances prefer less structure in z, with the Fourier mode preferential for growth being given by $n = 1$. An analogous investigation was performed for a different initial condition for the perturbations; jets of varying widths which were parameterised by β. Calculations have shown that there is no strong correlation between the rate of growth in magnetic and kinetic energy, and the width of the initial perturbation. Additionally, we have shown that there is an optimal wavenumber for growth of the magnetic and kinetic energies — this optimal wavenumber is consistent with that predicted by the quasi-static linear stability analysis. It is clear through the time-dependent linear stability analysis that the magnetic field generated from an initial target flow is sufficient to drive rapid growth, due to the increasing magnetic and kinetic energies. It is clear that after only a short time, the perturbations can be sufficiently large for nonlinearity to become important.

6.2 Future Work

Each chapter includes a conclusion with specific extensions relevant to the work therein. Here, therefore, we will discuss the thesis in a broad sense. The problem of performing a time-dependent linear stability analysis is complicated, and has really only been studied in the context of systems simpler than compressible MHD, e.g. incompressible fluid dynamics, and Rayleigh-Bénard convection. The idea of performing a non-modal stability analysis is certainly not new; however, it is difficult and often comes with problems such as defining a suitable stability boundary. In Chapter 5, we considered only interchange modes and one set of parameter values. An extension to this work would thus consider an extensive parameter survey, e.g., to consider varying values of magnetic field strength and Prandtl number. Furthermore, an obvious extension is to perform a full study of the evolution of 3D modes, i.e. $k \neq 0$. We have shown that the transient behaviour of the basic state changes dramatically over a long time scale, and in the case of an initial horizontal flow in the basic state, the time taken to reach equilibrium is of $\mathcal{O}(10^6)$. This raises the question of whether perturbations will decay after $t = 100$. It is therefore necessary to perform a time-dependent linear stability analysis in which we consider the evolution of the perturbations for times in excess of $t = 100$. Motivated by the Solar Tachocline, it would be of interest to extend the analysis to include the effects of rotation and also to consider the full spherical shell geometry.

Appendix A

Linear System of Equations for Chapter 3

Here, we derive the linear system of equations for the time-dependent basic state given by $\boldsymbol{U}_0 = (U_0(z), 0, 0)$, $\boldsymbol{B}_0 = (B(z,t), 0, 1)$, $T_0 = T(z)$, and $\rho_0 = \rho_0(z)$. We consider the set of perturbations to this basic state, such that

$$\boldsymbol{U} = \boldsymbol{U}_0 + \varepsilon \boldsymbol{u}, \tag{A.1}$$

$$\boldsymbol{B} = \boldsymbol{B}_0 + \varepsilon \boldsymbol{b}, \tag{A.2}$$

$$T = T_0 + \varepsilon \hat{T}, \tag{A.3}$$

$$\rho = \rho_0 + \varepsilon \hat{\rho}. \tag{A.4}$$

We substitute Eqs (A.1)-(A.4) into the governing equations of compressible MHD given by Eqs (5.1)-(5.5), and look for solutions of the form

$$f(\boldsymbol{x}, t) = \hat{f}(z) e^{st + ikx + ily}. \tag{A.5}$$

The governing system of linear equations are shown below, where we have dropped the hats from the temperature and density perturbations.

A.1 Continuity Equation

The continuity equation up-to our linear perturbations is given as

$$\frac{\partial \rho}{\partial t} + \nabla \cdot (\rho_0 u + U_0 \rho) = 0.$$

Then substituting in our perturbations we obtain the linear continuity equation to solve

$$s\rho = -ik\rho_0 u - il\rho_0 v - \rho_0 \frac{\partial w}{\partial z} - \rho_0' w - ikU_0 \rho. \tag{A.6}$$

A.2 Momentum Equation

The momentum equation at next leading order is given by

$$s\boldsymbol{u} = -\boldsymbol{U}_0 \cdot \nabla \boldsymbol{u} - \boldsymbol{u} \cdot \nabla \boldsymbol{U}_0 + \frac{\alpha}{\rho_0}(\boldsymbol{b} \cdot \nabla)\boldsymbol{B}_0 + \frac{\alpha}{\rho_0}(\boldsymbol{B}_0 \cdot \nabla)\boldsymbol{b} - \frac{1}{\rho_0}\nabla(\rho_0 T + T_0 \rho) - \frac{\alpha}{\rho_0}\nabla(\boldsymbol{B}_0 \cdot \boldsymbol{b}) + \theta(m+1)\frac{\rho}{\rho_0}\boldsymbol{e}_z + \frac{C_k \sigma}{\rho_0}\left(\nabla^2 \boldsymbol{u} + \frac{1}{3}\nabla(\nabla \cdot \boldsymbol{u})\right),$$

where $\boldsymbol{b} = (b_x, b_y, b_z)$ and $\boldsymbol{u} = (u, v, w)$.

The x-component: Taking the x-component gives

$$\begin{aligned} su =& -ikU_0 u - U_0' w + \frac{\alpha}{\rho_0}\left(B'(k^2+l^2) - \delta ik(k^2+l^2) + ik\delta\frac{\partial^2}{\partial z^2}\right)h - \frac{T_0}{\rho_0}ik\rho \\ & - ikT + il\delta\frac{\alpha}{\rho_0}\frac{\partial g}{\partial z} + \frac{C_k\sigma}{\rho_0}\left(-k^2 + l^2 + \frac{\partial^2}{\partial z^2}\right)u + \frac{C_k\sigma}{3\rho_0}\left(-k^2 u - klv + ik\frac{\partial w}{\partial z}\right). \end{aligned} \tag{A.7}$$

The y-component: Taking the y-component gives

$$\begin{aligned} sv =& -ikU_0 v + \frac{\delta\alpha}{\rho_0}\left(-il(k^2+l^2) + il\frac{\partial^2}{\partial z^2}\right)h - ilT + \frac{C_k\sigma}{3\rho_0}\left(-klu - l^2 v + il\frac{\partial w}{\partial z}\right) \\ & + \frac{C_k\sigma}{\rho_0}\left(-k^2 - l^2 - \frac{\partial^2}{\partial z^2}\right)v - \frac{T_0}{\rho_0}il\rho - \frac{\alpha}{\rho_0}\left((k^2+l^2) - ik\delta\frac{\partial}{\partial z}\right)g. \end{aligned} \tag{A.8}$$

The z-component: The z-component is given by

$$\begin{aligned} sw =& -ikU_0 w - U_0' w + \frac{\alpha}{\rho_0}\left(ik(k^2+l^2)B - ikB'\frac{\partial}{\partial z} - ikB\frac{\partial^2}{\partial z^2}\right)h + \theta(m+1)\frac{\rho}{\rho_0} \\ & - \frac{1}{\rho_0}\frac{\partial}{\partial z}\Big(\rho_0 T + T_0\rho\Big) + \frac{C_k\sigma}{3\rho_0}\left(ik\frac{\partial u}{\partial z} + il\frac{\partial v}{\partial z}\right) - \frac{\alpha}{\rho_0}\left(-ilB' - ilB\frac{\partial}{\partial z}\right)g \\ & + \frac{C_k\sigma}{\rho_0}\left(-k^2 - l^2 + \frac{4}{3}\frac{\partial^2}{\partial z^2}\right)w. \end{aligned} \tag{A.9}$$

A.3 Induction Equation

The Induction equation to leading order is given by

$$\frac{\partial \boldsymbol{b}}{\partial t} = \nabla \times (\boldsymbol{U}_0 \times \boldsymbol{b}) + \nabla \times (\boldsymbol{u} \times \boldsymbol{B}_0) + C_k \zeta \nabla^2 \boldsymbol{b}.$$

To ensure the magnetic field remains divergence free, we perform a poloidal-toroidal decomposition as follows;

$$b_x = ik\frac{\partial h}{\partial z} + ilg, \tag{A.10}$$

$$b_y = il\frac{\partial h}{\partial z} - ikg, \tag{A.11}$$

$$b_z = (k^2 + l^2)h. \tag{A.12}$$

The h-component The h-component of the induction equation

$$sh = -U_0 ikh + ikBw - ik\delta u - il\delta v - C_k\zeta\left(k^2 + l^2 - \frac{\partial^2}{\partial z^2}\right)h. \tag{A.13}$$

The g-component The g-component is

$$\begin{aligned}(k^2+l^2)\frac{\partial g}{\partial t} = &-il\frac{\partial u}{\partial z} + ik\frac{\partial v}{\partial z} - B(k^2+l^2)v + ilB'w + ilB\frac{\partial w}{\partial z} - (k^2+l^2)ilU_0'h \\ &+ (il^3U_0 + ik^2lU_0 - il(k^2+l^2))\frac{\partial h}{\partial z} \\ &+ \left(- ikl^2U_0 - ik^3U_0 - C_k\zeta\left(k^2+l^2-\frac{\partial^2}{\partial z^2}\right)(k^2+l^2)\right)g,\end{aligned} \tag{A.14}$$

where $\beta = (k^2+l^2)^{-1}$.

A.4 Temperature Equation

The Temperature equation to leading order is given by

$$\begin{aligned}\rho_0\frac{\partial T}{\partial t} = &-\rho_0\nabla\cdot(T_0\boldsymbol{u} + \mathbf{U}_0T) - (\gamma-2)\rho_0(T_0\nabla\cdot\boldsymbol{u} + T\nabla\cdot\boldsymbol{U}_0) \\ &+ \gamma C_k\nabla^2T + (\gamma-1)C_k\sigma\Phi + 2(\gamma-1)C_k\alpha\zeta(\nabla\times\boldsymbol{b})\cdot(\nabla\times\boldsymbol{B}_0).\end{aligned}$$

Then we write it out by expanding the vector quantities which gives

$$\begin{aligned}\rho_0\frac{\partial T}{\partial t} = &-\rho_0\left[T_0\left(iku + ilv + \frac{\partial w}{\partial z}\right) + T_0'w + ikU_0T\right] + \gamma C_k\left(-k^2 - l^2 + \frac{\partial^2}{\partial z^2}\right)T \\ &- (\gamma-2)\rho_0\left[T_0\left(iku + ilv + \frac{\partial w}{\partial z}\right)\right] + 2(\gamma-1)C_k\sigma\left(U_0'\frac{\partial u}{\partial z} + ikU_0'w\right) \\ &+ 2(\gamma-1)C_k\alpha\zeta\left(B'\frac{\partial b_x}{\partial z} - ikB'b_z\right),\end{aligned} \tag{A.15}$$

where δ is equal to either 0 or 1 — this is described in Chapter 2.

Appendix B

Asymptotic Analysis of the (Damped) Mathieu Equation

The damped Mathieu equation is given by

$$\frac{\mathrm{d}^2x}{\mathrm{d}t^2} + c\frac{\mathrm{d}x}{\mathrm{d}t} + (\delta + \varepsilon\cos t)x = 0, \tag{B.1}$$

where c is damping coefficient and ε is the amplitude of periodic forcing. First, we perform an analysis of the undamped ($c = 0$) Mathieu equation through two variable expansion methods — here, we will show the existence of multiple tongues. After that, we will show this analysis can be extended to the damped case. A more thorough analysis can be found in Kovacic et al. (2018).

B.1 Undamped Case, $c = 0$

Since the period of the forcing function in Eq (B.1) is $\tau = 2\pi$, we conclude that on the transition curves in the $\delta - \varepsilon$ parameter plane, there exists solutions of period 2π or 4π. Therefore, we look for solutions of the form

$$x(t) = \sum_{n=0}^{\infty} a_n \cos\frac{nt}{2} + b_n \sin\frac{nt}{2}. \tag{B.2}$$

Equation (B.2) represents a general periodic function with period 4π but includes functions with period 2π in the case when a_{odd} and b_{odd} are zero. Equation (B.2) is substituted into the Mathieu equation (with $c = 0$). We then perform the method of harmonic balance to give a set of algebraic equations for the coefficients a_n and b_n. This set of equations is infinite, and so for nontrivial solutions, the determinants must vanish. This group of

determinants is called *Hill's Determinants* and is given by

$$a_{even}: \quad \begin{vmatrix} \delta & \varepsilon/2 & 0 & 0 & \\ \varepsilon & \delta-1 & \varepsilon/2 & 0 & \dots \\ 0 & \varepsilon/2 & \delta-4 & \varepsilon & \\ & & \dots & & \end{vmatrix} = 0, \tag{B.3}$$

$$b_{even}: \quad \begin{vmatrix} \delta-1 & \varepsilon/2 & 0 & 0 & \\ \varepsilon/2 & \delta-4 & \varepsilon/2 & 0 & \dots \\ 0 & \varepsilon/2 & \delta-9 & \varepsilon/2 & \\ & & \dots & & \end{vmatrix} = 0, \tag{B.4}$$

$$a_{odd}: \quad \begin{vmatrix} \delta-1/4+\varepsilon/2 & \varepsilon/2 & 0 & 0 & \\ \varepsilon/2 & \delta-9/4 & \varepsilon/2 & 0 & \dots \\ 0 & \varepsilon/2 & \delta-25/4 & \varepsilon/2 & \\ & & \dots & & \end{vmatrix} = 0. \tag{B.5}$$

$$b_{odd}: \quad \begin{vmatrix} \delta-1/4-\varepsilon/2 & \varepsilon/2 & 0 & 0 & \\ \varepsilon/2 & \delta-9/4 & \varepsilon/2 & 0 & \dots \\ 0 & \varepsilon/2 & \delta-25/4 & \varepsilon/2 & \\ & & \dots & & \end{vmatrix} = 0. \tag{B.6}$$

It can be seen in Eqs (B.3)-(B.6) that a common pattern in all the rows besides the first one or two is given by

$$\dots \quad 0 \quad \varepsilon/2 \quad \delta - n^2/4 \quad \varepsilon/2 \quad 0 \quad \dots, \tag{B.7}$$

Each row represents a relationship between δ and ε, and this functional relationship describes a set of transition curves in $\delta - \varepsilon$ space. If we set $\varepsilon = 0$ then we can see when these transition curves intersect the δ axis: for the even cases, then the transition curves intersect at $\delta = n^2$ for $n = 0, 1, 2, \dots$; while for the odd case, the determinants intersect the δ axis at $\delta = (2n+1)^2/4$ for $n = 0, 1, 2, \dots$. Two transition curves emerge from these intersections along the δ axis, and are associated with the a and b determinants respectively. Therefore, the above intersections can be generalised to the following points:

$$\delta = \frac{n^2}{4}, \qquad n = 0, 1, 2, 3, \dots \tag{B.8}$$

The transition curve shown by the solid black line shown in Fig 4.6a correspond to $n = 1$, hence it intersects the δ axis at $\delta = 1/4$. Furthermore, it can be seen from Eq (B.8) that there is an infinite amount of transition curves, and therefore an infinite set of Arnold tongues. To actually calculate the transition curves, we 'detune' the resonance; this is done by expanding δ in the power series in ε,

$$\delta = \frac{n^2}{4} + \delta_1\varepsilon + \delta_2\varepsilon^2 + \dots \tag{B.9}$$

We substitute Eq (B.9) into Eq (B.3)-(B.6) and collect the terms by order of ε, to obtain expressions for δ_i. To illustrate this, we consider an example, by first truncating Eq (B.3)

into a 3×3 determinant, which yields

$$-\frac{\varepsilon^3}{8} - \frac{\delta\varepsilon^2}{2} + \frac{13\varepsilon^2}{8} + \frac{\delta^2\varepsilon}{2} - \frac{17\delta\varepsilon}{4} + \frac{225\varepsilon}{32} + \delta^3 - \frac{35\delta^2}{4} + \frac{259\delta}{16} - \frac{225}{64}. \tag{B.10}$$

We then substitute Eq (B.9) into Eq (B.10), collect the terms by order ε and truncate at $\mathcal{O}(\varepsilon^2)$, which gives

$$(12\delta_1 + 6)\varepsilon + \frac{(24\delta_2 - 16\delta_1^2 - 8\delta_1 + 3)}{2}\varepsilon^2 + \mathcal{O}(\varepsilon^3). \tag{B.11}$$

We require the coefficients of ε^n to vanish, which gives

$$\delta_1 = -\frac{1}{2}, \quad \delta_2 = -\frac{1}{8}. \tag{B.12}$$

This procedure can be continued for any order of truncation to obtain any amount of transition curves.

B.2 Damped Case, $c \neq 0$

Here, we consider the Mathieu equation (B.1) with $c \neq 0$. In order to pursue a perturbative approach as in appendix B.1, we let the damping coefficient c be order ε, i.e. $c = \varepsilon c_1$. To illustrate how to obtain the transition curves in the damped case, we consider expanding δ around the $\delta = 1/4$ intersection, i.e.

$$\delta = \frac{1}{4} + \varepsilon\delta_1 + \ldots, \tag{B.13}$$

$$x = x_0 + \varepsilon x_1 + \ldots. \tag{B.14}$$

We substitute of Eqs (B.13)-(B.14) into Eq (B.1), and equate terms by order of ε to obtain

$$\frac{\mathrm{d}^2 x_0}{\mathrm{d}t^2} + \frac{1}{4}x_0 = 0, \tag{B.15}$$

$$\frac{\mathrm{d}^2 x_1}{\mathrm{d}t^2} + \frac{1}{4}x_1 = -c_1\frac{\mathrm{d}x_0}{\mathrm{d}t} - \cos(t)x_0 - \delta_1 x_0. \tag{B.16}$$

The general solution for x_0 is given by

$$x_0(t) = a\cos\frac{t}{2} + b\sin\frac{t}{2}. \tag{B.17}$$

From Eq (B.17), we can determine x_1 by solving

$$x_1'' + \frac{1}{4}x_1 = -c_1\left(-a\sin\frac{t}{2} + b\cos\frac{t}{2}\right) - \cos t\left(a\cos\frac{t}{2} + b\sin\frac{t}{2}\right) - \delta_1\left(a\cos\frac{t}{2} + b\sin\frac{t}{2}\right), \tag{B.18}$$

which can be further simplified using trignometric identities to give

$$x_1'' + \frac{1}{4}x_1 = ac_1 \sin\frac{t}{2} - bc_1 \cos\frac{t}{2} - a\delta_1 \cos\frac{t}{2} - b\delta_1 \sin\frac{t}{2} - \frac{a}{2}\left(\cos\frac{3t}{2} + \cos\frac{t}{2}\right) - \frac{b}{2}\left(\sin\frac{3t}{2} - \sin\frac{t}{2}\right). \tag{B.19}$$

We remove the secular terms in Eq (B.19) and arrive at the system of equations

$$\begin{pmatrix} c_1 & \frac{1}{2} - \delta_1 \\ -\frac{1}{2} - \delta_1 & -c_1 \end{pmatrix} \begin{pmatrix} a \\ b \end{pmatrix} = \begin{pmatrix} 0 \\ 0 \end{pmatrix}. \tag{B.20}$$

For Eqs (B.20) to have nontrivial solutions, the determinant of the matrix must be equal to zero, i.e.

$$\begin{vmatrix} c_1 & \frac{1}{2} - \delta_1 \\ -\frac{1}{2} - \delta_1 & -c_1 \end{vmatrix} = 0. \tag{B.21}$$

We expand Eq (B.21) to obtain the relationship between δ_1 and c_1;

$$-c_1^2 - \left(\frac{1}{2} - \delta_1\right)\left(-\frac{1}{2} - \delta_1\right). \tag{B.22}$$

Equation (B.22) is a quadratic equation in δ and the roots are given by

$$\delta_1 = \pm\sqrt{\frac{1}{4} - c_1^2}. \tag{B.23}$$

Therefore, the $n = 1$ transition curve in the damped case is given by

$$\delta = \frac{1}{4} \pm \sqrt{\frac{\varepsilon^2}{4} - c^2}, \tag{B.24}$$

where $c^2 = \varepsilon^2 c_1^2$. These are the curves shown by the dashed and dash-dotted lines in Fig 4.6a. This same approach can be followed for higher order transition curves, however one must include higher orders of ε in the expansion of c. One would then use Eq (B.9) for larger values of n.

Appendix C

Linear System of Equations for Chapter 5

Here, we derive the linear system of equations for the time-dependent basic state given by $\boldsymbol{U}_0 = (U_0(z,t), 0, W_0(z,t))$, $\boldsymbol{B}_0 = (B(z,t), 0, 1)$, $T_0 = T(z,t)$, and $\rho_0 = \rho_0(z,t)$. We consider the set of perturbations to this basic state, such that

$$\boldsymbol{U} = \boldsymbol{U}_0 + \varepsilon \boldsymbol{u}, \tag{C.1}$$

$$\boldsymbol{B} = \boldsymbol{B}_0 + \varepsilon \boldsymbol{b}, \tag{C.2}$$

$$T = T_0 + \varepsilon \hat{T}, \tag{C.3}$$

$$\rho = \rho_0 + \varepsilon \hat{\rho}. \tag{C.4}$$

We substitute Eqs (C.1)-(C.4) into the governing equations of compressible MHD given by Eqs (3.8)-(3.13), and look for solutions of the form

$$f(\boldsymbol{x}, t) = \hat{f}(z,t) e^{ikx+ily}. \tag{C.5}$$

The governing system of linear equations are shown below, where we have dropped the hats from the temperature and density perturbations.

C.1 Continuity Equation

The continuity equation up-to our linear perturbations is given as

$$\frac{\partial \rho}{\partial t} + \nabla \cdot (\rho_0 u + U_0 \rho) = 0.$$

Then substituting in our perturbations we obtain the linear continuity equation to solve

$$\frac{\partial \rho}{\partial t} = -ik\rho_0 u - il\rho_0 v - \rho_0 \frac{\partial w}{\partial z} - \rho_0' w - W_0' \rho - ikU_0 \rho - W_0 \frac{\partial \rho}{\partial z}. \tag{C.6}$$

C.2 Momentum Equation

The momentum equation at next leading order is given by

$$\frac{\partial \boldsymbol{u}}{\partial t} = -\frac{\rho}{\rho_0}\frac{\partial \boldsymbol{U}_0}{\partial t} - \boldsymbol{U}_0\cdot\nabla\boldsymbol{u} - \boldsymbol{u}\cdot\nabla\boldsymbol{U}_0 - \frac{\rho}{\rho_0}\boldsymbol{U}_0\cdot\nabla\boldsymbol{U}_0 + \frac{\alpha}{\rho_0}(\boldsymbol{b}\cdot\nabla)\boldsymbol{B}_0 + \frac{\alpha}{\rho_0}(\boldsymbol{B}_0\cdot\nabla)\boldsymbol{b} - \frac{1}{\rho_0}\nabla(\rho_0 T + T_0\rho) - \frac{\alpha}{\rho_0}\nabla(\boldsymbol{B}_0\cdot\boldsymbol{b}) + \theta(m+1)\frac{\rho}{\rho_0}\boldsymbol{e}_z + \frac{C_k\sigma}{\rho_0}\left(\nabla^2\boldsymbol{u} + \frac{1}{3}\nabla(\nabla\cdot\boldsymbol{u})\right),$$

where $\boldsymbol{b} = (b_x, b_y, b_z)$ and $\boldsymbol{u} = (u, v, w)$.

The x-component: Taking the x-component gives

$$\frac{\partial u}{\partial t} = -\frac{\rho}{\rho_0}\frac{\partial U_0}{\partial t} - ikU_0u - W_0\frac{\partial u}{\partial z} - U_0'w - \frac{\rho}{\rho_0}U_0'W_0 - \frac{T_0}{\rho_0}ik\rho + il\delta\frac{\alpha}{\rho_0}\frac{\partial g}{\partial z} - ikT + \frac{\alpha}{\rho_0}\left(B'(k^2+l^2) - ik\delta(k^2+l^2) + ik\delta\frac{\partial^2}{\partial z^2}\right)h + \frac{C_k\sigma}{\rho_0}\left(-k^2 - l^2 + \frac{\partial^2}{\partial z^2}\right)u + \frac{C_k\sigma}{3\rho_0}\left(-k^2u - klv + ik\frac{\partial w}{\partial z}\right). \tag{C.7}$$

The y-component: Taking the y-component gives

$$\frac{\partial v}{\partial t} = -ikU_0v - W_0\frac{\partial v}{\partial z} + \frac{\delta\alpha}{\rho_0}\left(-il(k^2+l^2) + il\frac{\partial^2}{\partial z^2}\right)h - ilT - \frac{T_0}{\rho_0}il\rho - \frac{\alpha}{\rho_0}\left((k^2+l^2) - ik\delta\frac{\partial}{\partial z}\right)g + \frac{C_k\sigma}{\rho_0}\left(-k^2 - l^2 - \frac{\partial^2}{\partial z^2}\right)v + \frac{C_k\sigma}{3\rho_0}\left(-klu - l^2v + il\frac{\partial w}{\partial z}\right). \tag{C.8}$$

The z-component: The z-component is given by

$$\frac{\partial w}{\partial t} = -\frac{\rho}{\rho_0}\frac{\partial W_0}{\partial t} - ikU_0w - W_0\frac{\partial w}{\partial z} - U_0'w - \frac{\rho}{\rho_0}W_0W_0' - \frac{\alpha}{\rho_0}\left(-ilB' - ilB\frac{\partial}{\partial z}\right)g + \frac{\alpha}{\rho_0}\left(ik(k^2+l^2)B - ikB'\frac{\partial}{\partial z} - ikB\frac{\partial^2}{\partial z^2}\right)h - \frac{1}{\rho_0}\left(\rho_0\frac{\partial T}{\partial z} + \rho_0'T + T_0'\rho + T_0\frac{\partial \rho}{\partial z}\right) + \theta(m+1)\frac{\rho}{\rho_0} + \frac{C_k\sigma}{\rho_0}\left(-k^2 - l^2 + \frac{\partial^2}{\partial z^2}\right) + \frac{C_k\sigma}{3\rho_0}\left(ik\frac{\partial u}{\partial z} + il\frac{\partial v}{\partial z} + \frac{\partial^2 w}{\partial z^2}\right). \tag{C.9}$$

C.3 Induction Equation

The Induction equation to leading order is given by

$$\frac{\partial \boldsymbol{b}}{\partial t} = \nabla\times(\boldsymbol{U}_0\times\boldsymbol{b}) + \nabla\times(\boldsymbol{u}\times\boldsymbol{B}_0) + C_k\zeta\nabla^2\boldsymbol{b}.$$

To ensure the magnetic field remains divergence free, we perform a poloidal-toroidal decomposition as follows;

$$b_x = ik\frac{\partial h}{\partial z} + ilg, \tag{C.10}$$

$$b_y = il\frac{\partial h}{\partial z} - ikg, \tag{C.11}$$

$$b_z = (k^2 + l^2)h. \tag{C.12}$$

The h-component The h-component of the induction equation

$$\frac{\partial h}{\partial t} = -\frac{W_0}{\beta}(k^2+l^2)\frac{\partial h}{\partial z} - U_0 ikh + ilW_0 b_y + ikBw - ik\delta u - il\delta v + C_k\zeta\left(-k^2 - l^2 + \frac{\partial^2}{\partial z^2}\right)h. \tag{C.13}$$

The g-component The g-component is

$$\begin{aligned}(k^2+l^2)\frac{\partial g}{\partial t} = &-il\frac{\partial u}{\partial z} + \left(-ikl^2U_0 - ik^3U_0 - C_k\zeta\left(k^2+l^2-\frac{\partial^2}{\partial z^2}\right)(k^2+l^2)\right)g \\ &- B(k^2+l^2)v + ilB'w + ilB\frac{\partial w}{\partial z} - (k^2+l^2)ilU_0'h \\ &+ ik\frac{\partial v}{\partial z} + (il^3U_0 + ik^2lU_0 - il(k^2+l^2))\frac{\partial h}{\partial z},\end{aligned} \tag{C.14}$$

where $\beta = (k^2+l^2)^{-1}$.

C.4 Temperature Equation

The Temperature equation to leading order is given by

$$\begin{aligned}\rho_0\frac{\partial T}{\partial t} = &-\rho_0\nabla\cdot(T_0\boldsymbol{u} + \mathbf{U}_0T) - (\gamma-2)\rho_0(T_0\nabla\cdot\boldsymbol{u} + T\nabla\cdot\boldsymbol{U}_0) + \gamma C_k\nabla^2T \\ &+ (\gamma-1)C_k\sigma\Phi + 2(\gamma-1)C_k\alpha\zeta(\nabla\times\boldsymbol{B})\cdot(\nabla\times\boldsymbol{B}_0).\end{aligned}$$

Then we write it out by expanding the vector quantities which gives

$$\begin{aligned}&\rho_0\frac{\partial T}{\partial t} = -\rho\frac{\partial T_0}{\partial t} - \rho_0\left[T_0\left(iku + ilv + \frac{\partial w}{\partial z}\right) + T_0'w + W_0'T + ikU_0T + W_0\frac{\partial T}{\partial z}\right] \\ &- \rho(T_0W_0' + W_0T_0') - (\gamma-2)\rho_0\left[T_0\left(iku + ilv + \frac{\partial w}{\partial z}\right) + W_0'T\right] - (\gamma-2)\rho(T_0W_0') \\ &+ \gamma C_k\left(-k^2 - l^2 + \frac{\partial^2}{\partial z^2}\right)T + 2(\gamma-1)C_k\sigma\left(U_0'\frac{\partial u}{\partial z} + ikU_0'w + W_0'\frac{\partial w}{\partial z}\right) \\ &+ 2(\gamma-1)C_k\alpha\zeta\left(-ikB'(k^2+l^2) + B'ik\frac{\partial^2}{\partial z^2}\right)h + 2(\gamma-1)C_k\alpha ilB\frac{\partial g}{\partial z},\end{aligned} \tag{C.15}$$

where δ is equal to either 0 or 1. The terms in blue correspond to terms which are included

in the time-dependent linear analysis. The full linear system given by Eqs (C.6)-(C.15) are solved in the time-dependent linear analysis. Any terms involving the time derivative of a basic state quantity (i.e. subscript 0) are omitted in the quasi-static linear stability analysis. It is not necessary to write out the solonoidal condition, as we have performed a poloidal-toroidal decomposition to ensure the magnetic field is divergence free.

References

Acheson, D. J. (1979). Instability by magnetic buoyancy. *Solar Physics*, 62(1):23–50.

Basu, S., Antia, H. M., and Narasimha, D. (1994). Helioseismic measurement of the extent of overshoot below the solar convection zone. *Monthly Notices of the Royal Astronomical Society*, 267(1):209–224.

Bénard, H. (1900). Les tourbillons cellulaires dans une nappe liquide. *Revue Gén. Sci. Pur. Appl.*, 11(1261):32.

Benjamin, T. B. and Ursell, F. (1954). The stability of the plane free surface of a liquid in vertical periodic motion. *Proceedings of the Royal Society of London. Series A. Mathematical and Physical Sciences*, 225(1163):505–515.

Boussinesq, J. (1901). *Théorie analytique de la chaleur mise en harmonie avec la thermodynamique et avec la théorie mécanique de la lumière*, volume 2. Gauthier-Villars, Imprimeur-Libraire, Paris.

Brown, T. M. (1985). Solar rotation as a function of depth and latitude. *Nature (London)*, 317(6038):591–594.

Brunton, S. L., Noack, B. R., and Koumoutsakos, P. (2020). Machine learning for fluid mechanics. *Annual Review of Fluid Mechanics*, 52(1):477–508.

Carbone, V., Einaudi, G., and Veltri, P. (1987). Effects of turbulence development in solar surges. *Solar Physics*, 111(1):31–41.

Cattaneo, F. and Hughes, D. W. (1988). The nonlinear breakup of a magnetic layer: instability to interchange modes. *Journal of fluid mechanics*, 196:323–344.

Chandra, K. (1938). Instability of fluids heated from below. *Proceedings of the Royal Society of London. Series A - Mathematical and Physical Sciences*, 164(917):231–242.

Chandrasekhar, S. (1952). Xlvi. on the inhibition of convection by a magnetic field. *The London, Edinburgh, and Dublin Philosophical Magazine and Journal of Science*, 43(340):501–532.

Chandrasekhar, S. S. (1981 - 1961). *Hydrodynamic and hydromagnetic stability*. International series of monographs on physics (Oxford, England). Dover Publications, New York, dover edition. edition.

Choudhuri, A. R., Schussler, M., and Dikpati, M. (1995). The solar dynamo with meridional circulation. *Astronomy and Astrophysics*, 303:L29.

Coddington, E. A. (1955). *Theory of ordinary differential equations*. International series in pure and applied mathematics. McGraw-Hill, New York.

Conrad, P. W. and Criminale, W. O. (1965). The stability of time-dependent laminar flow: Parallel flows. *Zeitschrift für angewandte Mathematik und Physik ZAMP*, 16(2):233–254.

Cowling, T. G. (1933). The Magnetic Field of Sunspots. *Monthly Notices of the Royal Astronomical Society*, 94(1):39–48.

Dahlburg, R. B., Boncinelli, P., and Einaudi, G. (1998). The evolution of a plane jet in a neutral sheet. *Physics of Plasmas*, 5(1):79–93.

Dahlburg, R. B. and Karpen, J. T. (1994). Transition to turbulence in solar surges. *The Astrophysical Journal*, 434:766.

Dahlburg, R. B., Zang, T. A., Montgomery, D., and Hussaini, M. Y. (1983). Viscous, resistive magnetohydrodynamic stability computed by spectral techniques. *Proceedings of the National Academy of Sciences of the United States of America*, 80(18):5798–5802.

Degond, P. and Deluzet, F. (2017). Asymptotic-preserving methods and multiscale models for plasma physics. *Journal of Computational Physics*, 336:429–457.

Dikpati, M. and Charbonneau, P. (1999). A Babcock-Leighton flux transport dynamo with solar-like differential rotation. *The Astrophysical Journal*, 518(1):508–520.

Donnelly, R. J. (1964). Experiments on the stability of viscous flow between rotating cylinders iii. enhancement of stability by modulation. *Proceedings of the Royal Society of London. Series A. Mathematical and Physical Sciences*, 281(1384):130–139.

Drazin, P. G. (1961). Discontinuous velocity profiles for the Orr-Sommerfeld equation. *Journal of Fluid Mechanics*, 10(4):571–583.

Duvall, T. L., Dziembowski, W. A., Goode, P. R., Gough, D. O., Harvey, J. W., and Leibacher, J. W. (1984). Internal rotation of the sun. *Nature (London)*, 310(5972):22–25.

Dyke, M. V. (1975). *Perturbation methods in Fluid Mechanics*. Parabolic Press.

Ecke, R. E., Farmer, J. D., and Umberger, D. K. (1989). Scaling of the arnold tongues. *Nonlinearity*, 2(2):175–196.

Foster, T. D. (1965). Stability of a homogeneous fluid cooled uniformly from above. *Physics of Fluids*, 8(7):1249.

Gilman, P. A. (1970). Instability of magnetohydrostatic stellar interiors from magnetic buoyancy. i. *The Astrophysical Journal*, 162:1019.

Gough, D. (2007). An introduction to the solar tachocline. In Hughes, D. W., Rosner, R., and Weiss, N. O., editors, *The Solar Tachocline*, page 3–30. Cambridge University Press.

Graham, A. (1933). Shear patterns in an unstable layer of air. *Philosophical Transactions of the Royal Society of London. Series A, Containing Papers of a Mathematical or Physical Character*, 232(707-720):285–296.

Grimshaw, R. (1993 - 1993). *Nonlinear ordinary differential equations*. Applied mathematics and engineering science texts ; 2. CRC Press, Boca Raton, FL.

Guerrero, G. A. and Muñoz, J. D. (2004). Kinematic solar dynamo models with a deep meridional flow. *Monthly Notices of the Royal Astronomical Society*, 350(1):317–322.

Hale, G. E. (1908). On the probable existence of a magnetic field in sun-spots. *Journal of Geophysical Research*, 13(4):159–160.

Hughes, D. and Tobias, S. (2001). On the instability of magnetohydrodynamic shear flows. *Proceedings of the Royal Society. A, Mathematical, Physical, and Engineering Sciences*, 457(2010):1365–1384.

Hughes, D. W. (1985a). Magnetic buoyancy instabilities for a static plane layer. *Geophysical & Astrophysical Fluid Dynamics*, 32(3-4):273–316.

Hughes, D. W. (1985b). Magnetic buoyancy instabilities incorporating rotation. *Geophysical & Astrophysical Fluid Dynamics*, 34(1-4):99–142.

Hughes, D. W. (2018). Mean field electrodynamics: triumphs and tribulations. *Journal of Plasma Physics*, 84(4):735840407.

Hughes, D. W. and Cattaneo, F. (1987). A new look at the instability of a stratified horizontal magnetic field. *Geophysical & Astrophysical Fluid Dynamics*, 39(1-2):65–81.

Hughes, D. W. and Proctor, M. R. E. (1988). Magnetic fields in the solar convection zone: Magnetoconvection and magnetic buoyancy. *Annual Review of Fluid Mechanics*, 20(1):187–223.

Hughes, D. W., Rossner, R., and Weiss, N. O. (2007). *The solar tachocline*. Cambridge University Press, Cambridge.

Hunt, J. C. R. (1966). On the stability of parallel flows with parallel magnetic fields. *Proceedings of the Royal Society of London. Series A, Mathematical and Physical Sciences*, 293(1434):342–358.

Ince, E. L. (1927). *Ordinary differential equations*. Longmans, Green and Co, London.

Jardin, S. (2012). Review of implicit methods for the magnetohydrodynamic description of magnetically confined plasmas. *Journal of Computational Physics*, 231(3):822–838. Special Issue: Computational Plasma Physics.

Kerr, O. S. and Gumm, Z. (2017). Thermal instability in a time-dependent base state due to sudden heating. *Journal of Fluid Mechanics*, 825:1002–1034.

Kersalé, E., Hughes, D. W., and Tobias, S. M. (2007). The nonlinear evolution of instabilities driven by magnetic buoyancy: A new mechanism for the formation of coherent magnetic structures. *The Astrophysical Journal*, 663(2):L113–L116.

Kovacic, I., Rand, R., and Mohamed Sah, S. (2018). Mathieu's equation and its generalizations: Overview of stability charts and their features. *Applied Mechanics Reviews*, 70(2).

Matthews, P. C., Hughes, D. W., and Proctor, M. R. E. (1995). Magnetic Buoyancy, Vorticity, and Three-dimensional Flux-Tube Formation. *The Astrophysical Journal*, 448:938.

Michael, D. H. (1953). Stability of plane parallel flows of electrically conducting fluids. *Mathematical proceedings of the Cambridge Philosophical Society*, 49(1):166–168.

Mihaljan, J. M. (1962). A rigorous exposition of the Boussinesq approximations applicable to a thin layer of fluid. *The Astrophysical Journal*, 136:1126.

Newcomb, W. A. (1961). Convective instability induced by gravity in a plasma with a frozen-in magnetic field. *Physics of Fluids (1958)*, 4(4):391–396.

Oberbeck, A. (1879). Ueber die wärmleitung der flüssigkeiten bei berücksichtigung der strömungen infolge von temperaturdifferenzen. *Ann. Phys. Chem.*, 7(271):35.

Ossendrijver, M. (2003). The solar dynamo. *The Astronomy and Astrophysics Review*, 11(4):287–367.

Parker, E. N. (1955). The formation of sunspots from the solar toroidal field. *The Astrophysical Journal*, 121:491–507.

Parker, E. N. (1975). The generation of magnetic fields in astrophysical bodies. x. magnetic buoyancy and the solar dynamo. *The Astrophysical Journal*, 198(1):205–209.

Parker, E. N. (1993). A solar dynamo surface wave at the interface between convection and nonuniform rotation. *The Astrophysical Journal*, 408:707.

Rayleigh, L. (1916). On convection currents in a horizontal layer of fluid, when the higher temperature is on the under side. *Phil. Mag.*, 32(529).

Roppo, M. N., Davis, S. H., and Rosenblat, S. (1984). Bénard convection with time-periodic heating. *Physics of Fluids*, 27(4):796.

Rosenblat, S. and Herbert, D. M. (1970). Low-frequency modulation of thermal instability. *Journal of Fluid Mechanics*, 43(2):385–398.

Rosenblat, S. and Tanaka, G. A. (1971). Modulation of thermal convection instability. *Physics of Fluids*, 14(7):1319.

Route, M. (2016). The discovery of solar-like activity cycles beyond the end of the main sequence? *The Astrophysical Journal. Letters*, 830(2):L27–L27.

Sato, T. and Walker, R. J. (1982). Magnetotail dynamics excited by the streaming tearing mode. *Journal of Geophysical Research*, 87(A9):7453.

Schmid, P. J. (2007). Nonmodal stability theory. *Annual Review of Fluid Mechanics*, 39(1):129–162.

Silvers, L. J., Vasil, G. M., Brummell, N. H., and Proctor, M. R. E. (2009). Double-diffusive instabilities of a shear-generated magnetic layer. *The Astrophysical Journal Letters*, 702(1):L14–L18.

Spangenberg, W. G. and Rowland, W. R. (1961). Convective circulation in water induced by evaporative cooling. *Physics of Fluids*, 4(6):743.

Spiegel, E. A. and Veronis, G. (1960). On the Boussinesq approximation for a compressible fluid. *The Astrophysical Journal*, 131:442.

Spiegel, E. A. and Weiss, N. O. (1982). Magnetic buoyancy and the Boussinesq approximation. *Geophysical & Astrophysical Fluid Dynamics*, 22(3-4):219–234.

Spiegel, E. A. and Zahn, J. P. (1992). The solar tachocline. *Astronomy and Astrophysics*, 265:106–114.

Squire, H. (1933). On the stability for three-dimensional disturbances of viscous fluid flow between parallel walls. *Proceedings of the Royal Society of London. Series A, Containing Papers of a Mathematical and Physical Character*, 142(847):621–628.

Stern, M. E. (1963). Joint instability of hydromagnetic fields which are separately stable. *Physics of Fluids (1958)*, 6(5):636–642.

Stuart, J. T. (1954). On the stability of viscous flow between parallel planes in the presence of a co-planar magnetic field. *Proceedings of the Royal Society of London. Series A, Mathematical and Physical Sciences*, 221(1145):189–206.

Sutton, O. G. (1950). On the stability of a fluid heated from below. *Proceedings of the Royal Society of London. Series A. Mathematical and Physical Sciences*, 204(1078):297–309.

Tang, Q., Chacón, L., Kolev, T. V., Shadid, J. N., and Tang, X.-Z. (2022). An adaptive scalable fully implicit algorithm based on stabilized finite element for reduced visco-resistive mhd. *Journal of Computational Physics*, 454:110967.

Thomas, J. H. and Nye, A. H. (1975). Convective instability in the presence of a nonuniform horizontal magnetic field. *Physics of Fluids (1958)*, 18(4):490–492.

Thomson, J. (1882). On a changing tesselated structure in certain fluids. *Proceedings of the Philosophical Society of Glasgow*, 13(464).

Tobias, S. M. (2002). The solar dynamo. *Philosophical Transactions of the Royal Society of London Series A*, 360(1801):2741–2756.

Tobias, S. M. and Hughes, D. W. (2004). The influence of velocity shear on magnetic buoyancy instability in the solar tachocline. *The Astrophysical Journal*, 603(2):785–802.

Trefethen, L. N., Trefethen, A. E., Reddy, S. C., and Driscoll, T. A. (1993). Hydrodynamic stability without eigenvalues. *Science (American Association for the Advancement of Science)*, 261(5121):578–584.

Vasil, G. M. and Brummell, N. H. (2008). Magnetic buoyancy instabilities of a shear-generated magnetic layer. *The Astrophysical Journal*, 686(1):709–730.

Vasil, G. M. and Brummell, N. H. (2009). Constraints on the magnetic buoyancy instabilities of a shear-generated magnetic layer. *The Astrophysical Journal*, 690(1):783–794.

Venezian, G. (1969). Effect of modulation on the onset of thermal convection. *Journal of Fluid Mechanics*, 35(2):243–254.

Wang, S., Lee, L. C., Wei, C. Q., and Akasofu, S. I. (1988). A mechanism for the formation of plasmoids and kink waves in the heliospheric current sheet. *Solar Physics*, 117(1):157–169.

Wissink, J. G., Hughes, D. W., Matthews, P. C., and Proctor, M. R. E. (2000). The three-dimensional breakup of a magnetic layer. *Monthly Notices of the Royal Astronomical Society*, 318(2):501–510.

Yih, C.-S. (1963). Stability of liquid flow down an inclined plane. *Physics of Fluids*, 6(3):321.

Yih, C.-S. and Li, C.-H. (1972). Instability of unsteady flows or configurations. part 2. convective instability. *Journal of Fluid Mechanics*, 54(1):143–152.

Zagier, D. (1989). The dilogarithm function in geometry and number theory. In Askey, R., editor, *Number theory and related topics: Papers presented at the Ramanujan Colloquium, Bombay, 1988*, pages 274–295. Oxford University Press for Tata Institute of Fundamental Research, Bombay.

Zawawi, M. H., Saleha, A., Salwa, A., Hassan, N. H., Zahari, N. M., Ramli, M. Z., and Muda, Z. C. (2018). A review: Fundamentals of computational fluid dynamics (cfd). *AIP Conference Proceedings*, 2030(1):020252.